FERMILAB-Proposal-0649

Scientific Spokesperso
F.E. Taylor
Physics Department
North. Ill. Univ.
DeKalb, IL 60115
Phone (815) 753-1773

Proposal to Study Nucleon Structure Functions at High Q^2

D. Bogert, R. Brock, R. Fisk, T.Ohska, L. Stutte, J.K. Walker, J. Wolfson
Fermi National Accelerator Laboratory
Batavia, IL

J. Bofill
~~R. Burg~~, W. Busza, J. Friedman, M. Goodman, H. Kendall,
T. Lyons, T. Mattison, L. Osborne, L. Rosenson,
M. Tartaglia, S. Whitaker, G.P. Yeh
Massachusetts Inst. of Technology
Cambridge, MA

M. Abolins, A. Cohen, J. Ernwein, D. Owen, J. Slate
Michigan State University
East Lansing, MI

F.E. Taylor
Northern Illinois University
DeKalb, IL

Table of Contents

Proposal to Study

Nucleon Structure Functions at High Q^2

Abstract

The ultra small distance structure of the nucleon is to be measured by studying high energy deep inelastic neutrino-nucleon scattering in the Flash Chamber - Proportional Tube calorimeter located in Lab C. The fine grained sampling of this detector allows both the energy and angle of energy flow of the recoil showers to be determined. Thus the structure functions of both neutral current and charged current interactions can be measured. These measurements enable a determination of:

1) The Lorentz structure of the weak neutral current.
2) The Q^2 evolution of the structure functions up to high Q^2.

This will test gauge theories of electro weak interactions and confront the QCD theory of strong interactions in a new high energy range.

Nucleon Structure Functions at High Q^2

P 649 : FNAL, MIT, MSU, N. Ill. Univ.

I) Introduction:

We propose measuring the nucleon structure to ultra small distances by studying high energy deep inelastic neutrino - nucleon scattering in the Lab C Flash Chamber - Proportional Tube Calorimeter. The High Q^2 region $\lesssim 400\ (\mathrm{GeV}/c)^2$ unveiled by the Tevatron will allow structure in the range $\sim 10^{-2}$ fermi to be explored.

With the fine grained shower sampling capability of the Lab C detector, it is possible to measure both the energy as well as the direction of the recoiling hadron shower. This allows a complete reconstruction of the kinematics of both charged current and neutral current deep inelastic neutrino scattering in the narrow band neutrino beam. Hence the Lab C detector can determine the scaling variables $x = Q^2/2\, m_p E_h$ and $y = E_h/E_\nu$ for both of these interactions.

A measurement of the four deep inelastic cross sections: $\frac{d\sigma}{dxdy}$ $(\overset{(-)}{\nu}_\mu + N \rightarrow \overset{(-)}{\nu}_\mu + x)$ and $\frac{d\sigma}{dxdy}$ $(\overset{(-)}{\nu}_\mu + N \rightarrow \mu^\pm + x)$ (N=nucleon-isoscalar target) at the highest possible range of Q^2, x and y, will enable the following tests of our understanding of weak and strong interactions:

1) A comparison of the Lorentz structure of the neutral current interaction at high center of mass energies ($W \sim 30$ GeV) with that at low energies will extend the tested range of gauge theories. In particular this will allow a determination of $\sin^2\theta_W$ of the Weinberg-Salam theory in a new high energy regime.

2) A measurement of the Q^2 evolution of the structure functions F_2 and xF_3 for both neutral current and charged current interactions up to high $Q^2 \sim 400\ (\mathrm{GeV/c})^2$ is an excellent test of the currently popular QCD theory of strong interactions. Furthermore, a detailed comparison of the neutral current structure functions with the charged current structure functions tests that the nucleon structure is independent of the probe and gives a sensitivity to small differences in the strange and charm sea of the nucleon.

Experimentation at FNAL and the SPS has shown that violations to Bjorken scaling at large Q^2 are consistent with the predictions of QCD. However various theoretical ambiguities exist in an interpretation of the data. First order terms in QCD to determine α_s, the strength of the strong interaction coupling constant, are ambiguous to a scale factor. Second order terms must be included to determine the scale of the Q^2 dependence of α_s. This requires experiments at high Q^2. Comparisons of the data at low Q^2 with the QCD theoryhave further difficulties of interpretation. Higher twist effects can account for the scale violations at low Q^2. These effects are very poorly understood but are believed to fall with increasing Q^2 as an inverse power of Q^2. Hence only high $Q^2 \geq 10$ to $20\ (\mathrm{GeV/c})^2$ data can be used to unambiguously confront the QCD theory.[1,2]

Various probes can be used to study the small scale structure of the nucleon. The probe can be a virtual photon in deep inelastic electron or muon scattering. This probe couples to the charges of the quarks and has a $1/Q^4$ propagator dependence which gives a large suppression at high Q^2. Only two structure functions of the nucleon are determined by this type of experiment. For deep inelastic neutrino scattering, because of the large mass of the exchanged $W^{\pm}$ boson in charged currents or the Z^{0} boson in neutral currents, one expects almost no propagator effects at finite Q^2. ($Q^2 \lesssim 400$ $(GeV/c)^2$ propagator effects are ~ 10%). Hence the scattering cross section does not have the strong falloff at large Q^2. Futhermore, since parity is violated in the weak interaction, there are three structure functions in the deep inelastic scattering cross sections which enable one to directly probe the valence quark structure of the nucleon.

Although the structure of the nucleon is believed to be independent of the probe, (good evidence exists en, μn versus νn charged currents) model independent checks of this assumption can be made with an experiment which can simultaneously measure the nucleon structure functions as probed by the neutral current with those which are probed by the charged current. Subtle differences are expected to exist between the structure functions of these two probes, which depend on the difference between the charm and strange quark sea.[3]

At this time, it is believed that there are 6 point-like quarks; 5 quark flavors have been detected and the 6^{th} quark is being intensly searched for. There are many questions about the fundamental structure of matter. Why are there different flavor quarks? Is there another level of structure of matter - a subquark which is used to build quarks? Is color an exact symmetry? Can color be excited and fractionally charged quarks be resolved into integrally charged quarks of different colors? A subquark structure would give rise to an enhancement of $d\sigma/dxdy$ in the low x region at high Q^2. A color excitation would make the deep inelastic cross section rise at large Q^2. These questions demand further experimentation at the highest Q^2. Since the Tevatron will allow a new high range of Q^2 and W to be explored, there is the exciting possibility that some fundamental revelation in our understanding of the structure of matter will occur.

II) Structure Functions - Theoretical Formulation

In this section we present the theoretical formulation of deep inelastic neutrino - nucleon scattering for both the charged current and the neutral current interactions. We will use this formulation to simulate the response of the detector to neutrino events in the narrow band beam.

a) Basic quark model theory:

A neutrino (antineutrino) may interact with a nucleon by exchanging charged heavy bosons $W^{\pm}$, or a neutral heavy boson Z^{o}. In the quark-parton model of the nucleon, this scattering process takes place by the heavy gauge boson interaction with one of the quarks inside the nucleon. These processesare depicted in figure 1. The charged current is flavor changing and pure V-A, and the neutral current is believed to be flavor diagonal to a good approximation and contains a mixture of V-A and V+A amplitudes.

The Lagrangian for the charged current interaction as given in the standard notation of the quark model is:

$$L^{cc} = \frac{-G}{\sqrt{2}}\gamma_\alpha(\nu\gamma_\alpha \quad (1+\gamma_5)\mu)\ (\bar{d}c\ \gamma_\alpha(1+\gamma_5)u) + h.c. \qquad (1)$$

where G is the universal fermi constant = 1.17×10^{-5} GeV^{-2} and dc = d $\cos\theta_c$ + s $\sin\theta_c$, θ_c=Cabibbo angle, and u(x) is the probability that a u flavor quark has a momentum fraction x of the nucleon momentum, etc.

In the SU(2)x U(1) gauge theory of Weinberg-Salam there are two components to the neutral current: the photon and the Z^o boson. These two amplitudes are mixed by an angle θ_w. Hence the neutral current Lagrangian is given by (in the notation of Sakurai and Hung[4] (assuming no flavor changing neutral currents):

$$L^{nc} = \frac{-G}{2}\ \bar{\nu}\gamma_\lambda(1+\gamma_5)\nu \left\{ 1/2 \left[\bar{u}\gamma_\lambda(\alpha+\beta\gamma_5)\bar{u} - \bar{d}\gamma_\lambda(\alpha+\beta\gamma_5)d \right] \right. \qquad (2)$$

$$+1/2 \left[\bar{u}\gamma_\lambda(\gamma+\delta\gamma_5)u + \bar{d}\gamma_\lambda(\gamma+\delta\gamma_5)d \right] + \bar{s}(\gamma'+\delta'\gamma_5)s$$

$$\left. + \text{ possible } \bar{c}c,\ \bar{t}t,\ \bar{b}b \text{ terms} \right\} \quad .$$

For pure V-A, $\alpha = \beta$, and $\gamma = \delta$, but in general we have in the W.S. model:

$\alpha = 1 - 2\ \sin^2\theta w$ $\quad \beta = 1$

(isovector-vector) (isovector - axial vector) (3a)

$\gamma = -2/3\ \sin^2\theta w$ $\quad \delta = 0$

(isoscalar - vector) (isoscalar - axial vector)

(3b)

and with the GIM mechanism:

$$\gamma' = -1/2 + 2/3\ \sin^2\theta\ w, \qquad (3c)$$

$$\delta' = -1/2 \tag{3d}$$

Thus the neutral current interaction is in general not pure V-A since $\sin^2\theta_W \neq 0$.

These interactions lead to the following cross sections for an isoscalar target[3] (The threshold effects for charm production and quark flavors beyond charm are neglected). For charged currents:

$$\left(\frac{d\sigma^{\nu_\mu}}{dxdy}\right)_{cc} = \frac{G^2 m E_\nu}{\pi}\left\{[xq(x) + xs(X) - xc(x)] + (1-y)^2[x\bar{q}(x) + x\bar{c}(x) - x\bar{s}(x)]\right\} \tag{4}$$

and

$$\left(\frac{d\sigma^{\bar{\nu}_\mu}}{dxdy}\right)_{cc} = \frac{G^2 m E_\nu}{\pi}\left\{[x\bar{q}(x) + x\bar{s}(x) - x\bar{c}(x)] + (1-y)^2[xq(x) + xc(x) - xs(x)]\right\} \tag{5}$$

For neutral currents:

$$\left(\frac{d\sigma^{\nu_\mu}}{dxdy}\right)_{nc} = \frac{G^2 m E_\nu}{\pi}\Big\{ xV(x)\,[\delta_1{}^2 + \delta_2{}^2 + (\delta_3{}^2 + \delta_4{}^2)(1-y)^2) \tag{6}$$

$$+(x\bar{u}(x) + x\bar{d}(x))[\delta_1{}^2 + \delta_2{}^2 + \delta_3{}^2 + \delta_4{}^2](1+(1-y)^2)$$

$$+ (xs(x)+x\bar{s}(x))\;[\delta_2{}^2 + \delta_4{}^2]\;(1 + (1-y)^2)$$

$$+ (xc(x) + x\bar{c}(x))\;[\delta_1{}^2 + \delta_3{}^2]\;(1 + (1-y)^2)\Big\}$$

and

$$\frac{d\sigma^{\bar{\nu}_\mu}}{dxdy}_{nc} = \frac{G^2 m E_\nu}{\pi} \left\{ xV(x) \left[(\delta_1{}^2+\delta_2{}^2)(1-y)^2 + (\delta_3{}^2+\delta_4{}^2) \right. \right. \tag{7}$$

$$+ (x\bar{u}(x) + x\bar{d}(x)) [\delta_1{}^2 + \delta_2{}^2 + \delta_3{}^2 \ \delta_4{}^2](1 + \ (1-y)^2)$$

$$+ (xs(c) + x\bar{s}(x)) \ [\delta_2{}^2 + \delta_4{}^2] \ (1 + (1-y)^2)$$

$$+ (xc(x) + x\bar{c}(x)) \ [\delta_1{}^2 + \delta_3{}^2] \ (1 + (1 - y)^2)$$

where: $\delta_1 = 1/2 - 2/3 \ \mathrm{Sin}^2\theta w = u_L = 1/4(\alpha+\beta+\gamma+\delta)$ (8a)

$$\delta_2 = -1/2 + 1/3 \ \mathrm{Sin}^2\theta \ w = d_L = 1/4(\gamma-\alpha+\delta-\beta) \tag{8b}$$

$$\delta_3 = -2/3 \ \mathrm{Sin}^2\theta w = u_R = 1/4 \ (\alpha+\gamma-\beta-\delta) \tag{8c}$$

$$\delta_4 = 1/3 \ \mathrm{Sin}^2\theta w = d_R = 1/4 \ (\gamma+\beta-\alpha-\delta \ ) \tag{8d}$$

and

$$V(x) = u_v(x) + d_v(x) = q(x) - \bar{q}(x)$$

$$q(x) = \sum_i qi(x) \ , \qquad \bar{q}(x) = \sum_i \bar{q}i(x)$$

These cross sections may be written in terms of the familiar structure functions F_1, F_2, F_3 as follows:

$$\frac{d\sigma^{\nu/\bar{\nu}}}{dxdy} = \frac{G^2 m E_\nu}{\pi} \left\{ (1-y)F_2(x,Q^2) + xy^2 F_1(x,Q^2) \pm (1-\frac{y}{2}) xyF_3(x,Q^2) \right\} \tag{9}$$

Neglecting quark transverse momentum and assuming the Callen-Gross relation[5] ($2xF_1=F_2$) we form the following table of structure functions in terms of the scaled quark and antiquark momentum distributions.

Table I

	charged current	neutral current
$F_2^{\nu, \bar{\nu}}$	$x\Sigma(x)=xq(x)+x\bar{q}(x)$	$x\Sigma(x)\ [\delta_1^{\ 2}+\delta_2^{\ 2}+\delta_3^{\ 2}+\delta_4^{\ 2}]$ $+x\Delta^N(x)[\delta_1^{\ 2}+\delta_3^{\ 2}-\delta_2^{\ 2}-\delta_4^{\ 2}]$
$xF_3^{\nu, \bar{\nu}}$	$xV(x)\mp x\Delta^N(x)$ $=xq(x)-x\bar{q}(x)\mp(x\bar{c}(x)-x\bar{s}(x)+xc(x)-xs(x))$	$xV(x)[\delta_1^{\ 2}+\delta_2^{\ 2}-\delta_3^{\ 2}-\delta_4^{\ 2}]$

We note that xF_3 is for both neutral current and charged current interactions a flavor nonsinglet and is a measure of the valence quark x distribution. On the other hand F_2 for charged currents is a pure flavor singlet, the neutral current, however, contains both a singlet ($x\Sigma$) and a non-singlet term ($x\Delta^N$) (expected to be small) and measures the total quark distribution.

b) <u>QCD corrections to deep inelastic scattering</u>

Quantum chromodynamics (QCD) is an SU(3)c color gauge theory which models the interactions between quarks and gluons - the mediator of the strong interaction. In this theory, quarks are arranged in color triplets and have distinct flavors. The strong coupling constant $\alpha s(Q^2)$ becomes weaker at high Q^2 due to an anti-shielding of the gluon field around the bare quark color charge. This antishielding makes perturbation calculations of the theory more reliable at high Q^2.

Holding Q^2 fixed and measuring the structure functions versus x, determines the nucleon structure at a given distance scale. When a Z^o or $W^\pm$ boson strikes a quark at ever increasing Q^2, and thus at ever smaller distances, a quark can be resolved into a quark plus a gluon, and a gluon into a quark-antiquark pair or a gluon pair. These radiative corrections to a quark or a gluon are depicted in figure 2. Hence the scaled quark, and antiquark momentum distributions will depend on Q^2. Since these radiative processes tend to soften the hard boson-quark scattering at high Q^2, one would expect the large $x \gtrsim 0.4$ values of the structure functions F_2 and xF_3 to decrease and the small $x \lesssim 0.2$ values to increase with increasing Q^2. This qualitative behavior has been verified by extensive experimentation.

The Q^2 evolutions of the singlet structure function $F_2(x, Q^2)$ and the nonsinglet structure function $xF_3(x, Q^2)$ are expected to be different. To leading order, xF_3 can evolve by only gluon radiation (figure 2a), whereas $F_2(x, Q^2)$ is sensitive to both gluon radiation and quark-antiquark pair production (figure 2b) as well as indirectly dependent on the triplet gluon process (figure 2c). Hence $F_2(x, Q^2)$ at small x is expected to grow with increasing Q^2 more rapidly than $xF_3(x, Q^2)$.

The behavior of $xF_3(x, Q^2)$ does not provide an incisive test to distinguish between different theories of strong interactions, but does provide a necessary consistency check of QCD. However the singlet structure function $F_2(x, Q^2)$ can distinguish between different theories by the Q^2 behavior of the n=2 moment:

$$\int_0^1 F_2(x,Q^2)\, dx = < x\, \Sigma(Q^2) >_2$$

Only QCD predicts that this moment should decrease with increasing Q^2. Since this behavior is consistent with experimental data, certain other proposed theories are excluded.[6]

QCD makes predictions on the moments of the structure functions F_2 and xF_3. These have been extensively measured and compared with good agreement to theoretical predictions. However, certain ambiguities remain in the interpretation of these data. These ambiguities involve extending the theory to low Q^2. What remains to be measured? There are several contributions that a Tevatron experiment can make:

1) Measure the Q^2 evolution of F_2 and xF_3 up to the very highest value of Q^2. Higher twist terms should be small and thus the theory can be directly tested.

2) Compare the neutral current structure functions with the charged current structure functions. This tests that the structure functions are independent of the probe and checks that the $x\Delta^n(x)$ term is small.

3) Estimate the value of $R = F_L/F_2$, ($F_L(x,Q^2) = F_2(x,Q^2) - 2xF_1(x,Q^2)$) as a function of x for various values of Q^2. This ratio is sensitive to the triple gluon vertex. Since F_2 alone has little sensitivity to the triple gluon vertex there are few other ways of measuring this important aspect of the theory. The measurement of this quantity is very difficult, however.

III) Experimental Interpretation

The simultaneous measurement of $\frac{d\sigma}{dxdy}\ (\overset{(-)}{\nu}_\mu + N \rightarrow \overset{(-)}{\nu}_\mu + x)$ (neutral current) and $\frac{d\sigma}{dxdy}\ (\overset{(-)}{\nu}_\mu + N \rightarrow \mu^{\pm} + x)$ (charged current) will allow a determination of:

1) The couplings $(\delta_1{}^2 + \delta_2{}^2)$ and $(\delta_3{}^2 + \delta_4{}^2)$ and thus the Weinberg angle.

2) The structure functions $F_2(x,Q^2)$, $xF_3(x,Q^2)$ for both the neutral current and the charged current interaction.

To extract the information above, we formulate two tests of the data. The emphasis is on the x distribution of the neutral current, which to date has been rather poorly measured.[7, 8]

a) Test 1

The ratios of the neutral current cross sections to the charged current cross sections determine the couplings $(\delta_1{}^2 + \delta_2{}^2)$ and $(\delta_3{}^2 + \delta_4{}^2)$. This determination is independent of uncertainties in the incident neutrino flux. Any deviation of these ratios from a constant indicates the presence of the antiquark sea or unexpected structure in the neutral and/or charged current propagators at large Q^2.

Neglecting strange and charm quarks, and separately integrating the numerator and demon.inator over y we have:

$$R^{\nu_\mu}(x) = \frac{\frac{d\sigma^{\nu_\mu(nc)}}{dx}}{\frac{d\sigma^{\nu_\mu\ (cc)}}{dx}} = a + \frac{x\bar{q}(x)\ 4/3\ (b-a)}{xq(x) + 1/3\ x\bar{q}(x)} \tag{10a}$$

and:

$$R^{\bar{\nu}_\mu}(x) = \frac{\frac{d\sigma^{\bar{\nu}_\mu(nc)}}{dx}}{\frac{d\sigma^{\nu_\mu(cc)}}{dx}} = 3\bar{a} + \frac{x\bar{q}(x)\ (4/3\ b-4\bar{a})}{1/3\ x\ q(x) + x\bar{q}(x)} \tag{10b}$$

where:

$$a = \delta_1^{\,2} + \delta_2^{\,2} + 1/3\ (\delta_3^{\,2} + \delta_4^{\,2})$$

$$\bar{a} = 1/3\ (\delta_1^{\,2} + \delta_2^{\,2}) + \delta_3^{\,2} + \delta_4^{\,2}$$

$$b = \delta_1^{\,2} + \delta_2^{\,2} + \delta_3^{\,2} + \delta_4^{\,2}$$

The values of these ratios at large x determine the couplings $(\delta_1^{\,2} + \delta_2^{\,2}) = 3/8(3a-\bar{a})$ and $(\delta_3^{\,2} + \delta_4^{\,2}) = 3/8(3\bar{a}-a)$ and hence, in the Weinberg-Salam model, the value of $\sin^2\theta_W$. In terms of the coupling constants of Hung and Sakurai (equation 2), this ratio test gives:

$$\delta_1^2 + \delta_2^2 = 1/8 \left\{ (\alpha+\beta)^2 + (\gamma + \delta)^2 \right\} \quad \text{and}$$

$$\delta_3^2 + \delta_4^2 = 1/8 \left\{ (\alpha-\beta)^2 + (\gamma - \delta)^2 \right\} .$$ Hence $\alpha^2 + \beta^2 + \gamma^2 + \delta^2$, and $\alpha\beta+\gamma\delta$ are determined. There remain two ambiguities: 1) VA $\alpha \leftrightarrow \beta$, $\gamma \leftrightarrow \delta$, and 2) isoscalar - isovector $\alpha \leftrightarrow \gamma$, $\beta \leftrightarrow \delta$, which have to be resolved by other experiments.[4] More importantly, the establishment that these ratios are constant shows that the x dependence of the neutral current structure functions are the same as the charged current structure functions. This test is free of flux normalization uncertainties.

The antiquark remainder terms can be measured by observing any deviation of the ratios from a constant at small x where the $x\bar{q}$ term is expected to be at its maximum. However if $\sin^2\theta_W = 0.25$, then $a = 0.297$, $\bar{a} = 0.130$ and $b = 0.320$. Thus $4/3(b-a) = 0.031$ and $4/3\ b-4\bar{a} = 0.093$ and consequently the $x\bar{q}$ term is suppressed offering little sensitivity to the antiquark sea. Thus the ratios should be quite constant.

b) Test 2

By computing the sums and differences of the neutral current and charged current neutrino and antineutrino cross sections, the structure functions $F_2(x, Q^2)$ and $xF_3(x, Q^2)$ may separately be determined for each interaction. Referring to equation 9 and Table I, we have (assuming $R = 0$)[5]

Charged-Currents:

$$\frac{d\sigma^{\nu}}{dxdy} + \frac{d\sigma^{\bar{\nu}}}{dxdy} = \frac{G^2 mE_\nu}{\pi} F_2(x,Q^2)\ (1 + (1 - y)^2) \tag{11a}$$

$$\frac{d\sigma^{\nu}}{dxdy} - \frac{d\sigma^{\bar{\nu}}}{dxdy} = \frac{G^2 mE_\nu}{\pi} xF_3(x)\ (1 - (1-y)^2) \tag{11b}$$

Neutral Currents:

$$\frac{d\sigma^{\nu}}{dxdy} + \frac{d\sigma^{\bar{\nu}}}{dxdy} = \frac{G^2 mE_\nu}{\pi} (\delta_1{}^2 + \delta_2{}^2 + \delta_3{}^2 + \delta_4{}^2)F_2(x,Q^2)(1+(1-y)^2) \tag{12a}$$

$$\frac{d\sigma^{\nu}}{dxdy} - \frac{d\sigma^{\bar{\nu}}}{dxdy} = \frac{G^2 mE_\nu}{\pi} (\delta_1{}^2 + \delta_2{}^2 - \delta_3{}^2 - \delta_4{}^2)xF_3(x,Q^2)(1-(1-y)^2) \tag{12b}$$

Since $(\delta_1{}^2 + \delta_2{}^2)$ and $(\delta_3{}^2 + \delta_4{}^2)$ are computed by Test 1, the structure functions for the neutral currents are completely determined. These tests depend on the relative flux normalization between the neutrino and antineutrino narrow band beam exposures. This relative normalization should be good to $\sim$ 3%, and in fact the measurement errors of this test should be dominated by statistical uncertainties.[9]

We can integrate $d\sigma/dxdy$ over x to formulate another ratio test. By computing $\frac{d\sigma}{dy}^{(\bar{\nu})}nc \;/\frac{d\sigma}{dy}^{(\bar{\nu})}cc$, we compare the y dependence of the neutral current scattering to that of the charged current scattering. This comparison determines again the coupling constants $(\delta_1{}^2 + \delta_2{}^2)$ and $(\delta_3{}^2 + \delta_4{}^2)$ as well as the ratio of the total antiquark momentum fraction to the total quark momentum fraction. However this information can be extracted from Test 1 and 2 above. Hence this y dependence ratio test will only serve as a useful consistency check.

The results of Test 2 directly confront QCD. This analysis will provide a direct test of the Q^2 evolution of the structure functions for both charged current and neutral current interactions.

IV. Design of the Experiment

a) Method

The incident neutrino energy must be known to determine the neutral current kinematics. Thus the data have to be taken in the narrow band beam. The calorimeter will determine the energy and angle of the recoil hadron shower and the recoil muon momentum in the case of the charged current event. This information determines the complete neutral current kinematics (0c fit) and over determines the charged current events. The kinematics for 500 GeV incident neutrino energy - a typical value, is shown in figure 3.

To reduce the uncertainties in the comparison of charged current events with neutral current events, a subclass of charged current events will be analyzed with the same cuts which are applied to the neutral current events. Since the kinematics of this subclass of events is overdetermined by using the muon momentum, an important check of the method of analyzing the neutral currents can be performed.

In the narrow band beam, the energy of the neutrino is fixed by measuring the angle of the neutrino about the K/π momentum direction. The K/π ambiguity for neutral current events is resolved by demanding that the recoil hadron energy of the event be greater than the neutrino energy from $\pi \rightarrow \mu\nu$ decay at that particular angle. This results in a y_{min} cut at low y. The incident neutrino angle is measured by the radius of vertex of the neutrino interaction and the average distance of the K/π decay point from the neutrino detector.

A Monte Carlo simulation of the energy versus radius of the proposed narrow band beam D-61G is shown in figure 4. This was computed by taking the K/π momentum to be 600 GeV/c and assuming gaussian angular and momentum divergences of $\sigma(\theta\,) \backsim 0.05$ mrad and $\sigma p/p \backsim 5\%$ respectively. The corresponding energy resolution versus radius is shown in figure 5.

b) Resolutions:

The kinematic variables of interest are $x = Q^2/2m_pE_h$, $y = E_h/E_\nu$ and $Q^2 = 2E_\nu E_\nu'(1 - \cos\theta_\nu')$ (E_ν' and θ_ν' $\rightarrow$, E_μ', θ_μ' respectively for charged current events.) By the small angle approximation:

$$Q^2 \cong E_\nu E_\nu'\theta_\nu'^2 \cong \frac{(E_h\,\theta\,h)^2}{(1 - y)}, \text{ thus } x = \frac{E_h\,\theta\,h^2}{2m_p(1-y)}$$

The resulting errors in x are then:

$$\left(\frac{\sigma x}{x}\right)^2 = 4\left(\frac{\sigma\theta}{\theta}\right)^2 + \frac{1}{(1-y)^2}\left(\frac{\sigma Eh}{Eh}\right)^2 + \left(\frac{y}{(1-y)}\right)^2\left(\frac{\sigma E\nu}{E\nu}\right)^2$$

and the corresponding measurement errors in y are:

$$\left(\frac{\sigma y}{y}\right)^2 = \left(\frac{\sigma E\nu}{E\nu}\right)^2 + \left(\frac{\sigma Eh}{Eh}\right)^2$$

Only the hadron shower energy and angle are measured in neutral current interactions. Figures 6 and 7 show the hadron energy and shower angle distributions respectively for accepted neutral current events. Approximately 70% of the events have a hadron energy below 200 GeV. Good angular resolution at "low" energies is important even at the Tevatron. The energy and angle resolutions are discussed in Appendix A.

The resolutions in x, using $\sigma(\theta_h)$ given by figure A6 for various values of y at E_ν = 500 GeV as shown in figure 8. The primary error in σ_x is caused by the uncertainty in θ_h. The resolution in x degrades as y increases. The contribution due to Fermi motion of the target nucleons is estimated to be $\frac{\sigma x}{x} \approx 15\%$. Hence the uncertainties in x are primarily caused by the uncertainty in θ_h over much of the y region. Estimating $\sigma(E\nu)/E\nu \sim 10\%$ and $\sigma(E_h)/E_h \sim \frac{100\%}{\sqrt{E_h}}$ for $E_h >$ 200 GeV (proportional tubes pulse height) and $\sigma(Eh)/Eh \sim 7\%$ for Eh <200 GeV (flash chambers cell counting), we obtain the resolution in y given by figure 9.

In section VI we will show by a Monte Carlo simulation that these x and y resolutions are adequate to discern QCD effects in the $Q^2 \lesssim 400$ $(GeV/c)^2$ range, and to make a good comparison of the neutral current structure functions with charged current structure functions.

c) <u>Beam Energy:</u>

A K/π momentum of 600 GeV/c is chosen to compromise between high energy (large Q^2), and event rate. The Q^2 - y values for various choices of x are given in figure 10. We see that $Q^2 \lesssim 400$ $(GeV/c)^2$ is accessible. In figure 11, we have plotted the hadron mass distribution for neutrino-neutral current events. Masses up to $\sim$30 GeV/c^2 are accessible.

V) Event Rates:

The event rates in the narrow band beam D-61G (L. Stutte)[10] in a 100 fiducial ton (340 Ton total) lab C detector are given in Table II . The K/π momentum was chosen to be 600 GeV/c at the Tevatron operating at 1000 GeV. The beam exposure was taken at 4.4 x 10^{18} protons on target for antineutrino running and 1.0 x 10^{18} protons on target for neutrino running. This corresponds to one year of beam at the "standard" Tevatron delivering 10^{13} protons on target each 60 seconds. Both the neutral current and the charged current event rates include the y_{min} cut to separate neutrinos for K decay from neutrinos from π decay. No y_{min} cut has been applied to the π decay events.

Table II

		K	π	Total
Neutral Current	ν	5000	3960	8960
	$\bar{\nu}$	1000	4920	5920
charged current	ν	16700	12000	28700
	$\bar{\nu}$	2900	14500	17420

grand total 61,000

With this beam exposure, the number of events per 12 GeV^2 bin in Q^2 is shown in figure 12. Thus, the measurable Q^2 range extends to $Q^2 \sim 400$ $(GeV/c)^2$.

VI) Monte Carlo Simulation

a) Method

In this section we describe the results of a monte carlo simulation of the neutral current and the charged current deep inelastic scattering in the narrow band beam. The object is to generate events with QCD effects, experimental uncertainties, and the statistics imposed by the event rates of Table II.

The elements of the simulation are:

1) The narrow band beam D-61G with $P_{K/\pi} = 600$ GeV/c, $\sigma(\theta) = 0.05$ mrad, $\sigma p/p \sim 5\%$. (See figures 4 and 5).

2) The experimental uncertainties of the hadron energy and angle determination given by figures 4 and 6 of Appendix A.

3) The shower containment requiring 99% longitudinal and 95% lateral (see figure 3 Appendix A) containment.

4) The neutrino-nucleon cross sections given by equations 4 through 7, but neglecting the strange and charm sea. $\sin^2\theta_W = 0.25$.

5) The QCD effects are put into $F_2(x,Q^2)$ and $xF_3(x,Q^2)$ using the parameterization of Buras and Gaemers.[11] $R = F_L(x,Q^2)/F_2(x,Q^2)$ is taken to be 0.

6) The statistics imposed by 5000 neutrino events and 1000 antineutrino events.

The simulated data are analyzed to extract a cross section $\frac{d\sigma}{dxdy}$ corrected for experimental effects as follows:

$$\frac{d\sigma}{dxdy} = \frac{\frac{dN}{dxdy}}{\frac{dM}{dxdy}} \left(\frac{d\sigma}{dxdy} \text{ theory}\right)$$

where $\frac{dN}{dxdy}$ = accepted Monte Carlo events with QCD effects, experimental measurement uncertainties, and shower containment; $\frac{dM}{dxdy}$ = accepted Monte Carlo events without QCD, but everything else mentioned above, and $\frac{d\sigma}{dxdy}$ theory = monte carlo generating function (x and y distributions) of $\frac{dM}{dxdy}$. The "measurement" should be roughly independent of the choice of $\frac{dM}{dxdy}$ and its generator $\frac{d\sigma}{dxdy}$ theory.

b) <u>Results</u>

The results of Test 1, where we compute the ratio of neutral current cross sections to charged current cross sections for both neutrino and antineutrino interactions, are shown in figures 13a and 13b. From this ratio test, we determine the value of $(\delta_1{}^2 + \delta_2{}^2) = 0.29 \pm 0.01$ and $(\delta_3{}^2 + \delta_4{}^2) = 0.035 \pm 0.008$, and finally we retrieve $\mathrm{Sin}^2\theta_W = 0.25 \pm 0.01$.

The extraction of the structure functions F_2 and xF_3 in Test 2 is accomplished by taking the sum and differences of the neutrino and anti-neutrino cross sections and is therefore subject to the neutrino flux normalization errors. These errors have been estimated to be $\sim$ 3 % .[9] The results of this test are shown in figure 14 for the neutral current interactions and in figure 15 for the charged current interactions. The lines through the data are the input functions with QCD effects according to Buras and Gaemers.

To see the Q^2 evolution of the structure functions more directly, we plot $F_2(x,Q^2)$ for a given constant value of x versus Q^2. These are shown in figures 16 and 17 for neutral currents and charged currents respectively. The lines through the data are the input functions of Buras and Gaemers. The data follow the input functions quite closely, showing that the measurement of the structure functions is limited by statisticaland not systematic errors due to resolution smearing effects. From these graphs it is evident that most of the Q^2 dependence is in the region $Q^2 < 50\ (GeV/c)^2$. Above $Q^2 \sim 100\ (GeV/c)^2$, $F_2(x,Q^2)$ for constant x is almost flat.

Since the QCD effects are logarithmic, the variation with Q^2 of $F_2(x,Q^2)$ for Q^2 between 50 $(GeV/c)^2$ and 400 $(GeV/c)^2$ is typically less than $\sim$ 20%. Hence, in the high Q^2 region, scaling should again be approximately true. Any deviation from the predictions of QCD should be quite striking. In fact, boson propagator effect should be $\sim$ 10% for $Q^2 \sim 400\ (GeV/c)^2$ and should eventually dominate the QCD effects at high Q^2.

Finally, to make the comparison between neutral current structure functions and the charged current structure functions more explicit, we plot the ratios of the two. This is shown in figures 18 and 19. Hence, detailed comparisons of the two interactions will be possible, and in particular the smallness of the term $x\Delta^N(x)$ (see Table I) can be measured.

Multi-lepton Events and New Phenomena

Some hints that there may be interesting new phenomena lurking at higher energies is given by the observation at Fermilab of some extraordinary events that do not readily fit into the accepted mold. These "super" events have visible energy greater than 100 GeV and are characterized by extremely high muon energies. If these events do in fact represent a new interaction seen at Fermilab and not at CERN because of the somewhat harder neutrino spectrum, then the Tevatron neutrino beam could be an extremely copious source of these events. Any attempt at estimating the rates are highly conjectural but if we assume a phase space type excitation with a threshold of 10 GeV then we might expect several hundred such events in our detector in a year's time.

We emphasize that our detector has excellent angular resolution ($\sim$1mr) and good $P_\perp$ resolution of the hadrons ($\sim$0.5 - 1.0 GeV/c) permitting detailed analysis of these new events that could lead to an understanding of their origin.

VII) Requests

To achieve adequate momentum resolution at Tevatron energies, we require drift chambers between the toroids as described in Appendix A. We require $\sim$ one year of narrow band beam at $\sim 10^{13}$ protons/spill, 1 spill/minute, (5.4×10^{18} protons on target) on the narrow band beam train.

VIII) Conclusions:

We can measure the nucleon structure function for both charged currents and neutral currents to very high Q^2 and thereby test QCD. In addition, we will test the Weinberg-Salam Theory in a new energy range. The very fine granularity of the detector will allow many details of the high energy neutrino interactions to become visible.

Footnotes and References

1) J. Ellis; "Status of Perturbative QCD", Photon-Lepton Conf. Fermilab (1979).

2) R.M. Barnett; "Testing QCD with Structure Functions at Tevatron Energies", Fermilab Tevatron Muon-Neutrino Workshop (1980).

3) *A.J. Buras; Fermilab - Pub - 79/17-thy*

4) J.J. Sakurai; International School of Subnuclear Physics, Erice, Sicily (1976).

5) In the Monte Carlo calculations of this proposal, we have assumed that $R = F_L(x,Q^2)/F_2(x,Q^2) = 0$. However, there are good theoretical reasons and some experimental data to believe that this assumption is not true. In fact, the Q^2 evolution of $F_L(x,Q^2)$ depends critically on the gluon density. This in turn depends on the gluon self coupling (figure 2c), which is a crucial element of the Yang - Mills structure of QCD. Hence there is a strong motivation for attempting the difficult measurement of this quantity. (See E. Reya; DESY 79/15, and G. Altarelli and G. Martinelli; Phys. Lett. 76B, 89(1978)).

In principle, R may be determined by measuring:

$$\frac{d\sigma^{\nu}}{dxdy} + \frac{d\sigma^{\bar{\nu}}}{dxdy} = \frac{G^2 m E_\nu}{\pi} F_2(x,Q^2) \left[1 + (1-y)^2 - Ry^2\right]$$

at a fixed x and Q^2, while varying y. Thus, the incident neutrino energy must be varied while holding E_h constant. This procedure is aided by the wide range of energies in the Tevatron narrow band beam.

By the equation above, the extraction of $F_2(x,Q^2)$ depends on R. But $xF_3(x,Q^2)$ does not, since it is determined by the differences of cross sections. Altarelli and Martinelli estimate that R will be large at small x and Q^2, and will become smaller as both Q^2 and x increase. For $Q^2 \sim 100(\text{GeV/c})^2$, $R \lesssim 0.1$, thus at $y = 0.9$, R being non zero contributes less than a 8% effect to the extraction of $F_2(x,Q^2)$. At $Q^2 \sim 2(\text{GeV/c})^2$ and $y \sim 0.9$, the effect of R will be $\lesssim$ 24% and should be measurable at least for the charged current data.

6) E. Reya; DESY 79/30.

7) C. Baltay, et al., Phys. Rev. Lett 44, 916(1980)

8) U. Amaldi; "Advances in Semileptonic Currents", Neutrino-79 Bergen, Norway (1979).

K. Winter; "Review of Experimental Measurements of Neutral Current Weak Interactions", Photon-Lepton Conf. Fermilab (1979).

9) M. Shaevitz; "E-616 - Lab E Neutrino Detector Present Capabilities and Future Plans", Fermilab Tevatron Muon-Neutrino Workshop (1980).

10) L. Stutte; TM-841 (1979).

11) A.J. Buras and K.J.F. Gaemers; Nuc. Phy. B132, 249(1978).

Figure Captions

Figure 1a: The charged current interaction: flavor changing

Figure 1b: The neutral current interaction: flavor diagonal

Figure 2a: gluon radiation by bremsstrahlung

Figure 2b: quark-antiquark pair production

Figure 2c: gluon triple vertex

Figure 3: Neutral current kinematics for a typical neutrino energy.

Figure 4: The energy versus radius for neutrinos from K and from π decay. $P_{K/\pi} = 600$ GeV/c

Figure 5: The neutrino energy resolution for the proposed D61G beam with $\frac{\sigma p}{p} \sim 5\%$ and $\sigma(\theta) \sim 0.05$ mrad.

Figure 6: The expected hadron energy distribution of neutral current events in the neutrino narrow band beam.

Figure 7: The expected polor angle distribution.

Figure 8: The resolution in $x = Q^2/2m_p E_h$ as a function of x for various values of y. The resolutions in θ_h, E_h are given in Appendix A. $E_\nu = 500$ GeV.

Figure 9: The resolution in $y = E_h/E_\nu$ as a function of y.

Figure 10: Q^2 versus y for various values of x for $E_\nu = 500$ GeV. Q^2 values up to 400 $(\text{GeV/c})^2$ are accesible. Cuts in a given Q^2 range limit the x range, e.g. low x are inaccessible at large Q^2.

Figure 11: The hadron mass distribution for $P_{K/\pi} = 600$ GeV/c narrow band beam neutrino events.

Figure 12: The experimental Q^2 distribution for neutrino and antineutrino exposures.

Figure 13a: The results of Test 1: The ratio of neutral currents to charged currents for neutrinos.

Figure 13b: The result of Test 1 for antineutrinos.

Figure 14a: The reconstructed neutral current structure functions for $2 \leq Q^2 \leq 40$ $(GeV/c)^2$. The solid line is the input function for $F_2(x,Q^2)$ and the dotted line in the input function of $xF_3(x,Q^2)$ from Buras and Gaemers.

Figure 14b: $40 \leq Q^2 \leq 80$ $(GeV/c)^2$

Figure 14c: $80 \leq Q^2 \leq 180$ $(GeV/c)^2$

Figure 14d: $180 \leq Q^2 \leq 500$ $(GeV/c)^2$

Figure 15a: The corresponding structure functions for the charged current events analyzed in the same manner, with the same cuts as the neutral current events. $2 \leq Q^2 \leq 40$ $(GeV/c)^2$

Figure 15b: $40 \leq Q^2 \leq 80$ $(GeV/c)^2$

Figure 15c: $80 \leq Q^2 \leq 180$ $(GeV/c)^2$

Figure 15d: $180 \leq Q^2 \leq 500$ $(GeV/c)^2$

Figure 16: $F_2(x,Q^2)$ for neutral current events for a constant x versus Q^2. The lines through the data are the QCD input functions of Buras and Gaemers.

Figure 17: $F_2(x,Q^2)$ versus Q^2 for constant x for charged currents.

Figure 18: The ratio of F_2 - neutral current to F_2 - charged currents for given Q_2 bins

Figure 19: The ratio xF_3 - neutral current to xF_3 charged currents for given Q^2 bins

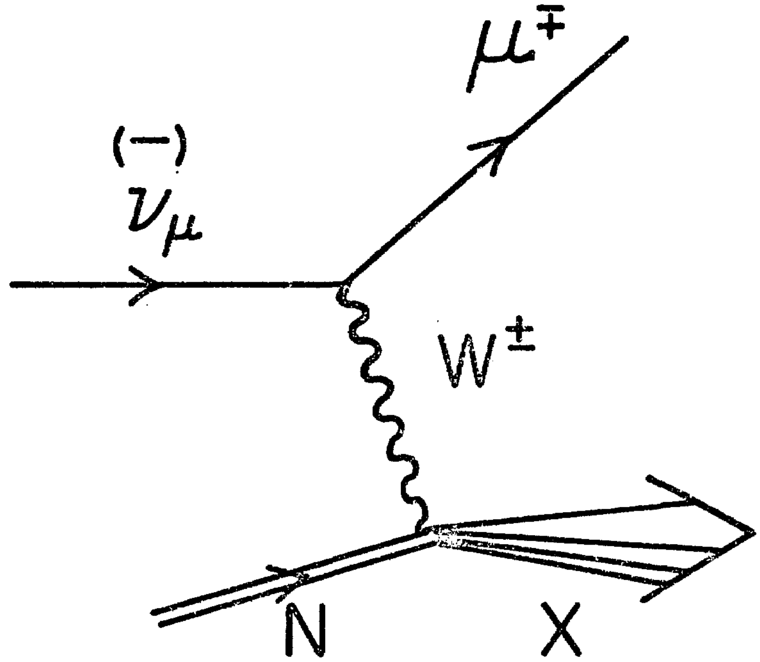

CHARGED CURRENT

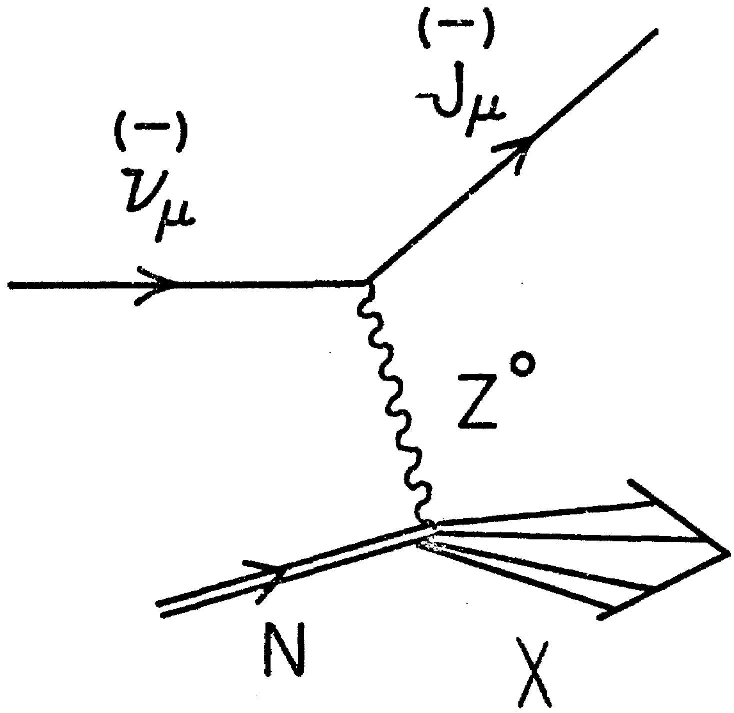

NEUTRAL CURRENT

Figure 1

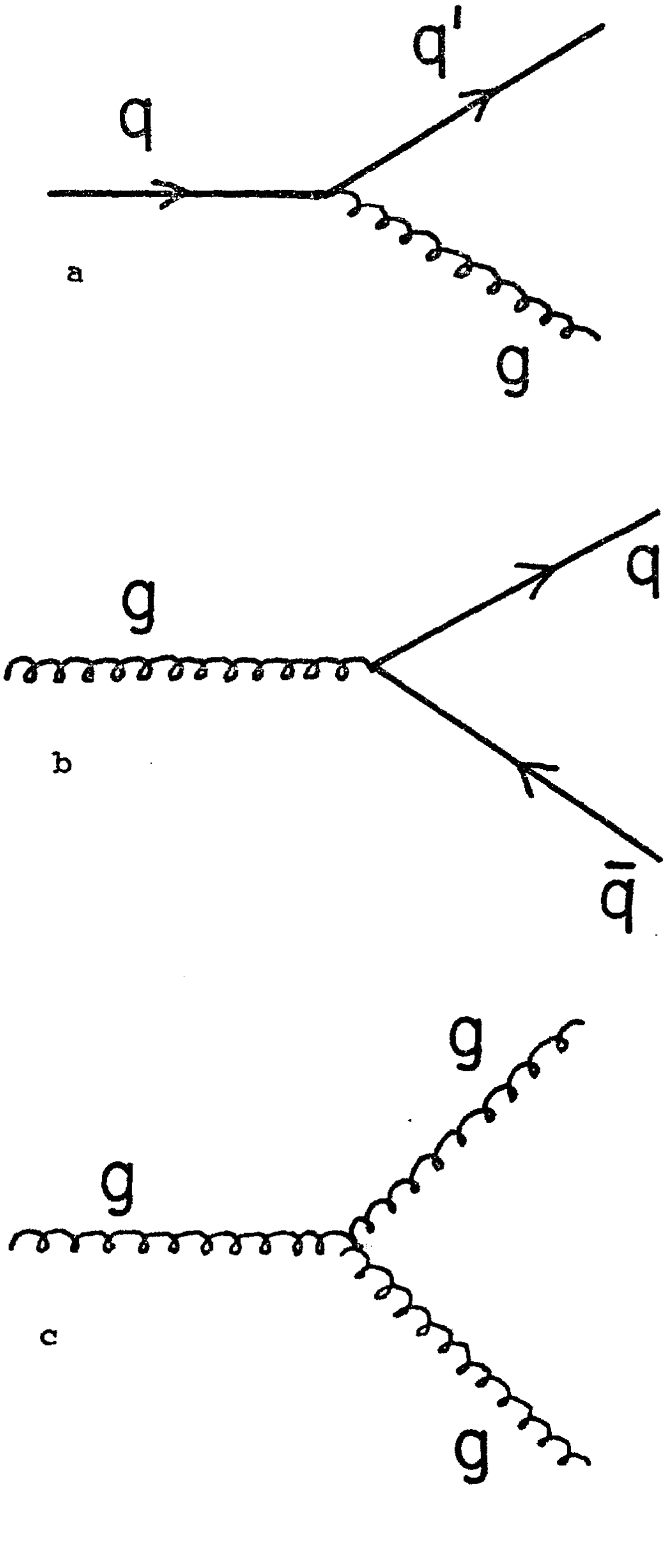

Figure 2

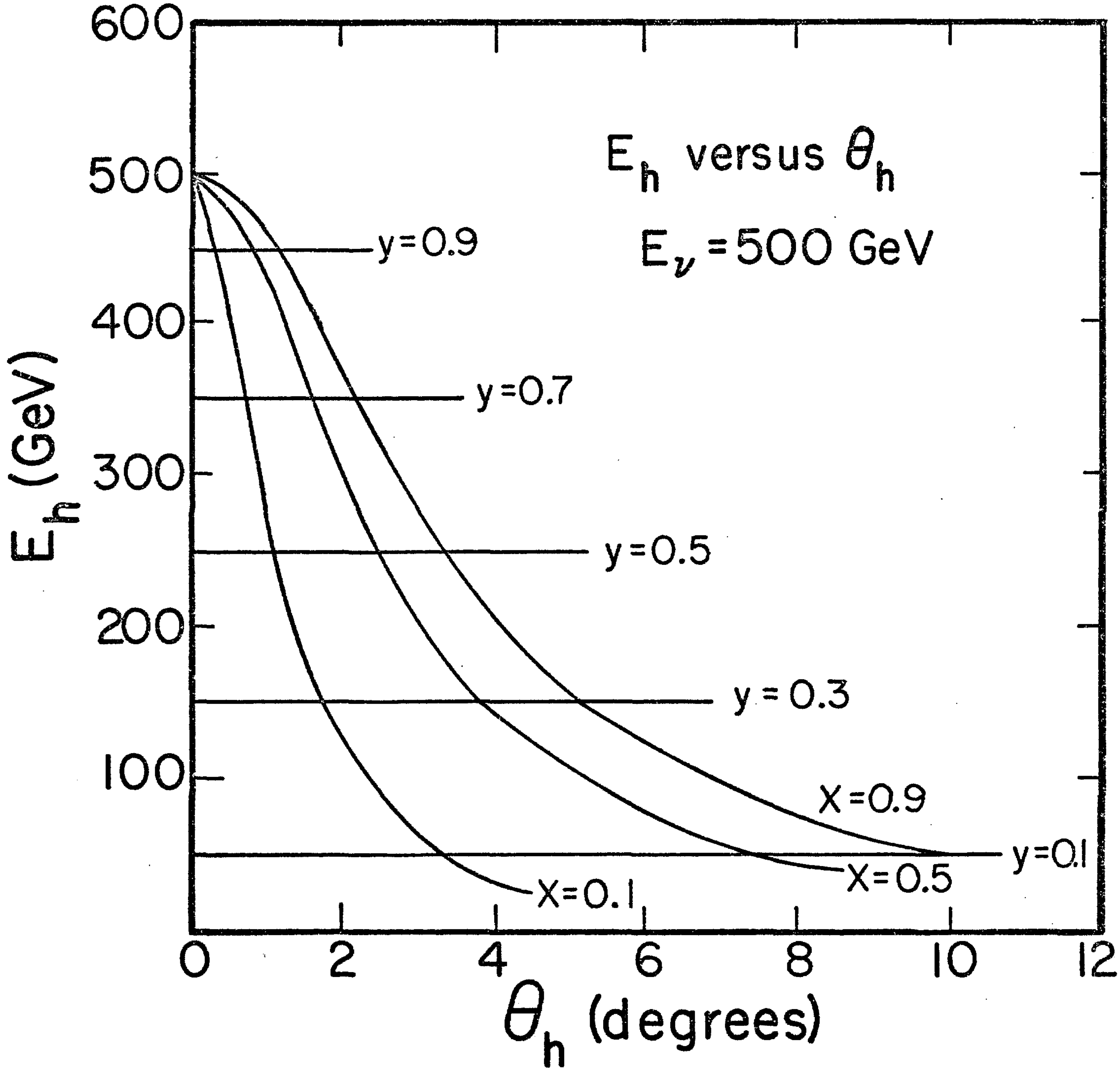

E_h versus θ_h
E_ν = 500 GeV
y=0.9
y=0.7
y=0.5
y=0.3
y=0.1
X=0.9
X=0.5
X=0.1
600
500
400
300
200
100
0
2
4
6
8
10
12
E_h (GeV)
θ_h (degrees)

Figure 3

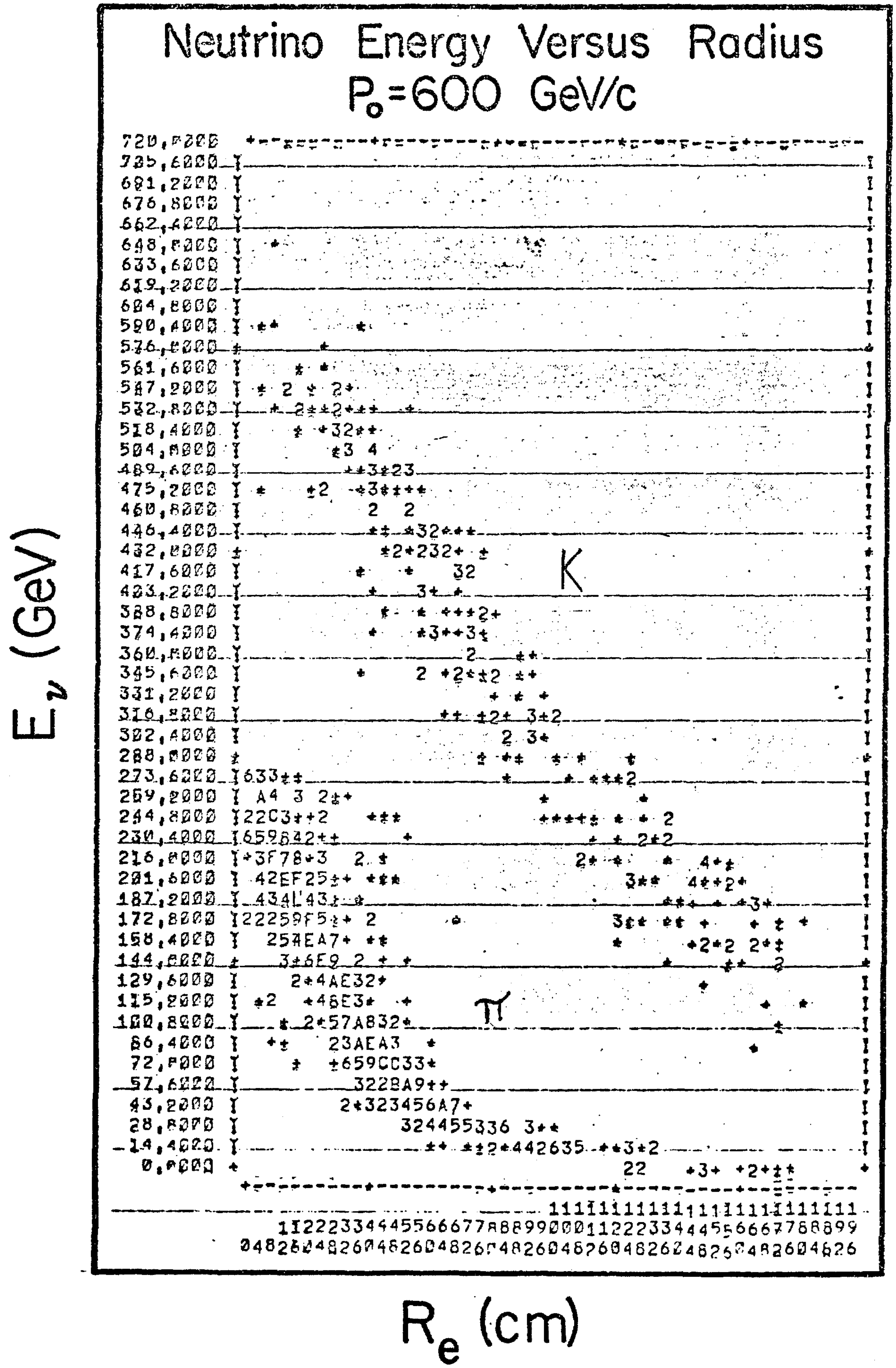
Neutrino Energy Versus Radius
P_o=600 GeV/c
K
π
E_ν (GeV)
R_e (cm)

Figure 4

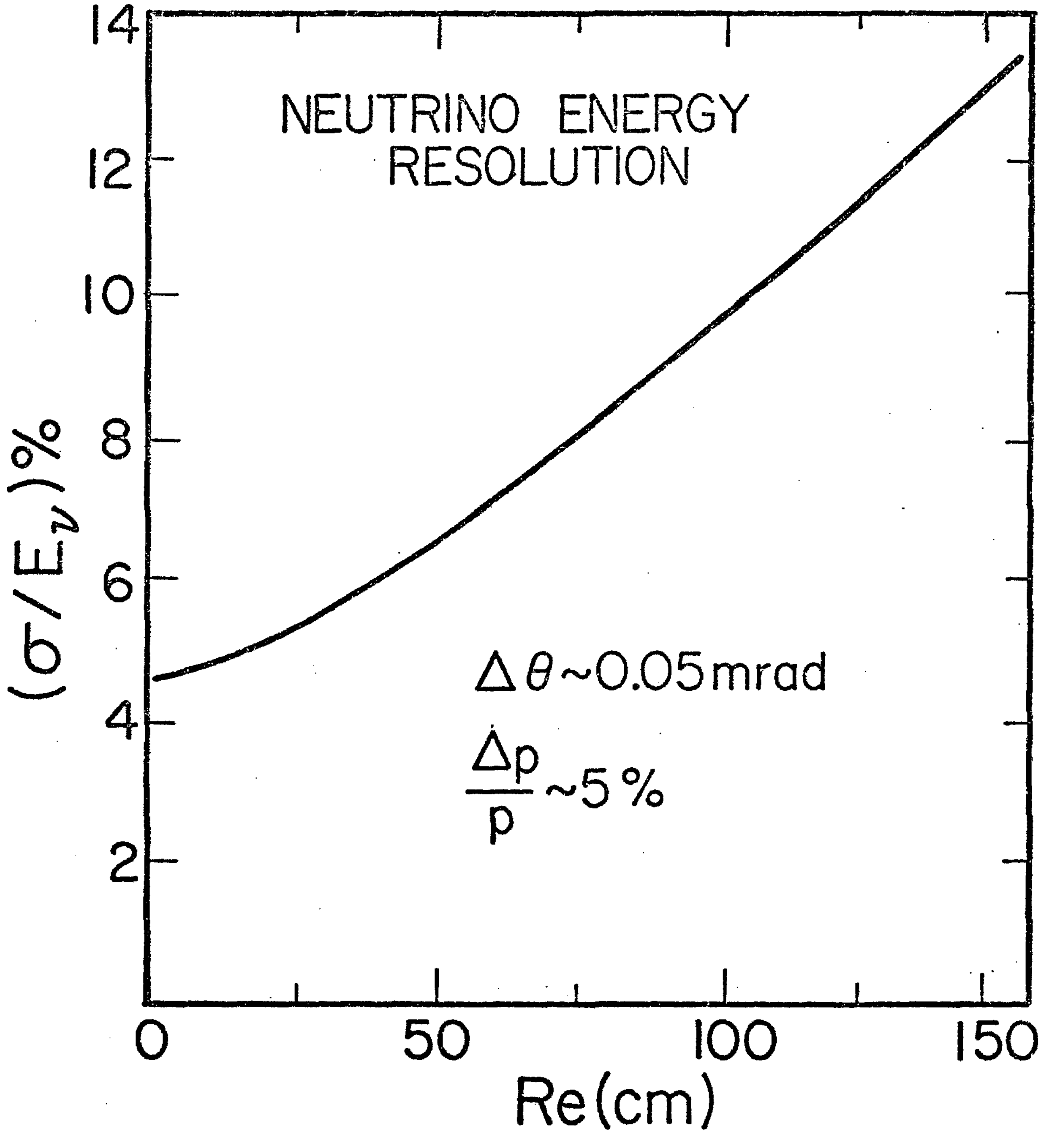
NEUTRINO ENERGY
RESOLUTION
$\Delta\theta \sim 0.05$ mrad
$\frac{\Delta p}{p} \sim 5\%$
$(\sigma/E_\nu)\%$
Re(cm)
0
50
100
150
2
4
6
8
10
12
14

Figure 5

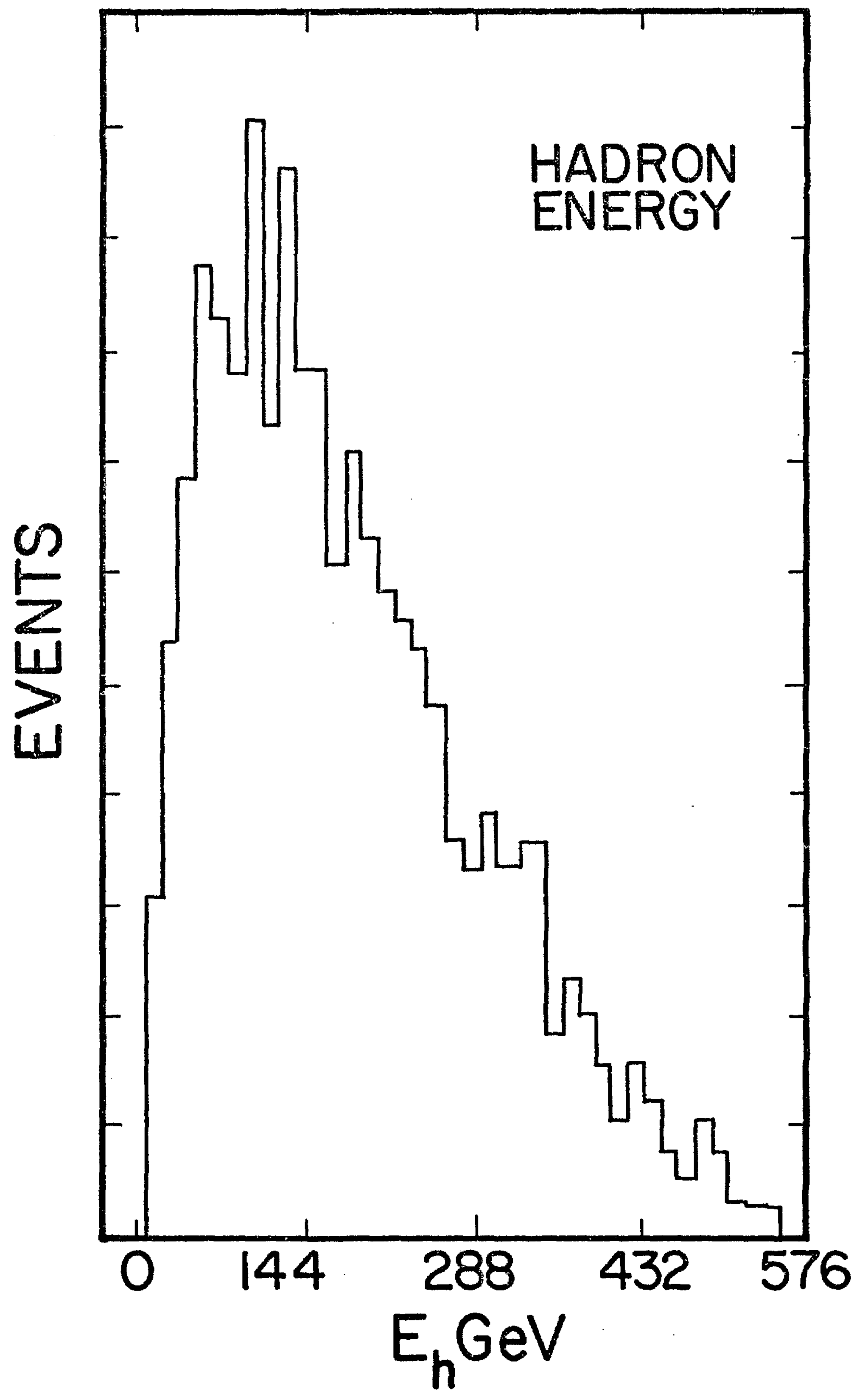

Figure 6

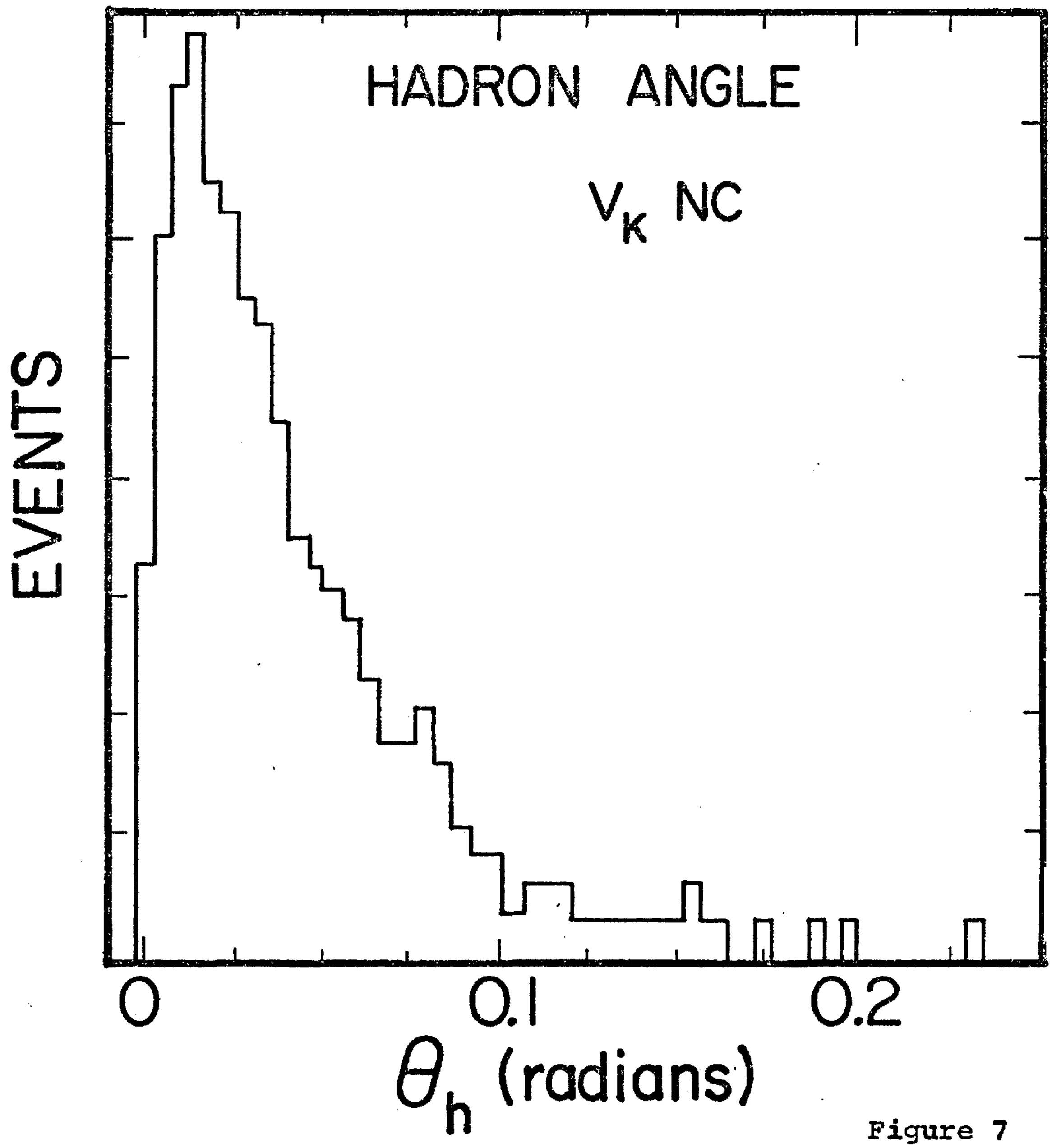

Figure 7

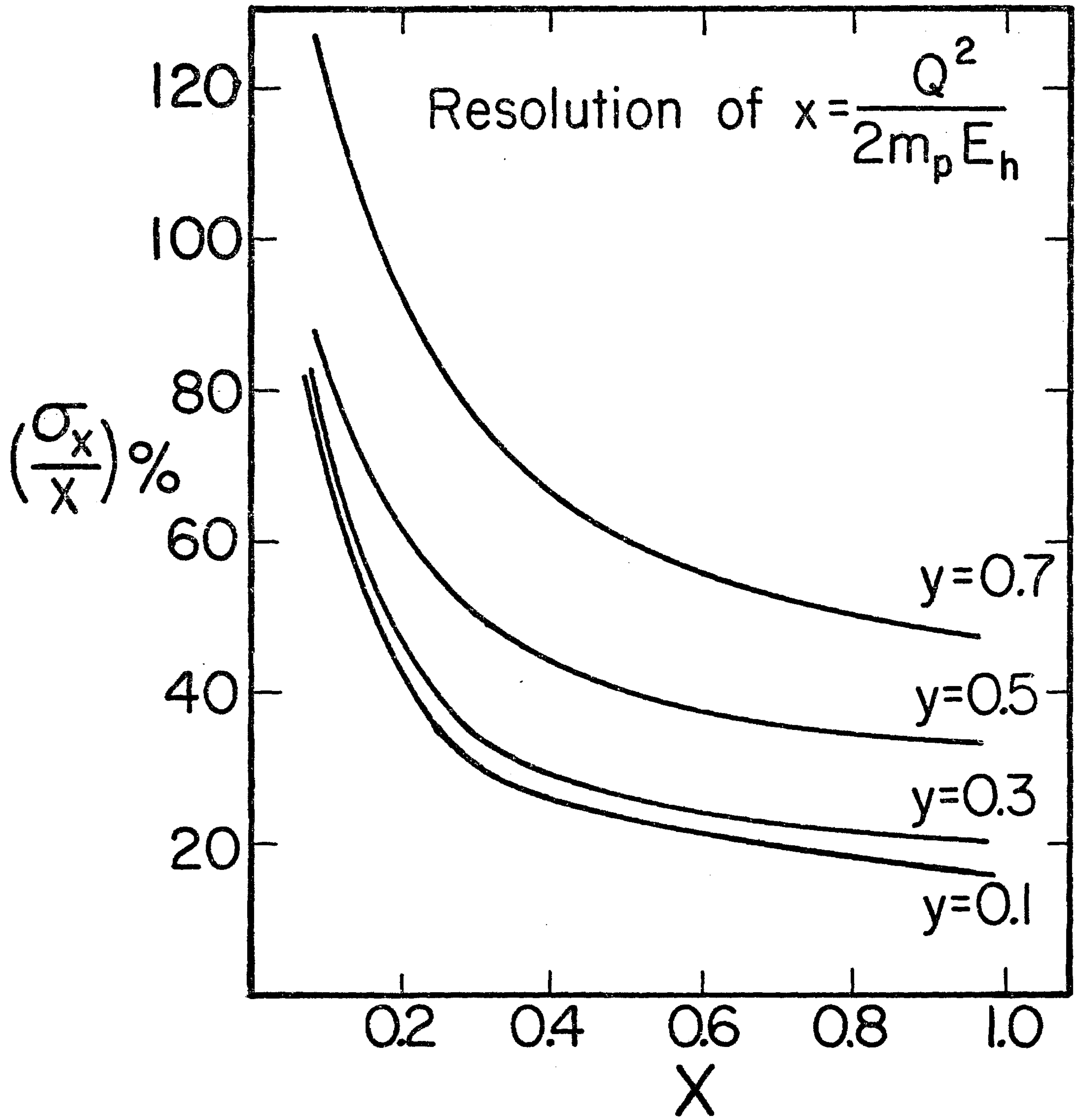

Resolution of $x = \frac{Q^2}{2m_p E_h}$
120
100
80
60
40
20
$\left(\frac{\sigma_x}{x}\right)\%$
y=0.7
y=0.5
y=0.3
y=0.1
0.2
0.4
0.6
0.8
1.0
X

Figure 8

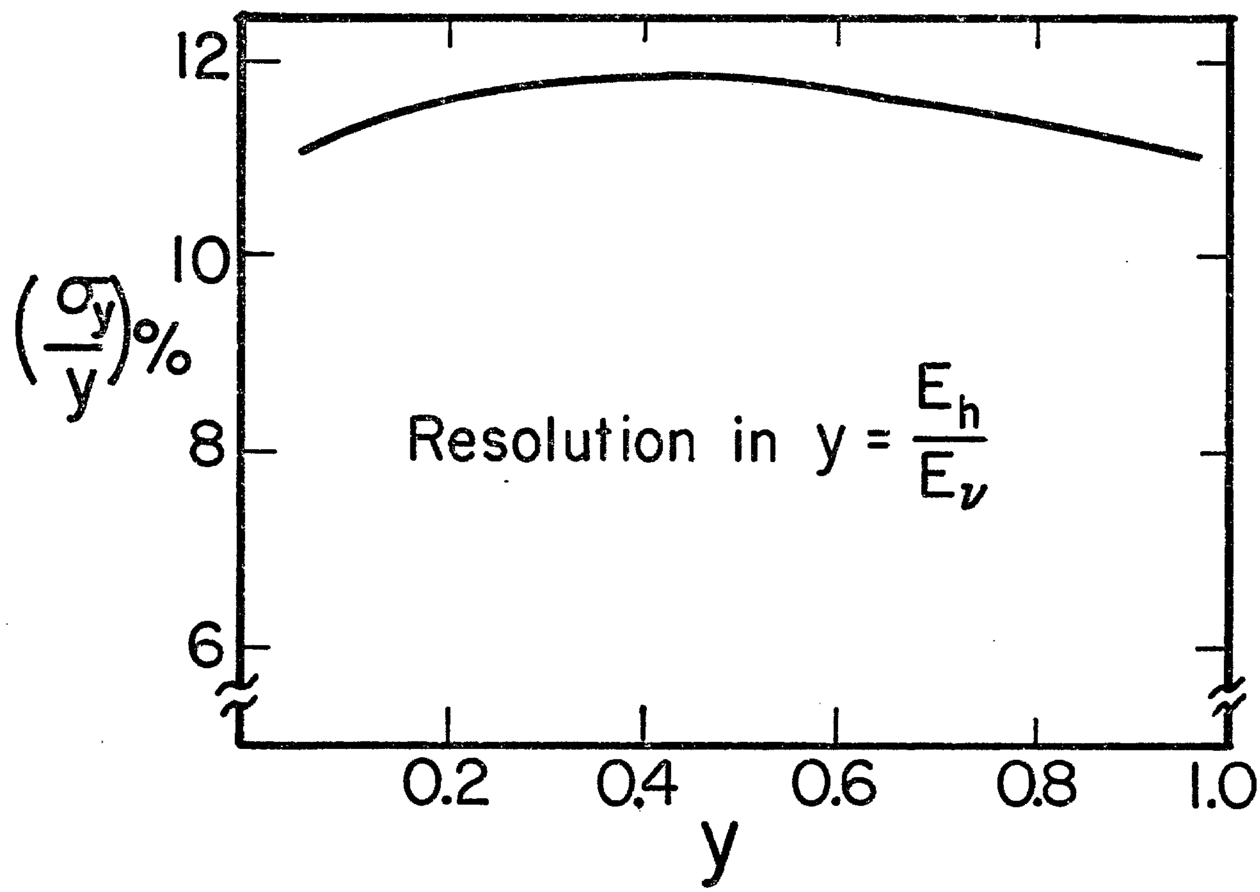

12
10
8
6
$\left(\frac{\sigma_y}{y}\right)\%$
Resolution in $y = \frac{E_h}{E_\nu}$
0.2
0.4
0.6
0.8
1.0
y

Figure 9

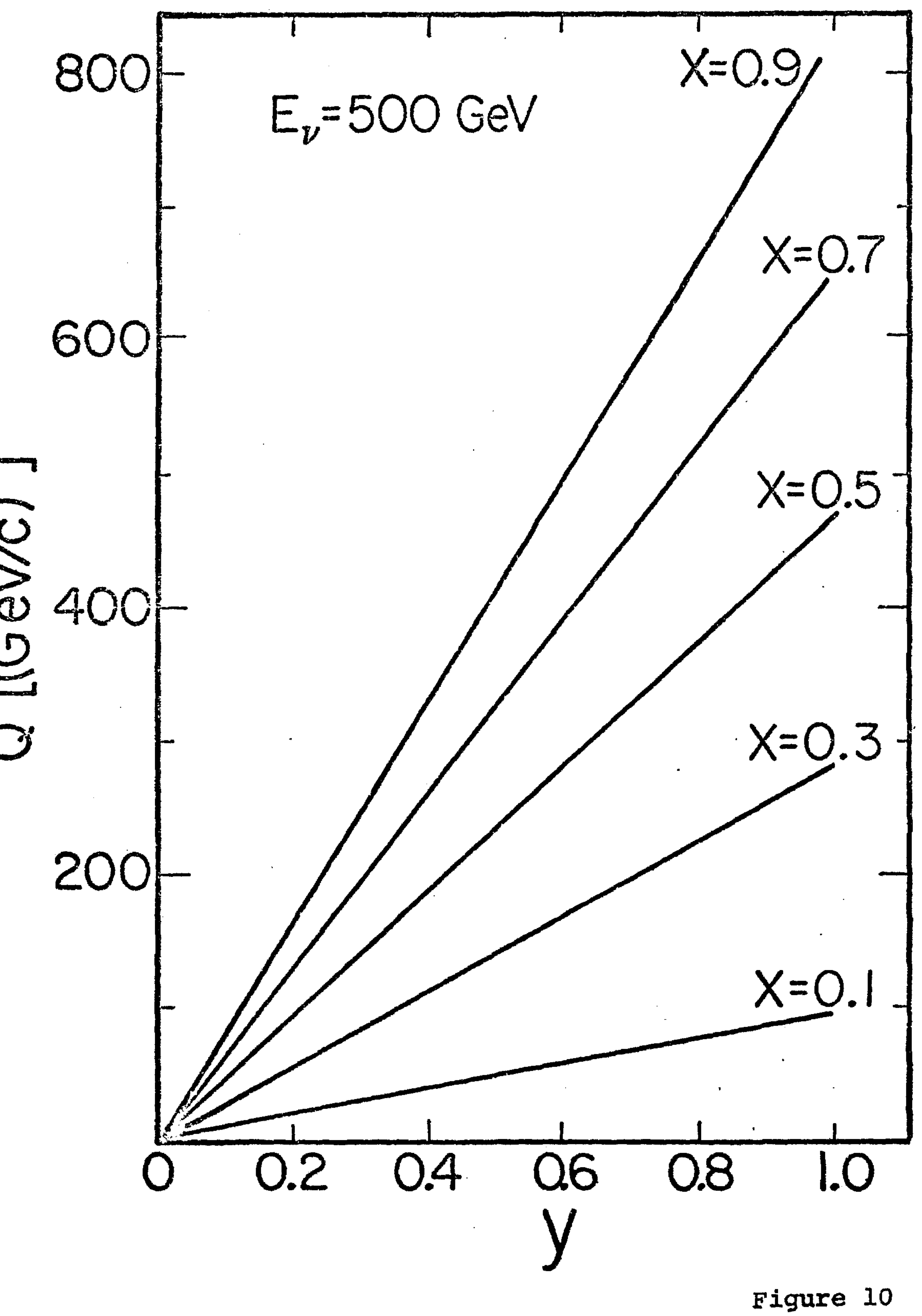

E_ν=500 GeV
X=0.9
X=0.7
X=0.5
X=0.3
X=0.1
800
600
400
200
$Q^2[(GeV/c)^2]$
0
0.2
0.4
0.6
0.8
1.0
y

Figure 10

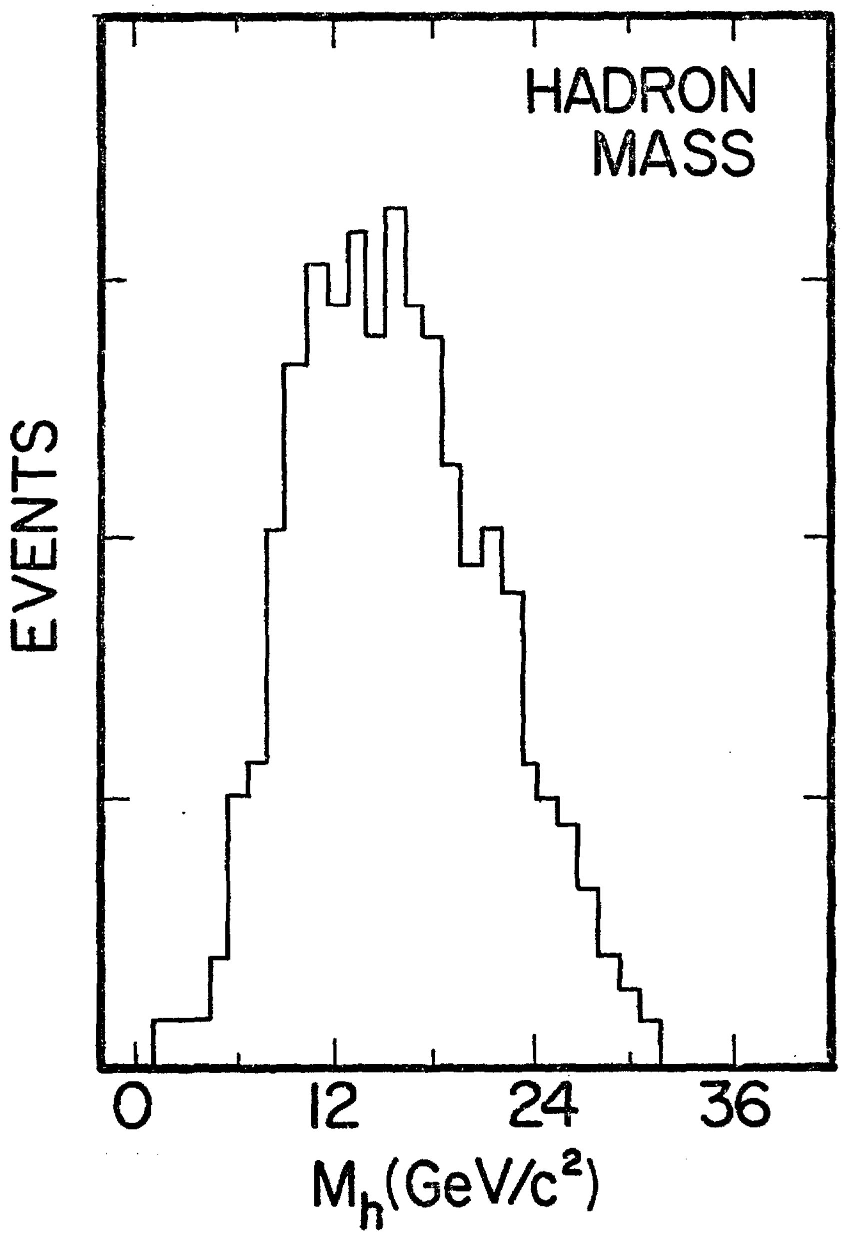

Figure 11

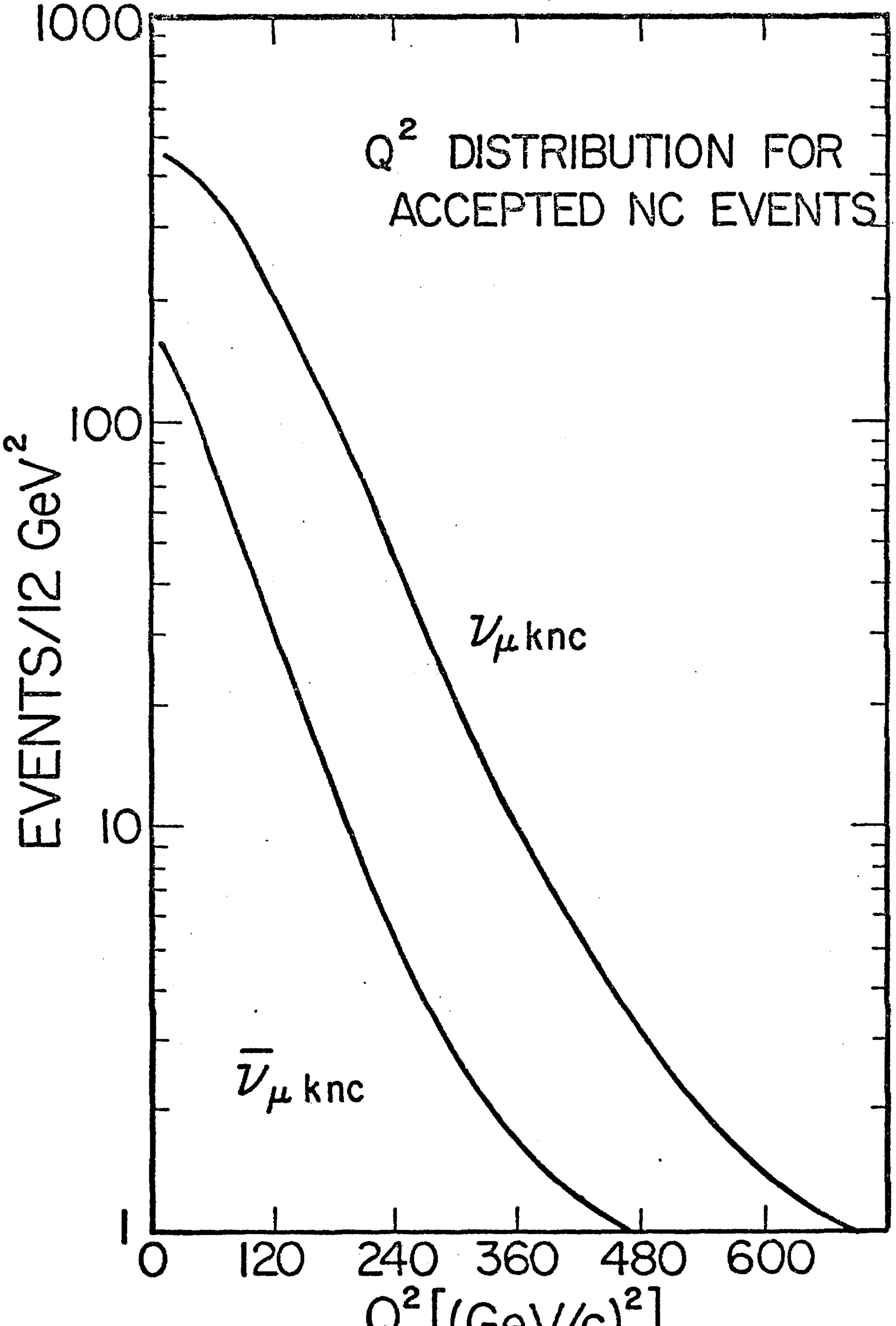

Q² DISTRIBUTION FOR
ACCEPTED NC EVENTS
ν_μ knc
$\bar{\nu}_\mu$ knc
EVENTS/12 GeV²
1000
100
10
1
0
120
240
360
480
600
Q² [(GeV/c)²]

Figure 12

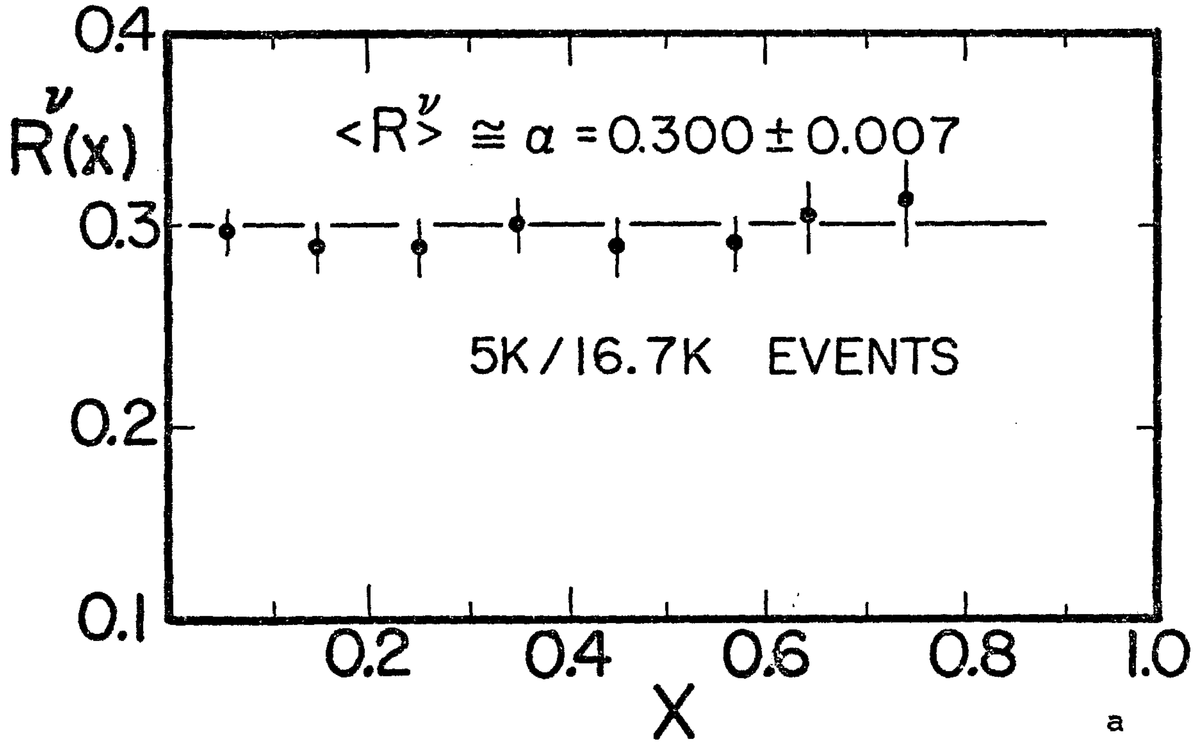
0.4
$R^{\nu}(x)$
$\langle R^{\nu}\rangle \cong \alpha = 0.300 \pm 0.007$
0.3
5K / 16.7K EVENTS
0.2
0.1
0.2
0.4
0.6
0.8
1.0
X

a

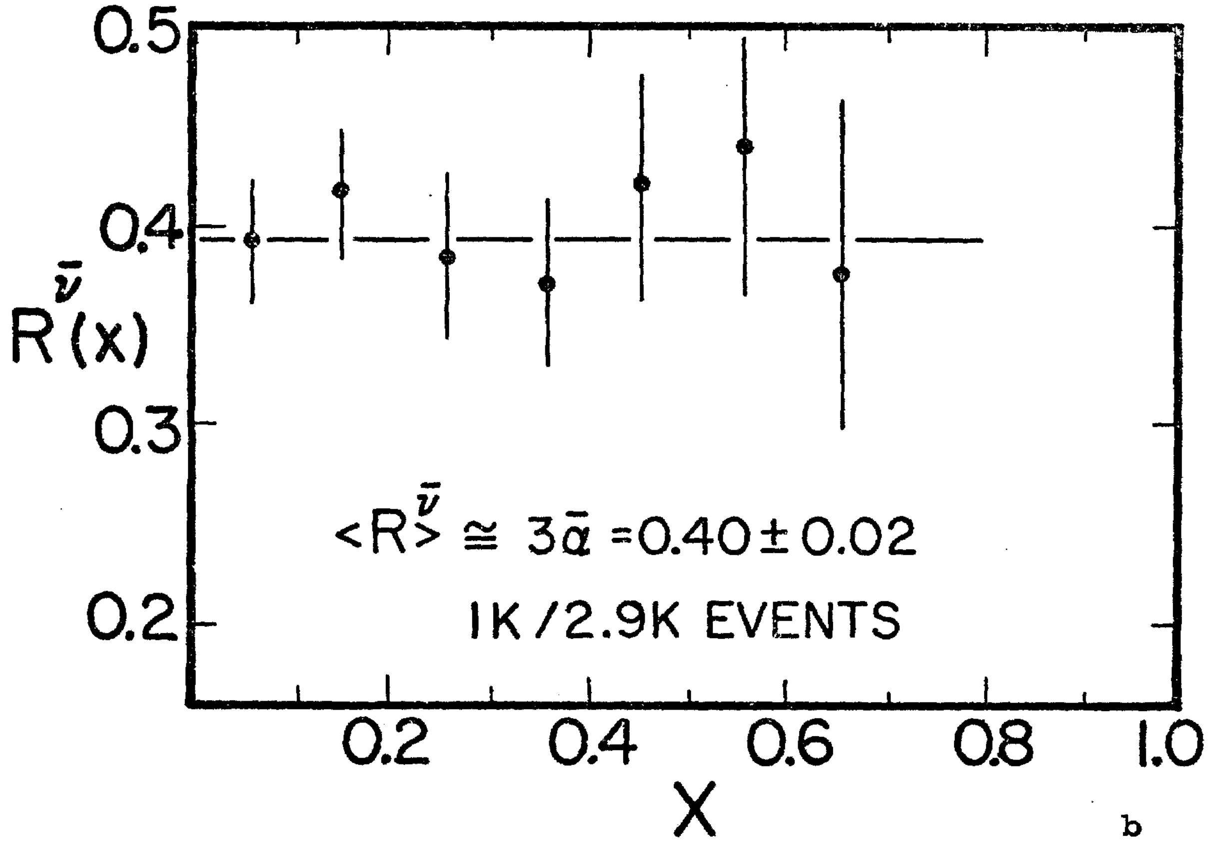
0.5
0.4
$R^{\bar{\nu}}(x)$
0.3
$\langle R^{\bar{\nu}}\rangle \cong 3\bar{\alpha} = 0.40 \pm 0.02$
1K / 2.9K EVENTS
0.2
0.2
0.4
0.6
0.8
1.0
X

b

Figure 13

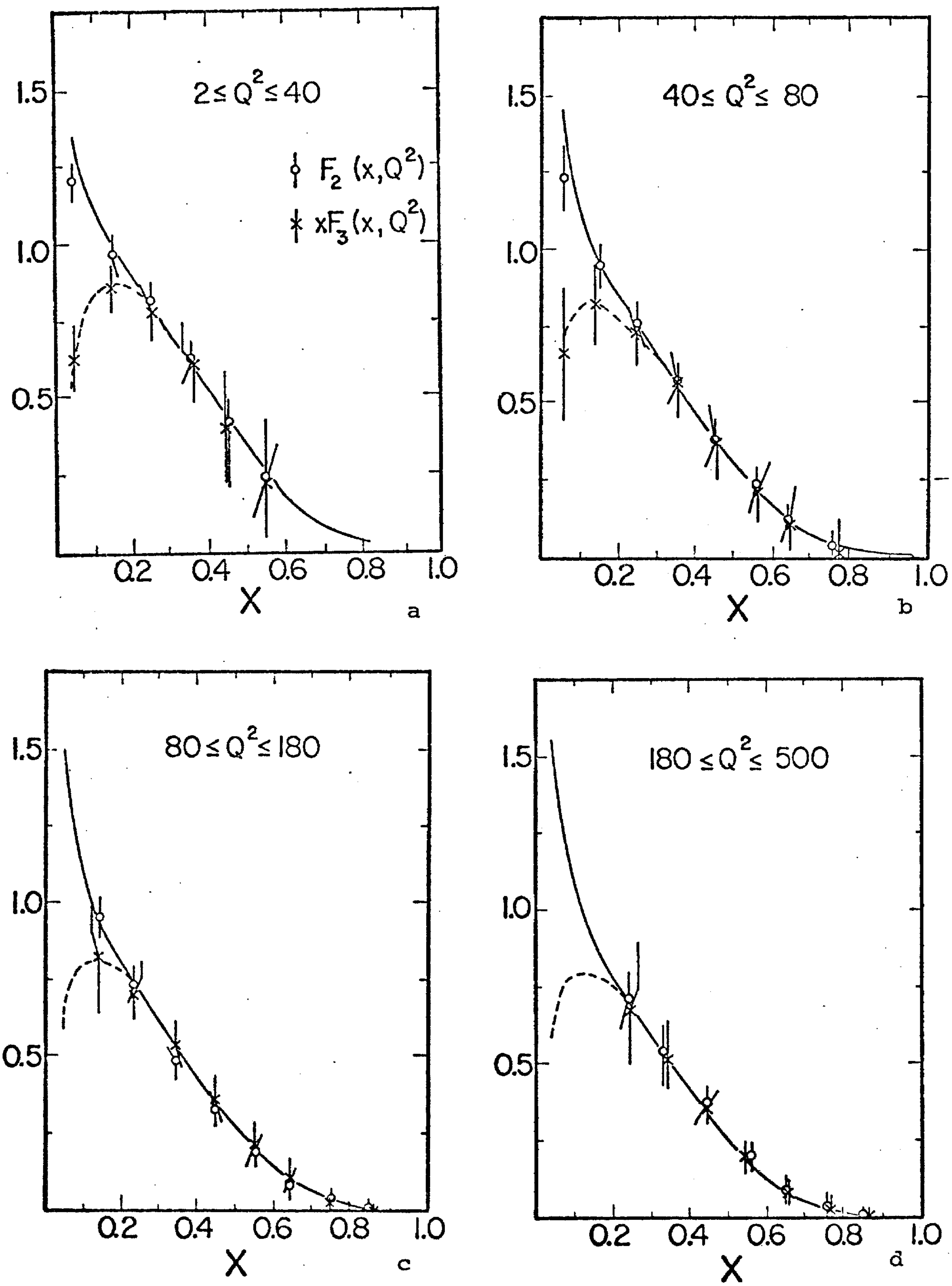

1.5
1.0
0.5
0.2
0.4
0.6
0.8
1.0
X
2 ≤ Q² ≤ 40
F₂ (x, Q²)
xF₃ (x, Q²)
a
40 ≤ Q² ≤ 80
b
80 ≤ Q² ≤ 180
c
180 ≤ Q² ≤ 500
d

Figure 14

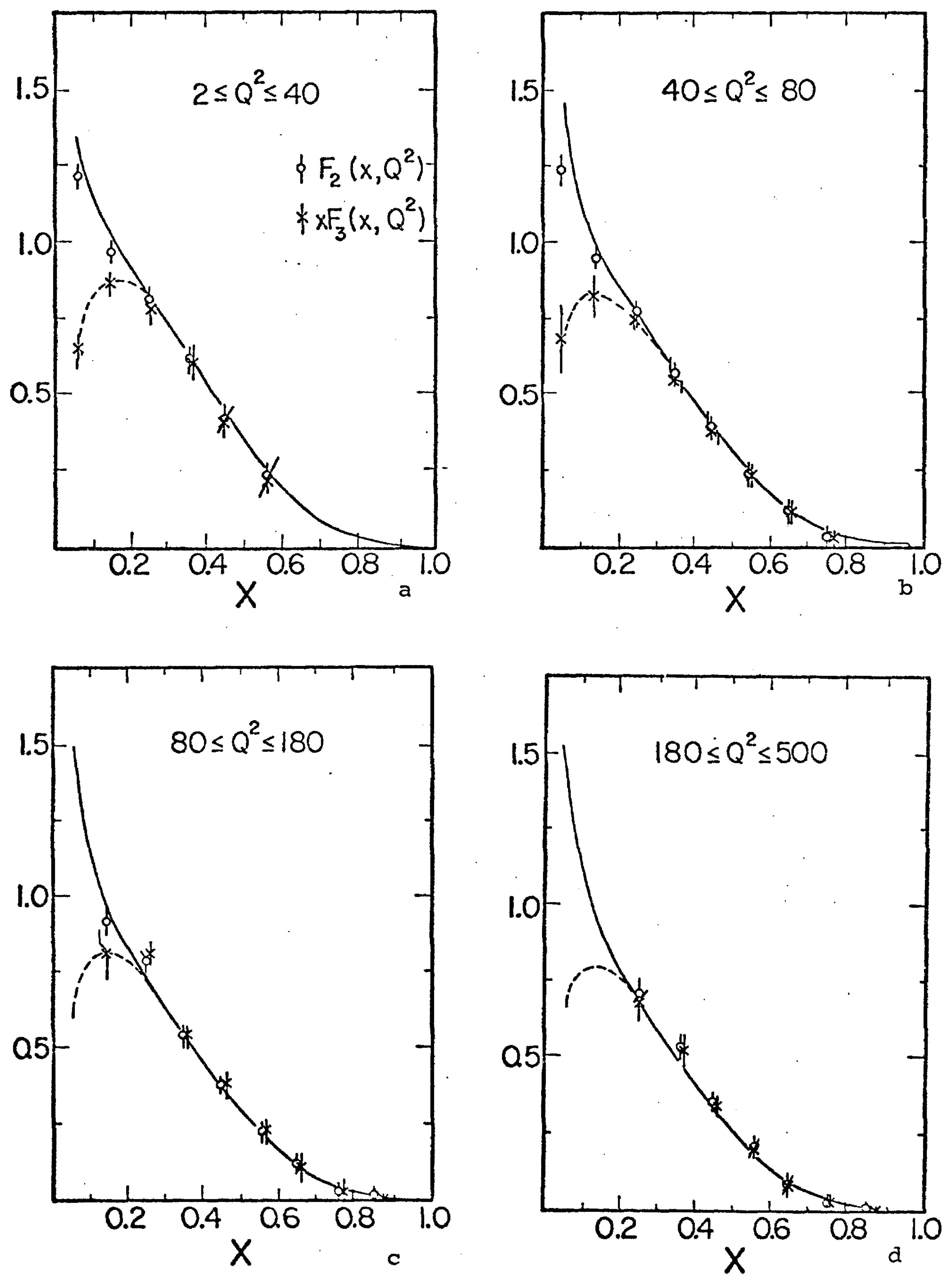
1.5
1.0
0.5
$2 \le Q^2 \le 40$
$F_2(x,Q^2)$
$xF_3(x,Q^2)$
0.2 0.4 0.6 0.8 1.0
X
a
$40 \le Q^2 \le 80$
b
$80 \le Q^2 \le 180$
c
$180 \le Q^2 \le 500$
d

Figure 15

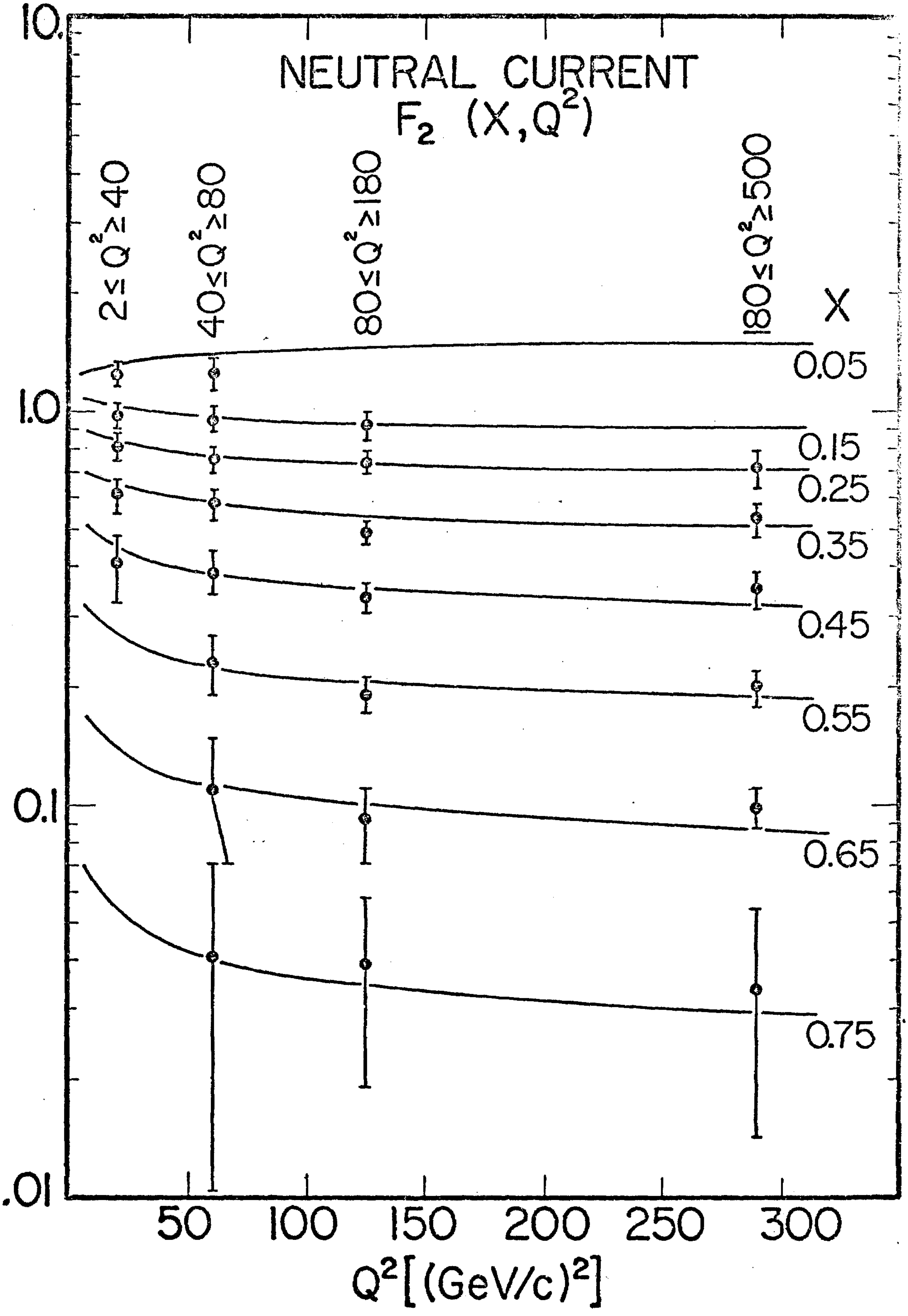
NEUTRAL CURRENT
$F_2(X,Q^2)$
$2 \leq Q^2 \geq 40$
$40 \leq Q^2 \geq 80$
$80 \leq Q^2 \geq 180$
$180 \leq Q^2 \geq 500$
X
0.05
0.15
0.25
0.35
0.45
0.55
0.65
0.75
10.
1.0
0.1
.01
50
100
150
200
250
300
$Q^2[(GeV/c)^2]$

Figure 16

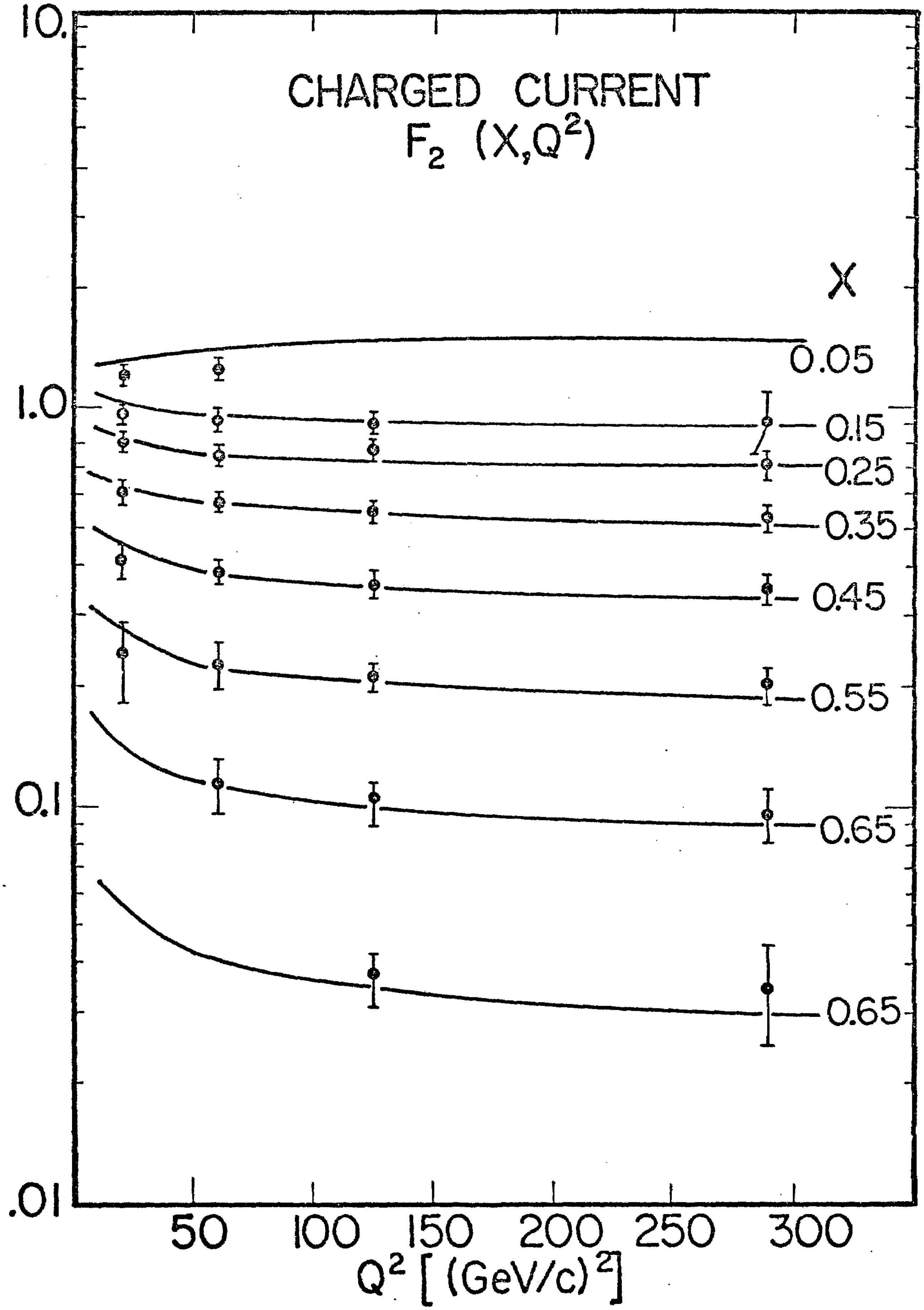
CHARGED CURRENT
F2 (X,Q2)
X
0.05
0.15
0.25
0.35
0.45
0.55
0.65
0.65
10.
1.0
0.1
.01
50
100
150
200
250
300
Q2 [(GeV/c)2]

Figure 17

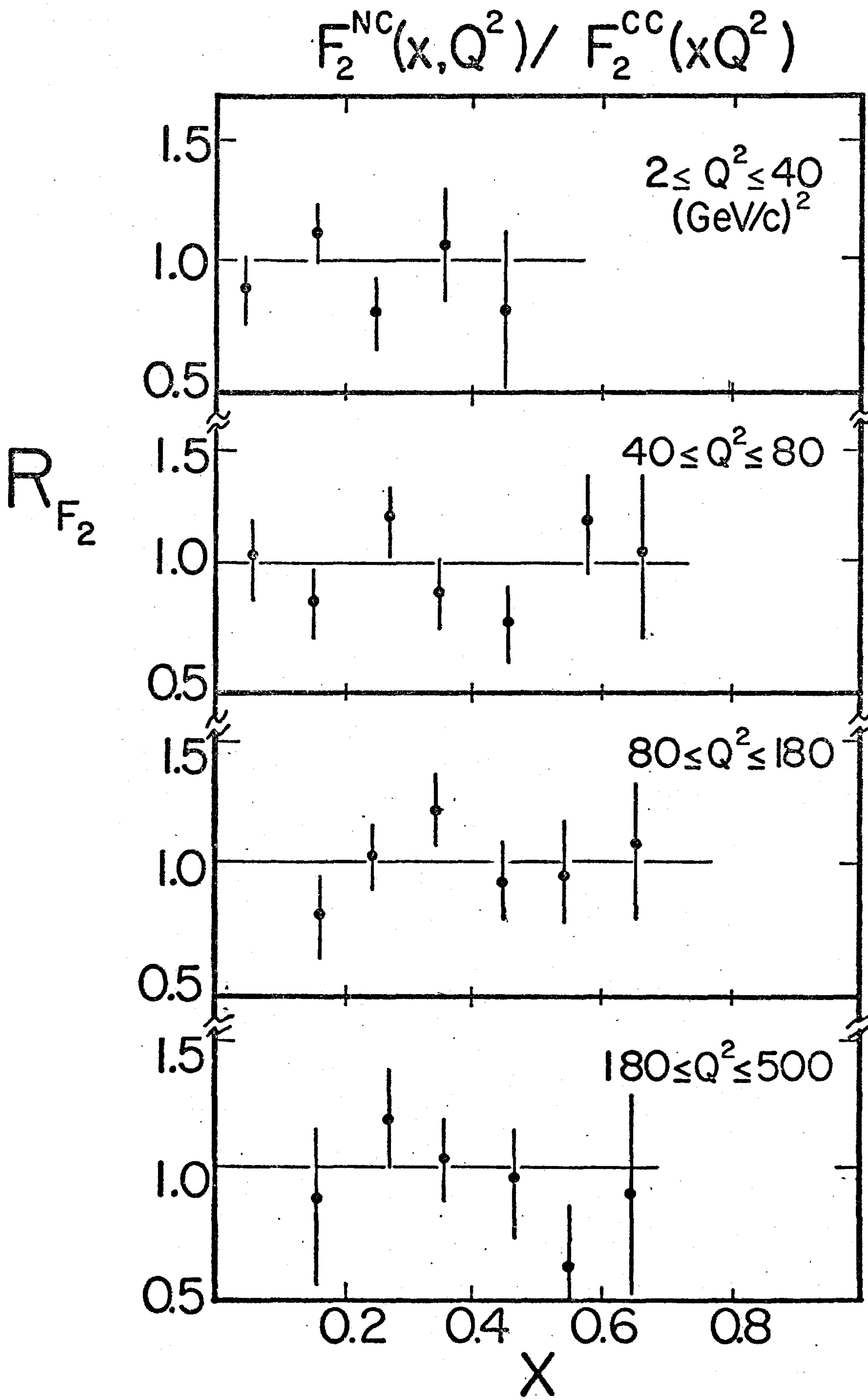

$F_2^{NC}(x,Q^2)/\ F_2^{CC}(xQ^2)$
R_{F_2}
$2 \leq Q^2 \leq 40$ $(GeV/c)^2$
$40 \leq Q^2 \leq 80$
$80 \leq Q^2 \leq 180$
$180 \leq Q^2 \leq 500$
1.5
1.0
0.5
0.2
0.4
0.6
0.8
X

Figure 18

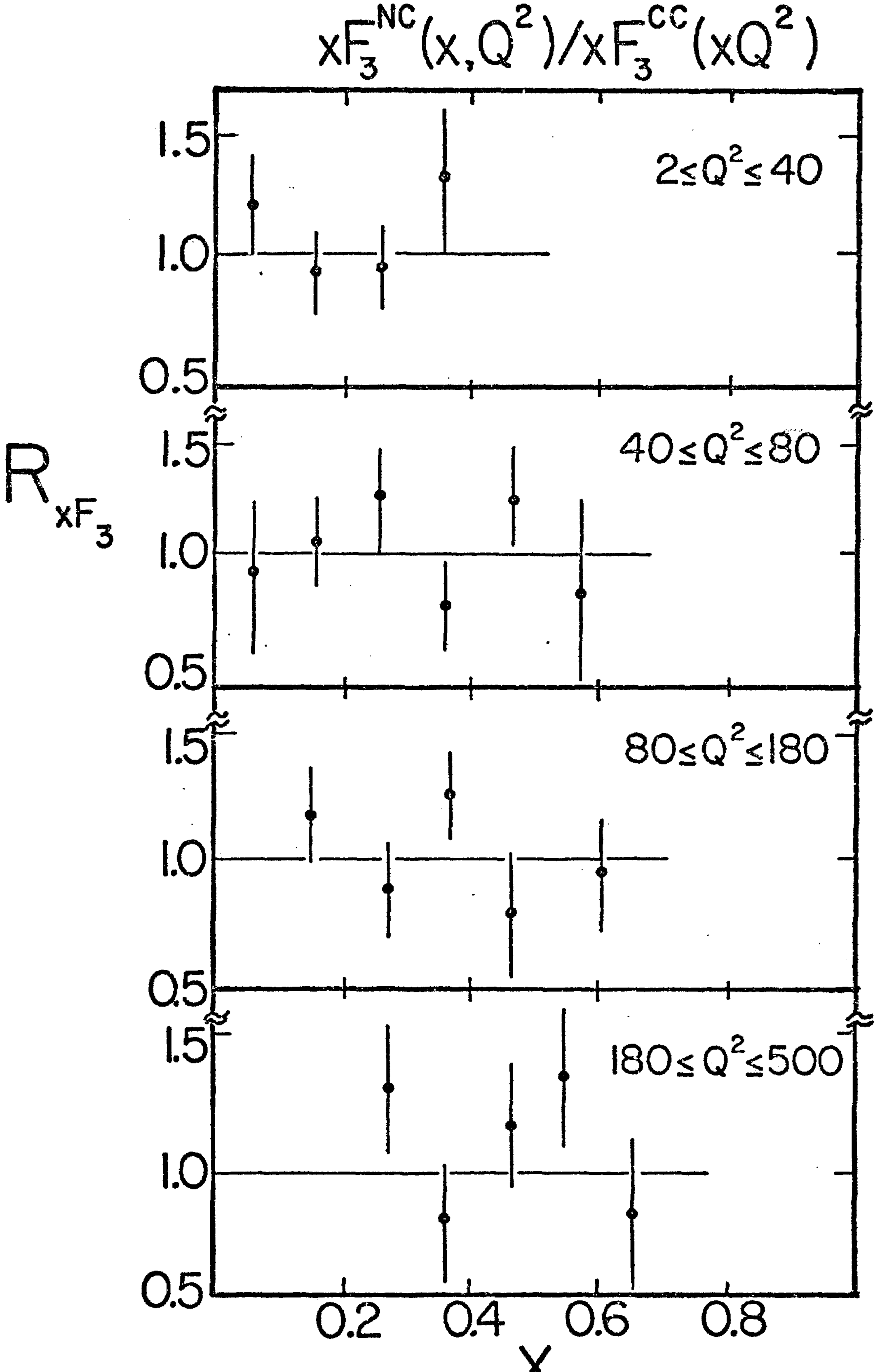
$xF_3^{NC}(x,Q^2)/xF_3^{CC}(xQ^2)$
R_{xF_3}
$2 \le Q^2 \le 40$
$40 \le Q^2 \le 80$
$80 \le Q^2 \le 180$
$180 \le Q^2 \le 500$
1.5
1.0
0.5
0.2
0.4
0.6
0.8
X

Figure 19

APPENDIX A: THE APPARATUS

I. INTRODUCTION

The Lab C flash chamber - proportional tube calorimeter is well suited for Tevatron era neutrino physics. It is ideal for studying neutral and charged current interactions, ν-e scattering and beam dump ν_τ physics. The calorimeter is fine grained (~400,000 flash tube cells) with a sampling step every 3% of an absorption length and 22% of a radiation length. It can distinguish electromagnetic from hadronic showers and has good energy and angular resolution for both. It has an excellent pattern recognition capability. Good muon momentum resolution at Tevatron energies is achieved by the 24' and 12' iron toroids which will be instrumented with drift chambers.

II. DESCRIPTION OF THE CALORIMETER

A. Arrangement of the Calorimeter

The flash chamber - proportional tube calorimeter is 60 feet (18 meters) long comprising 340 metric tons (see Fig. 1). The flash chambers are arranged in three views (X, Y and U) with cells which run 0°, 80° and 100° relative to horizontal (see Fig. 2). Each flash chamber is sandwiched by a sand plane and a steel shot plane. These target-absorber planes are made from extruded acrylic plastic sheets with 5/8" x 5/8" x 12' vertical cells filled with either sand or steel shot. Table I shows the arrangement of the target-absorber planes within the flash chambers and lists the corresponding absorption and radiation lengths. The proportional tube planes are located one every 16 flash chambers. Hence between adjacent proportional planes are 0.5 absorption lengths (64 g/cm^2) or 3.5 radiation lengths. The proportional tubes are alternately vertical and horizontal.

B. <u>General Properties</u>

The average density of the calorimeter is 1.40 g/cm^3. The average nuclear charge Z is 19.1. This low average Z was obtained by using sand as a part of our target-absorber and allows us to measure the angle of electromagnetic showers well. The average collision, absorption and radiation lengths in the calorimeter are 51.8, 83.1 and 11.7 cm respectively. The size of hadronic showers in the calorimeter, or more precisely the dimensions required for containment of the shower energy, is given in Fig. 4. The curves in Fig. 4 were obtained using shower depth calculations in liquid scintillator by the HPWF group.[1] The hadronic shower resolutions, discussed later, demand at least 99% of the shower is contained in the calorimeter longitudinally and at least 95% laterally. The calorimeter properties are summarized in Table II.

C. <u>The Flash Chambers</u>

There are about 600 flash chambers, each with approximately 650 5 mm x 5 mm cells. This fine granularity of the flash chambers allows a small sampling step of the recoil showers leading to excellent energy and angle determination, pattern recognition and muon track finding. The flash chambers are made of extruded black polypropylene with aluminum foil electrodes glued on both sides. Each flash chamber has an active area of 12' x 12' (3.66 m x 3.66 m). Standard spark chamber gas: 90% Ne, 10% He, is circulated through the cells.

When an event is detected, a high voltage pulse of 4.5 kV is applied across each chamber for 0.5 μsec. During this high voltage pulse, a plasma discharge is developed in the hit cells of the flash chambers. This plasma discharge propagates down the full 12' length of the flash chamber cell and into a read out region at the end of each cell. A copper strip for each cell is glued over this 2-ft long read out region and develops a current pulse when the cell is hit. The current pulse is then read out by magnetostrictive techniques.

D. The Proportional Tubes

The trigger and energy determination at large energies are provided by planes of proportional tubes. There are 37 such planes, each containing 144 tubes. The planes are made of extruded aluminum. Each tube is 1" x 1" x 12' and is strung with a single 2 mil gold plated tungsten wire. Four tubes are connected to one amplifier to reduce the cost of electronics while still maintaining adequate granularity for triggering purposes. An argon-ethane (50%-50%) gas mixture is used to give fast drift times ($\lesssim$200 ns) needed to form the trigger within the flash chamber sensitive time.

The trigger will be based on the total energy deposition and on the topology of the energy deposition. Discrimination in the trigger between electromagnetic and hadronic showers will be accomplished using the shower length (the number of proportional planes hit) and the shower width (the separation of hit channels within a plane).

E. Scintillation Counters

Liquid scintillation counters with a 12' x 12' sensitive area are placed every 80 flash chambers throughout the calorimeter. The most upstream counter serves as a front wall veto counter. The other scintillation counters will be used for efficiency measurements and corroborative information on hadronic shower energy deposition. They will also provide time of flight information.

F. The Muon Spectrometer

The muon momentum for charged current interactions and multi-muon events will be measured in the muon spectrometer at the rear of the apparatus (see Fig. 1). There are three 24-ft diameter by 2-ft thick iron toroids immediately downstream of the calorimeter and four 12-ft diameter by 4-ft thick iron toroids behind these. The muons travel through the equivalent of approximately 13 kG in 5 meters of magnetized iron, corresponding to a $p_\perp$ kick of about 2 GeV/c.

The toroids are instrumented with scintillation counters to supply trigger information regarding the presence or absence of a muon in the toroids. Behind each of the seven toroids will be four planes of drift tubes. The planes are made of extruded aluminum, each tube having a 1" x 1" cross section. Two of the four planes will have vertical tubes: the tubes of one plane being offset one-half of a tube with respect to those of the other plane to resolve right-left ambiguities. The other two planes of the set of four will have horizontal tubes.

III. RESOLUTIONS

A. Energy Resolution

The hadronic shower energy is measured by the flash chambers at low energies and the proportional tubes at high energies (see Fig. 4). Because of their fine grained sampling, the flash chambers provide good resolution as low as 10 GeV. At high energies (above 200 GeV), where multiple hits per cell degrade the flash chamber resolution, the proportional tubes provide a good energy measurement. Figure 5 shows the electromagnetic shower energy resolution determined only by the flash chambers. For both kinds of showers, the flash chamber energy measurement is determined by cell counting. The proportional tube energy measurement is determined by summing the analog signals from all the wires.

The preliminary flash chamber energy resolutions in Figs. 4 and 5 were directly measured in a hadron and electron beam using our test calorimeter.[2] The test calorimeter was made with plastic flash chambers, smaller in size and number than our Lab C chambers, and read out optically. The longitudinal sampling of the test calorimeter: 3.5% λ_{abs} and 24% X_o, was almost as good as the Lab C calorimeter. Therefore only corrections for the limited hadronic shower containment of the test calorimeter were made to the measured resolutions. The proportional tube resolution of Fig. 4 was estimated by scaling Anderson et al.[3] to our sampling step, giving

$$\frac{\sigma(E_h)}{E_h} \cong \frac{104\%}{\sqrt{E_h}}$$

B. Angular Resolution

The hadronic and electromagnetic shower angular resolutions determined by the test flash chamber calorimeter are shown in Figs. 6 and 7. The angular resolutions depend critically on the spatial resolution of the shower vertex. The angle of the showers is computed by first locating the vertex and then using the "center of gravity" of the shower as a function of shower depth.

Because every cell of the test calorimeter ran horizontal, the sampling step per view was approximately a factor of two finer in the test calorimeter than in the Lab C calorimeter. By ignoring every other plane in the test calorimeter's angle measurement, therefore, we were able to plot the expected angular resolution of the Lab C calorimeter. The test calorimeter confirmed the expectation of good angular resolution at low energies: an important feature for beam dump physics. Figure 8 shows test calorimeter showers at all energies. Note the good vertex determination even at low energies.

C. Pattern Recognition

We will be able to distinguish electromagnetic from hadronic showers by their size, shape and structure. This is an important capability for the study of ν-e scattering where hadronic backgrounds are large. As seen in the test calorimeter showers of Fig. 8, electromagnetic showers are easily distinguished from high energy hadronic showers by differences in their size. We distinguish low energy hadronic from electromagnetic showers by the presence of large angle secondaries in the hadronic showers. Also, unlike electromagnetic showers, tracks are visible within the hadronic showers. Using the test calorimeter in a hadron beam with about 1% electron contamination, we were able to experimentally confirm that less than 1% of hadron showers are misidentified as electron showers.

We will also be able to observe and locate the muon track in charged current interactions. We expect a very small amount of charged current interactions posing as neutral current interactions because the muon could not be seen.

D. Muon Momentum Resolution

Figure 9 shows the muon momentum resolution we expect to achieve when the 24 and 12-ft iron toroids are instrumented with drift tubes. The drift tubes will provide position measurements with an estimated σ of 1 mm. The flash chambers will supply information regarding the muon's trajectory at the point of entry into the first toroid. The resolutions corresponding to the drift tube and flash chamber position measurements, as well as multiple scattering were used to produce the resolution shown.

IV. PERFORMANCE OF THE CALORIMETER

A. Flash Chamber Performance

We have debugged and operated 320 flash chambers. From our experience we find that the flash chambers have performed well.[4] Using cosmic ray muons, we have measured their efficiency at the proportional tube trigger time delay (650 ns from the event to the time high voltage appears across the chambers) to be between 80 and 90%. The multiplicity (cells lit per flash chamber per cosmic ray) is 1.3. Adequate recirculation of the neon-helium gas was found to be 1.5% of the volume per minute. For the entire detector, this implies a recirculation rate of 900 liters per minute. The high voltage plateau region is broad: 3.5 to 5.5 kV (see Fig. 10). The signal-to-noise ratio of the amplified signals on the magnetostrictive lines is 10:1. Our maximum repetition rate with almost no cell reignition <u>thus far</u> is ~1 flash per second. We have not added any electronegative gas to try to improve this.[5] The readout dead time (up to the computer) is ~70 ms. Because data transfer time to the disk is 50,000-80,000 words per second, the computer cannot handle much more than one event per second. If we wanted to take data at a faster rate, we could transfer data without the disk by obtaining much more addressable core memory (such as a VAX) or by using a 6250 BPI tape drive.

Figure 11 shows a cosmic ray muon in 160 of our chambers. (Offline alignment corrections have not yet been made.) In Fig. 12, a cosmic ray muon initiated an electromagnetic shower. In Fig. 13, which shows a cosmic ray muon interacting, 320 of our chambers were in operation.

B. <u>Proportional Tube Performance</u>

The proportional tubes have also performed well. Using 50% argon - 50% ethane gas and running at a high voltage of 2000 volts gives us a gas gain of about 2000 and drift times of $\lesssim$200 ns. The amplifier gain is 1 mV/fC. A minimum ionizing particle gives a signal of 8 mV: a factor of 8 above noise. The linear swing is 0-4 volts or 0-500 particles. This is a factor of 2 or so above the largest number of particles per channel expected for Tevatron energy showers. The tube to tube uniformity has been measured to be very good: a plot of Cd^{109} peaks for a large sample of tubes shows a σ of $\lesssim$5%.

V. CONCLUSION

The flash chamber - proportional tube calorimeter is a high tonnage, fine grained device with good energy and angle resolutions for both hadronic and electromagnetic showers. It has a good hadronic-electromagnetic shower distinction capability and a low average Z, making it ideal for the study of ν-e scattering. Its good vertex determination and good muon momentum resolution make it ideal for studying charged and neutral current interactions. Its good pattern recognition and angle determination at low energies make it an excellent beam dump detector. It will be a powerful device for studying a number of interesting physical processes at Tevatron energies.

REFERENCES

1. F. J. Sciulli, Proceedings of the Calorimeter Workshop (Fermilab), 79 (1975).
2. See Appendix A of the E594 Proposal (February 1978) and F. E. Taylor et al., IEEE Trans. Nucl. Sci. NS-25, 312 (1978).
3. R. L. Anderson et al., IEEE Trans. Nucl. Sci. NS-25, 340 (1978) and private communication with D. M. Ritson.
4. F. E. Taylor et al., IEEE Trans. Nucl. Sci. NS-27, 30 (1980).
5. Chaney and Breare, by adding 1% methane to the neon-helium, have been able to pulse their flash chambers at 50 Hz with no reignition. See J. E. Chaney and J. M. Breare, Nucl. Instrum. and Methods 124, 61 (1975).

TABLE I

Arrangement of Calorimeter Components

flash chambers:	U		X		Y		X	. . .
		↑		↑		↑		↑	
absorber planes:		shot		sand		shot		sand	
absorption lengths:		3.7%		2.5%	} 6.1% per view (7.2 g/cm^2)				
radiation lengths:		36%		8%	} 44% per view				

TABLE II

General Properties

Tonnage:	340 metric tons
Fiducial Tonnage for a Neutral Current Experiment:	100 metric tons
Fiducial Tonnage for a ν-e Scattering Experiment:	225 metric tons
Average Density:	1.40 g/cm^3
Average Z:	19.1
Average λ_{COL}:	51.8 cm
λ_{ABS}:	83.1 cm
X_o:	11.7 cm

LIST OF FIGURES

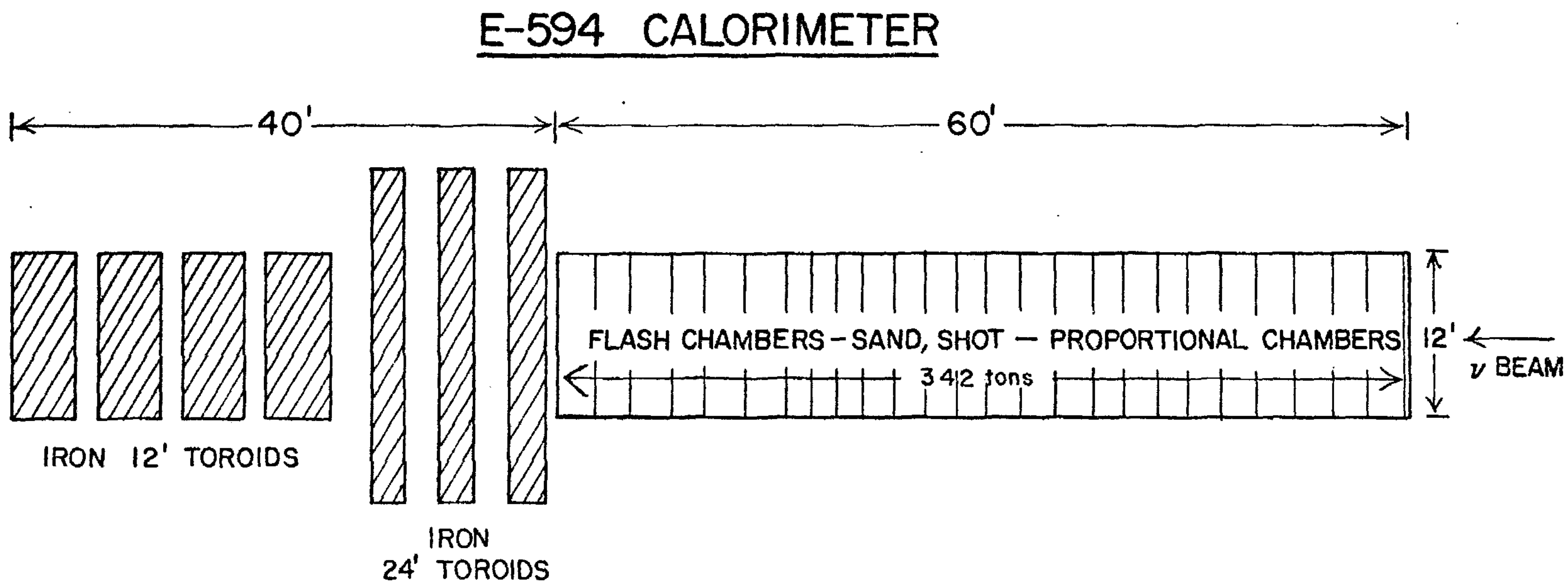
E-594 CALORIMETER
40'
60'
IRON 12' TOROIDS
IRON
24' TOROIDS
FLASH CHAMBERS - SAND, SHOT — PROPORTIONAL CHAMBERS
342 tons
12'
ν BEAM

Figure 1a

Figure 1b

FLASH CHAMBER CALORIMETER CONSTRUCTION

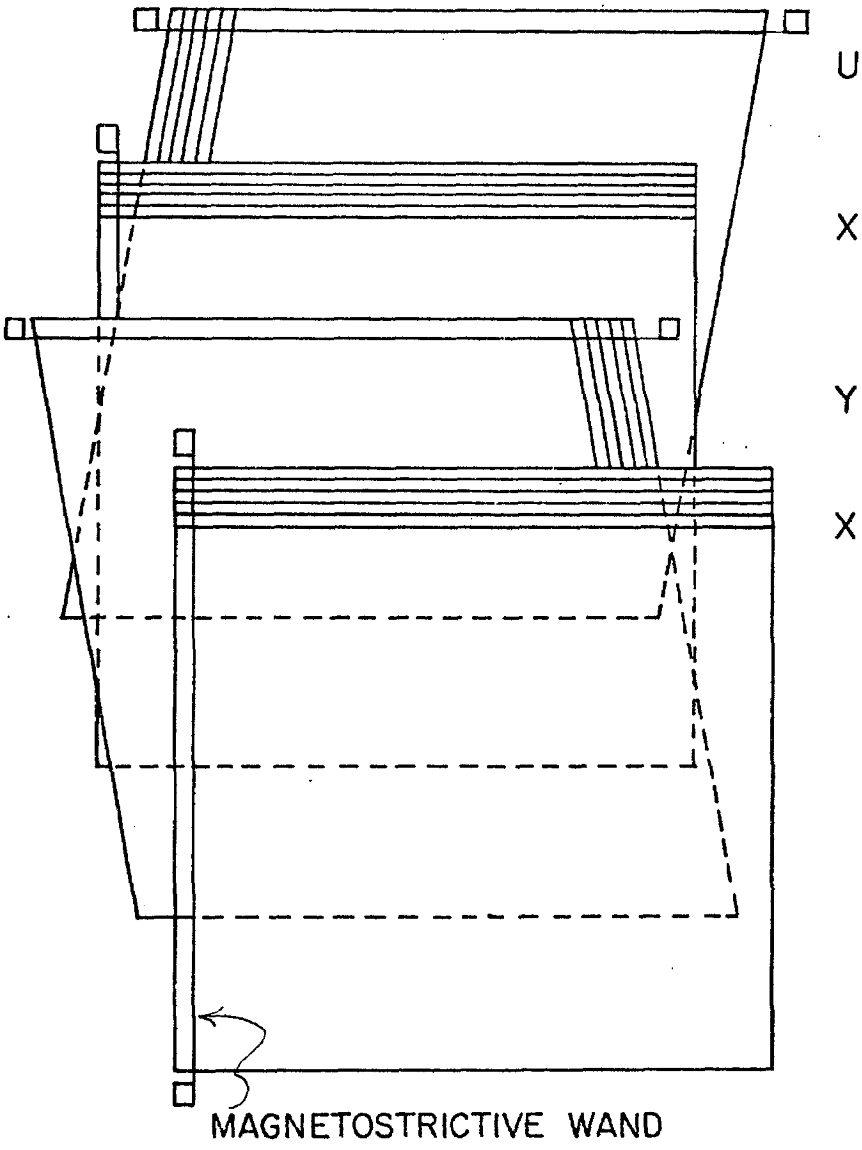

Figure 2

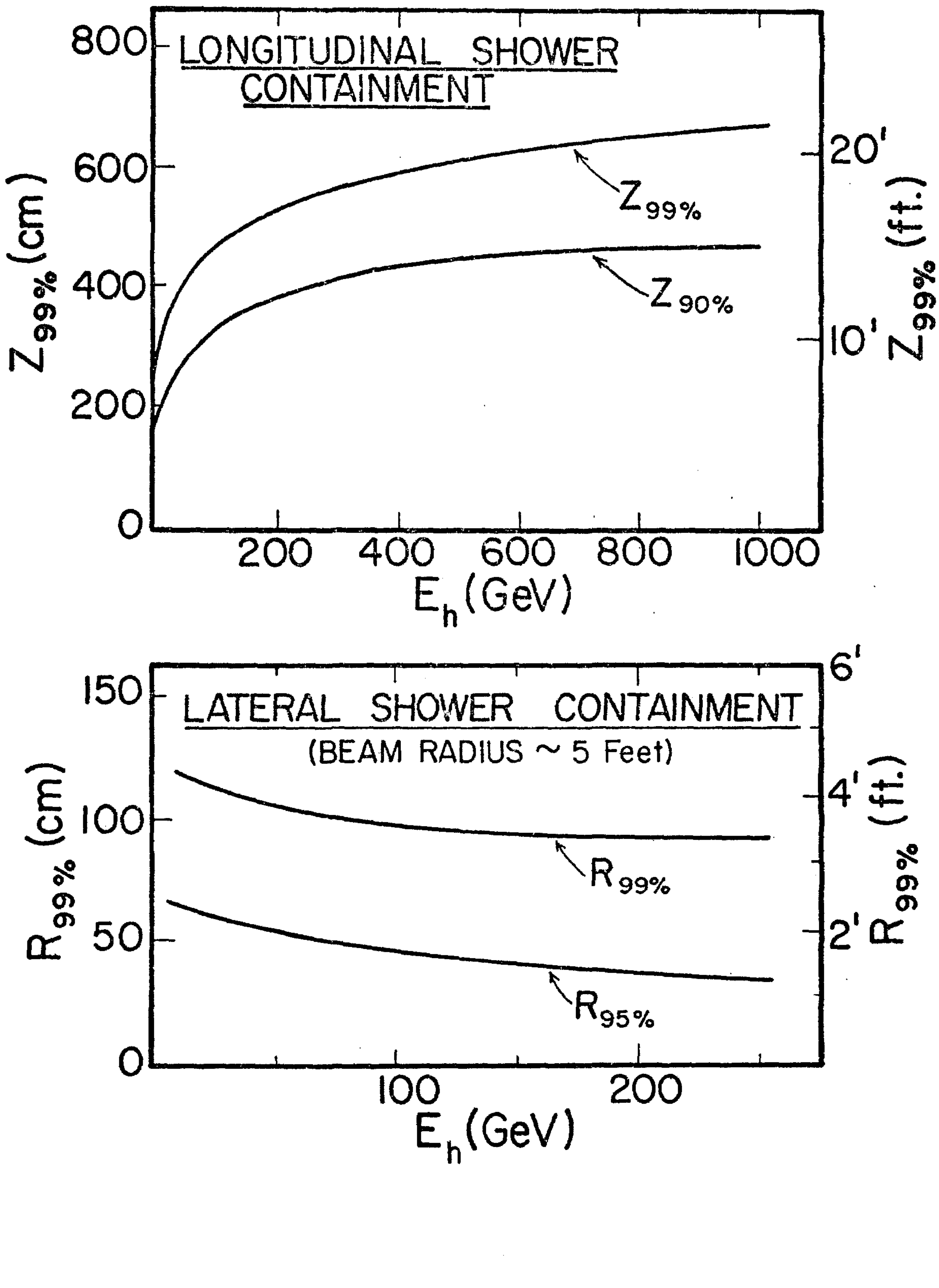
LONGITUDINAL SHOWER CONTAINMENT
800
600
400
200
0
200
400
600
800
1000
E_h (GeV)
$Z_{99\%}$ (cm)
$Z_{99\%}$ (ft.)
20'
10'
$Z_{99\%}$
$Z_{90\%}$
LATERAL SHOWER CONTAINMENT
(BEAM RADIUS ~ 5 Feet)
150
100
50
0
100
200
E_h (GeV)
$R_{99\%}$ (cm)
$R_{99\%}$ (ft.)
6'
4'
2'
$R_{99\%}$
$R_{95\%}$

Figure 3

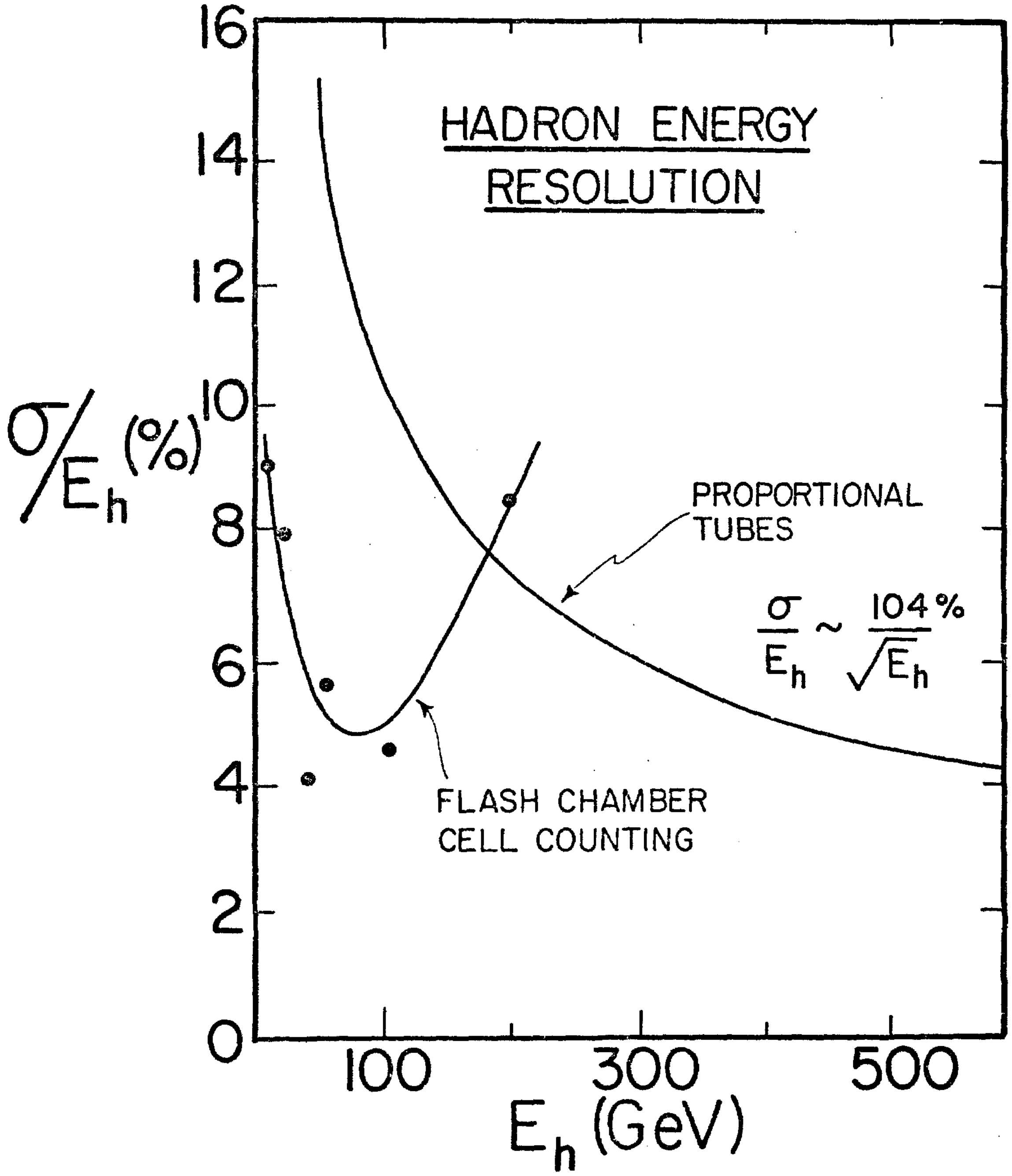
HADRON ENERGY RESOLUTION
σ/E_h (%)
16
14
12
10
8
6
4
2
0
100
300
500
E_h (GeV)
PROPORTIONAL TUBES
$\frac{\sigma}{E_h} \sim \frac{104\%}{\sqrt{E_h}}$
FLASH CHAMBER CELL COUNTING

Figure 4

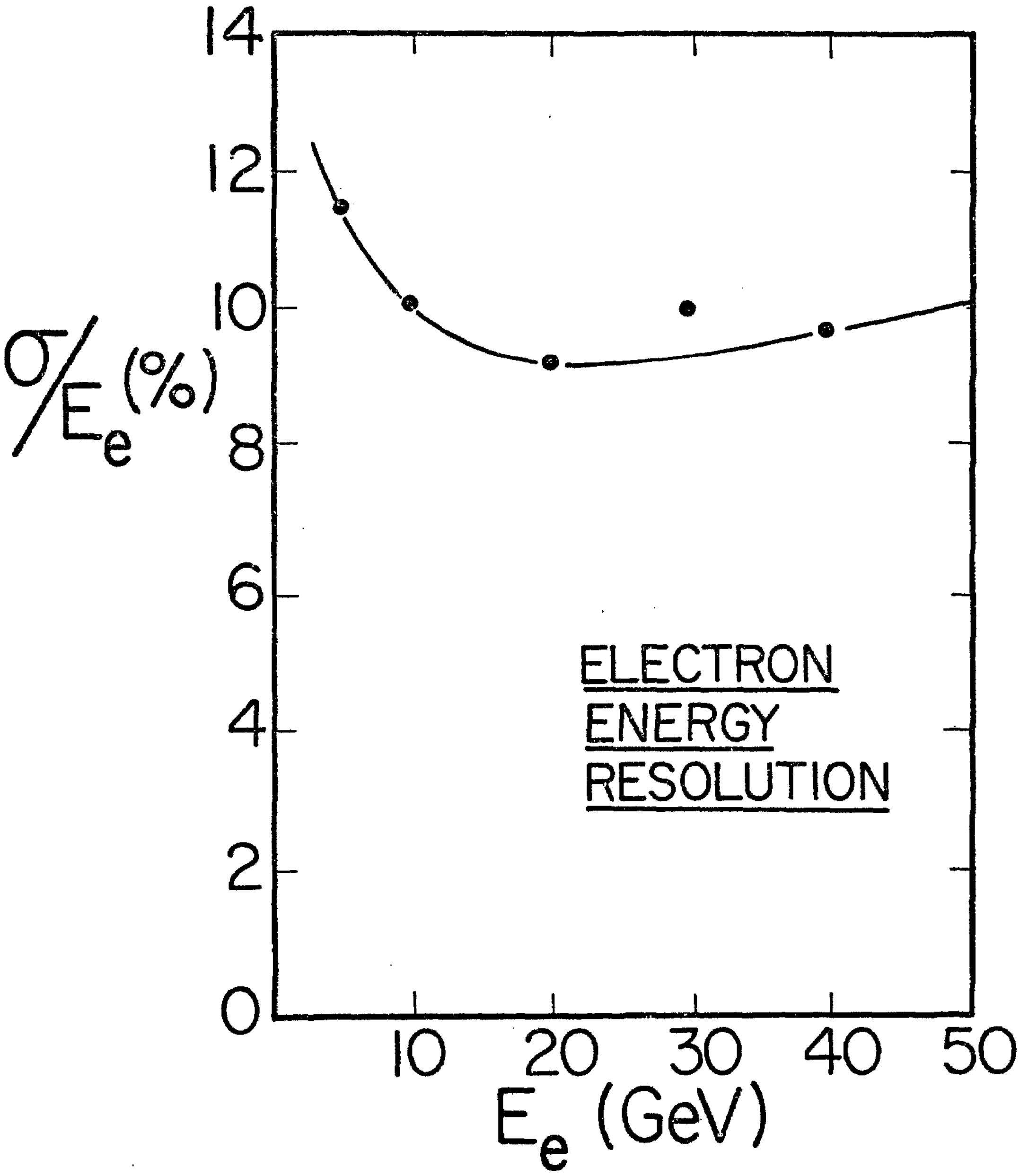
14
12
10
8
6
4
2
0
σ/E_e (%)
10
20
30
40
50
E_e (GeV)
ELECTRON
ENERGY
RESOLUTION

Figure 5

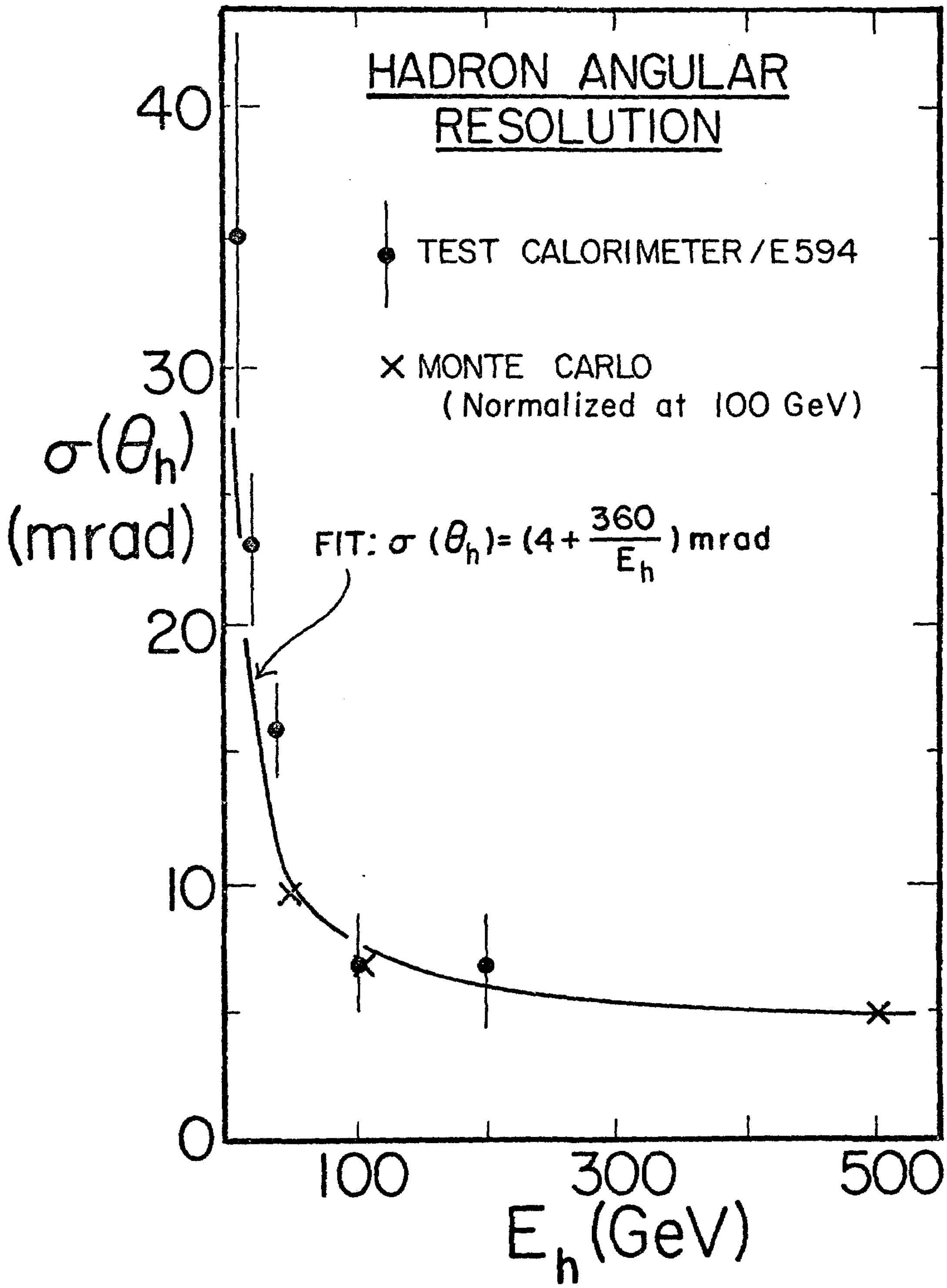
HADRON ANGULAR RESOLUTION
TEST CALORIMETER / E594
× MONTE CARLO (Normalized at 100 GeV)
FIT: $\sigma(\theta_h) = (4 + \frac{360}{E_h})$ mrad
$\sigma(\theta_h)$ (mrad)
40
30
20
10
0
100
300
500
E_h (GeV)

Figure 6

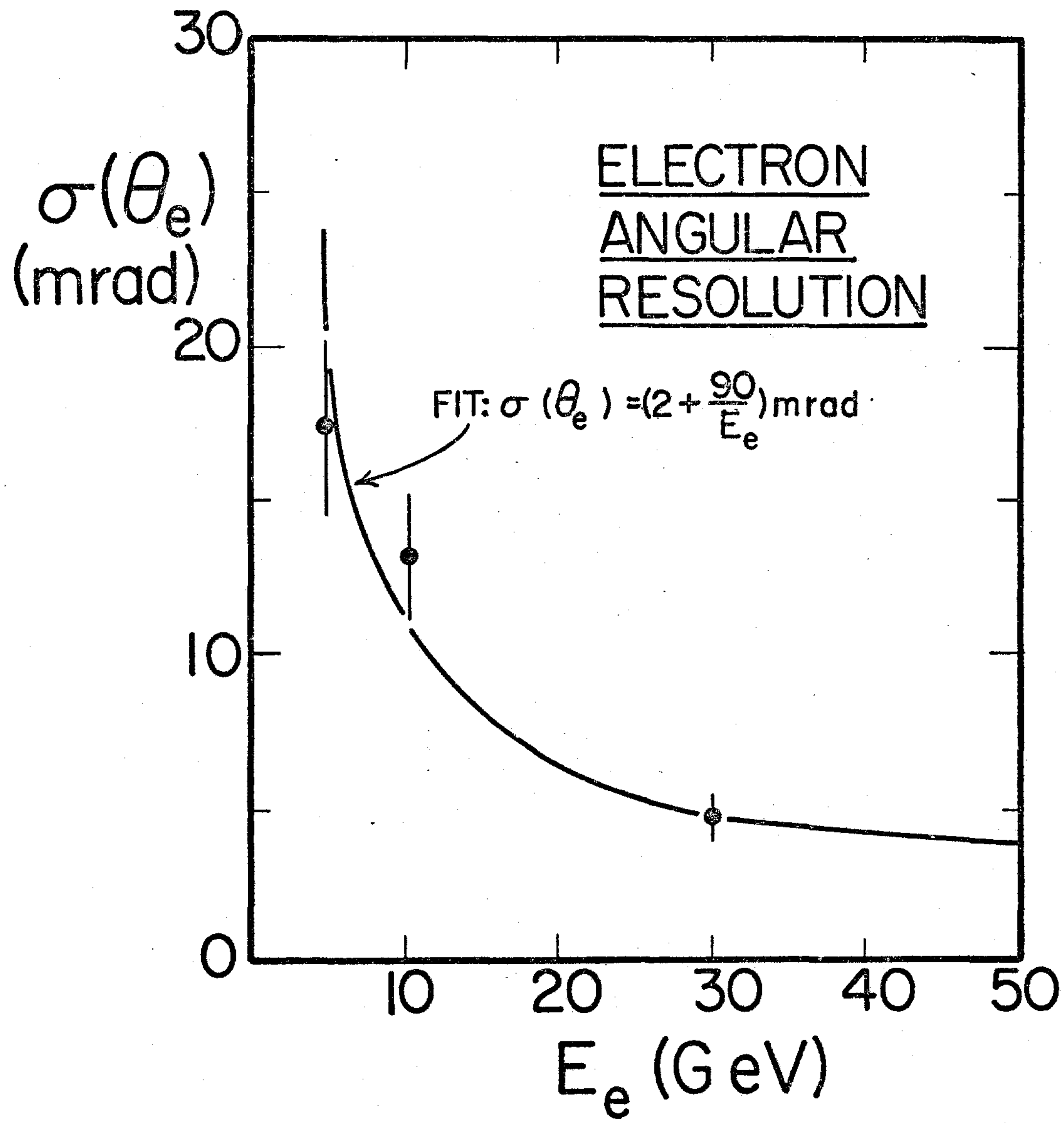
30
$\sigma(\theta_e)$
(mrad)
20
10
0
ELECTRON
ANGULAR
RESOLUTION
FIT: $\sigma(\theta_e) = (2 + \frac{90}{E_e})$ mrad
10
20
30
40
50
E_e (GeV)

Figure 7

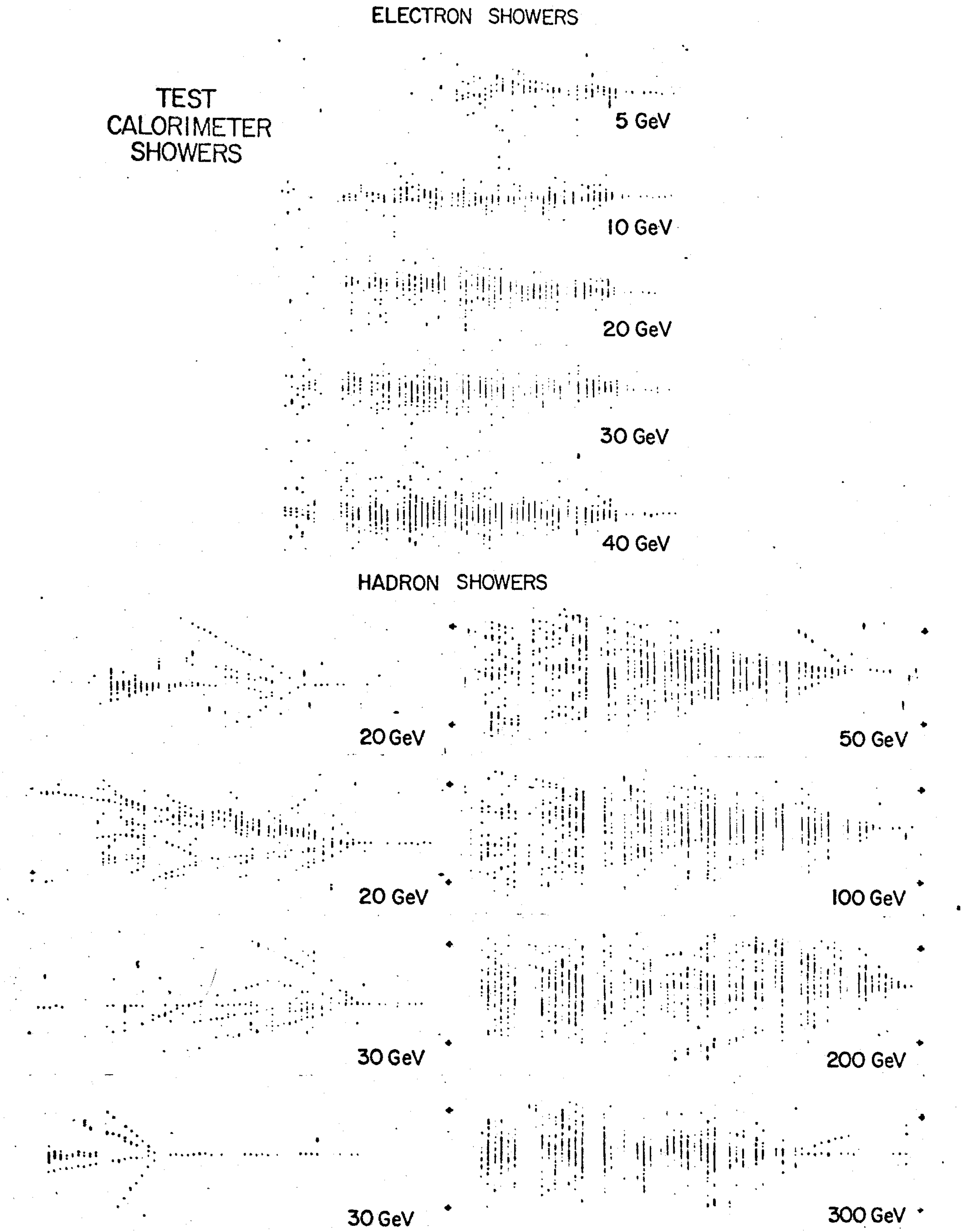
ELECTRON SHOWERS
TEST
CALORIMETER
SHOWERS
5 GeV
10 GeV
20 GeV
30 GeV
40 GeV
HADRON SHOWERS
20 GeV
50 GeV
20 GeV
100 GeV
30 GeV
200 GeV
30 GeV
300 GeV

Figure 8

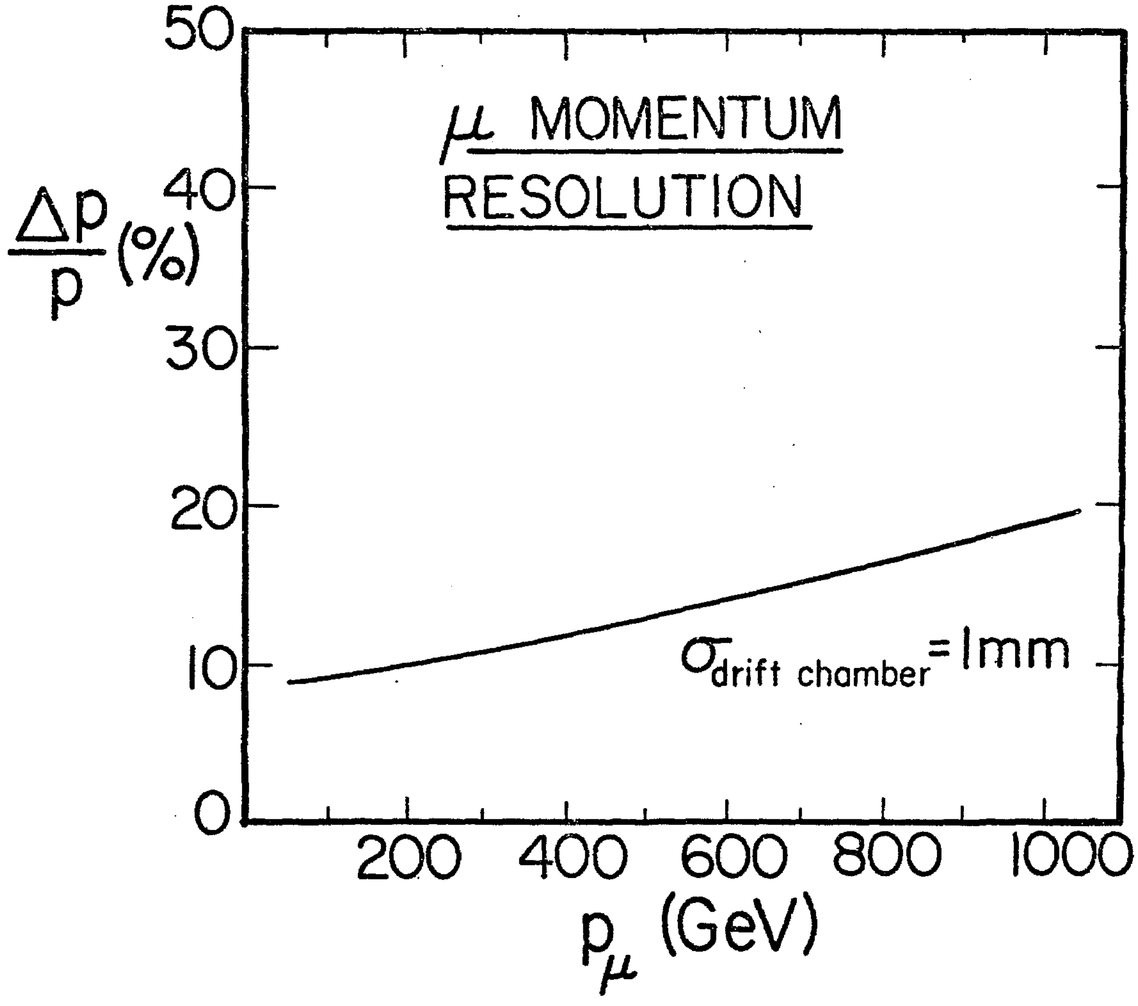

μ MOMENTUM RESOLUTION
$\frac{\Delta p}{p}$ (%)
50
40
30
20
10
0
$\sigma_{drift\ chamber}$ = 1mm
200
400
600
800
1000
p_μ (GeV)

Figure 9

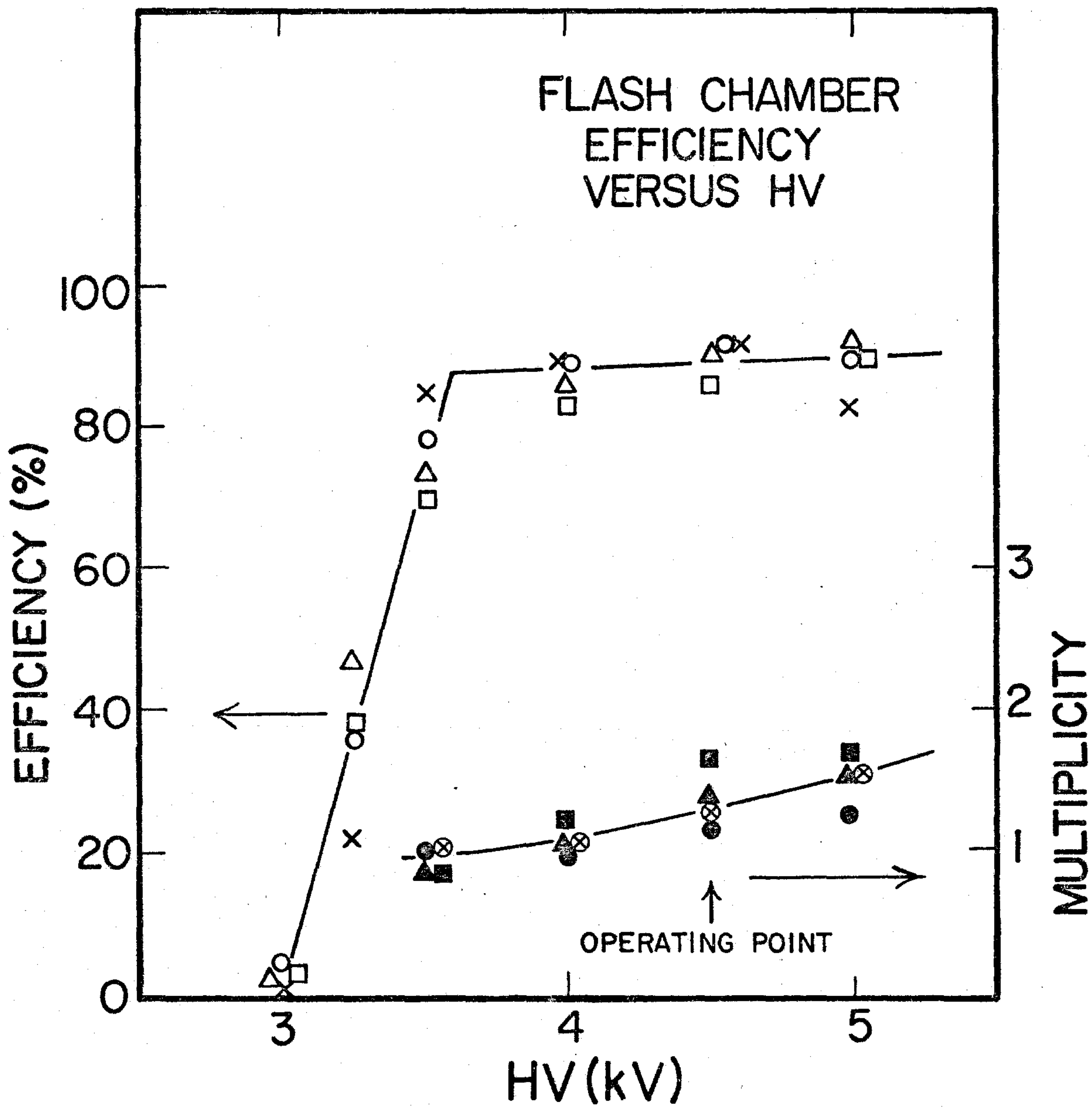
FLASH CHAMBER
EFFICIENCY
VERSUS HV
100
80
60
40
20
0
EFFICIENCY (%)
3
2
1
MULTIPLICITY
OPERATING POINT
3
4
5
HV (kV)

Figure 10

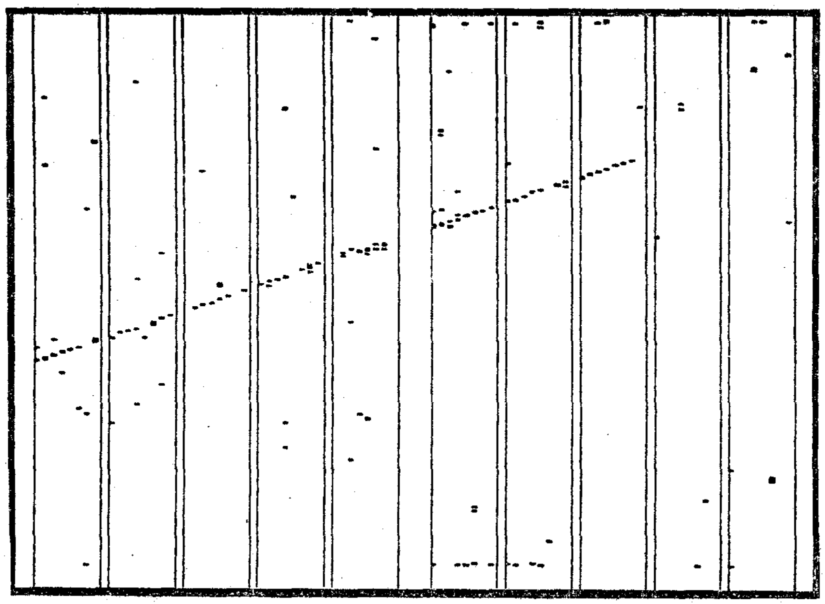

X VIEW

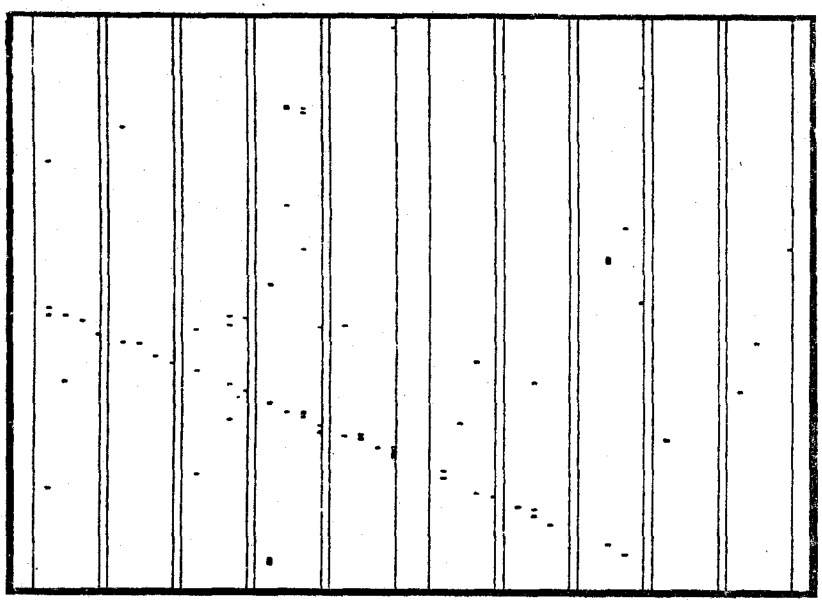

U VIEW

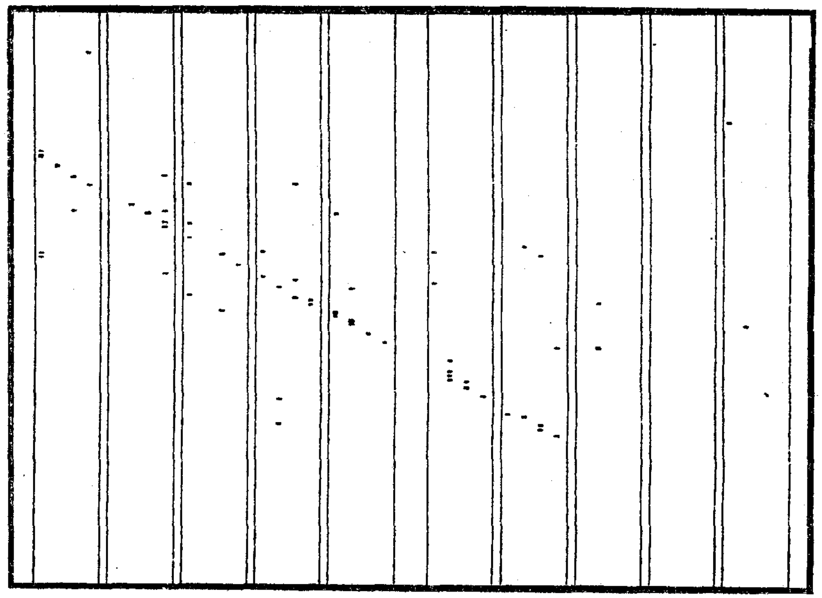

Y VIEW

Figure 11

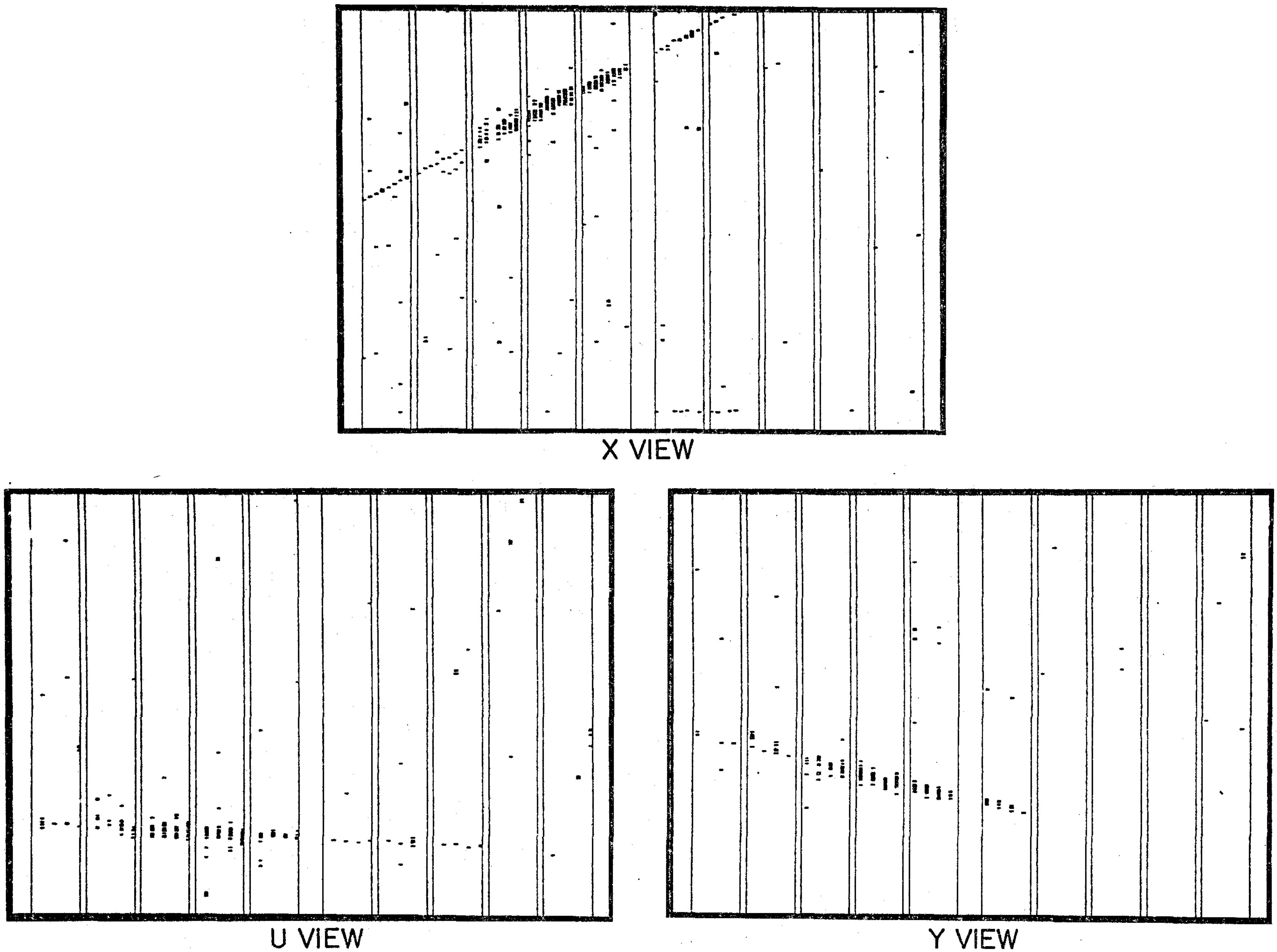

Figure 12

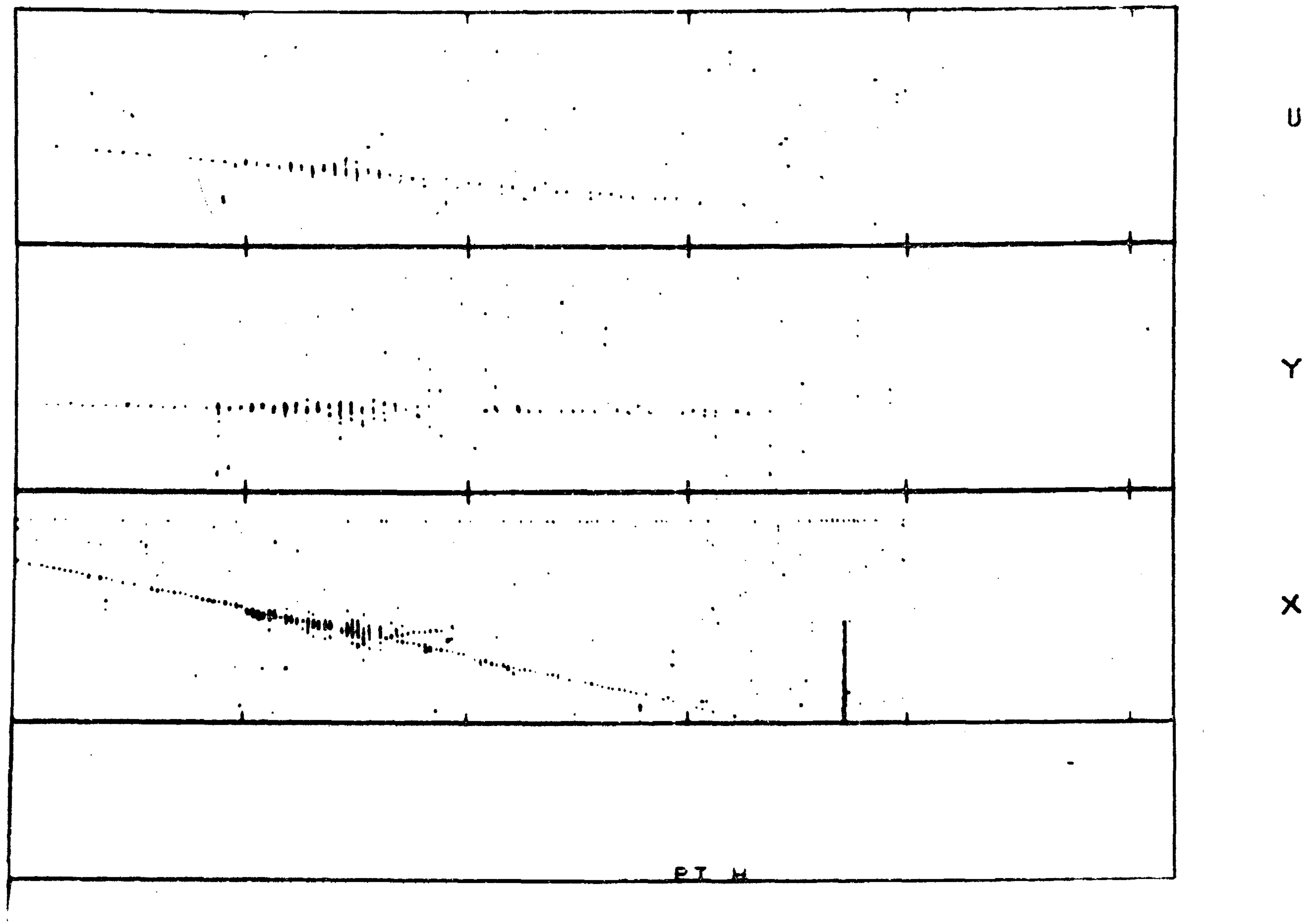

Figure 13

June 1, 1982

Update on Proposal - 649:

PROPOSAL TO STUDY NUCLEON STRUCTURE FUNCTIONS AT HIGH Q^2

Fermi National Accelerator Laboratory
Batavia, Illinois

Massachusetts Institute of Technology
Cambridge, Massachusetts

Michigan State University
E. Lansing, Michigan

Northern Illinois University
DeKalb, Illinois

Physics Goals

The small distance structure of the nucleon is to be measured using high energy neutrino deep inelastic scattering in the fine grained flash chamber - proportional tube calorimeter in Lab C. The calorimeter allows a determination of the structure functions of both charged and neutral current neutrino interactions. These measurements will test gauge theories of electroweak interactions and confront QCD theory in a new high energy range.

After this proposal was made in April 1980, extensive data in both a broad band neutrino beam (1981) and a narrow band beam (1982) have been taken. These data have demonstrated a good signal for the process $\nu_\mu + e \longrightarrow \nu_\mu + e$ and will yield the x-dependence of weak neutral current structure functions. In addition, the detector has been calibrated with beams of hadrons, electrons and muons in the energy range 5 to 125 GeV. (See the Appendix for calibration beam results).

Resolutions

Because P-649 was proposed before the flash chamber-proportional tube calorimeter was completely constructed and before it was calibrated, the resolution in the resolution in the scaling variable $x = Q^2/2M_\rho E_H$ for neutral current events in the narrow band beam has to be re-examined. The resolution in this variable arises from the hadron shower energy resolution, the resolution in the angle of hadron energy flow and on the incident neutrino energy. Using the resolutions from the 1980 calibration given in the appendix, we obtain the resolutions for E_ν=500 GeV compared to E_ν=150 GeV. This is shown as a ratio in Figure 1. There is little difference between the two energy regions. Furthermore, the achieved resolution in x is close to that used in the Monte Carlo simulation given in P-649. The corresponding ratio for charged current events is shown in Figure 2.

The resolution in the other scaling variable y, can also be calculated. The ratio of the y resolution for neutral current interactions at 500 GeV beam energy compared to 150 GeV is shown in Figure 3. The corresponding result for charged current interactions is shown in Figure 4. We see no degradation at the new energy region offered by the Tevatron.

Present Status of the 400 GeV Narrow Band Data

At this time, data are being taken in the narrow band beam. During the run we have made checks of the quality of the data.

Perhaps the most significant of these is the reconstruction of neutrino energy for charged current events. Figure 5 shows the reconstructed neutrino energy for +165 and -165 GeV narrow band momentum. Similar plots exist for the other energies we have studied. These plots indicate that the muon momenta as well as hadron energies are being measured properly. All resolutions appear to be consistent with expectations at this stage of the analysis.

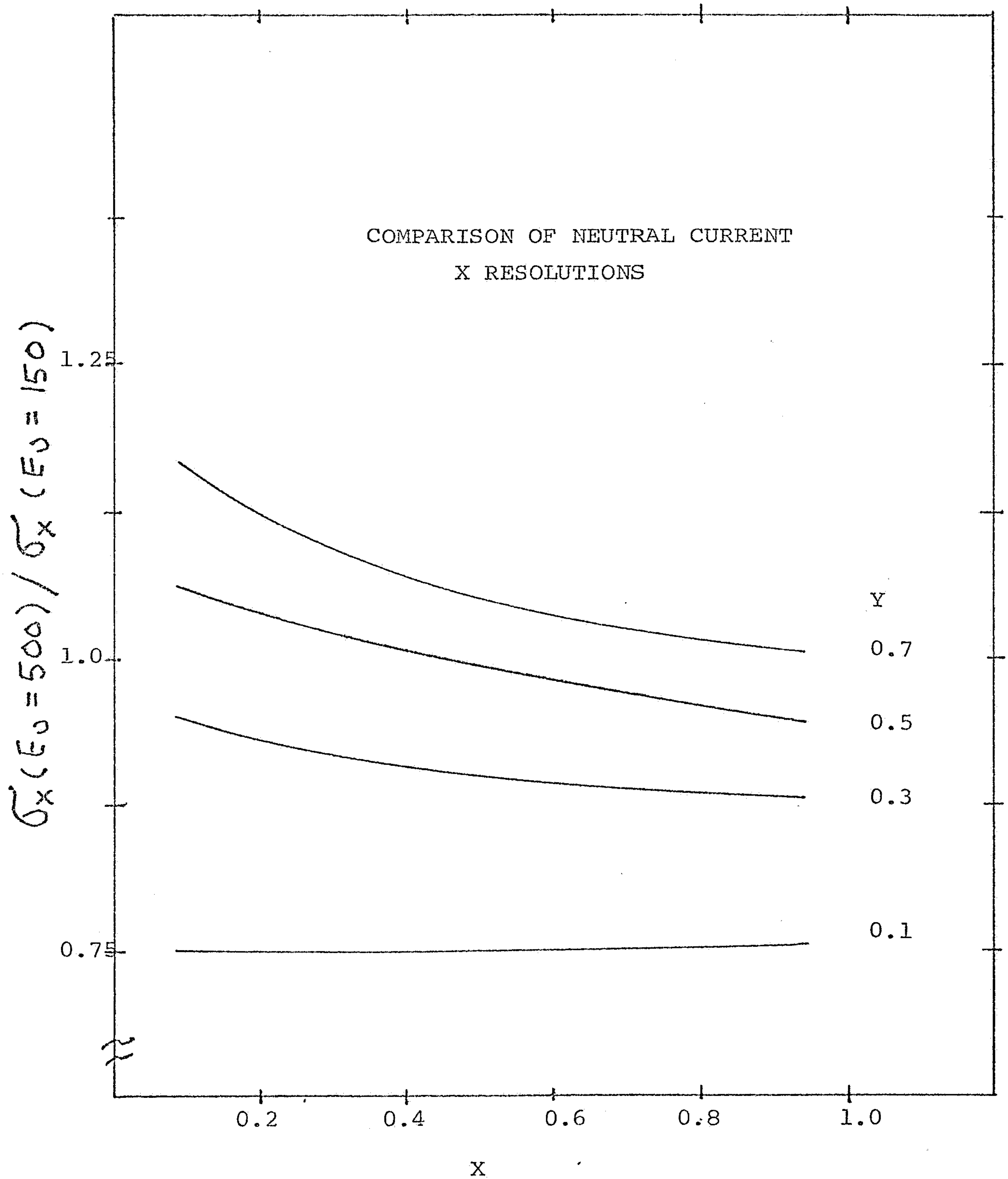
COMPARISON OF NEUTRAL CURRENT
X RESOLUTIONS
σx(Eν=500)/σx(Eν=150)
1.25
1.0
0.75
Y
0.7
0.5
0.3
0.1
0.2
0.4
0.6
0.8
1.0
X

Figure 1

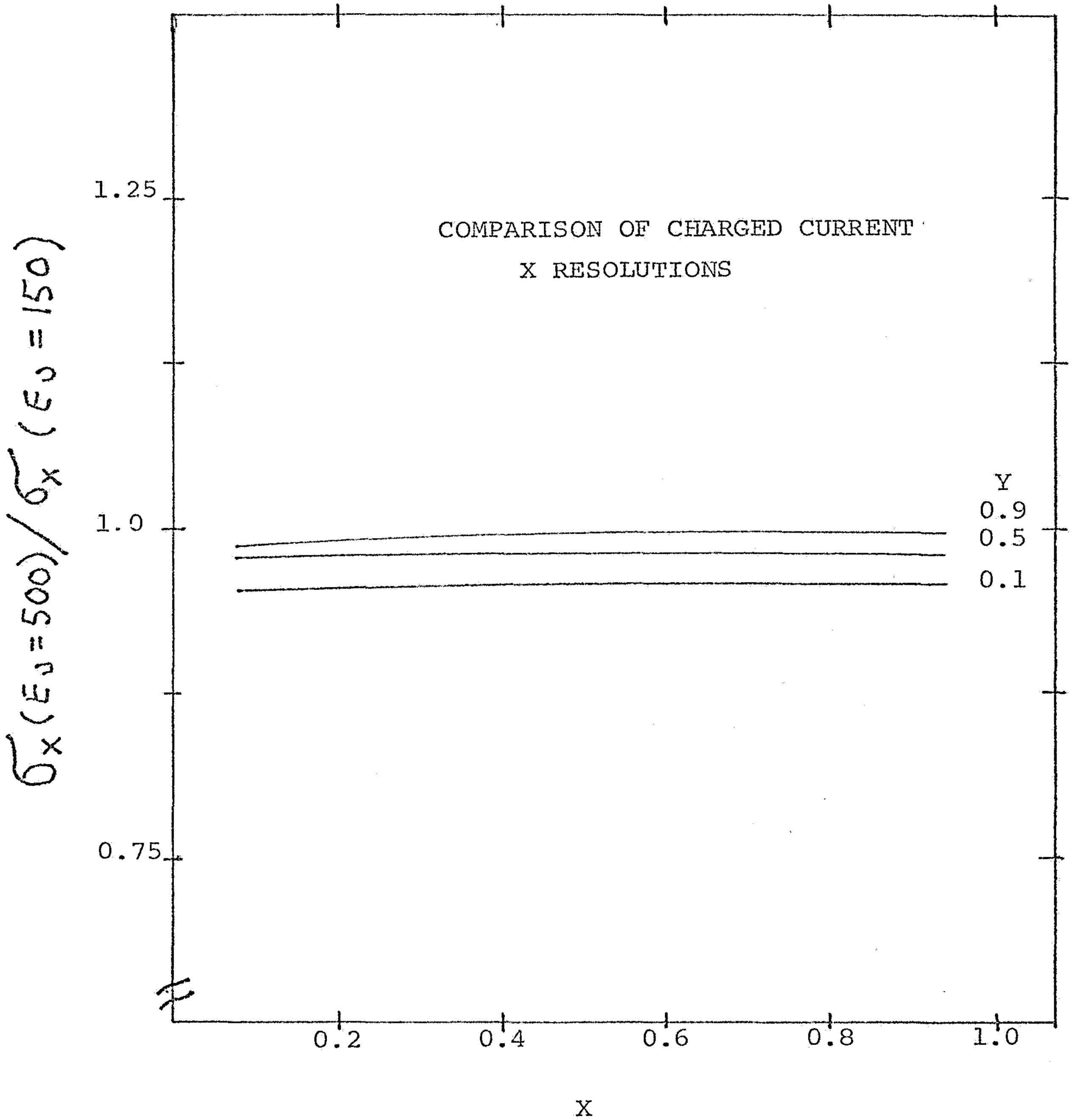
COMPARISON OF CHARGED CURRENT
X RESOLUTIONS
1.25
1.0
0.75
Y
0.9
0.5
0.1
0.2
0.4
0.6
0.8
1.0
X
$\sigma_x(E_\nu=500)/\sigma_x(E_\nu=150)$

Figure 2

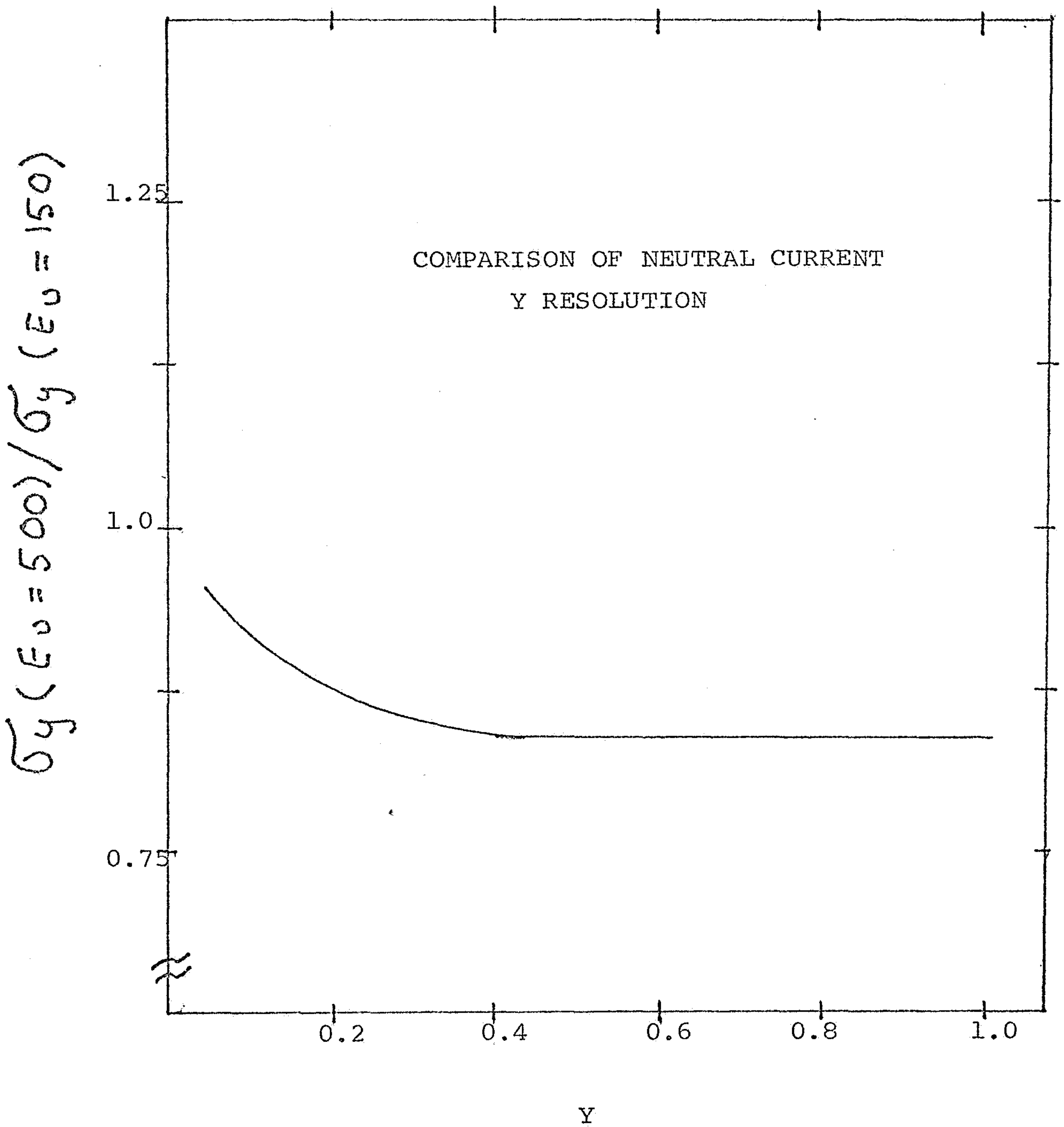
COMPARISON OF NEUTRAL CURRENT
Y RESOLUTION
1.25
1.0
0.75
0.2
0.4
0.6
0.8
1.0
Y
$\sigma_y(E_\nu = 500)/\sigma_y(E_\nu = 150)$

Figure 3

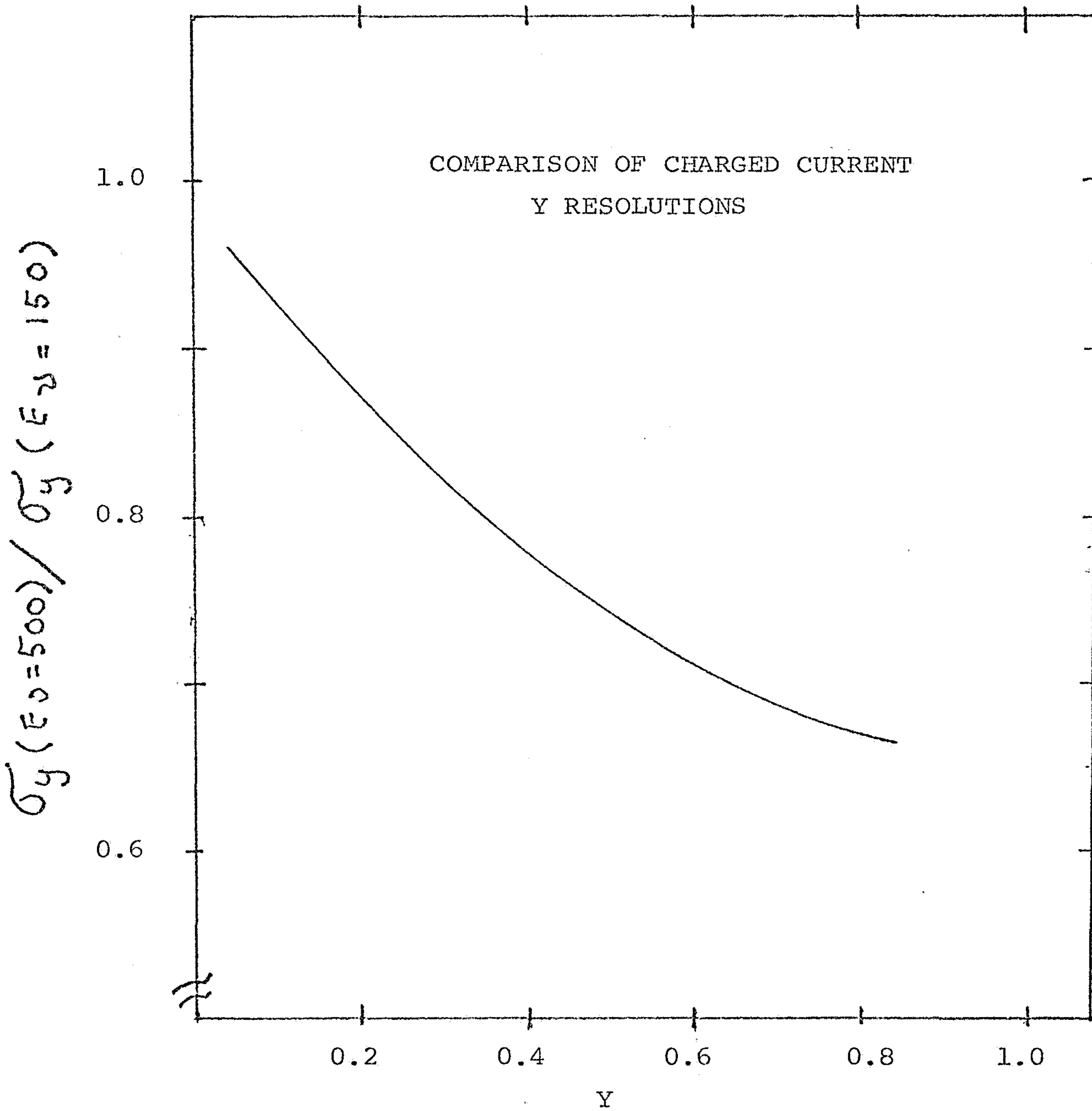

COMPARISON OF CHARGED CURRENT
Y RESOLUTIONS
1.0
0.8
0.6
0.2
0.4
0.6
0.8
1.0
Y
$\sigma_y(E_\nu=500)/\sigma_y(E_\nu=150)$

Figure 4

ENEU -CC- (EVENT)

HBOOK ID = 57 DATE 82/05/14

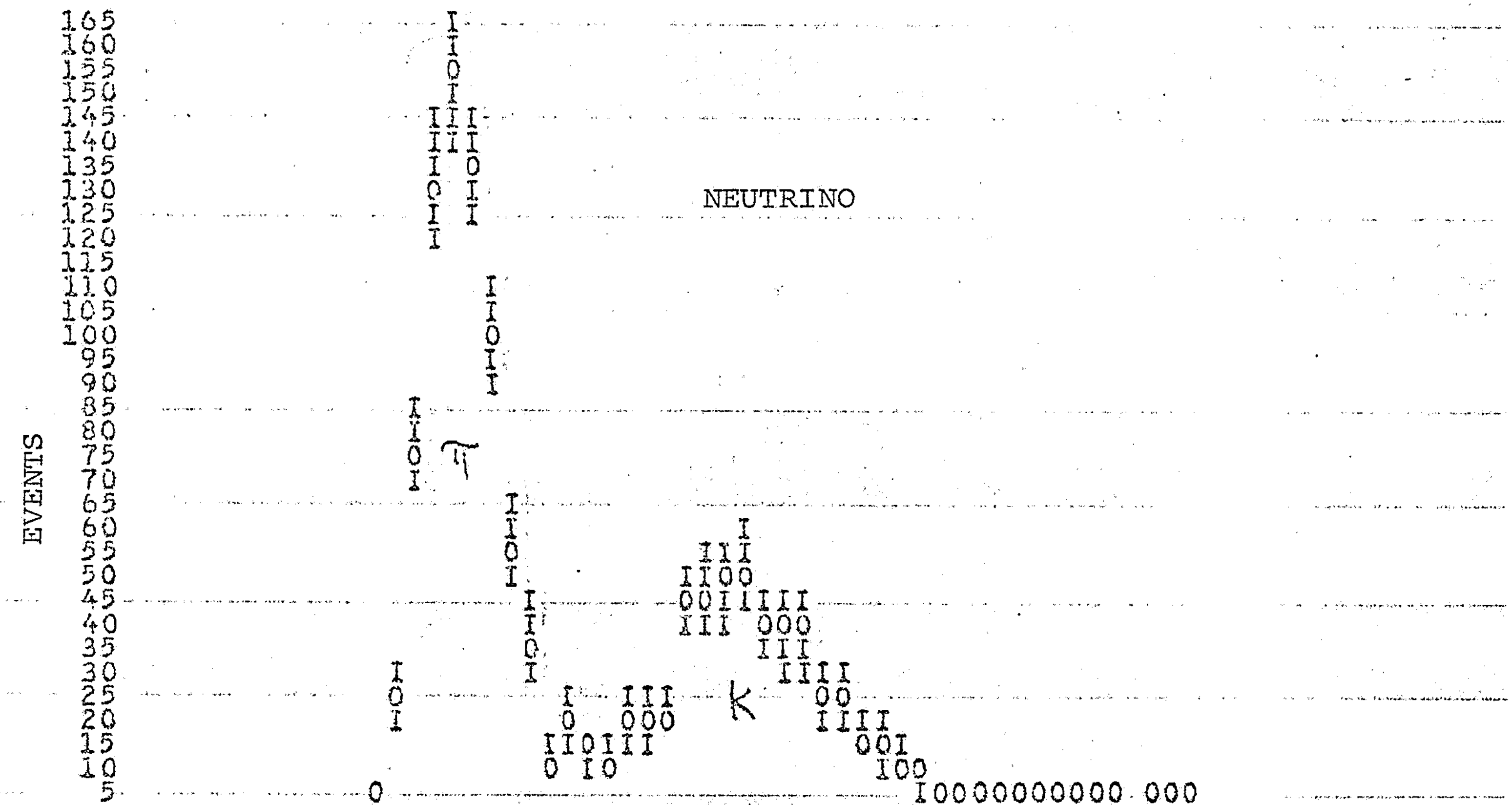


```
CHANNELS 10   0         1         2         3         4         5
          1   12345678901234567890123456789012345678901234567890

CONTENTS 100            111
          10           27353953 1111124444333222111
          1.          245013755971077035698664353061313322312 121

INTEGRAT1000                               1111111111111111111111111
         100            1235667777777888990001111111111112222222222
          10           2038116012346804938269245788899990000000111
          1.          26112527218996336176406038117812580256889122

LOW-EDGE 100                  1111111111111111111122222222222222222
          10     1123344566778899001223345566788990112234455677889
          1.    6284062840628406284062840628406284062840628406284
```

E ν_μ (GeV)

Figure 5a

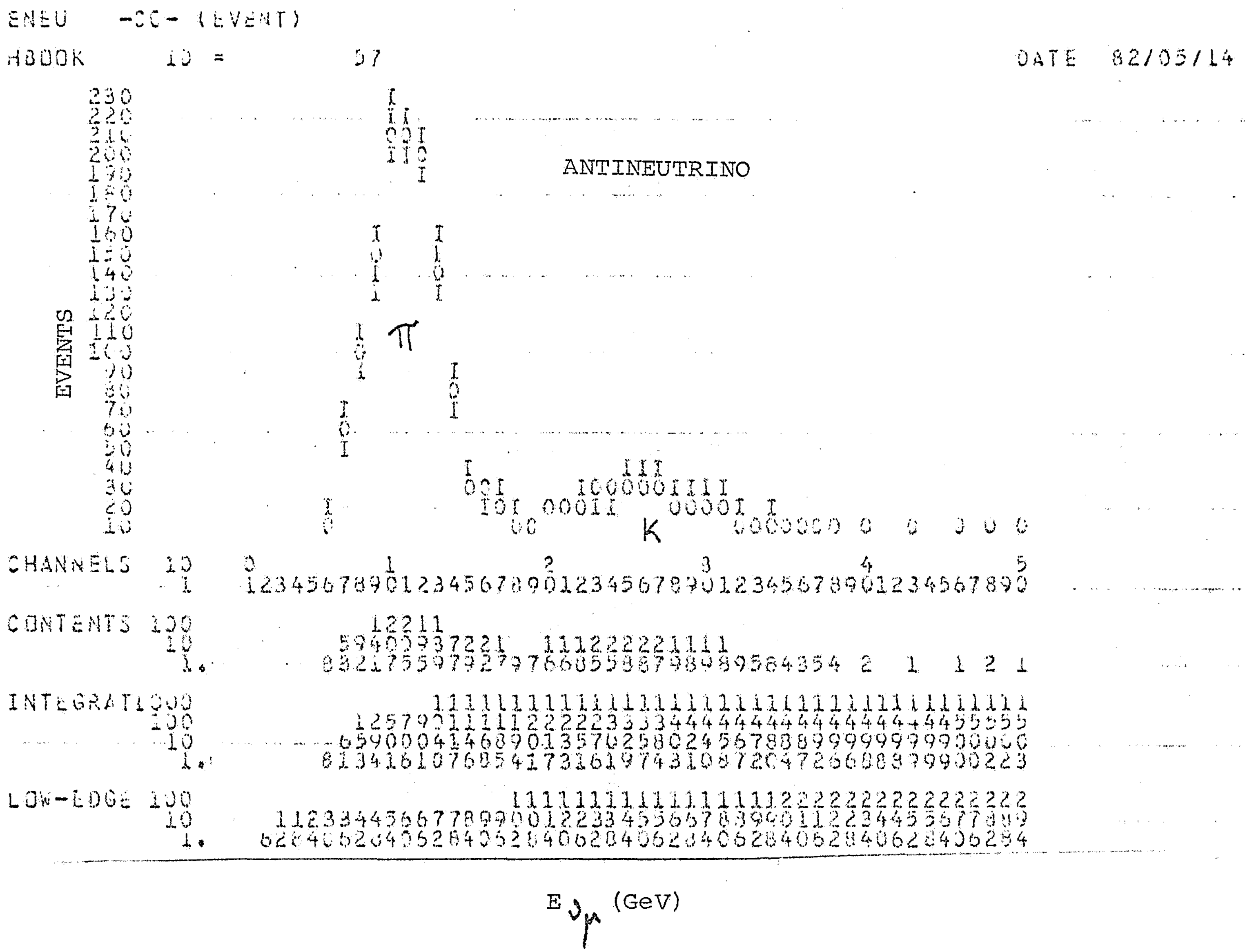
ENEU -CC- (EVENT)
HBOOK ID = 57
DATE 82/05/14
ANTINEUTRINO
EVENTS
π
K
CHANNELS
CONTENTS
INTEGRAT
LOW-EDGE
E νμ (GeV)

Figure 5b

APPENDIX

IEEE Transactions on Nuclear Science, Vol. NS-29, No. 1, February 1982

THE OPERATION OF A LARGE FLASH CHAMBER NEUTRINO DETECTOR AT FERMILAB

D. Bogert, R. Brock, R. Burnstein*, S. Fuess, R. Fisk, J. Morfin,
M. Peters**, L. Stutte, and J.K. Walker
Fermi National Accelerator Laboratory
Batavia, Illinois

J. Bofill, R. Burg, W. Busza, J.I. Friedman, M.C. Goodman, H.W. Kendall,
T. Lyons, T. Mattison, L. Osborne, R. Pitt, L. Rosenson, A. Sandacz,
M. Tartaglia, R. Verdier, S. Whitaker, G.P. Yeh
Massachusetts Inst. of Technology
Cambridge, MA

M. Abolins, A. Cohen, J. Ernwein***, D. Owen, J. Slate
Michigan State University
East Lansing, MI

F.E. Taylor
Northern Illinois University
DeKalb, IL

Abstract

The operation of a large flash chamber neutrino detector at Fermilab is described. The detector consists of 608 flash chambers, and 37 proportional chambers with an active area of 12'x12'. Planes of sand and steel shot are interleaved with the flash chambers and proportional chambers to provide a fine grain sampling of recoil showers. The mass of the detector is 340 tons. The calibration of the instrument for electrons and hadrons in the energy range of 5 to 125 GeV is described.

* Perm. address Illinois Inst. of Technology
Chicago, Illinois 60616
** Perm. address University of Hawaii
Honolulu, Hawaii 96822
*** Perm. address CEN Saclay
B.P. No2,
91190 Gif-Sur-Yvette,
France

Introduction

To study neutrino-induced weak neutral current interaction it is necessary to have a massive neutrino detector capable of measuring both the energy and the direction of the reaction products. A pattern recognition capability of the showers resulting from the primary neutrino interaction is also a useful design consideration, and allows the study of rare processes. To realize these latter capabilities, the neutrino detector must be fine grained. In this paper we describe such a fine grained detector which we have built at Fermilab. The detector is based on polypopylene flash chambers and proportional tube chambers. These devices allow a very high degree of segmentation in both the data as well as selectivity to rare processes in the trigger. The experience we have obtained in long period operation of the detector in quadrupole triplet and single horn neutrino beams and the results of a calibration of the detector for electrons, hadrons and muons will be described in this paper.

The Detector-General Description

The flash chamber - proportional tube calorimeter is 60 feet long (18.3m) and has a 12'x12' (3.66mx3.66m) cross section and a mass of approximately 340 metric tons. The flash chambers are used to determine the pattern of the neutrino reaction products thereby furnishing an identification of the event type as well as determining the energy and angle of energy flow. The proportional tube chambers are used to trigger the flash chambers and to provide another measurement of the energy of the shower. The layout of the detector is shown in Figure 1.

The flash chambers are arranged in three views (x,y,u) with cells which run 0°, 80°, 100° relative to the horizontal plane respectively. Each flash chamber plane is

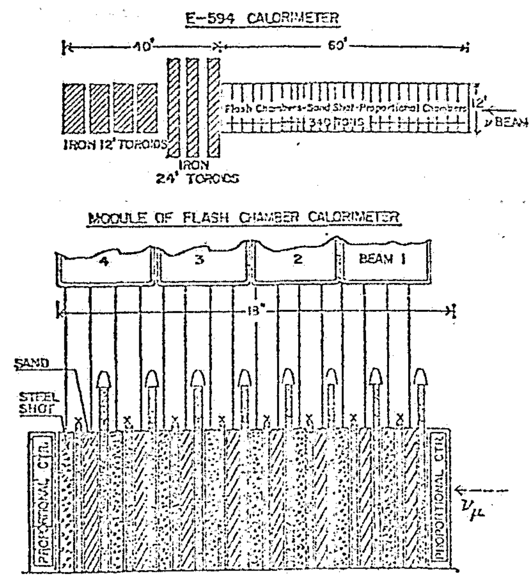

Fig. 1: Layout of the detector.

sandwiched between a sand filled plastic extrusion plane and a steel shot plane. The flash chambers are read out electronically. The details of this system have been described earlier[1].

The proportional tube planes are located every 16 flash chamber planes (one module) in an alternating horizontal - vertical pattern. Each module weighs approximately 9 tons.

The proportional tube chambers are instrumented with an amplifier for every 4 wires with a wire separation of 1 inch (2.54 cm). This high level of segmentation gives pattern recognition at the trigger level as well as analog information on the energy deposition of the shower profile.

This arrangement of flash chambers - proportional tube chambers - sand and steel shot has an average radiation length of 12 cm sampled every 22% X_0 by the flash chamber and every 3.5 X_0 by the proportional tube chambers. The average absorption length is 83 cm (116 g/cm^2) and is sampled every 3%λ by the flash chambers and every 50%λ by the proportional tube chambers. The average density is 1.4 g/cm^3 and the average Z is approximately 21. This properity of low density and low Z is important in achieving good energy flow measurements for hadron showers.

Downstream of the flash chamber - proportional tube chamber calorimeter is an iron toroid muon spectrometer. This spectrometer is instrumented with double plane proportional tube chambers and is described in detail elsewhere in this conference.

In addition to the proportional tube chambers there are 10 12'x12' liquid scintillation counters. One plane is at the upstream end of the detector to act as a charged particle veto, one plane is downstream of the muon spectrometer, and one plane is placed every 80 flash chamber planes. They are used to provide an independent muon trigger of the calorimeter for dignostic and monitoring purposes.

The pattern recognition capabilities of the detector are evident in Figure 2, which shows an online display of a high energy neutrino interaction taken during the spring 1981 engineering run. Shown are the 3 views of flash chamber planes (x,u,y on the display). Each dot drawn on the display represents a struck cell in the calorimeter. The total number of struck cells is shown as the quantity HITSUB, which is 1036 in this event. (There are roughly 400,000 cells in the calorimeter.) Since the total number of hit cells is proportional to the energy of the shower, we estimate the energy of this event to be ~25 GeV.

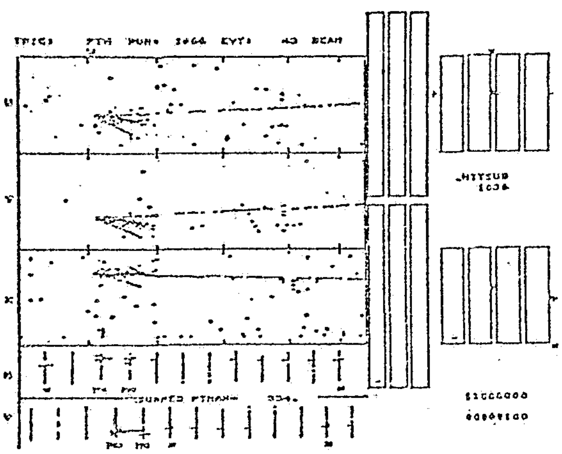

Fig. 2: Typical high energy charged current neutrino interaction. The high degree of segmentation of the data is evident.

Also shown in Figure 2 are the pulse heights of the proportional tube planes which provided the trigger of this event. These pulse heights appear as bar graphs along the lower edge of the picture for the horizontal (H) and vertical (V) plane orientation. The lateral profile of energy deposition of the 150 GeV shower is evident.

The toroids are shown at the right of Figure 2. The "+" signs indicate the track of the muon through the spectrometer in the horizontally (bottom) and vertically (top) oriented proportional planes.

We have operated the calorimeter for two major running periods. The first period was April to June 1980 during which time 180 tons of the detector were instrumented. Data were taken during this running period on neutrino interactions in the quad-triplet beam and the response of the detector was measured to a test beam consisting of electrons, muons, and hadrons. The second running period was January to May 1981, during which time 240 tons of the detector were instrumented. The detector was exposed to a single horn wide band neutrino beam. Various selective triggers were developed during this period and data were accumulated on deep inelastic neutrino scattering as well as various rare processes.

1) Operation of the Flash Chamber

The flash chamber system of the calorimeter has three major components: 1) the gas system, 2) the high voltage pulsing system, and 3) the readout system.

1) Operation of flash chamber gas system

The gas mixture and the gas purity affect the efficiency, reignition probability and the sensitive time characteristics of the flash chambers. Owing to the diffusion of the gasses through the (0.5mm thick) polypropylene walls of the flash chambers, and the long term outgassing of the polypropylene, it is necessary to change the gas in the flash chambers at a rate of approximately one chamber volume/hour. The gas is recirculated and purified by a two sieve gas purification system, which can purify up to 5.4×10^4 liters/hour.

The initial operation of the flash chambers was carried out with a standard Ne-He (90%-10%) mixture. (Under long term operation conditions this gas mixture changes to 96% Ne, 4% He by the diffusion of He gas out of the system.) This mixture gave a good HV plateau with good efficiency versus delay characteristic, and was used during the 1980 run. However, the reignition probability, that is, the probability that a given hit cell in the flash chamber will refire, was rather high (6 to 8%), and gave rise to an after-imaging of the previous event, even with a time between events of 10 seconds.

Considerable experimentation was invested in reducing this reignition probability. A two phase solution was found:

a) By introducing a small amount of argon at the concentration of ~0.2% of the Ne-He gas content the long lived meta-stable excited states of Ne were de-excited by the Penning effect. The exact amount of Ar was determined by the chamber performance, and by the practical constraint that too much Ar would rapidly contaminate the cold sieve of the gas purification system. The addition of the Ar gas makes the plasma discharge stronger at a given high voltage and therefore allows the high voltage operating point to be lowered. Measurements have shown that the reignition probability is unaffected by the addition of Ar at a given HV, but since the Ar allows the operating point to be lowered, a reduction in the reignition probability is achieved.

b) A small amount of electronegative gas was introduced into the Ne-He-Ar mixture. This was accomplished by passing roughly 1/3 of the recirculating gas back into the chambers without going through purification by the gas system. The electronegative gases were the O_2, N_2 and H_2O which naturally contaminate the flash chamber gas through diffusion and outgasing. The electronegativity was controled by monitoring the O_2, N_2 and H_2O content with a gas chromatograph. The gas mixture returning to the flash chambers was 96%Ne, 4% He, 0.17% Ar, 0.10% H_2O and 0.04% O_2 and N_2.

The flash chamber characteristics for various gas mixtures are shown in Figure 3. It is evident from this Figure that the reignition probability is not reduced at a fixed high voltage by the addition of the Ar gas alone, but by the lowering of the high voltage operating point allowed by the lower HV characteristics of the Ne-He-Ar mixture, and by the addition of small levels of electronegative gases, the reignition probability is reduced from 6 to 8% to 1 to 2% at a 10 second repetetion rate. The efficiency remains the same under this condition. The addition of too much Ar or too much electronegative gas degrades the uniformity of the single muon efficiency across the 12' sensitive area of the flash chambers.

Other gas mixtures using a different ratio of Ne to He were investigated. It was found that the flash chambers work well for a mixture of 30% Ne and 70% He with roughly 0.17% Ar. This gas mixture is less expensive than the 90% Ne-10% He, but the gas losses from He diffusion are greater, making gas replacement larger. More experimentation using this gas mixture is planned.

The various chamber characteristics were measured throughout the run, and were found to be reasonably stable. The chamber efficiency was slightly affected by the ambient humidity, degrading by roughly 1.4% for every additional g/m^3 of H_2O in the surrounding air. This small variation can be controlled by air conditioning.

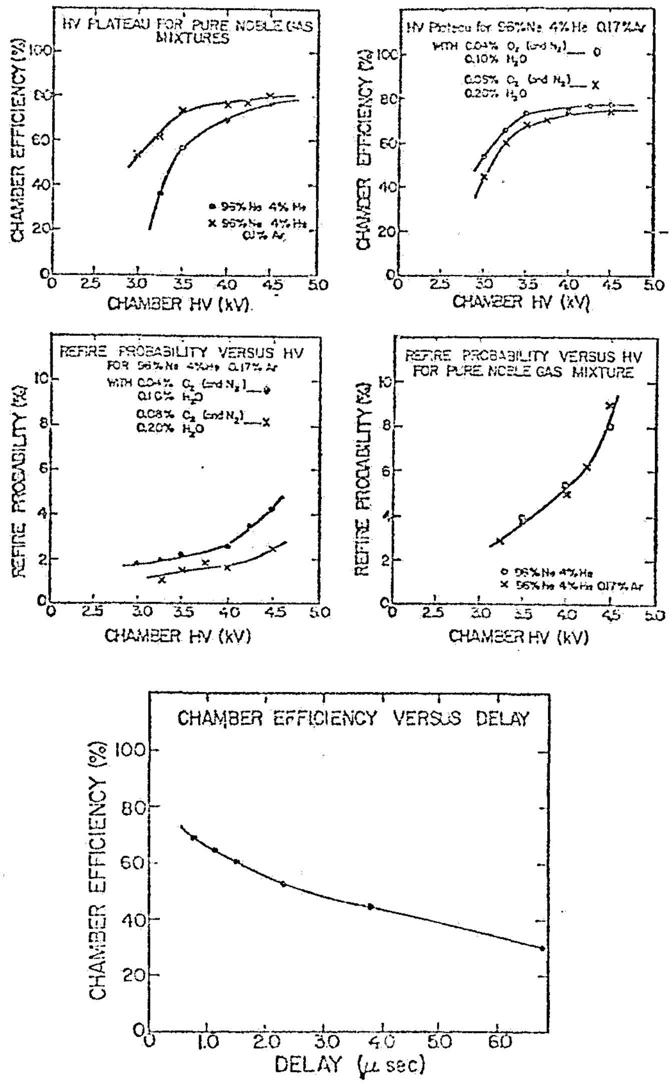

Fig. 3: Flash chamber operation characteristics for various gas mixtures.

2) Operation of the HV System

Each flash chamber is equipped with a pulse forming network (pfn) (see Figure 4) which generates a high voltage pulse of roughly 60 nsec rise time, 4.5 kV magnitude, and 500 nsec duration. The pfn's are triggered roughly 700 nsec after the event. In order to maintain consistency in the HV pulse quantity, a computer based monitoring system was designed.

The system measures the total charge in each of the high voltage pulses applied to the chambers, checks the front-edge timing, and verifies that no spurious pulsing takes place between triggers.

The system, shown in Figure 5a, has a capacity of monitoring 640 channels and consists of 8 special crates of electronics controlled by an LSI 11-23 based computer system. Each of the crates holds a crate controller module and five data modules. Each data module contains the electronics to monitor 16 pulsers as well as an 8 bit serial shift register readout system shown in Figure 5b. The inputs to the data modules come from a monitor output connector on each high voltage pulser via RG-174 coaxial cable which are derived from the high voltage pulse through a 100 to 1 resistor voltage divider.

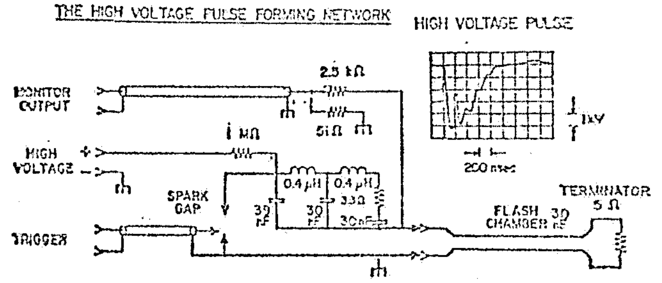

Fig. 4: Circuit diagram for the HV pulses (pulse forming networks -pfn).

The high voltage pulsers, shown schematically in Figure 4, upon receiving a trigger, switch the charge stored in their capacitors (99 nF) across the chambers. The pulse monitor system then a) checks whether the front edges arrive in proper synchronism with the trigger, b) determines whether there is spurious pulsing, and c) measures the total charge in each pulse.

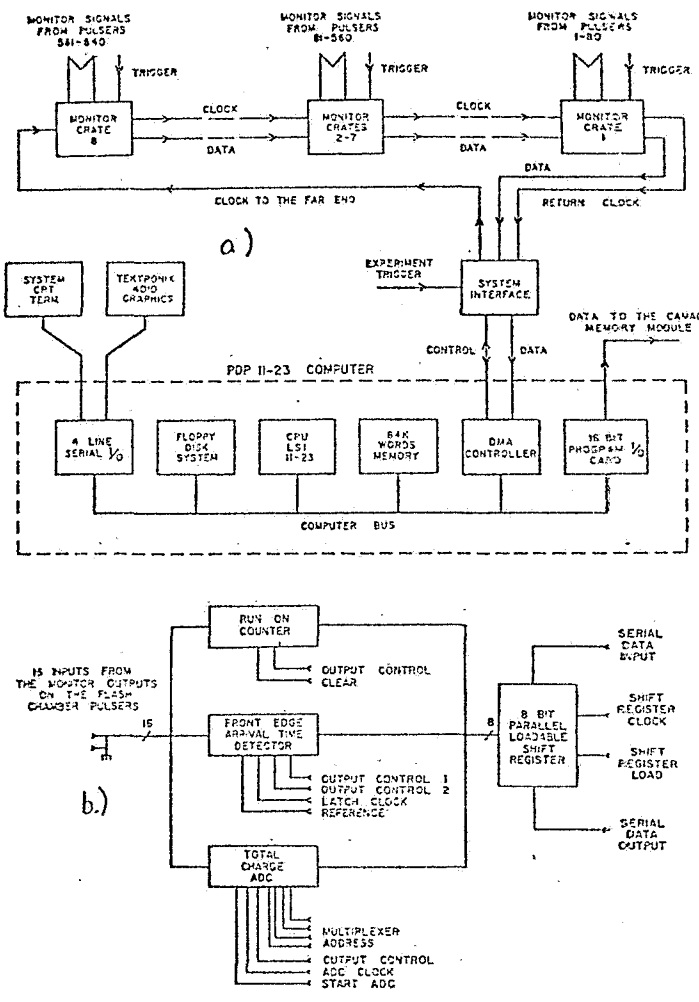

Fig. 5: The HV monitoring system.

a) The front edge arrival time is considered satisfactory if the pulse amplitude exceeds a preset comparator level by the time a signal derived from the trigger arrives at the crate controller. A channel with a bad front edge is flagged by setting a bit in a storage register for later readout. The comparator level for all 80 channels in a crate is set by adjusting a ten-turn potentiometer on the controller module.

b) To check for spuriously firing (runaway) spark gaps, each 16 channel data module contains two 4 bit "run-on" counters. The input to each of these is the logical "OR" of 8 adjacent monitor channels. This arrangement results in the run-on counters containing a count of 1 if the pulsers have worked properly. In the event of a spurious discharge of any of the 8 pulsers being monitored, the count in the run-on counter is increased by 1. Thus, a runaway pulser can easily by located to a group of eight from where it can be spotted visually.

c) To measure the total charge in the high voltage pulse, the monitor signal for each channel is integrated with a resistor capacitor combination and then digitized using an 8 bit analog - to - digital digital converter (ADC). The details of this circuitry are shown in Figure 5. A single 40 pin integrated circuit contains the necessary analog multiplexer and ADC to service a 16 channel module. The voltage across the 16 integrating capacitors are digitized in succession with each conversion taking about 100 μsec. The capacitors are allowed to discharge during this process with a time constant of 50 msec, a rate that insures complete discharge by the time the next pulse arrives (> 10 sec). No dispersion in the measured pulse-heights is introduced by the capacitor discharge since the digitization of the charge is always done at the same time relative to the monitor pulse.

The information from the three - pulse - analysis section in a data module is read into the computer by a single shift register bit serial data path linking all the modules. The program used for data acquisition and display is an RT-11 version of MULTI[2] with special data handlers to accomodate our hardware configuration. Further details of this readout system can be found in reference[3].

3) Operation of Flash chamber Readout System

The flash chambers are electronically read out using a magnetostrictive system. There are 1216 magnetostrictive amplifiers and a corresponding number of discriminator-comparator circuits. Proper operation of this system is maintained by assuring that the magnetostrictive wire magnatization remains constant. This is achieved by automatically pulsing a solenoidal magnet wrapped around each magnetostrictive wand every 200 flash chamber pulses. The locations of the fiducial markers on the magnetostrictive outputs are monitored and are found to be stable to within ~2 mm (1 digitizing clock count) over long periods. This readout system, once set up and tuned, requires very little maintenance.

Calibration of the Calorimeter

The energy and angle resolutions of the calorimeter were determined by measuring the response to beams of known properties. The calibration beam contained electrons, muons or hadrons with electrons identified by a Cerenkov counter. The energy range of the calibration data was 5 to 125 GeV.

1) Electrons

The angle resolution of electron showers is shown in Figure 6a. The electron shower angle was computed by a weighted least squares method using the flash chamber hit cell information. The weights in the fit were determined by the average shower characteristics and the statistics associated with the hit cells.

The electron energy resolution is shown in Figure 6b. The electron energy has been computed by counting the number of hit cells in the shower. We have compensated for the saturation effect caused by more than one particle going through a given cell by estimating the actual number of particles given through each cut from the local density of hit cells. This compensation makes the energy response of the detector nearly linear and improves the energy resolution.

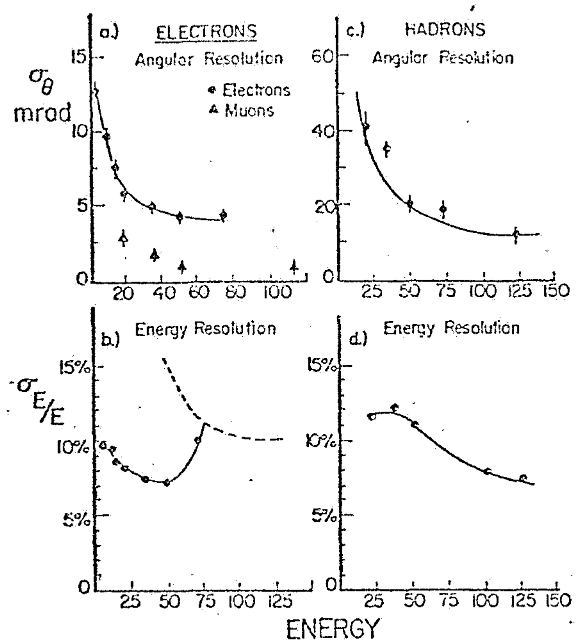

Fig. 6: a) The projected resolution of electron showers and muon tracks versus energy. A fit to the electron resolution is $\sigma(\theta_e) = (3.5+53/E)$ mrad.. b) The electron energy resolution. c) The projected hadron shower angle resolution. A fit to the data is $\sigma(\theta_h) = (6+640/E)$ mrad.. d) The hadronic energy resolution.

2) Muons

The muon angle resolution is shown in Figure 5a. The muon angles were computed by a least squares procedure with a weighting along the track length determined by multiple scattering. The observed resolution is in close agreement with the limit set by multiple scattering and the finite flash chamber cell size (0.577 cm). The muon momentum resolution has not yet been measured but is estimated to be $\Delta p/p \simeq 15\%$.

3) Hadrons

The hadron shower angle resolution is shown in Figure 6c. This is computed in the same way as the electron shower angle resolution but with different weights determined by the much larger fluctuations. The quoted resolutions are the average r.m.s. resolutions of the x and of the y/u views.

The hadron shower energy resolution is shown in Figure 6d. The hit cell saturation effect was compensated for as in the electron shower case. This made the energy response of the calorimeter linear and improved the energy resolution by almost a factor of 2 at high energies. The calorimeter energy response to electrons and hadrons as well as the saturation - corrected response is shown in Figure 7.

The electron energy and angle resolutions are roughly what was predicted by a small test calorimeter. The hadron energy and angle resolutions are somewhat degraded from the test calorimeter prediction because of an overly optimistic compensation of the shower noncontainment effects in the test calorimeter.

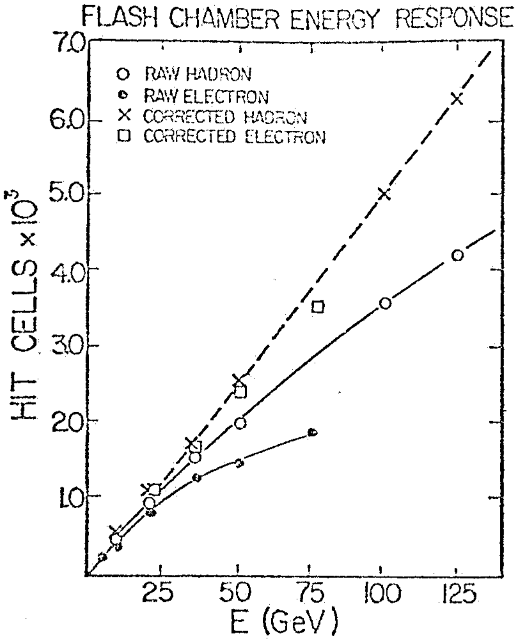

Fig. 7: Flash chamber energy response.

Operation of Proportional Tube Chambers

The proportional tube chambers 12'x12' extruded aluminum planes with 1"x1" cells. Each cell has a 50 μm gold-plated tungsten wire ganged four to each amplifier. The system was operated at 1650 v corresponding to a gas gain of approximately 3000. The gas used in these chambers is the standard "P-10" gas 90% Ar - 10% methane. The entire system consists of roughly 5,300 wires and 1,300 amplifiers. The gains of the proportional tubes were monitored by taking source calibration data of the end of every spill. The pedestals were monitored every 2 to 4 hours and were found to be stable to within 10%. The temperature and barametric pressure influences on the proportional tube gains were monitored in the calibration cycle.

Event Triggering and Electronics

Minimizing the response time of the detector to neutrino-induced events is a key consideration in the design of a trigger. Further, in order to trigger the detector with many interactions occuring in a given spill requires real-time pattern recognition capabilities. In this section we describe a system using the proportional tubes designed to satisfy these requirements.

The funadamental constraint on a proportional tube based trigger system is the fluctuations in the time response due to the different drift times of different through particles. We have reduced these fluctuations to a minimum by employing a simple and fast pre-trigger. The "higher level" (and slower) logic then follows the satisfaction of the pre-trigger requirement allowing for signal development without introducing further significant delays.

Each of the 36 amplifier channels in a proportional plane is capable of generating a fast, differential analog output pulse (F0). The trigger electronics are block-diagrammed in Figure 8. Fast processing electronics on each plane distriminates these 36 F0 signals with respect to a programmed threshold. These discriminated F0 signals are then combined to generate the several analog and logic signals used in an event trigger. A brief description of each follows:

1. Sumout (Σ_i):

   This signal is the linear sum of the undiscriminated individual F0 signals from plane i making a single analog output pulse for each plane.

CALORIMETER TRIGGERING SYSTEM

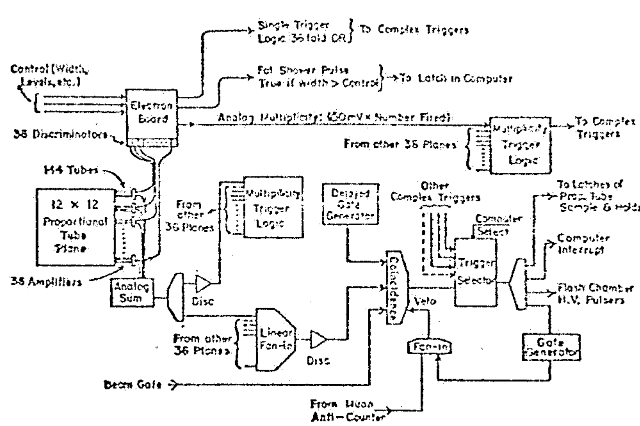

Fig. 8: Calorimeter triggering system.

2. Analog Multiplicity (AM_i):
   This is an analog signal with a pulse height equaling a constant (60 mV) times the number of F0 above the discriminator threshold of 20 mV in plane i.

3. Single (S_i):
   This output is the logical "OR" of all discriminated F0 in plane i. The single plane efficiency for a single muon at the 20 mV operating threshold is 80%.

4. Fat Shower Veto (FSV_i):
   This output is a logic pulse generated when the ionization pattern width in plane i is determined to have exceeded a programmed width (a multiple of 4" segments).

The pre-trigger requirement (M) demands that the Σ_i signals of any two or more planes be above a common threshold of 50 mV which is slightly below the minimum ionizing particle pulse height.

The simplest second level criterion employed in an event trigger was the requirement that the total pulse height summed from all proportional planes ($\Sigma\Sigma$) be above some predetermined threshold level. This is essentially a requirement of a minimum energy deposition. The level was chosen by the requirements of the physics reaction of interest and the requirement of minimizing the additional dead time from cosmic rays and spurious coincidence triggers. These false triggers contributed about 8% and 2% respectively to the low-bias trigger with $\Sigma\Sigma$ = 750 mV.

This unique, versatile triggering system allows the exploitation of trigger-time pattern recognition required for minimal dead time in rare-reaction searches.

Summary

The flash chamber-proportional tube calorimeter has been calibrated, has taken data in an engineering run, and has remained stable for long periods of time. Various improvements in the operating characteristics have been made. Additional data will be taken with the full 608 flash chambers - 37 proportional tube chambers in operation in a narrow band neutrino beam during 1982.

References

1. F.E. Taylor et al., IEEE NS-25, 312 (1978).

   F.E. Taylor et al., IEEE NS-27, 30 (1980).

2. J.F. Bartlett et al., IEEE NS-26, 4427 (1979).

3. D.L. Edmonds et al., "A High Voltage Pulse Monitor System for a Flash Chamber Neutrino Detector," to be published in Nuclear Instruments and Methods. 1981.

Update of Experiment 649

D. Bogert, S. Fuess,
L. Stutte, J. K. Walker
Fermi National Accelerator Laboratory
Batavia, Illinois 60510

J. Bofill, J. I. Friedman, M. C. Goodman
H. W. Kendall, V. Kistiakowsky, T. Lyons,
L. Osborne, R. Pitt, L. Rosenson, B. Strongin,
F. E. Taylor+, R. Verdier

Massachusetts Institute of Technology
Cambridge, Massachusetts 02139

M. Abolins, R. Brock, R. Hatcher,
D. Owen, G. Perkins, M. Tartaglia

Michigan State University
East Lansing, Michigan 48824

+ spokesman

May 15, 1984

Table of Contents

(I) Physics Goals

In Experiment 649 we will probe the structure of the nucleon using the deep inelastic scattering of neutrinos and antineutrinos through the neutral current process. We will compare this structure with that determined by the charged current process from data to be taken simultaneously. The kinematical variables of these neutral current events will be reconstructed from the recoil hadron shower information gathered in the flash chamber-proportional tube calorimeter located in Lab C. A narrow band neutrino and antineutrino beam will be used to fix the incident neutrino beam.

Although the observed structure of the nucleon is believed to be essentially independent of the probe, it is important to make model independent checks of this assumption. In fact, subtle differences are expected to exist between the nucleon structure functions as determined by the two weak gauge bosons probes since the charged current interaction must transform the charge (weak isospin) of the struck quark and thus couple different quark flavors, whereas the neutral current interaction is believed to be "flavor diagonal" and does not couple different quark flavors. In addition to searching for differences of the structure functions in the context of the standard model, there could be some as yet unobserved quark structure which interacts preferentially with the weak neutral current. These quarks could be heavy and thus would appear at high $Q.^2$

Since the outgoing lepton can not be detected in weak neutral current deep inelastic scattering, as it is in electron (muon)- nucleon scattering, the kinematics of a given neutral current neutrino event have to be reconstructed by measuring the recoil hadron shower energy and angle. The energy versus radius correlation of the narrow band neutrino beam is used to estimate the incident neutrino energy.

This measurement requires a special kind of neutrino detector which is both massive and highly segmented to allow both the recoil shower energy and angle to be measured. The technique presents a considerable technical challenge since the recoil hadron shower is difficult to define owing to intrinsic fluctuations in the the shower development. Figure 1 shows a deep inelastic charged current event and a deep inelastic neutral current event. The segmentation of the detector is 5 mm lateral and 1.6 cm longitudinal which corresponds to 3% of an absorbtion length and 12 % of a radiation length.

A list of our physics goals for E-649 is given below.

1) Determine both the neutral current and the charged current structure functions.

2) Measure the electro-weak coupling parameters at high energy accessible in deep inelastic scattering with an isoscalar target.

3) Measure the total neutrino cross section as a function of energy.

4) Search for anamolous events occuring only at high energy or high Q^2.

The high energy of the Tevatron neutrino beam and the large mass (340 Tons) and the fine granularity of our detector are ideal for such a search.

Secondary physics opportunities will arise from actually using the flux monitoring data we will take with a quasi-elastic neutrino nucleon scattering trigger. Within this data sample will be events of the inverse muon decay process. A measurement of these events in the narrow band beam will allow the absolute cross section to be determined and will lead to limits on V+A interactions and right handed neutrinos. A signal of roughly 50 events from this process have been observed in the E-594 narrow band data. A comparable data set is expected to be obtained during the E-649 beam exposure.

(II) Comparison with Other Experiments

There is no other massive, fine grained calorimeter at the Tevatron that will address the neutral current structure function measurement. Hence there is no experiment in direct competition with E-649. The closest comparable experiments are the CHARM I and CHARM II detectors CERN. The CHARM I detector has been used to measure the neutral current structure functions in a 200 GeV narrow band neutrino beam as well as neutrino - electron elastic scattering in a broad band beam at CERN. The CHARM II detector is an upgraded version of the CHARM I detector and will be used to study neutrino - electron elastic scattering and inverse muon decay at the CERN SPS. We do not know if this collaboration plans to study deep inelastic scattering with their upgraded detector. In their proposal, the CHARM II Group emphasize the purely leptonic reactions. The comparison of these detectors is shown in Table I below.

Table I

Comparison of E-649 with CHARM I and II

	E-649	CHARM I +	CHARM II ++
Mass	340	180	618
Lateral sampling	0.5 cm	15 cm scint. or 3 cm prop. drift tubes	1 cm streamer tubes
Longitudinal sampling	12% Xo	100% Xo	33% Xo
Target material	sand and shot	marble	glass

+ A.N.Diddens, et al.;NIM 178 (1980) p. 27

++ C.Busi, et al.;CERN/SPSC/83-24 April 1984

(III) Test Results

There are no test results from E-649 since there has not been a high energy calibration run or any neutrino data taken by this experiment. However there are results from the proceeding experiment E-594, which used the same apparatus and which measured the deep inelastic neutrino and antineutrino nucleon scattering at the 400 GeV machine. The E-594 physics goals were much the same as the goals of E-649.

The essence of the neutral current experiment is to be able to measure the angle of the recoil hadron shower since the Bjorken-x scaling variable of the neutral current events is determined by the expression below (using small angle approximations):

$$x \cong \frac{E_h\, \theta^2}{\left(1-\frac{E_h}{E_\nu}\right) 2M_p}$$

Hence the x resolution depends critically on the recoil hadron shower angle resolution. To demonstrate that there is a measurement of the hadron angle, we look at the transverse momentum balance for charged current events where we can compare the transverse momentum of the hadron shower to that of the outgoing muon. Figure 2 shows the transverse momentum correlation between the muon and the recoil hadron shower. We see that there is an evident correlation indicating that there is a measurement of the recoil hadron shower angle.

In the predecessor experiment E-594, we have measured the ratio of the neutral current deep inelastic x-distribution with that of the charged current neutrino - nucleon scattering. This is called TEST 1 in the E-649 proposal. The ratio directly compares the charged current structure functions with the neutral current structure functions. The preliminary results from E-594 are shown in Figure 3 for each of the 4 secondary beam settings of our data set. The dotted line in the figure are the expectation from a monte carlo simulation of the experiment. We see that the ratios are roughly flat and a detailed analysis is under way to determine the shape parameters of the neutral current structure functions. We expect that the results of E-649 will have a comparable statistical weight but be of higher energies and Q^2 values and thus extend the range of comparison between the two interactions.

(IV) Schedule for Construction and Installation

The basic calorimeter is completely constructed and has been used to gather narrow band neutrino data at the 400 GeV machine. The only major upgrade of the flash chamber-proportional tube calorimeter planned for E-649 is the installation of drift instrumentation in the proportional tube chambers in the iron toroid spectrometer. At this time, the 12′ chambers are constructed and installed. Tests of their spatial resolution are underway. Drift planes are being installed in the rear of the calorimeter just upstream of the 24′ toroid magnets to furnish an accurate entrance position and angle of muon tracks. These will be tested during this calibration run (Spring 1984). The construction and cosmic ray tests of the 24′ planes will take place this summer. Since the drift system has to work for the E-733 experiment, it should be well understood and tested for the E-649 effort scheduled to take place a year and half from now.

(V) Requests

No major construction is forseen for E-694. To maintain and perform small but important upgrades necessary to have a successful experimental program, we request continued technical support for the work in Lab C. The new dichromatic beam has to be tested and the flux monitoring instrumentation has to be developed and tested. We request that a sustained effort be exerted on this very necessary part of the experiment. Finally, we request that the calibration beam presently being commissioned be maintained and made available for at least 2 months during the fall and winter of 1984-1985. There is a further possibility that we will require a check of our calibration at the beginning of the narrow band running presently scheduled for the fall and winter of 1985-1986.

A continuing effort is underway to upgrade the calorimeter instrumentation. We are examining the possibility of a gain control feedback system for the proportional tube planes in the calorimeter, and studies are in progress to improve the operation of the flash chambers.

Figure Captions

Figure 1: A typical charged current and a typical neutral current event in the Lab C neutrino detector. These events were taken in the 1982 narrow band neutrino beam exposure.

Figure 2: The transverse momentum of the outgoing muon in deep inelastic charged current scattering is plotted against the transverse momentum of the recoil hadron shower. The momenta are correlated, indicating that the hadron angle can be measured. Also shown is the difference of projected momenta in comparison with the monte carlo simulation.

Figure 3: The ratio of the x-distribution of neutral current events to that of charged current events for data taken in the 1982 narrow band beam exposure of E-594 is shown. The 4 plots are for the 4 secondary momentum settings of the narrow band beam. The dotted line shows the monte carlo simulation.

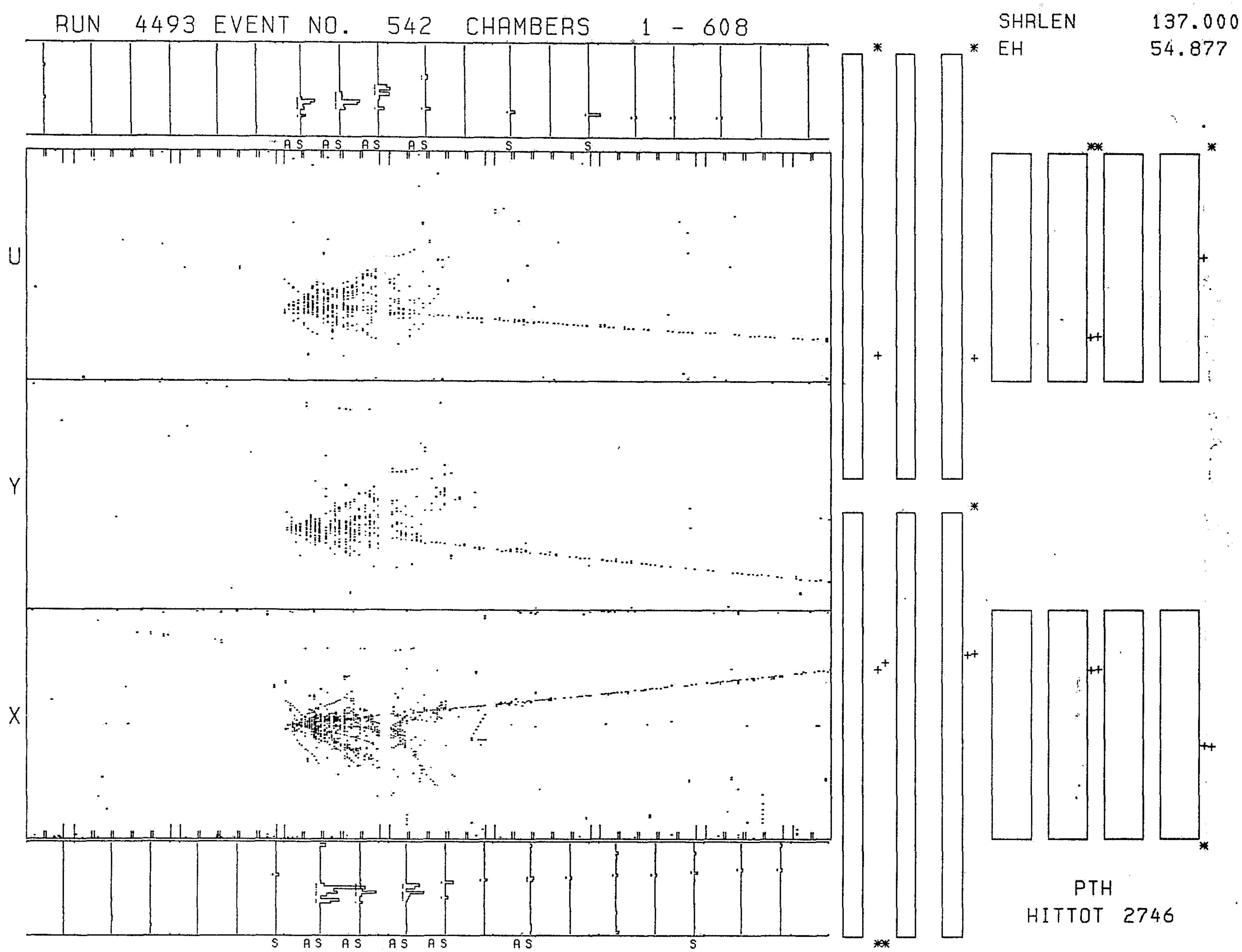
RUN 4493 EVENT NO. 542 CHAMBERS 1 - 608
SHALEN 137.000
EH 54.877
U
Y
X
AS AS AS AS S S
S AS AS AS AS AS S
PTH
HITTOT 2746

Figure 1a

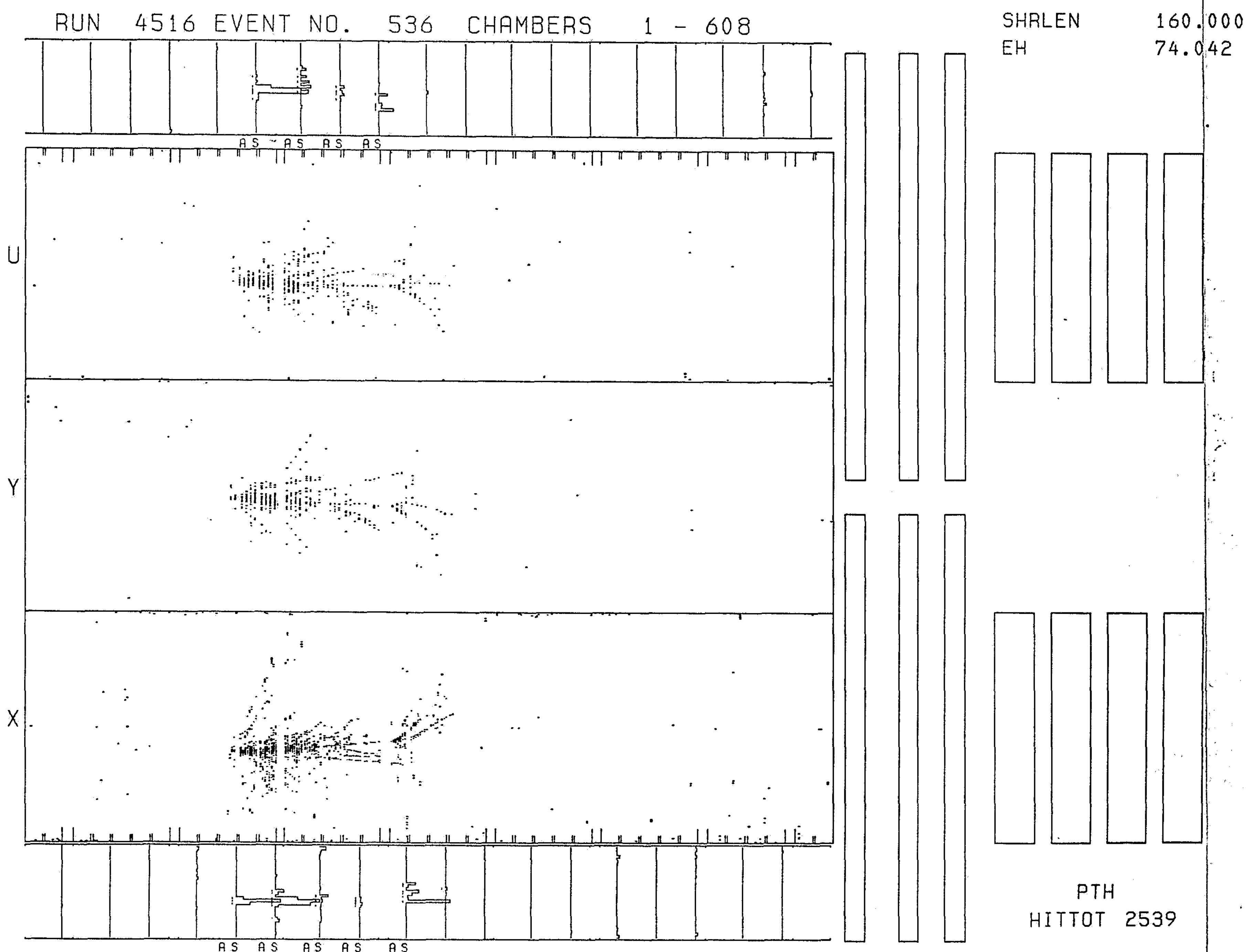
RUN 4516 EVENT NO. 536 CHAMBERS 1 - 608
SHRLEN 160.000
EH 74.042
AS AS AS AS
U
Y
X
AS AS AS AS AS
PTH
HITTOT 2539

Figure 1b

DATA   +165

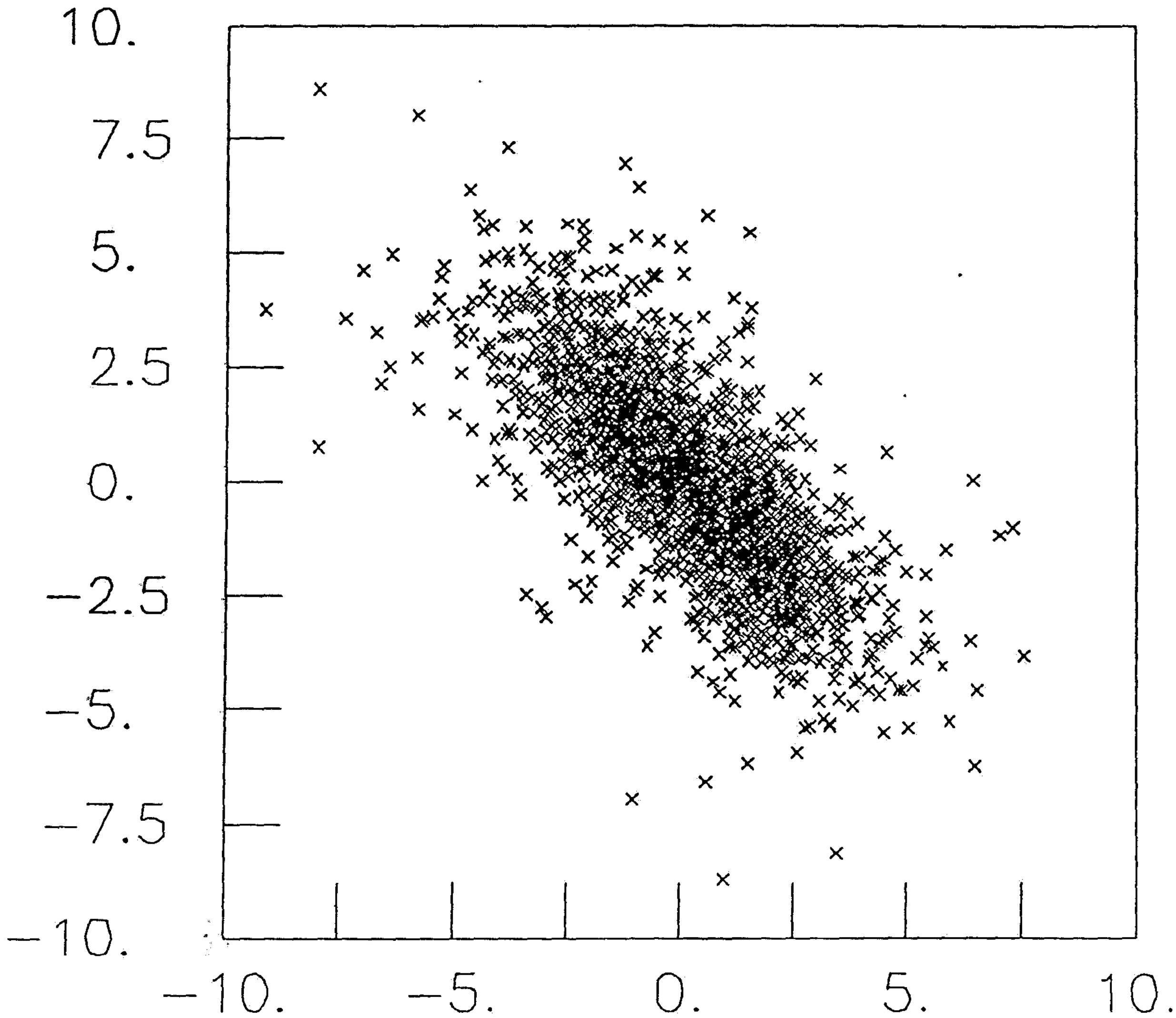

Figure 2a

DATA +165

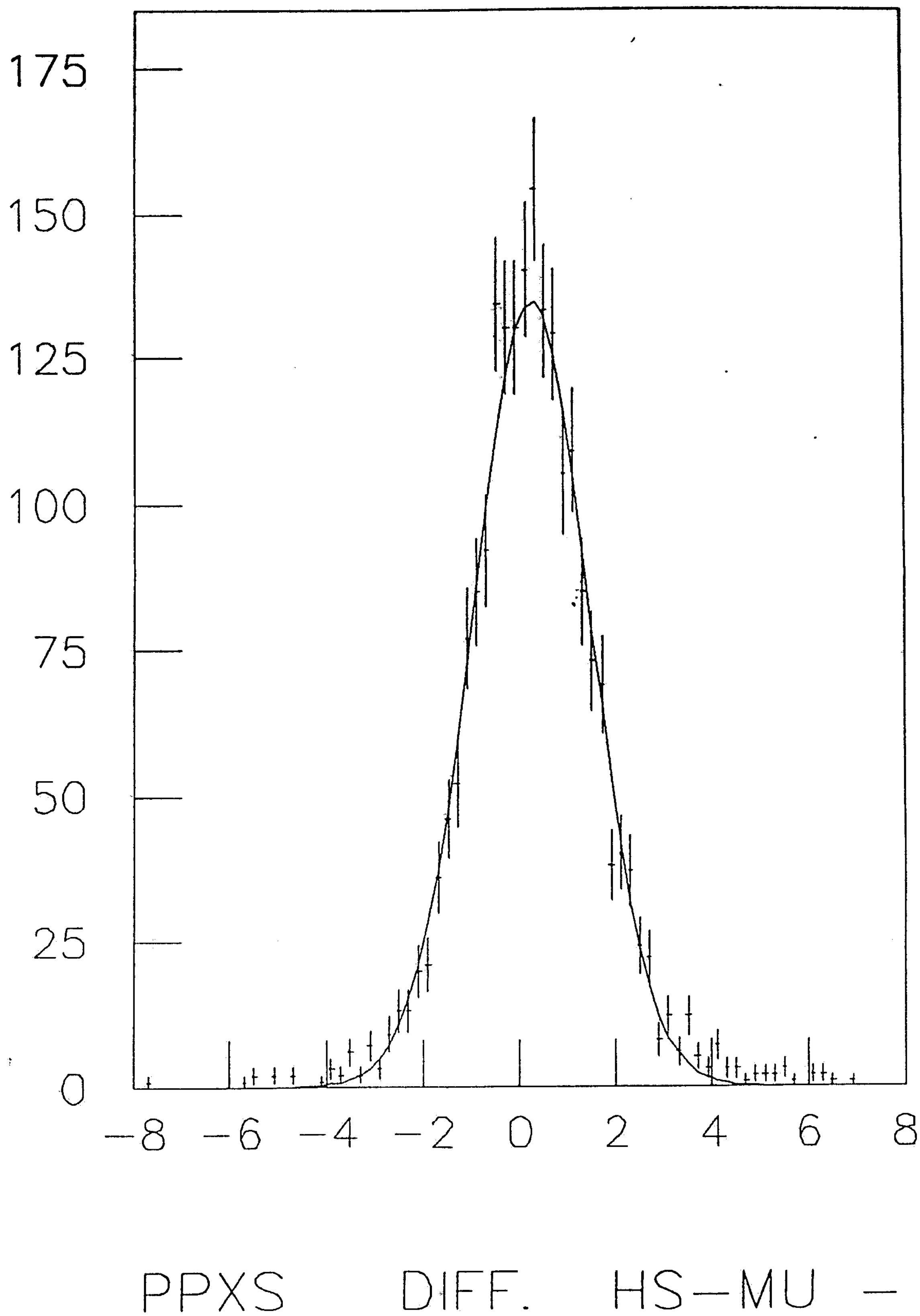

Figure 2b

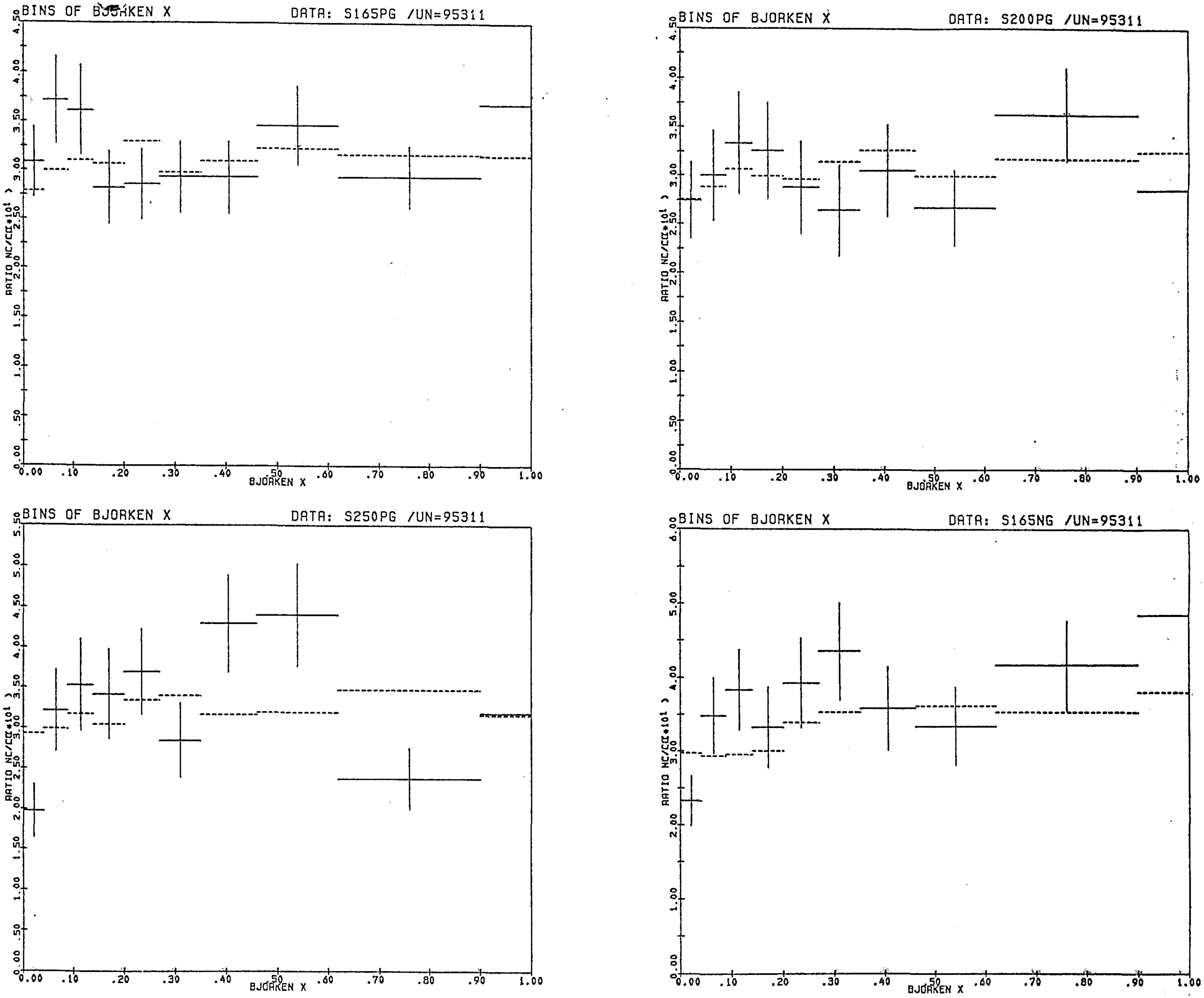
BINS OF BJORKEN X
DATA: S165PG /UN=95311
DATA: S200PG /UN=95311
DATA: S250PG /UN=95311
DATA: S165NG /UN=95311
RATIO NC/CC(*10¹)
BJORKEN X
0.00 .10 .20 .30 .40 .50 .60 .70 .80 .90 1.00

Fig.3

Update of the E-649 Proposal

Proposal to Study the Nucleon Structure Functions at High Q^2

D. Bogert, G.M. Koizumi, L. Stutte,
Fermilab
R. Belusevic, J. K. Walker, A. White
University of Florida
P. Anthony, M. Baker, J. I. Friedman, S. Fuess, H. W. Kendall
V. Kistiakowsky, L. Osborne, L. Rosenson, B. Strongin
F. E. Taylor*, R. Verdier
Massachusetts Institute of Technology
M. Abolins, R. Brock, W. Cobau, R. Hatcher
G. Perkins, M., Tartaglia, H. Weerts
Michigan State University

*spokesman

Summary:

High energy neutrino interactions induced by a dichromatic (anti)neutrino beam are to be studied using the 340 ton fine grained calorimeter located in Lab C. The calorimeter is instrumented with plastic flash chambers and proportional tube chambers endowing it with good pattern recognition capabilities. An iron toroid spectrometer located at the rear of the calorimeter is instrumented with drift chambers to give good muon momentum resolution on the outgoing muons from deep inelastic charged current interactions. With data taken in a dichromatic neutrino beam we are able to reconstruct the kinematics of both neutral current and charged current events. Emphasis will be on the study of the neutral current. The structure functions will be determined, and a measurement of $\sin^2\theta_W$ and ρ will be performed. The total neutrino-nucleon cross section will be measured up to 500 GeV.

Table of Contents

(I) Introduction

Despite the great success of the Standard Model of electroweak interactions, there remain parts of the theory which are poorly understood. The Higgs sector of the theory is free, and there is no explanation for the different quark and lepton generations. There may be supersymmetric companions to the spin 1/2 particles, and quarks and leptons may really be composite. Some glimmer of light may be shed on these questions by a careful measurement of high energy neutrino interactions.

The dichromatic neutrino beam at the Tevatron offers the exciting possibility of studying high energy neutrino interactions under controlled conditions. In this beam the energy and flux of the incident neutrinos can be absolutely determined. The hard energy spectrum of the dichromatic beam allows deep inelastic scattering through the weak neutral current interaction to be studied. Therefore a new probe of the nucleon structure using the weak neutral current becomes available in an unexplored region of higher energy and smaller distances.

By taking data in the narrow band beam, the following topics will be addressed:

(1) Measurement of the total neutrino - nucleon cross section up to 500 GeV. Is there a threshold opening up at high energy? Does the cross section continue to grow in a linear fashion at high energies?

(2) Precision determination of $\sin^2\theta_W$ and ρ under controlled conditions. The systematic errors arising from event-type confusion and charmed quark production in the charged current interaction become small at high energy. Is $\sin^2\theta_W$ independent of Q^2 and E_υ?

(3) Determination of both the neutral current and the charged current

structure functions. Are there any observable differences between the x-dependencies of the two interactions?

(4) Search for exotic final states, such as heavy neutral leptons, which could be produced in deep inelastic scattering. The energy constraints of the narrow band beam will allow a measurement of the missing neutral energy. Limits on the mass and lifetime can be set. The fine granularity of our calorimeter will allow the associated event topology to be observed.

We have used our detector to explore neutrino interactions in the narrow band beam during the 1982 exposure at the 400 GeV machine. From these data we have addressed the following topics: (1) Compared the neutral current structure functions with those of the charged current[1], (2) Determined[2] $\sin^2\theta_W$ and ρ, (3) Measured[3] the total neutrino-nucleon cross section σ_t, (4) Extracted the value of the mean parton p_t in deep inelastic charged current scattering[4], (5) Set a limit on $\nu_\mu \to \nu_x$ oscillations[5], and (6) Tested[6] the standard V-A theory of weak interactions by the reaction: $\nu_\mu + e^- \to \mu^- + \nu_e$.

We believe that another dichromatic neutrino run is necessary to complete our program. The narrow band beam technique is the only way to study the x-dependence of the neutral current interaction, to determine the absolute normalization of the total neutrino cross section, and to measure $\sin^2\theta_W$ with small systematic errors. The higher energy available at the Tevatron will significantly extend our previous measurements.

(II) Theory

(1) General:

The nucleon presents a rich structure when it is examined on any distance scale. At short distances, the nucleon contains quark-antiquark pairs of various flavors. On the long distance scale the nucleon may contain intrinsic heavy quark flavor states[7] as well as the three valence u and d quarks. These heavy quark states may account for the like sign dimuons seen in high energy neutrino-nucleon scattering. They may also lead to exotic heavy baryons which can be produced in both neutral current and charged current scattering.

In the Standard $SU(2)\otimes U(1)$ Model, the neutral current Z^0-quark coupling depends on the weak isospin, the quark electric charge, and $\sin^2\theta_W$. The basic neutral current interaction is believed to be an elastic scattering process which is flavor conserving and has no energy thresholds associated with the mass of the participating quark. In deep inelastic neutrino-nucleon scattering the Z^0-nucleon coupling is given by:

$$(g/\cos\theta_W)\ \Sigma_\alpha \langle q_\alpha | T_3^{\alpha} - Q^{\alpha}\sin^2\theta_W | q_\alpha \rangle \qquad (1)$$

where T_3^{α} is the weak isospin of the quark of flavor α, and Q^{α} is the quark electric charge. The mixing parameter $\sin^2\theta_W$ is free in the Model.

In contrast, the charged current interaction is flavor mixing and has an energy threshold associated with the light to heavy quark mass transitions. The $W^{\pm}$ - nucleon coupling is given by:

$$(g/\sqrt{2})\ \Sigma_{\alpha\beta} \langle q_\alpha | U^{\alpha\beta} | q_\beta \rangle \qquad (2)$$

where $U^{\alpha\beta}$ is Kobayashi-Maskawa matrix. The threshold suppression for the terms in the cross section associated with the light-to-heavy quark mass transitions is accounted for by changing the scaling variable $x = Q^2/2My E_\nu$ into the so-called slow rescaling variable $\xi = x + m_\beta^2/2MyE_\nu$.

In the expression for ξ, m_β is the mass of the final state quark, M is the nucleon mass, E_υ is the incident neutrino energy, $y = (E_h - M)/E_\upsilon$ where E_h is the energy of the hadronic recoil system. The components of the cross section associated with the light-to-heavy quark transitions have a threshold factor $(1-y+xy/\xi)$ which suppresses the heavy quark production near threshold. Figure 1 shows the basic neutrino-quark scattering for the two interactions.

(2) The Cross Section and Structure Functions:

The deep-inelastic scattering cross section is given by the following:

$$d^2\sigma/dxdy=(G_f{}^2ME_\upsilon/\pi)\left[(1-y)F_2(x,Q^2)+y^2xF_1(x,Q^2)\pm(y-y^2/2)xF_3(x,Q^2)\right] \quad (3)$$

where the structure functions $F_i(x,Q^2)$ contain the information of the quark distributions inside the nucleon. We assume the Callan-Gross relation $2xF_1 = F_2$. By using the couplings given above but neglecting the heavy quark thresholds, we express the charged current structure functions for an isoscalar target as:

$$\begin{aligned} F_2{}^{cc}(x,Q^2) &= x\Sigma(x,Q^2) = xq(x,Q^2) + x\overline{q}(x,Q \\ xF_3{}^{cc}(x,Q^2) &= xV(x,Q^2) \pm 2(xC(x,Q^2)-xS(x,Q^2)) \qquad (4) \\ xV(x,Q^2) &= xq(x,Q^2) - x\overline{q}(x,Q^2) \end{aligned}$$

where xC and xS are the charm and strange quark x distributions. The corresponding neutral current structure functions are:

$$\begin{aligned} F_2{}^{nc}(x,Q^2) &= (\,u^2{}_L + d^2{}_L + u^2{}_R + d^2{}_R\,)\, x\Sigma(x,Q^2) \\ &\quad - (\,u^2{}_L - d^2{}_L + u^2{}_R - d^2{}_R\,)\, 2(xC(x,Q^2)-xS(x,Q^2)) \\ xF_3{}^{nc}(x,Q^2) &= (\,u^2{}_L + d^2{}_L - u^2{}_R - d^2{}_R)\, xV(x,Q^2) \qquad (5) \end{aligned}$$

where u_L is the left-handed Z^0-quark coupling and is given by $T_3 - Q\sin^2\theta_W$. T_3 is the weak isospin assignment of the charged 2/3 quarks. d_L is the corresponding coupling for the charged -1/3 quarks. u_R and d_R are the right handed couplings.

The charged current F_2^{cc} is a pure isosinglet, and xF_3^{nc} is a function of only the valence quarks and the weak neutral current couplings. Significant differences in the two interactions arise from the fact that the neutral current has both a V-A interaction as well as a small but finite V+A interaction.

The presence of these extra V+A terms has the consequence that the neutral current - nucleon deep inelastic scattering has a larger contribution of sea quarks than the charge current cross section does. For $\sin^2\theta_W \approx 0.23$ we expect:

$$F_2^{nc}(x,Q^2) / xF_3^{nc}(x,Q^2) \approx 1.2\, F_2^{cc}(x,Q^2)/xF_3^{cc}(x,Q^2) \qquad (6)$$

This greater coupling to the sea quarks in the neutral current cross sections would be interesting to observe in E-649. In particular we expect that the neutral current structure functions should have a somewhat stronger Q^2 dependence through QCD effects than the charged current structure functions.

(III) Design of the Experiment

(1) Narrow Band Beam Settings:

The choice of the narrow band beam (NBB) setting of the E-649 data run involves a compromise between optimizing the high energy neutrino flux and the overall event rate. The physics of interest is at the highest incident neutrino energy where the large values of Q^2 and W^2 become accessible. But the flux of energetic pions and kaons which are allowed to decay to produce the narrow band beam decreases as a steep function of the scaling variable[8] $x_f \approx x_R = E^*/(\sqrt{S}/2)$ as $(1-x_R)^{n\approx 3}$.

The energy of a neutrino in the narrow band beam arising from the two body decays $\pi^\pm \rightarrow \mu^\pm + \nu_\mu$, and $K^\pm \rightarrow \mu^\pm + \nu_\mu$ is given by:

$$E_\nu \approx (m^2 - m_\mu{}^2)/(m^2/P + P\theta_\nu{}^2) \qquad (7)$$

where m is the pion or kaon mass, P is the narrow band beam central momentum, and θ_ν is the angle of the neutrino with respect to the parent beam direction.

There is sizable folding of the decay kinematics at high energies when the neutrino angle θ_ν subtended by the detector can become larger than m/P. For angles above this limit the mean neutrino energy decreases for increasing P, whereas for angles below m/P the incident neutrino energy increases for increasing P. This broadens the accepted neutrino spectrum at a given train setting. Consequently, only a few settings of the NBB train are necessary to cover a wide neutrino energy range. The neutrinos from the kaon band are a much bigger fraction of the flux at the Tevatron than at the 400 GeV machine. Figures 2a, 2b, and 2c show the energy versus radius (angle θ_ν) correlation for secondary momentum settings of 300 and 500 and -300 GeV/c secondaries, respectively.

(2) The Number of Events:

Putting all of these factors together we compute the neutrino event rate as a function of P. Figure 3 shows the results for two different values of the accelerator energy. We note that the 800 GeV setting has roughly a factor of two fewer neutrinos per incident proton on target (pot) than the 1 TeV setting. Hence our choice of beam settings depends somewhat on the accelerator condition. In this design we will assume that the energy of the accelerator is 900 GeV. Examining the neutrino energy spectrum and the event rate versus P, we find that the settings of 300 GeV/c and 500 GeV/c allow a smooth coverage of incident neutrino energies up to ≈500 GeV.

As a practical experiment we assume a neutrino beam exposure of 5×10^{17} pots (the last E-733 beam exposure accumulated 4×10^{17} pots) with the time split in the ratio of 1 to 4 for the 300 and 500 GeV beam settings, respectively. Using a fiducial mass of 100 tons corresponding to a radius of 1.35 m about the beam axis, we will obtain the following number of events.

Table Ia

Number of Neutrino Events

Po(GeV/c)	π + K	π-Band		K-Band	
	NC+CC	NC	CC	NC	CC
300	9050	1327	4423	762	2538
500	23200	2354	7846	3000	10000

To compliment the neutrino data, an antineutrino beam exposure is proposed. The number of accepted events for 5×10^{17} pots at a train setting of -300 GeV/c is given in the table below.

Table Ib

The Number of Antineutrino Events

Po(GeV/c)	π+K	π-Band		K-Band	
	NC+CC	NC	CC	NC	CC
-300	7424	1514	3986	530	1394

For a total beam exposure of 1×10^{18} pots we can accumulate 32,250 neutrino events and 7,424 antineutrino events. The corresponding number of events in E-594 was about 15,000 in the neutrino beam and 3,000 at the antineutrino setting. A fiducial mass of 55 tons was used for the E-594 analysis. The smaller fiducial tonnage was choosen in E-594 to reduce the kaon neutrino background in the pion band neutral current analysis. With the E-594 tonnage, the number of events in E-649 would be reduced from the figures above by only about 17%.

The energy spectrum for accepted charged current events is shown in Figures 4a and 4b for the neutrino and the antineutrino beam exposure, respectively. The corresponding distributions in E_h and Q^2 for the three narrow band beam settings are shown in Figures 5a and 5b, respectively.

(3) Kinematic Regions:

The study of the weak neutral current depends on controlling the background events. These come from charged current events which are confused as neutral current events, from neutral current events which are induced by the three body kaon decays K_{e3} and $K_{\mu 3}$, and from $K_{\mu 2}$ decays which are not kinematically separated from the pion band neutrinos.

By making kinematic cuts and defining three regions in the plot of hadron energy-versus-event radius the backgrounds can be reduced and understood. The pion band neutral current events are required to satisfy an upper $y_{\pi} < 0.8$ cut, where the incident neutrino is assumed to come from the pion band. This will eliminate most of the charged current events which are misidentified as neutral current events. The kaon band neutral current events are required to satisy $y_{\pi} > 1.2$ and $y_K < 0.8$. Since the kaon neutrino flux increases with increasing radius, the pion band region is cut into two radial regions which will have two levels of $K_{\mu 2}$ background. The π_1 region is defined for the event radius r_{υ}<40cm and the π_2 region for 40cm<r_{υ} <135cm. Figure 6 is a schematic illustration of the three kinematic regions.

The defining cuts and the major backgrounds for each region are summarized in the following table.

Table II

Kinematic Regions of the Neutral Current Analysis

Region	cuts	remarks
	$E_h - M_p > 10$ GeV	clean $\pi_{\mu 2}$ data
π_1	$y_\pi < 0.8$	$\approx 10\%$ $K_{\mu 2}$ background
	$r_\upsilon < 40$cm	equivalent to E-594
	$E_h - M_p > 10$ GeV	$\pi_{\mu 2}$ data
π_2	$y_\pi < 0.8$	$\approx 27\%$ $K_{\mu 2}$ background
	$40 < r_\upsilon < 135$cm	
	$E_h - M_p > 10$ GeV	$K_{\mu 2}$ data
K	$y_\pi > 1.2$	NC events $\approx 18\%$
		$K_{e3} + K_{\mu 3}$ background
	$y_K < 0.8$	

The corresponding number of accepted events for event type for each energy region is given in the Table III.

Table III

The Number of Accepted Events for Neutral Current Analysis

P = 300 GeV/c	NC	CC
π_1 Region	496	1633
π_2 Region	462	1467
K Region	576	1582
P = 500 GeV/c		
π_1 Region	1619	5368
π_2 Region	631	2038
K Region	1897	5255
P = -300 GeV/c		
π_1 Region	579	1639
π_2 Region	486	1392
K Region	271	598
	Σ 5681	Σ17343

(4) Separation of Neutral Current from Charged Current Events:

One of the main experimental problems in studying the weak neutral current is to separate them from charged current events. Our fine grained calorimeter enables the event type to be separated on an event-by-event basis with a small error. To determine how well this separation operates at high energies, we have performed a Monte Carlo simulation of the experiment in which actual hadronic showers were generated in the calorimeter according to the expected distributions determined by the physics, the narrow band beam, and the detector properties. The Monte Carlo events were analyzed with the same programs that will be used on the data.

The major correction in the neutral current data comes from misidentified charged current events which are concentrated at high y. The Monte Carlo calculation of the charged current identification efficiency as a function of the energy of the outgoing muon is shown in Figure 7 for both E-594 and E-649. We see from the figure that the identification efficiency is a function of the muon energy and is not very strongly dependent on the hadron energy or the incident neutrino energy.

Taking $E_\mu > 3$ GeV to be the region where the efficiency becomes high, we observe that the corresponding y range where charged current events are mistaken for neutral current events is reduced by a factor of 2 in going from E-594 to E-649. Thus, the overall detection efficiency increases with increasing neutrino energy. Consequently the systematic error associated with misidentified events will decrease in E-649. Given the y cuts defined in Table II above, the fraction of misidentified charged current events is roughly <1% for the π_1 region, <9% for π_2, and <7% for the K region.

The fraction of neutral current events which are misidentified as charged current events has been measured using our hadron calibration data. Figure 8 shows this background as a function of hadron energy. We note that over the energy range of the experiment that this background is always less than 4%.

(5) Kinematic Reconstruction:

The kinematics of the neutral current deep inelastic scattering events are reconstructed by measuring both the energy and angle of the recoil hadron shower. The incident neutrino energy is inferred by the energy-versus-radius correlation in the narrow band beam. The Bjorken scaling variable $x = Q^2/2MyE_\nu$ is computed by E_h and θ_h observable in a neutral current event:

$$x \approx E_h\theta_h{}^2/2M(1-y) \qquad (8)$$

and the inelasticity is given by:

$$y = (E_h - M)/E_\nu(r) \qquad (9)$$

where $E_\nu(r)$ is the energy of the incident narrow band beam given by the energy versus radius correlation. Figure 9 shows the deep inelastic scattering kinematics in terms of the energy and angle of the recoil hadronic system.

The x resolution depends strongly on the hadron angle resolution through the $\theta_h{}^2$ dependence. The E_h and E_ν dependence makes the x resolution become poor as y approaches 1. Therefore the $y < 0.8$ cut, which has to be imposed to reduce the number of confused charged current events, has the added benefit of avoiding this poor x-resolution-region.

Contributions to the x resolution smearing come from the hadron energy resolution and the incident neutrino energy resolution. The later arises from the intrinsic width of the energy-versus-radius correlation determined by the two body decay kinematics and the momentum dispersion of the narrow band train and from ambiguous neutrino parentage such as the $K_{\mu 2}$ background in the $\pi 1$ region. (See Appendices A and B.)

The x-resolution may be estimated by:

$$(\sigma_x/x)^2 \approx 4(\sigma_\theta/\theta)^2 + (1/(1-y)^2)(\sigma_{Eh}/Eh)^2 + (y/(1-y))^2(\sigma E_\nu/E_\nu)^2 \quad (10)$$

A typical value of the x resolution when all of these effects are put together is $\sigma_x \approx x$. The treatment of this smearing is the central experimental challenge in the measurement of the neutral current structure functions.

The deep inelastic charged current scattering events are reconstructed either as neutral current events after the calorimeter energy of the outgoing muon track has been removed or as a charged current event using the measured muon momentum. The charged current events can be used to check the neutral current x reconstruction resolution.

(IV) The Total Charge Current Cross Section

(1) Physics:

The total deep inelastic scattering cross section in neutrino physics is analogous to the ratio R in e^+e^- physics. Given a new energy regime in either physics setting there is an imperative to measure these fundamental quantities. The measurement of the total cross section, as the determination of the ratio R, is one of the fundamental experiments in the exploration of a new high energy frontier.

The recent total cross section analyses of E-616 at Fermilab and the new data from the CDHS collaboration at CERN are now in agreement after a long and difficult period[9]. Our own result from E-594 is forthcoming[10]. These measurements reach only to 300 GeV incident neutrino energy. The Tevatron offers a factor of two in incident neutrino energy and E-649 will be able to extend the measurement of the total cross section up to 500 GeV.

In the quark-parton model, the total neutrino-nucleon charged current cross section is dependent on the number of quark flavors and is controlled by their scaled momentum distribution inside the nucleon. If the quarks are point-like spin 1/2 particles, the elementary neutrino-quark scattering will be given by:

$$d\sigma/dy = (G_f^2 M E_\upsilon/\pi) \quad \ldots\ldots\ldots\ldots\ldots \quad \upsilon\, q \text{ or } \overline{\upsilon}\,\overline{q} \text{ scattering}$$

$$d\sigma/dy = (G_f^2 M E_\upsilon/\pi)(1-y)^2 \quad \ldots\ldots \quad \upsilon\,\overline{q} \text{ or } \overline{\upsilon}\, q \text{ scattering} \qquad (11)$$

By summing over all the quarks and antiquarks inside the nucleon, the total neutrino-nucleon charged current cross section is given by the following:

$$\sigma_t = (G_f^2 M E_\upsilon/\pi)\int\int (1/(1+Q^2/M_W^2)^2\{(1-y)F_2(x,Q^2)+y^2xF_1(x,Q^2)$$
$$\pm(y-y^2/)xF_3(x,Q^2)\}dxdy \qquad (12)$$

where the scaling variables are defined by $x=Q^2/2MyE_\nu$ and $y=(E_h-M)/E_\nu$, M_W is the vector boson mass. The structure functions F_2, xF_1, and xF_3 contain the sums of the quark and antiquark scaled momentum distributions.

In the absence of heavy quark production, the total neutrino-nucleon cross section will have an exactly linear energy dependence in E_ν if the boson propagator mass is infinite and if there is no Q^2 evolution of the structure functions. However these two Q^2 effects are expected to become significant at high E_ν and will make an observable distortion of a naive linear E_ν dependence. In Figure 10, the deviation from the linear E_ν dependence from the propagator and the QCD evolution of the structure functions is shown. We note that the distortion from linearity is a 12% drop of the cross section over the E-649 energy range. The major part of the effect is in the QCD evolution of the structure functions, with the boson propagator effect contributing only 4% to the 12% deviation. A measure of this deviation from linearity will roughly determine the QCD scale breaking parameter Λ, with certain model dependent assumptions, without measuring structure functions.

This deviation from linearity would be difficult to see in lower energy data since the energy range of the measurements is limited and pion band - kaon band relative flux normalizations contribute a significant error. The kinematic folding of the neutrino energy spectrum at the Tevatron will make the flux normalizations easier since the neutrino data can be accumulated in only two narrow band train settings.

It is interesting to ask why the QCD effect diminishes the cross section rather than increasing it. At these energies and Q^2 values the major part of the structure functions is still associated with valence quarks which can only evolve by gluon emission. The fraction of the nucleon's scaled momentum carried by the valence quarks decreases with increasing Q^2. The minor part of the structure functions associated with the quark sea term comes from quark-antiquark production which grows with increasing Q^2. Thus the overall effect is a slower than linear growth of total cross section. This will be an interesting effect to observe in E-649.

The production of heavy quark flavors or second order weak interactions, such as the production of the Higgs scalar, would increase σ_t. These processes, even if they exist, are expected to have quite small cross sections. Figure 11 shows the increase in σ_t when a quark mass of 10 GeV/c^2 is produced as a heavy charmed quark with the same K-M mixing terms. The resulting increase in σ_t is only 2% up to 500 GeV and would be very difficult to observe.

(2) Method:

The calculation of the total neutrino-nucleon cross section is performed by taking the ratio of the observed number of events over the predicted incident neutrino flux. The difficulty of the technique involves the determination of the neutrino flux. We envision that this be done in the same manner as was E-594/E-701 during the 1982 narrow band run.[3] (See R. Blair et al., NIM 226, p281,(1984))

Figure 12 is a schematic of the monitors used in the previous data run. The ion chambers and RF cavity which were used to monitor the sum of the pion, kaon, and proton beam are suitable for Tevatron use. However, the Cerenkov counter will have to be rebuilt since the old counter has insufficient resolution in β to resolve pions from kaons at 500 GeV/c. Appendix C gives the design parameters for this counter. Previous experience indicates that the incident neutrino flux can be inferred to an accuracy of about 5%. We think that we will attain the same accuracy in E-649.

The measurement of the total neutrino-nucleon cross section in E-649 will extend the present measurements by roughly 200 GeV. The comparison of the observed energy dependence with our expectation will be quite interesting.

(V) Determination of $\sin^2\theta_W$ and ρ

The electroweak coupling parameters $\sin^2\theta_W$ and ρ control the strength of the neutral-current neutrino-quark coupling. Considerable experimental effort has been expended in the measurement of these fundamental parameters of the Standard Model. These measurements range from the very small Q^2 region of the atomic physics experiments to the CERN SPS Collider experiments which have actually produced the weak bosons themselves.[11]

Recent high statistics measurements of deep inelastic neutrino-nucleon scattering at the CERN SPS have pushed the experimental errors to new low values.[12] Our own measurement in E-594 has used tight kinematic cuts to reduce the K_{e3} and charged current background in the neutral current data sample.[2] (See Appendix D). The present world's data is in general agreement with a unique value of $\sin^2\theta_W$ within the Q^2 dependent renormalization corrections. So why measure these parameters again?

A measurement of $\sin^2\theta_W$ at the Tevatron will extend the tested energy range of the Standard Model by a factor of 2, and the systematic errors will be reduced by a factor of 2. All of the machinery of the Standard Model has to be assumed in extracting $\sin^2\theta_W$ in deep-inelastic neutrino-nucleon scattering. Thus the measurement is a sensitive integral test of the Model.

Certain possible deviations of the Standard Model can be considered. For example, if there were a heavy quark species which coupled preferentially to the weak neutral current there would be a deviation of $\sin^2\theta_W$ from prediction as the threshold for the new quark flavor is encountered. This could make $\sin^2\theta_W$ depend on Q^2, the incident neutrino energy, or the recoil hadron energy. The extended energy range of the Tevatron will allow a search for such possibilities.

The most statistically potent values of $\sin^2\theta_W$ and ρ come from the analyses of the ratios R_ν and $R_{\bar{\nu}}$ in deep-inelastic neutrino-nucleon scattering data. However, in the present world's data there are significant theoretical corrections that have to be applied which arise from the limited range of the incident neutrino energy. These determinations of $\sin^2\theta_W$ and ρ come from neutrino experiments performed in narrow band neutrino beams. The pre-Tevatron data are therefore limited to energies of about 75 GeV for the pion band events and 150 GeV for the kaon events. Given the nature of the narrow band beam technique, most of the data is in the pion band.

The kaon band data can be used to increase the energy range of the experiment, but neutral current events in that kinematic region suffer from a rather large (20%) background of electron neutrino charged current events. The electron neutrinos come from K_{e3} decays.

Therefore one is forced to use the pion band for the most part. At this low incident average neutrino energy the magnitude of the charged current cross section is dependent on: (1) How the charmed quark threshold suppression is calculated, and (2) The magnitude of the strange sea. Should the mass of the charmed quark be m_c = 1.5 GeV/c^2? Should it evolve with Q^2? The specific choice of the charmed quark mass significantly affects the value of $\sin^2\theta_W$.

To see why charmed quark production is important in the extraction of $\sin^2\theta_W$, we will now consider some aspects of heavy quark production in deep inelastic scattering. The kinematics of heavy quark production has been worked out by Barnett[13], and Kaplin and Martin.[14] The definition of variables is illustrated below.

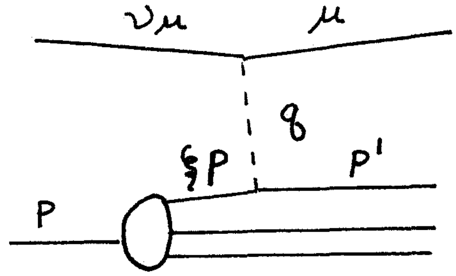

Heavy Quark Production

Since the mass of the heavy quark is given by: $m^2 = p'^2 = (q + \xi p)^2$, the scaling variable which accounts for the quark mass m can be expressed as: $\xi = x + m^2/(2M_pE_\nu y)$, where E_ν is the incident neutrino energy, M_p is the nucleon mass, and $y=(E_h-M_p)/E_\nu$. The heavy quark production threshold requires $\xi < 1$ resulting in the x and y regions being confined to the region:

$$x < 1 - m^2/(2M_pE_\nu) \text{ and } y > m^2/[2M_pE_\nu(1-x)]. \qquad (13)$$

These limits suppress the component of the cross section which corresponds to the production of the heavy quark flavor of mass m. In our calculations below we will assume that the heavy flavor is charm. Bottom quark production should be strongly suppressed by kinematic factors and K-M matrix terms.

The charged current cross section including the strange sea and charmed quark production is expressed by using this modified scaling variable ξ for the quark components which involve the heavy quark production. For neutrino scattering off an isoscalar target:

$$
\begin{aligned}
d\sigma/dxdy = (G^2M_pE_\nu/\pi)\,\{\,[&xu + xd + (x\bar{u} + x\bar{d})(1-y)^2|U_{ud}|^2 \\
&+2xs|U_{us}|^2 + (x\bar{u}+x\bar{d})(1-y)^2|U_{us}|^2 \\
&+2xc(1-y)^2(|U_{dc}|^2 + |U_{sc}|^2) \qquad\qquad (14) \\
&+(\xi u + \xi d)|U_{cd}|^2(1-y+xy/\xi)\theta(1-\xi) \\
&+2\xi s|U_{cs}|^2(1-y+xy/\xi)\theta(1-\xi)\,,
\end{aligned}
$$

where the terms U_{ud}, etc. are the K-M matrix terms. A similar expression pertains to the antineutrino-nucleon scattering.

The charged current deep inelastic scattering cross section given above will be smaller than the naive quark-parton cross section by the inequality:

$$(xu + xd)|U_{ud}|^2 + (\xi u + \xi d)|U_{dc}|^2(1-y+xy/\xi)\theta(1-\xi) < (xu + xd). \quad (15)$$

These complications are confined to the (anti)neutrino charged current scattering. No such kinematic suppression is expected in the neutral current cross section since the neutral weak current is flavor diagonal and there are no mass thresholds to overcome.

To estimate the sensitivity of $\sin^2\theta_W$ to the charmed quark threshold we note that the NC/CC ratio R_ν decreases with increasing $\sin^2\theta_W$ by roughly the amount $dR_\nu/d\sin^2\theta_W \approx -0.7$. Taking the CDHS determination[15] for the magnitude of the strange sea $2s/(\bar{u} + \bar{d}) = 0.52 \pm 0.09$, we find that the ratio R_ν changes by about 3% for the pion band data, where $E_\nu \approx 75$ GeV, making a 5% increase in $\sin^2\theta_W$.

The charm quark production energy threshold becomes a smaller effect with increasing incident neutrino energy. With the narrow band beam at the Tevatron, the ambiguity in $\sin^2\theta_W$ becomes roughly one half of its value in the present world's data set. The uncertainties associated with the strange quark sea and the neutral current - charged current event separation also become smaller. Figures 13 and 14 show the diminishing systematic error associated with the magnitude of the strange sea and the charmed quark production threshold, respectively.

One might expect that QCD effects will become important at the higher Q^2 values of the Tevatron. These effects arise from the slightly different couplings of the neutral current to the valence and the sea quarks compared to the corresponding couplings of the charged current interaction. Since the sea quarks and the valence quarks evolve differently with Q^2 there can in principle be a Q^2 dependent correction to $\sin^2\theta_W$. However the estimate of this effect using the Duke and Owens QCD parameterization[16] indicates that it is quite small. Therefore, the Tevatron narrow band beam will in principle enable $\sin^2\theta_W$ to be measured with greater precision than before.

The comparison of the theoretical and experimental uncertainties in the determination of $\sin^2\theta_W$ in E-594 with E-649 is shown in the following Table. The E-594 experiment had an average neutrino energy of about 75 GeV which is typical of all narrow band pre-Tevatron experiments.

Table IV

Estimated Errors in the $\sin^2\theta_W$ Determination

Error source	E-594	E-649
NC/CC separation	±4.2%	±2%
muon track elimination	± 2%	±1%
$2s/(\overline{u} + \overline{d}) = 0.5\pm.2$	±0.4%	±0.13%
QCD $\Lambda = 200\ {+200}\ {-100}$ Mev/c	±0.1%	±0.1%
charm quark mass	±2%	±1.2%
m_c=1.5±0.4 GeV/c^2		
total error	±5.1%	±2.5%

We see that the total error in $\sin^2\theta_W$ is reduced by a factor of 2 in E-649 relative to E-594. The higher energy has the benefit of reducing both the experimental and the theoretical uncertainties.

To estimate the statistical and systematic uncertainties in the determination of $\sin^2\theta_W$ and ρ in E-649 we have performed a Monte Carlo simulation of the experiment with the expected number of accepted events given in Table III above. Using an input value of $\sin^2\theta_W$=0.246 in the Monte Carlo we find by using both the neutrino and the antineutrino data in only the π_1 and π_2 regions that $\sin^2\theta_W$=0.251±0.011±0.006 (±statistical ±systematic) for the single parameter fit and $\sin^2\theta_W$=0.246±0.031±0.008 and ρ=0.994±0.02±0.013 for the two parameter fit. If there were no antineutrino beam exposure we would not be able to determine ρ, but our single parameter $\sin^2\theta_W$ errors would be the same. By including the K regions and correcting for the K_{e3} background in the NC events, we reduce the statistical error on $\sin^2\theta_W$ to 0.008 for the single parameter fit and 0.023 for the double parameter fit.

The statistical errors are comparable to or lower than what we achieved in E-594 and the systematic errors are reduced by 1/2. For comparison we note that the CDHS collaboration quotes ±0.004 for the statistical error of their latest narrow band beam data and a systematic error of ±0.003. It would be hard to match their statistical error by running at the Tevatron. But it is important to observe that their systematic error is on corrections which can be as large as 20% (for the NC-CC event separation) at an incident neutrino energy where the charm quark mass threshold is a large effect. The E-649 measurement would extend the tested energy range of the Standard Model by a factor of two and will be in an energy range where the systematic errors are in principle smaller.

(VI) The Neutral Current Structure Functions

(1) General:

The weak neutral current provides a method of investigating the nucleon structure which does not involve quark-flavor transitions. Most of the determinations of the Z^0-quark coupling in neutrino physics have been through integral tests of the theory. The measurement of $\sin^2\theta_W$ is such a test. These experiments probe the overall strength of the neutral current coupling, but do not measure the detailed structure of the neutral current interaction.

The measurement of the y-dependence of the neutral current interaction determines the integral of the quark x-distributions and therefore the overall strength of the left-handed to the right-handed coupling terms. But again this differential test does not approach the details of the actual Z^0-quark interaction. That level of experimentation can only be done by the measurement of the x-dependence of the neutral current structure functions themselves.

Only the CHARM collaboration at CERN[17] and our effort E-594[1] have published high statistics results on the nucleon structure using the Z^0 as a probe. Since the details of the neutral current neutrino-quark coupling become visible in this type of experiment, the data will be useful in extending our understanding of the structure of the nucleon.

Certain questions can be addressed: (1) Is there some neutral component of the nucleon that the neutral current preferentially couples to? (2) Does the scaled momentum distribution probed by the neutral current agree with the predictions from the charged current data? It is interesting to continue these tests with higher statistics and at higher energies. This is one of the major physics goals of E-649.

(2) The Ratio Test:

To directly compare the x distributions of the neutral current with the charged current interaction we compute the ratio:

$$R_\nu(x) = [dN^{nc}/dx]/[dN^{cc}/dx] = \sigma(\nu_\mu+N\to\nu_\mu+X)/\sigma(\nu_\mu+N\to\mu+X) \quad (16)$$

This will reduce our sensitivity to possible systematic errors associated with hadron energy and angle scale errors. By explicitly expressing the the couplings u_L ,etc. in terms of $\sin^2\theta_W$ the ratio $R_\nu(x)$ above is:

$$R_\nu(x) = 1/2 - \sin^2\theta_W + (20/27)\sin^2\theta_W$$
$$+ (40/81)\sin^4\theta_W\, x\bar{q}(x)/(\, xq(x) + x\bar{q}(x)/3\,) \quad (17)$$
$$R_{\bar{\nu}}(x) = 1/2 - \sin^2\theta_W + (20/9)\sin^2\theta_W$$
$$- (40/27)\sin^4(x)\, x\bar{q}(x)/(\, xq(x)/3 + x\bar{q}(x)\,)$$

Thus we expect that the neutral current/charged current ratio should be approximately flat except possibly at small x where the $x\bar{q}(x)$ term could be important. The antineutrino ratio should be more sensitive to this term than the neutrino ratio. The presence of the sea term will make the antineutrino ratio increase slightly as one increases x from x = 0, whereas the effect on the neutrino ratio is to make a slight decrease in going from low x to high x.

An estimate of the magnitude of this effect at $Q^2 \approx 11\ (GeV/c)^2$ for E-594 indicates that the neutrino ratio decreases by only about 1%, whereas the antineutrino ratio increases by 8%. Resolution smearing and finite statistics make the effect less obvious. The higher Q^2 range of E-649 should increase the effect and make this low x-dependence of the ratios an interesting feature to search for.

In E-594 we measured the NC/CC ratios given above. (see Appendix E). The results are shown in Figures 15a and 15b. We note that the ratios appear to be roughly flat within the expectation of the Standard Model.

we conclude that at the mean $Q^2 \approx 11$ $(GeV/c)^2$ of our E-594 data the $x\overline{q}(x)$ remainder term in the ratio is relatively small.

To quantify the difference between the neutral current and the charged current x distributions, we performed two different fits. In Fit1 we assumed that the valence distributions for both the neutral current and the charged current had the form:

$$xV(x) = Ax^{1/2}(1-x)^{\beta} \qquad (18)$$

and the nonstrange sea quark distributions by the form:

$$2x\overline{q}(x) = C(1-x)^{\gamma}. \qquad (19)$$

The strange sea was assumed to be 0.52 $x\overline{u}(x)$. In Fit2 we changed the assumed form of the valence distribution to:

$$xV(x) = 3\Gamma(\alpha+\beta+1)/(\Gamma(\alpha)\Gamma(\beta+1))x^{\alpha}(1-x)^{\beta}. \qquad (20)$$

The line through the data in Figure 15 is the result of both Fits1 and 2 for the neutral current structure functions $xF_3(x)$ and $x\overline{q}(x)$. The details are given in Table II of App endix E.

E-649 will carry these ratio comparisons to a higher incident neutrino energy and Q^2 region. Figure 16 shows what we expect the ratios to look like in E-649. For simplicity no QCD evolution effects were included in the simulation. The results of a Monte Carlo simulation with the expected statistics given in Table III is shown below. For the charged current structure function parameters we have assumed that A=3.28, α=1/2, β=3, and C=1.0.

Table V

Neutral Current Structure Function Fits

Region:		π_1	π_2	K	All
Beams (GeV/c):					
300	A	2.47±.43	2.80±.75		2.90±.33
500	β	2.45±.28	2.84±.48		2.74±.19
-300	C	1.13±.19	1.19±.26		1.01±.13
300	A	2.26±.67		2.26±.64	2.50±.54
500	β	2.32±.43		2.38±.44	2.52±.33
	C	1.26±.39		1.29±.45	1.24±.30
300	α	0.38±.07		0.59±.10	0.44±.05
500	β	2.24±.37		3.59±.55	2.60±.29
-300	C	1.07±.17		1.26±.16	1.00±.11

No fits were performed for the cases left blank.

The π_1 region alone has a statistical error comparable to E-594. The fits using all three kinematic regions have a statistical error of about 1/2 of our earlier experiement. We note that the antineutrino exposure helps reduce the overall error. The fits using only the neutrino data have errors which are ≈1.7 times larger than those using both the neutrino and antineutrino data.

In E-594 the systematic error of the fits was calculated to be roughly the same as the statistical error. The corresponding systematic error in E-649 will be roughly 1/2 of the E-594 value primarily due to the diminishing errors in the neutral current/charged current event separation. Thus the systematic error should track the increased statistical power of E-649.

(3) Unfolding the Neutral Current Structure Functions:

The effect of the resolution in the measured variables E_h and θ_h, which are used to reconstruct the neutral current kinematics is to smear the reconstructed Bjorken scaling variable x. To see this resolution smearing we plot in Figure 17 the true value of x and the experimentally reconstructed value of x. A resolution tail at high x is quite evident. The x-resolution depends on several variables but it has the rough value of $\sigma_x \approx x$. With such a large smearing it is important to consider the bin-to-bin correlations in the x-distribution.

The resolution smearing and acceptance corrections can be represented by a smearing matrix A_{ij} which transforms the exact x distribution x_j into the observed distribution b_i. The transformation is given by:

$$b_i = \sum A_{ij} x_j \qquad (21)$$

The smearing matrix A can be calculated by Monte Carlo methods, using the detector resolutions as input without requiring any a priori assumptions of the shape of the true distibution x_j. The true x distribution can be obtained by inverting the matrix A by the following equation:

$$x_i = \sum A^{-1}{}_{ij} b_j \qquad (22)$$

as long as the matrix A can be inverted. However the solution gives large correlations in the errors of the components of x_i which mask the true resolving power of the experiment.

It is therefore more instructive[18] to examine the χ^2 function defined by:

$$\chi^2 = \sum (1/\sigma_i^2)(b_i - \Sigma A_{ij}x_j)^2 \qquad (23)$$

By this definition, the solution x_i which produces the minimum at $\chi^2 = 0$ is the same as that obtained by solving the inversion equation given above. But in a more general sense, we have determined the x_i which gives the minimum in χ^2 , and we now have the ability to look at variations of χ^2 about the minimum.

The x_i which gives the minimum in χ^2 is the solution to the equation $\partial\chi^2/\partial x_k = 0$. Thus:

$$\sum(\Sigma A_{ij}A_{ik}/\sigma_i^2)\, x_j = \sum b_i A_{ik}/\sigma_i^2 \qquad (24)$$

By defining the matrices:

$$H_{jk} = \sum A_{ij}A_{ik}/\sigma_i^2$$

$$R_k = \sum b_i A_{ik}/\sigma_i^2 \qquad (25)$$

we see that the x_i are solutions to the equation:

$$\sum H_{jk}x_j = R_k \qquad (26)$$

The matrix H_{jk} contains the information about the variation of χ^2 about the minimum. The multidimensional surface representing a unit of increase of χ^2 is an ellipsoid centered about the minimum. The principal axes of this ellipsoid are in the direction of the eigenvectors of H with lengths proportional to the eigenvalues.

The solution x_i which minimizes the χ^2 function can be expanded as a series in the eigenvectors of H. In this orthogonal basis, the errors in the coefficients are uncorrelated. The solution x_i can then be constructed as a sum of uncorrelated components, each with a specific contribution to the χ^2. The eigenvectors with the largest eigenvalues have the largest statistical significance and will make the largest contribution to the χ^2. The eigenvectors with the smallest eigenvalues represent the high frequency structure, which after resolution smearing, tend to contribute little to the observed x distribution.

The resolution of the detector provides a cutoff in the expansion of significant eigenvectors, where we find that the higher frequency components represent the unresolvable structure in the true distribution. The point of truncation can be determined by Monte Carlo simulation.

The truncated eigenvector expansion is a visual display of the unfolded distribution. The full summation is the exact solution to the complete unfolding problem. Therefore, any fits to the unfolded distribution must use the complete series.

We have applied this method to both the E-594 data (in progress) and to the E-649 simulation. We give our result in terms of the cross section integrated over y by the structure functions $F_{\pm}$, where $F_{\pm}$ is defined by the following:

$$d\sigma/dx = (G_f^2 M/2\pi)\, F_{\pm}(x). \qquad (27)$$

Note that the neutral current structure functions $F_{\pm}^{nc}$ contain the coupling constant terms. See Equation 5.

The preliminary deconvoluted x-distributions[19] (not normalized) for E-594 are shown in Figure 18. These plots represent about 1/3 of the neutrino data and all of the antineutrino data.

The deconvoluted E-649 Monte Carlo simulation is given in Figure 19. In this figure the expansion of the eigenvectors has been truncated at the point where additional terms contribute a neglectable amount to the χ^2 of the fit. The line in the figure represents the exact structure functions used in the Monte Carlo simulation.

We have also fit the unfolded structure functions $F_{\pm}(x)$ of the simulation above in terms of the valence and sea parameterizations. In these fits the full expansion was used. The results are: $\alpha = 0.50 \pm 0.057$, $\beta = 3.16 \pm 0.33$, and $C = 1.03 \pm 0.10$. These errors are comparable to those given in Table V of the ratio test described above.

The method has been carried further to actually deconvolute the neutral current valence and sea distributions as well as F_2 and xF_3. The results of the Monte Carlo study are shown in Figure 20. We see that these separate distributions can actually be resolved. The errors represent the sum of the statistical and the deconvolution errors.

(VII) Exotics

(1) General Remarks:

Often discoveries are made when small discrepancies are observed in a physics setting where there is a "good" understanding. The Standard Model is mature and thus there are many well defined predictions to test with the data. In this section we consider the possibility of detecting heavy neutral leptons and exotic hadronic states. These objects may be produced in a high energy deep inelastic neutrino-nucleon scattering. The narrow band technique will enable certain kinematic constraints to be imposed which will enhance the detection of such objects and increase the possibility of understanding them.

(2) Heavy Neutral Lepton Search:

In certain extensions of the Standard Model there may exist heavy neutral leptons.[20] These objects may be produced in a neutral-current deep inelastic neutrino-nucleon scattering if there is a sufficiently large mixing between the ordinary neutrino and the heavy one. The production threshold E_ν^{th} will be given by:

$$E_\nu^{th} = m_L + m_L^2/2M \qquad (28)$$

where m_L is the heavy neutral lepton mass, and M is the nucleon mass. In the narrow band beam at the Tevatron, the maximum energy in the center of mass is $\sqrt{s} \approx 30$ GeV, and thus quite massive objects $m_L \lesssim \sqrt{s}$ in principle can be produced.

If the heavy lepton is point-like, it will have an excitation curve relative to deep inelastic scattering which will go roughly as $E(s) \approx (s-m_L^2)/s$.

For a certain range of masses and lifetimes it will be possible to observe the heavy lepton in our calorimeter. We would see the decay of the object as a shower located downstream of the primary vertex of the interaction. This shower could be electromagnetic, or hadronic. The decay could also be into muons.

The fine granularity of our detector will allow the decay products of the heavy lepton to be observed down to rather low energies which we estimate to be on the order of 2 to 3 GeV. Furthermore, the construction of the detector permits hadronic showers to be easily distinguished from electromagnetic showers. Therefore some of the details of the decay would be accessible.

The phase space available for the heavy neutral lepton search is controlled by the length of the calorimeter, and the average length of the recoil hadron shower. Our detector is about 20 meters long, and the average shower length is about 480 cm. Therefore laboratory lifetimes in the range of 25 to 50 nsec can be observed.

To study the electromagnetic decay signature of the heavy lepton, we have performed a Monte Carlo simulation. In this calculation, the heavy lepton of some chosen mass has been allowed to decay into an electromagnetic shower at some distance from the primary neutrino-nucleon interaction vertex determined by the dilated lifetime. A typical Monte Carlo event is shown in Figure 21. We note that the downstream electromagnetic shower points back to the primary vertex and is easily visible.

As a first pass estimate, the detection efficiency as a function of mass and lifetime was determined by scanning these Monte Carlo events. Other mass-lifetime combinations were scaled from the original Monte Carlo curve. The results are shown in Figure 22. We see that the detection efficiency is never more than about 55%. This efficiency is determined by both the random location of the primary interaction vertex and the finite length of the recoil shower.

The sensitivity of the heavy lepton search can also be estimated by using bremsstrahlung showers along the outgoing muon track in ordinary deep inelastic charged current events. By removing the muon track but retaining the electromagnetic shower, the electromagnetic decay signature is simulated. Figure 23 shows a typical bremsstrahlung event.

On the basis of the Monte Carlo simulation of the experiment we estimate that for a total of 5700 deep inelastic neutral current scattering events, the 90% confidence upper limit for the non-observation of such objects corresponds to a probability of < 6.5 $\times 10^{-4}$. The kinematic region in mass-lifetime which would be excluded can be estimated from Figure 22.

If we were to be so lucky to see a statistically significant signal, the ratio of m_L/τ_0 could be determined by the data. The energy of the scattered lepton is fixed by the hadronic shower energy and the energy of the incident neutrino (to within the K-π band ambiguity) by: $E_L \approx E_\nu(r) + M - E_h$. Therefore the measured length distribution of the downstream vertex can be scaled by the computed outgoing lepton energy to give a curve characteristic of the mass and lifetime of the object:

$$dN/(E_L d\lambda) = N_0 \exp(-\lambda(m_L/\tau_0 c)) \qquad (29)$$

where $\lambda = L/E_L$ is the scaled length. Background vertices coming from neutral hadrons boiling off the primary hadronic shower will not give a universal slope in λ. Thus the λ distribution could help in discriminating against background events.

The muonic decays of a heavy lepton can also be detected. Figure 24 shows a candidate event with a very low hadronic energy and two muons coming from the primary vertex which could be a heavy lepton event.

The data of E-649 will be scanned for strange topologies. The hard energy spectrum and kinematic constraints of the narrow band beam make it a good place to search for heavy neutral leptons.

(2) Exotic Hadronic States:

It has been suggested that the nucleon contains intrinsic heavy quark states.[7] These states have been postulated to account for the same-sign dilepton puzzle in neutrino scattering and the large diffractive production of charmed hadrons at large longitudinal momentum in high enegy proton-nucleon scattering and pion-nucleon scattering.

The same-sign dimuon signal has been observed by several experiments and has been found to be quite small, $< 10^{-4}$ of the ordinary charged current events. At this level there would be only a few of these events in the narrow band beam exposure. But there is the possibility of observing the hypothetical intrinsic heavy quark states in another mode.

In the narrow band beam the mass of the hadronic recoil system can be calculated for both charged current and neutral current events. The mass W of the system is given in terms of the observables by:

$$W^2 = M^2 + 2M(E_h - M)(1 - x) \qquad (30)$$

A hadronic resonance would appear as a perturbation in the otherwise smooth W^2 distribution. However, the x resolution smearing, especially in the neutral current analysis, will make the mass resolution rather poor. A better chance of observing some anomaly occurs if one assumes that the x distribution of the exotic hadronic state is peaked near $x \approx 0$. Thus solving the equation for the recoil energy we find:

$$E_h = M + (W^2 - M^2)/(2M(1-x)) \qquad (31)$$

Therefore the hadronic energy distribution will develop a step corresponding to the threshold of the production of the new hadron state. Since the detection of the step involves the measuring of only the hadronic energy E_h, the resolution of the effect should be better than actually trying to measure W.

Because of their large masses, the heavy quark states will carry a large fraction of the nucleon's momentum.[7] Using the slow rescaling phenomenology given above but assuming that ξ is peaked near 1, (x can still be near 0), we can simulate the perturbation of the hadronic energy spectrum corresponding to the production of some hypothetical object. The recoil hadronic energy spectrum for the excitation of a mass $\approx$ 9 GeV/c^2 state is shown in Figure 25. We expect that the width of the energy spectrum distortion will grow as the incident neutrino energy increases, but the lower edge will remain fixed.

The recoil hadronic energy spectrum in deep inelastic scattering is determined by the y-distribution and the incident neutrino spectrum and therefore should be known. Small corrections of the event-type confusion have to be made, but they should be easy to control given various Monte Carlo studies and self consistency checks of the data.

A search of this kind is more difficult in the wide band beam because the neutral current - charged current event separation is more uncertain. The control over the incident neutrino energy spectrum is lost in a broad band beam so that the excitation curve of the object can not be studied.

(VIII) Requests

Beam:

(1) To perform this experiment we need at least 5×10^{17} pots with the narrow band train transporting positive secondaries for neutrino running, and 5×10^{17} pots with negative secondaries for antineutrino running. Since the neutrino beam is a tertiary beam, there is considerable benefit in operating the accelerator at the highest available energy. Even though the event rates are low in the narrow band beam, we would like the beam to be delivered in a multi-ping mode to keep our deadtime to a minimum. A rate of 4 to 6 pings evenly distributed over the 20 second flat top is ideal.

(2) A hadron calibration beam of variable energy from 20 GeV to 400 Gev operational during the neutrino data taking will enable us to continuously calibrate the detector under various conditions.

Technical Support:

(1) We would like to have technical support for the beam monitoring system. This includes the design and construction of the new Cerenkov counter and the reinstallment of the narrow band beam monitoring system. We would like to collaborate with the Laboratory on this important aspect of the narrow band beam program.

Since the Cerenkov counter is large and complex it would be wise to build and test it before the narrow band data run. If the construction of the device is started now (March 1986), it could be installed in the the decay pipe and tested during the next running period using the protons that are transported to the NWest area.

(2) Continued technical support is needed for the design and installation of the new magnetostrictive magnetizing circuit. This system will enhance the operation of the flash chambers.

Online Computer Upgrade:

We would like to install a MicroVax2 computer to augment our PDP-11 online computing capability. The new system would be dedicated to monitoring the narrow band beam operation.

References:

(1) D. Bogert et al. Phys. Rev. Lett. 55 ,574, (1985); G. P. Yeh, Ph. D. Thesis, MIT, Sept. 1984; T. Mattison, Ph. D. Thesis, MIT

(2) D. Bogert et al. Phys. Rev. Lett. 55,1969, (1985)

(3) T. Eldridge, Ph. D. Thesis, MIT, June 1985

(4) A. Mukherjee, Ph. D. Thesis, MIT

(5) J. Bofill, Ph. D. Thesis, MIT,1985

(6) R. Magahiz, Ph. D. Thesis, MIT, May 1985

(7) S. Brodsky, C. Peterson, N. Sakai, Phys. Rev. D23, 2745, (1981)

(8) J. R. Johnson et al. Phys. Rev. D17, 1292, (1978)

(9) CFRR group, R. Blair et al. Phys. Rev. Lett. 51,343, (1983); CDHS group, A. Para, FNAL Exp. Theo. Seminar, Dec. 1985

(10) Our preliminary values of the cross sections are:

σ_t/E_ν = (.613±.007±.031)x10^{-38} cm^2/GeV neutrinos

σ_t/E_ν = (.332±.009±.002)x10^{-38} cm^2/GeV antineutrinos

(11) G. Barbiellini, C. Santoni, CERN EP/85-117

(12) CDHS group-J. Wotschok, FNAL Exp. Theo. Seminar Feb. 1986

(13) R. M. Barnett, Phys. Rev. D14, 70, (1976)

(14) J. Kaplin and F. Martin, Nucl. Phys. 115, 333, (1976)

(15) H. Abramowicz et al., Zeit. fur Physik, 15, 19, (1982)

(16) D. W. Duke and J. F. Owens, Phys. Rev. D30, 49, (1984)

(17) M. Jonker et al., Phys. Lett., 128B, 117, (1983)

(18) V. Blobel, DESY 84-118, (1984): T. Mattison Ph. D. Thesis.

(19) T. Mattison, Ph. D. Thesis

(20) M. Gronau, C.N. Leung, J.L.Rosner, Phys. Rev., D29, 2539, (1984)

Figure Captions:

Figure 1a: Feynman diagram for the charged current interaction.

Figure 1b: Diagram for the neutral-current interaction.

Figure 2: The energy-versus-radius correlation for the three setting of the narrow band beam in E-649.

Figure 3: The neutrino and antineutrino event rates as a function of the narrow band beam train setting. The rates are for a 100 ton calorimeter at Lab C.

Figure 4a: The incident neutrino energy spectrum for accepted charged current events. The two beam settings are indicated as well as the combined distribution.

Figure 4b: The corresponding antineutrino energy spectrum.

Figure 5a: The hadron energy spectrum for the three beam settings.

Figure 5b: The Q^2 distribution for the three settings.

Figure 6: A schematic representation of the three kinematic regions used in the neutral current analysis.

Figure 7: The detection efficiency as a function of E_μ for charged current events for a typical E-594 setting compared with a typical E-649 setting. The efficiency as a function of E_μ appears to be independent of the beam setting. Monte Carlo simulations were used for this estimate.

Figure 8: The misidentification probability for neutral current as a function of hadron energy. Calibration data was used in this estimate.

Figure 9: The deep inelastic scattering kinematics in terms of the observables of neutral current events for an incident neutrino energy of 150 GeV. Typical resolutions of θ_h and E_h are shown.

Figure 10: The effect of the vector boson propagator and the QCD evolution of the structure functions on the linearity of the total charged current cross section.

Figure 11: The effect of the a heavy quark flavor of 10 GeV/c^2 produced as the charmed quark of the strange sea. The same KM mixing terms which are operational in charmed quark production were used.

Figure 12: Schematic diagram of the beam monitoring system used in the 1982 narrow band beam run.

Figure 13: The systematic error in the determination of $\sin^2\theta_W$ arising from the ambiguity in the strange sea.

Figure 14: The systematic error in $\sin^2\theta_W$ from the ambiguity in the charmed quark mass.

Figure 15a: The ratio of the charged current cross section over the neutral current cross section as a function x measured in E-594.

Figure 15b: The corresponding antineutrino ratio.

Figure 16a: The simulated E-649 ratio for all of the neutrino data.

Figure 16b: The corresponding antineutrino ratio.

Figure 17: The unsmeared x-distribution is compared with the smeared distribution from the E-649 Monte Carlo simulation.

Figure 18a: The preliminary deconvoluted E-594 $F_+(x)$ structure function for both charge currents and neutral currents.

Figure 18b: The corresponding antineutrino function $F_-(x)$.

Figure 19: The results of the eigenvector expansion of the deconvolution of the E-649 Monte Carlo. The line represents the input x-dependence.

Figure 20: The deconvoluted valence and sea distributions in E-649. Also shown are the structure functions F_2 and xF_3. The errors represent the statistical and unfolding errors of the deconvolution procedure.

Figure 21: A typical Monte Carlo event for the production of a heavy neutral lepton. The downstream electromagnetic shower is clearly visible. The Monte Carlo was actually performed for the E-594 conditions but the detection efficiency should not be very sensitive to the incident neutrino energy.

Figure 22: The detection efficiency for a heavy neutral lepton for several fixed masses as a function of life time. The results were obtained from a scan of Monte Carlo events.

Figure 23: A typical bremsstrahlung shower after the muon has been removed. These events can be used to simulate the heavy lepton events.

Figure 24: A dimuon event with very little hadronic energy. This is the signature for a heavy neutral lepton decaying into a neutrino and 2 muons.

Figure 25: The hadron energy spectrum for a 9 GeV/c^2 object produced with a ξ distribution near 1.

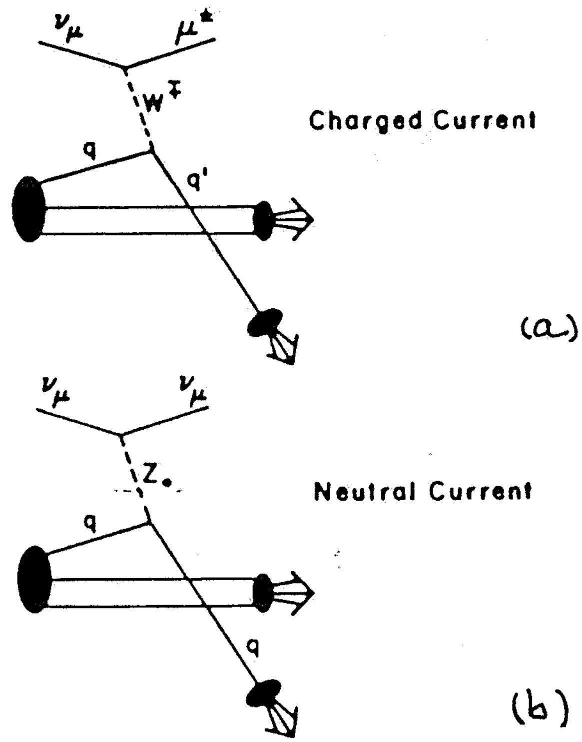
ν_μ
$\mu^\pm$
$W^\mp$
Charged Current
q
q'
(a)
ν_μ
ν_μ
Z_0
Neutral Current
q
q
(b)

Figure 1

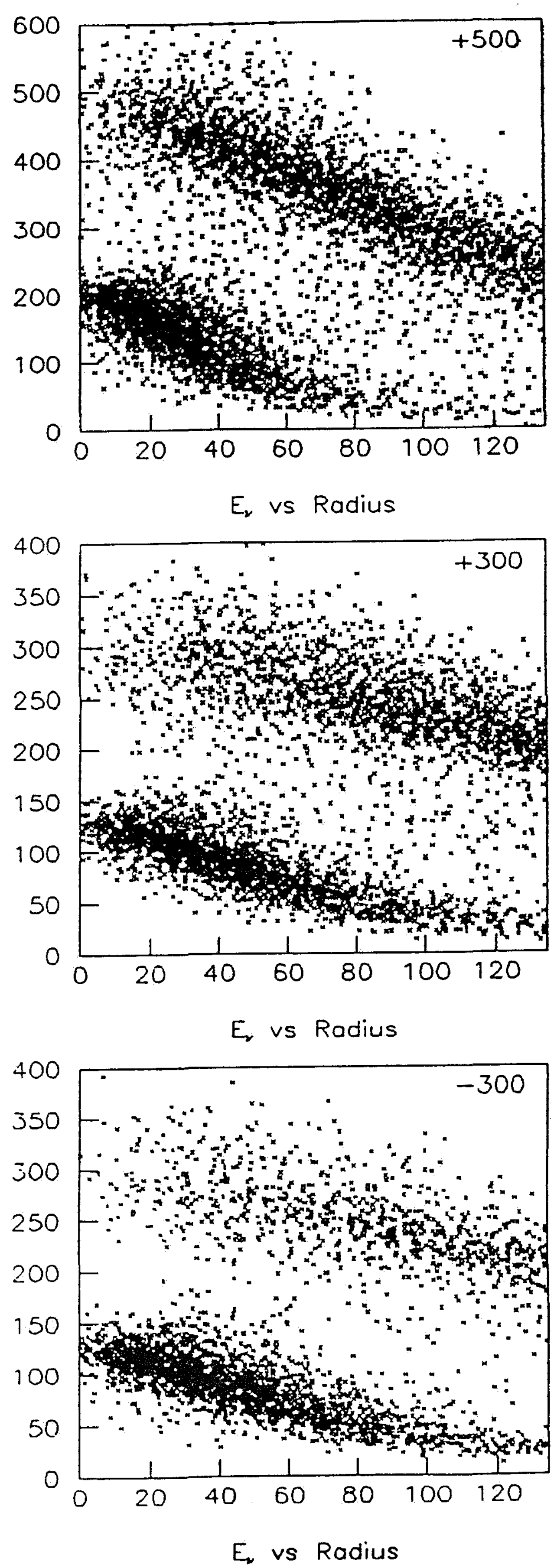

Figure 2

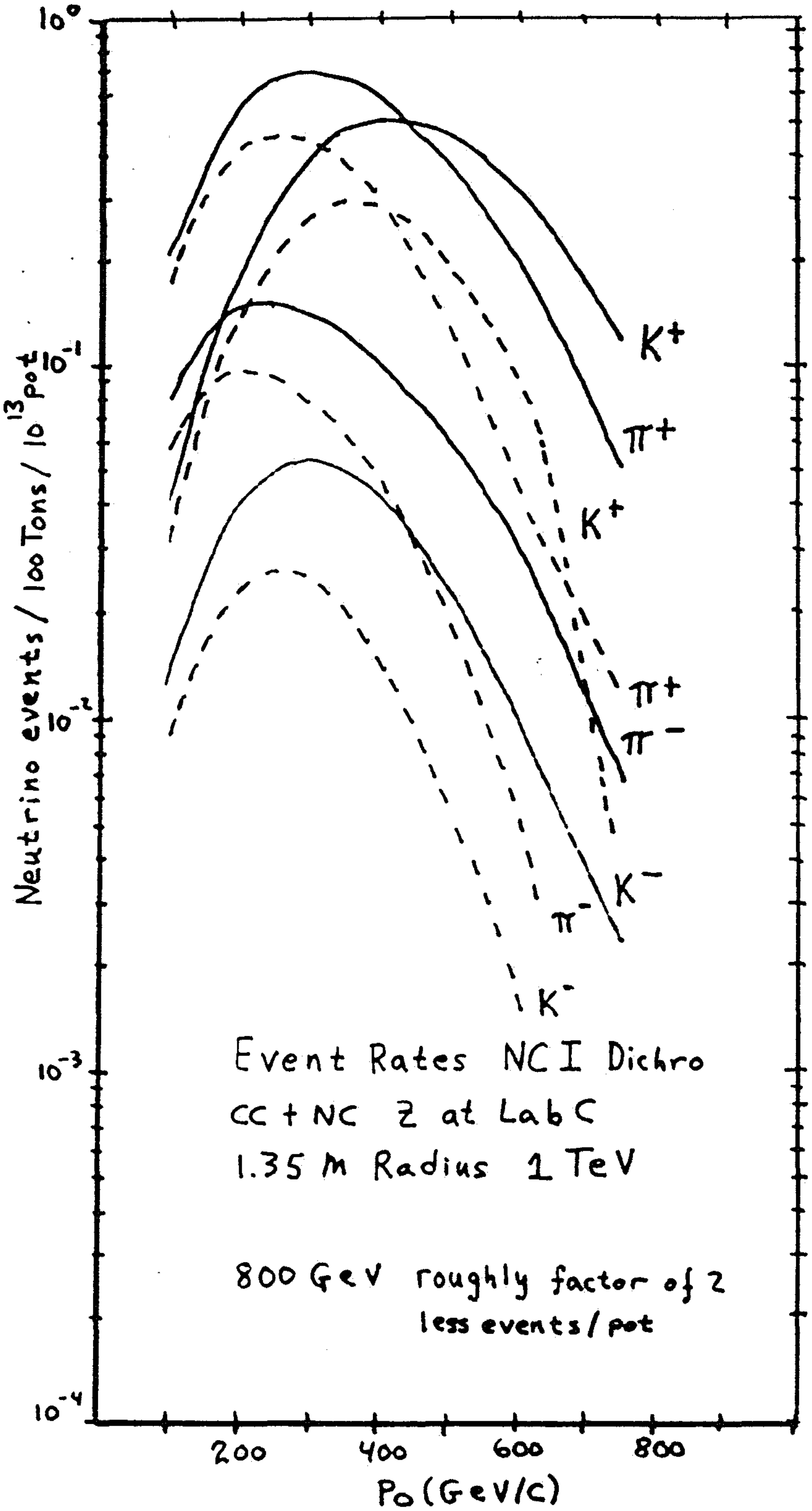

10^0
10^{-1}
10^{-2}
10^{-3}
10^{-4}
Neutrino events / 100 Tons / 10^{13} pot
K^+
π^+
K^+
π^+
π^-
K^-
π^-
K^-
Event Rates NC I Dichro
CC + NC Z at Lab C
1.35 M Radius 1 TeV
800 GeV roughly factor of 2
less events / pot
200
400
600
800
Po (GeV/c)

Figure 3

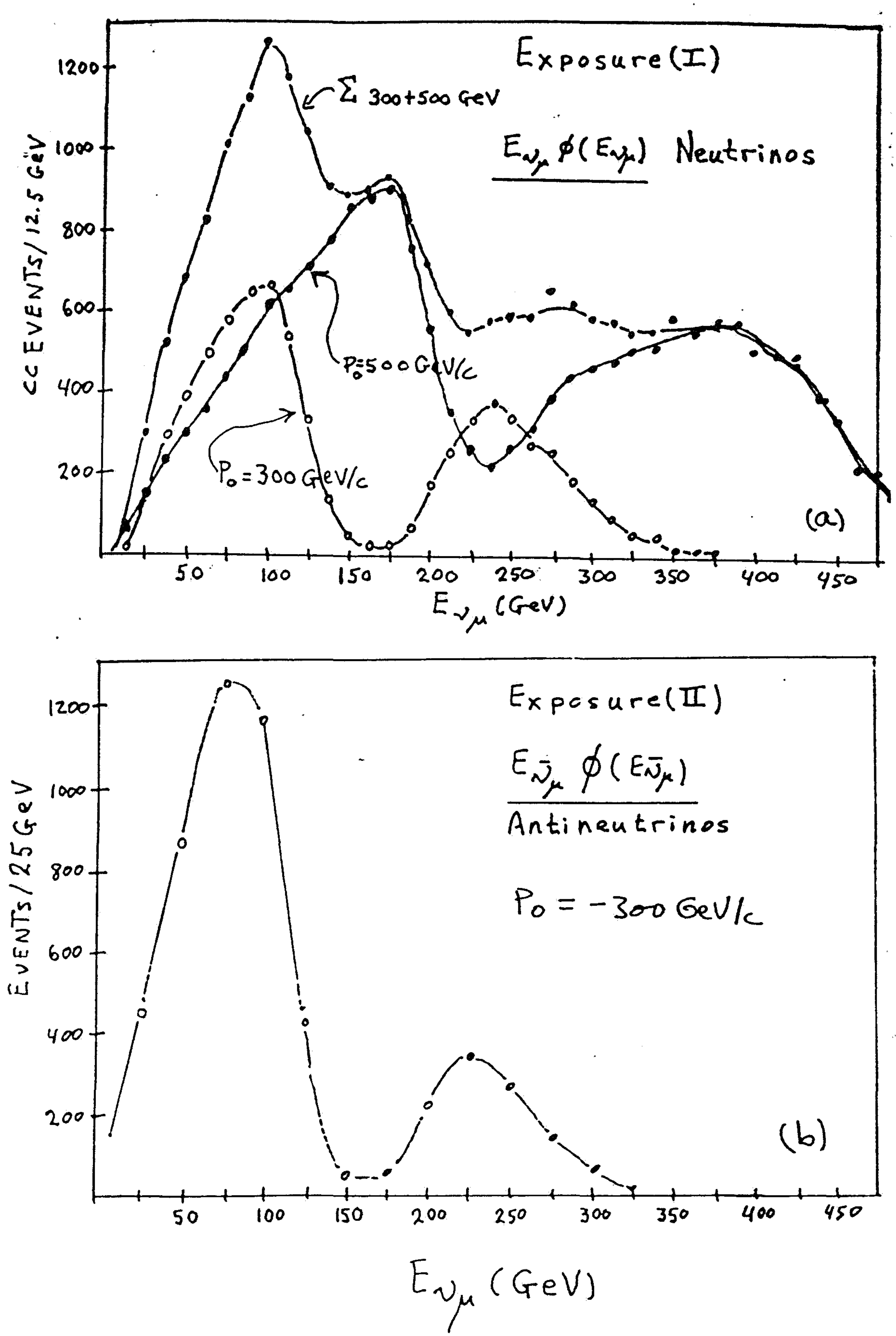

Exposure(I)
Σ 300+500 GeV
$E_{\nu_\mu}\phi(E_{\nu_\mu})$ Neutrinos
CC EVENTS/12.5 GeV
1200
1000
800
600
400
200
P_o=500 GeV/c
P_o=300 GeV/c
(a)
50
100
150
200
250
300
350
400
450
E_{ν_μ} (GeV)
Exposure(II)
$E_{\bar{\nu}_\mu}\phi(E_{\bar{\nu}_\mu})$
Antineutrinos
P_o = −300 GeV/c
EVENTS/25 GeV
(b)
E_{ν_μ} (GeV)

Figure 4

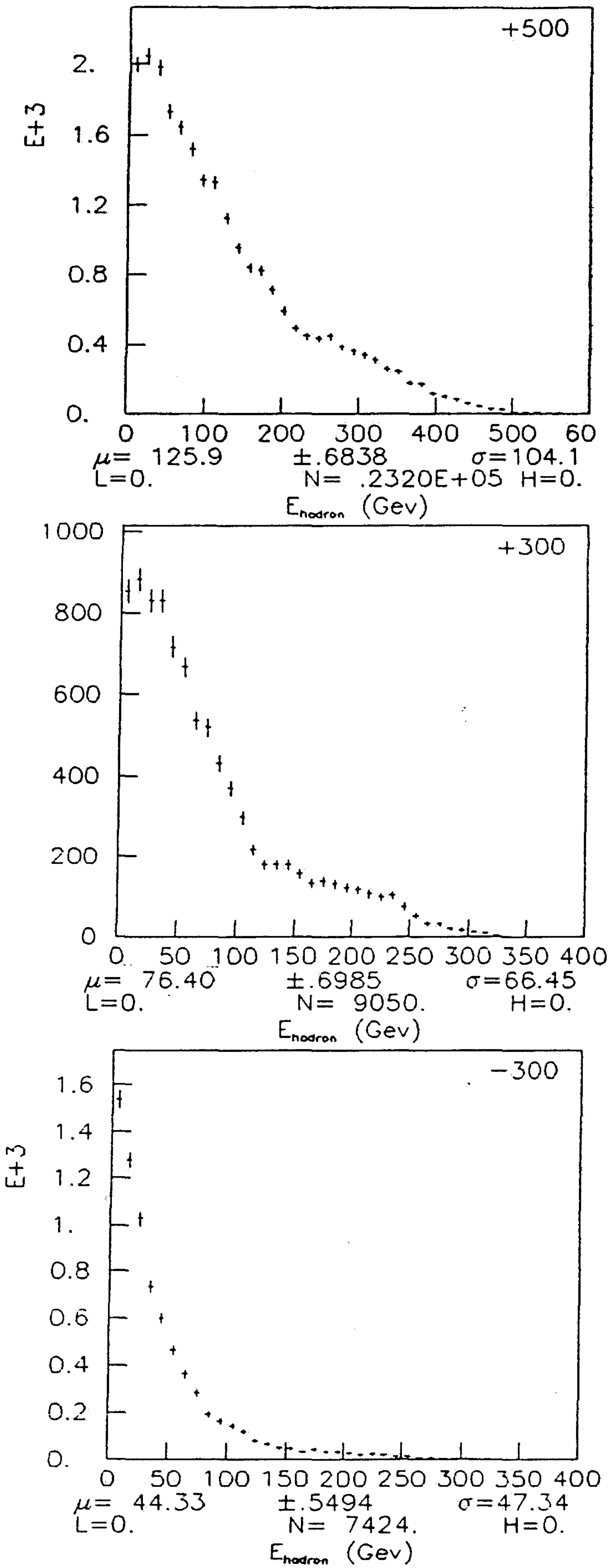
+500
E+3
2.
1.6
1.2
0.8
0.4
0.
0 100 200 300 400 500 60
μ= 125.9 ±.6838 σ=104.1
L=0. N= .2320E+05 H=0.
E hadron (Gev)
+300
1000
800
600
400
200
0
0 50 100 150 200 250 300 350 400
μ= 76.40 ±.6985 σ=66.45
L=0. N= 9050. H=0.
E hadron (Gev)
−300
E+3
1.6
1.4
1.2
1.
0.8
0.6
0.4
0.2
0.
0 50 100 150 200 250 300 350 400
μ= 44.33 ±.5494 σ=47.34
L=0. N= 7424. H=0.
E hadron (Gev)

Figure 5a

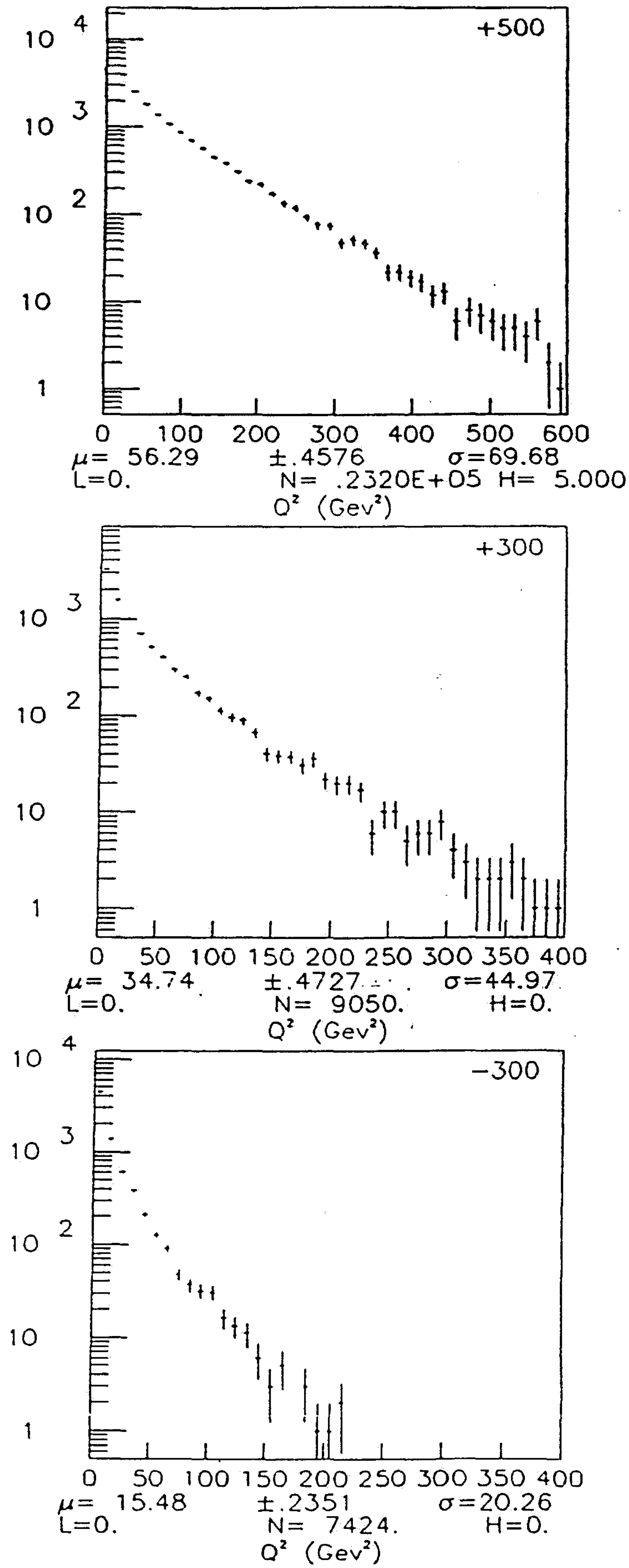
+500
10 4
10 3
10 2
10
1
0 100 200 300 400 500 600
μ= 56.29 ±.4576 σ=69.68
L=0. N= .2320E+05 H= 5.000
Q² (Gev²)
+300
10 3
10 2
10
1
0 50 100 150 200 250 300 350 400
μ= 34.74 ±.4727 σ=44.97
L=0. N= 9050. H=0.
Q² (Gev²)
−300
10 4
10 3
10 2
10
1
0 50 100 150 200 250 300 350 400
μ= 15.48 ±.2351 σ=20.26
L=0. N= 7424. H=0.
Q² (Gev²)

Fig. 5b

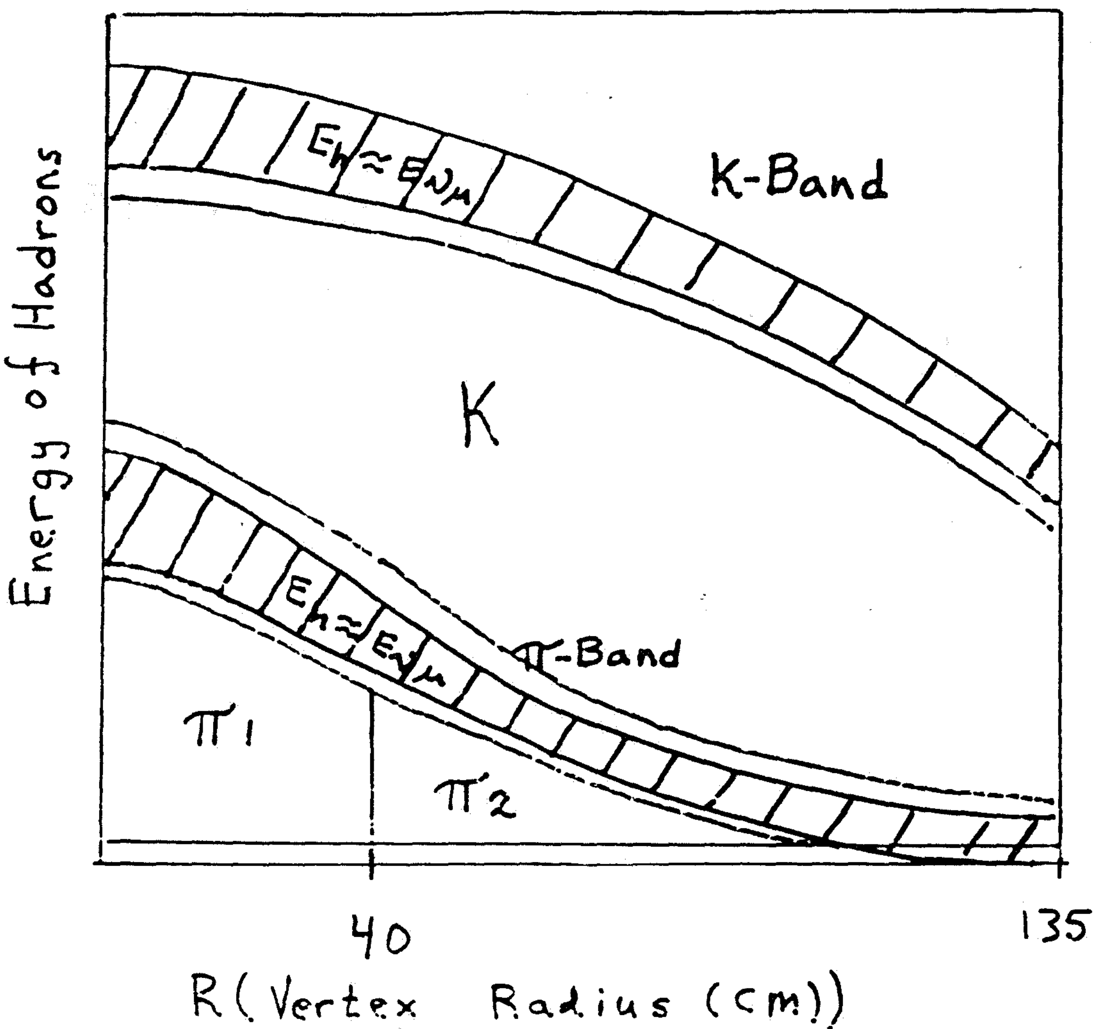

K-Band
$E_h \approx E_{\nu_\mu}$
K
$E_h \approx E_{\nu_\mu}$
π-Band
π1
π2
40
135
R(Vertex Radius (cm))
Energy of Hadrons

Figure 6

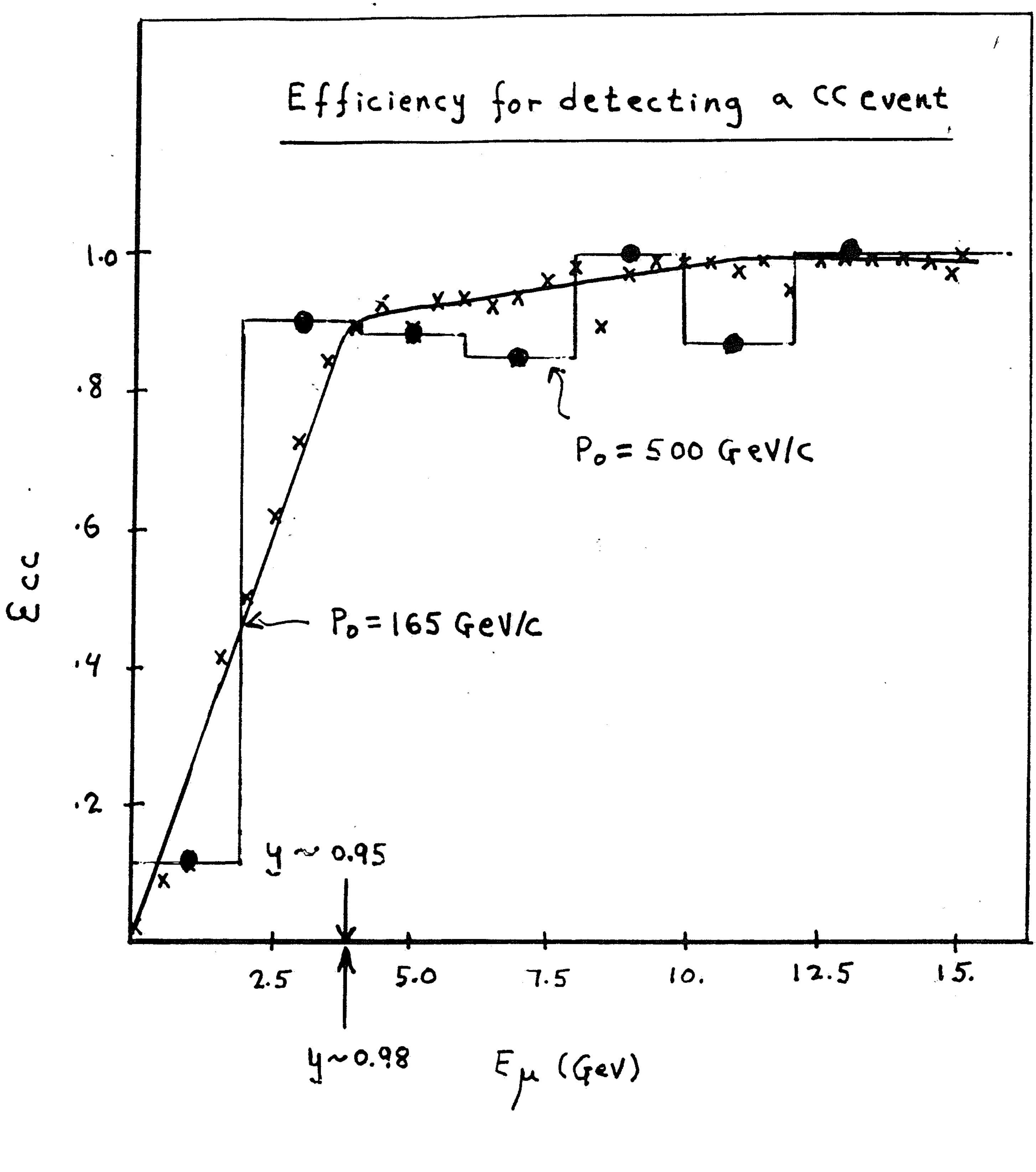

Efficiency for detecting a CC event
1.0
.8
.6
.4
.2
ε_{cc}
$P_o = 500$ GeV/c
$P_o = 165$ GeV/c
y ~ 0.95
2.5
5.0
7.5
10.
12.5
15.
y ~ 0.98
E_μ (GeV)

Figure 7

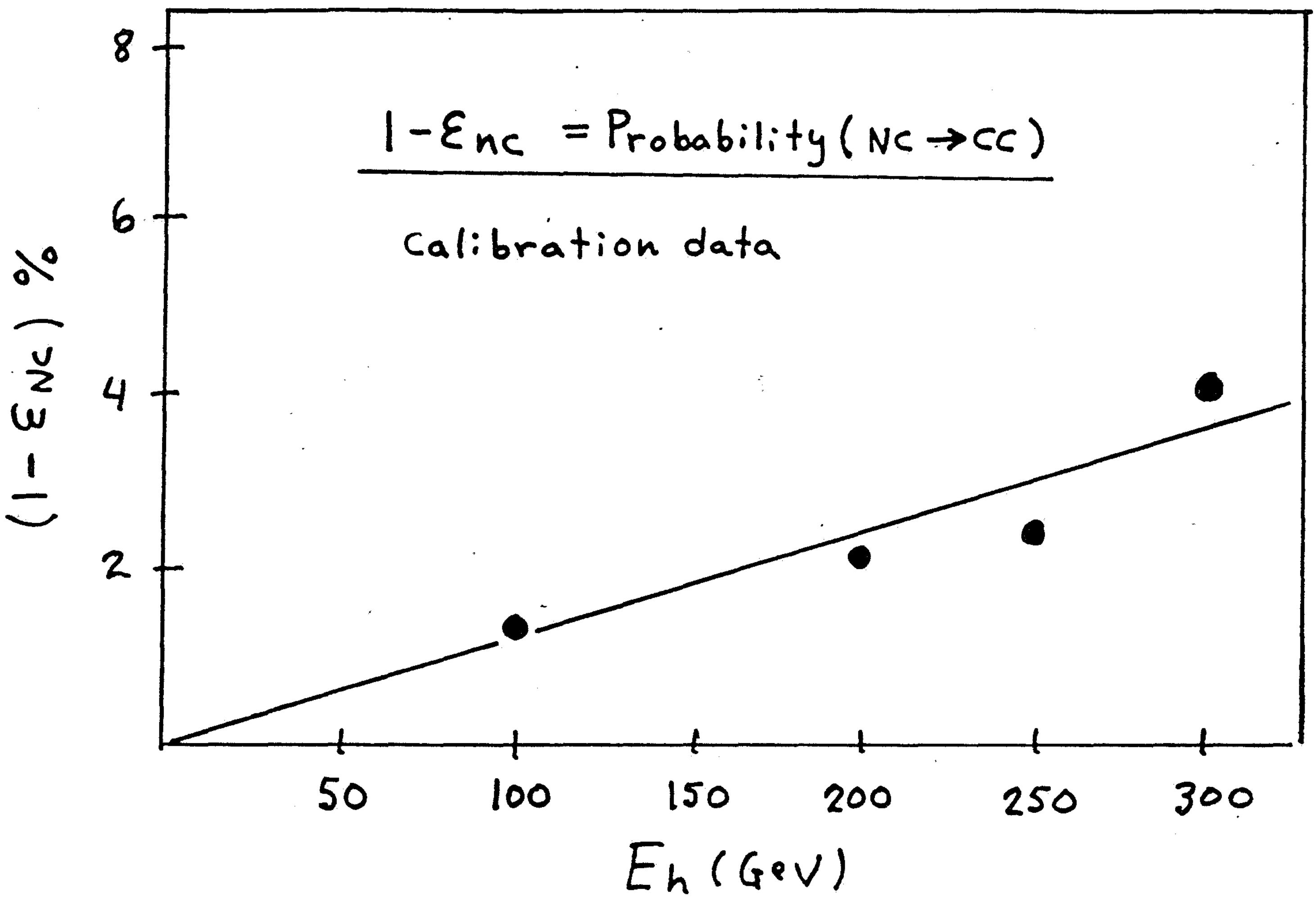

1 - ε_nc = Probability (NC → CC)
Calibration data
(1 - ε_NC) %
8
6
4
2
50
100
150
200
250
300
E_h (GeV)

Figure 8

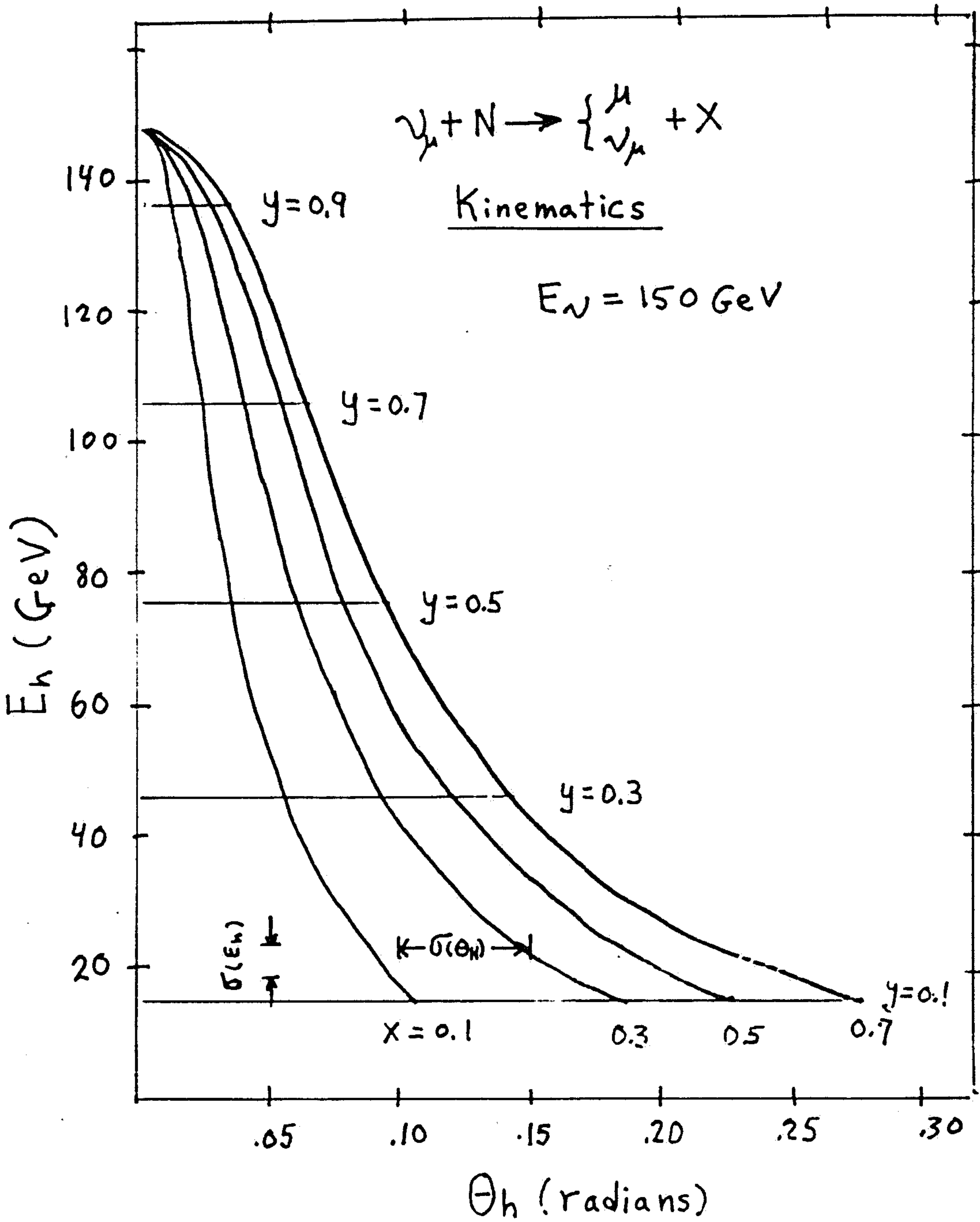

$\nu_\mu + N \to \left\{ \begin{matrix} \mu \\ \nu_\mu \end{matrix} \right. + X$
Kinematics
$E_\nu = 150$ GeV
y=0.9
y=0.7
y=0.5
y=0.3
y=0.1
X=0.1
0.3
0.5
0.7
$\sigma(E_h)$
$\sigma(\theta_h)$
140
120
100
80
60
40
20
E_h (GeV)
.05
.10
.15
.20
.25
.30
θ_h (radians)

Figure 9

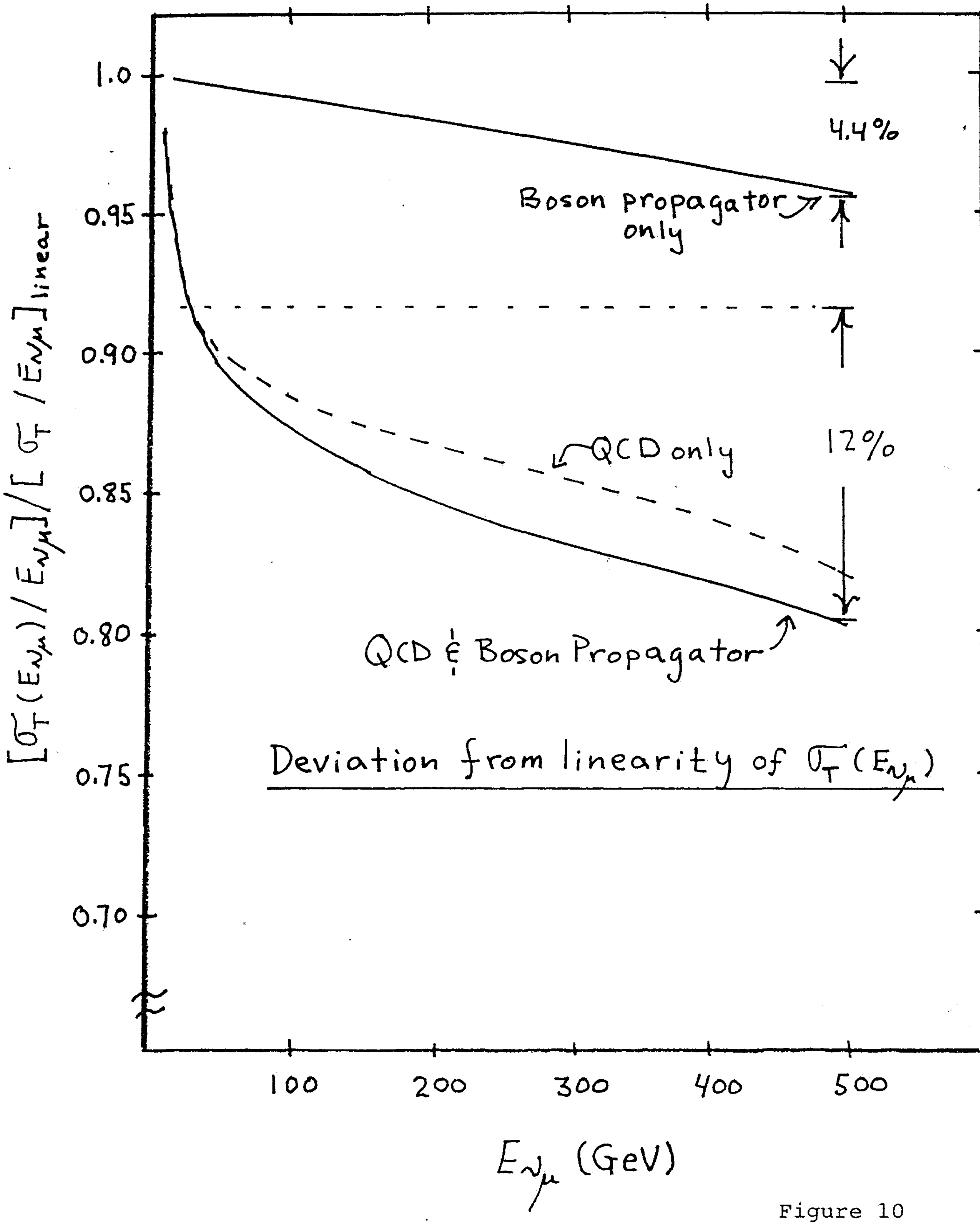
1.0
0.95
0.90
0.85
0.80
0.75
0.70
$[\sigma_T(E_{\nu_\mu})/E_{\nu_\mu}]/[\sigma_T/E_{\nu_\mu}]_{linear}$
4.4%
Boson propagator only
12%
QCD only
QCD & Boson Propagator
Deviation from linearity of $\sigma_T(E_{\nu_\mu})$
100
200
300
400
500
E_{ν_μ} (GeV)

Figure 10

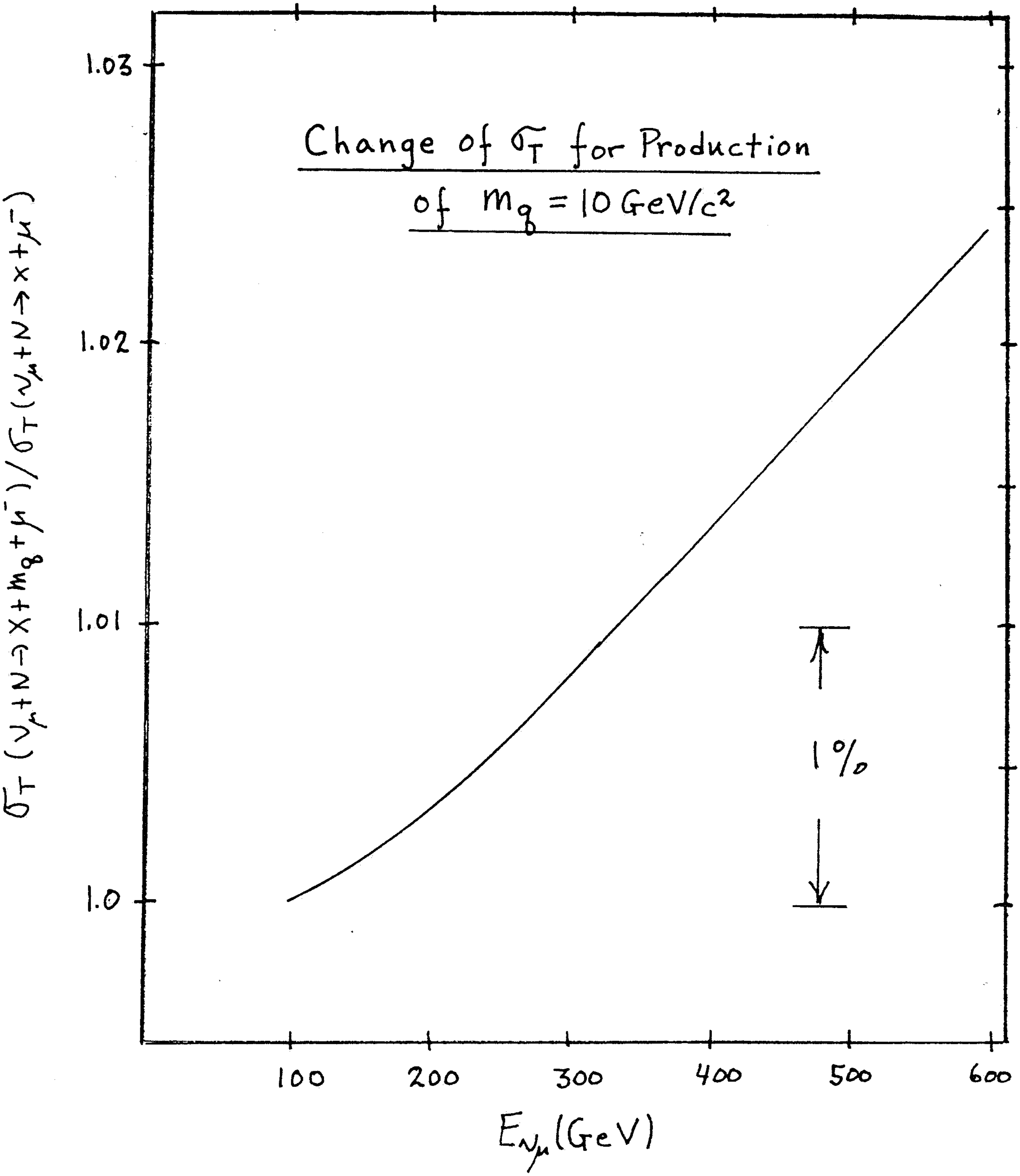
Change of σ_T for Production
of $m_q = 10\ GeV/c^2$
$\sigma_T(\nu_\mu + N \to X + m_q + \mu^-)/\sigma_T(\nu_\mu + N \to X + \mu^-)$
1.03
1.02
1.01
1.0
1%
100
200
300
400
500
600
E_{ν_μ}(GeV)

Figure 11

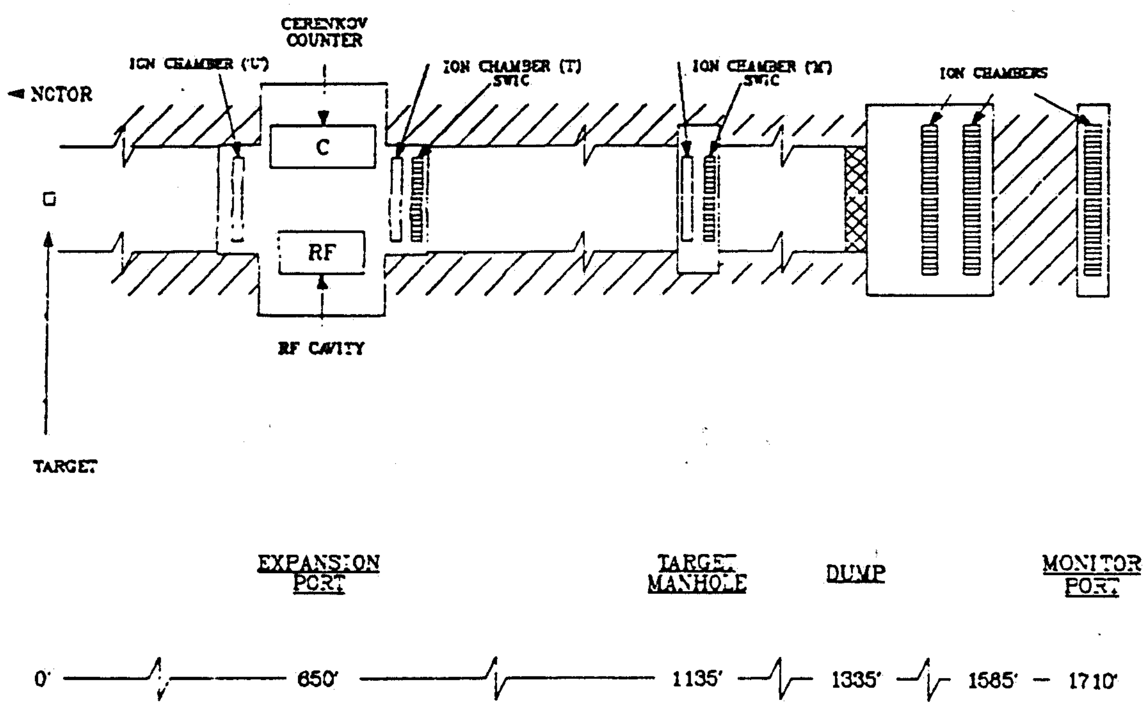
CERENKOV COUNTER
ION CHAMBER (U)
ION CHAMBER (T)
SWIC
ION CHAMBER (M)
SWIC
ION CHAMBERS
NCTOR
C
RF
RF CAVITY
TARGET
EXPANSION PORT
TARGET MANHOLE
DUMP
MONITOR PORT
0'
650'
1135'
1335'
1585'
1710'

Figure 12

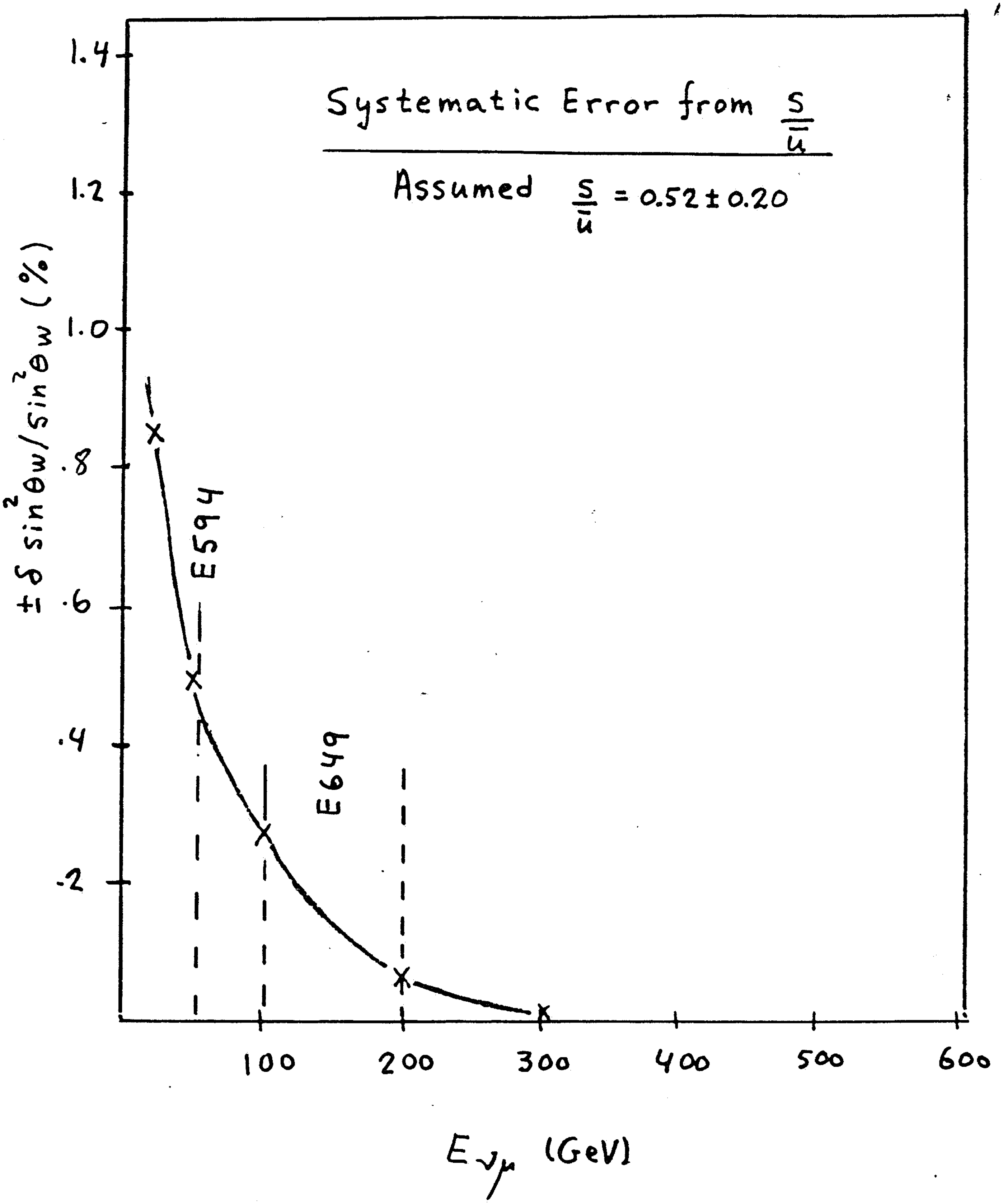

Systematic Error from $\frac{s}{\bar{u}}$
Assumed $\frac{s}{\bar{u}} = 0.52 \pm 0.20$
$\pm \delta \sin^2\theta_W / \sin^2\theta_W$ (%)
1.4
1.2
1.0
.8
.6
.4
.2
E594
E649
100
200
300
400
500
600
E_{ν_μ} (GeV)

Figure 13

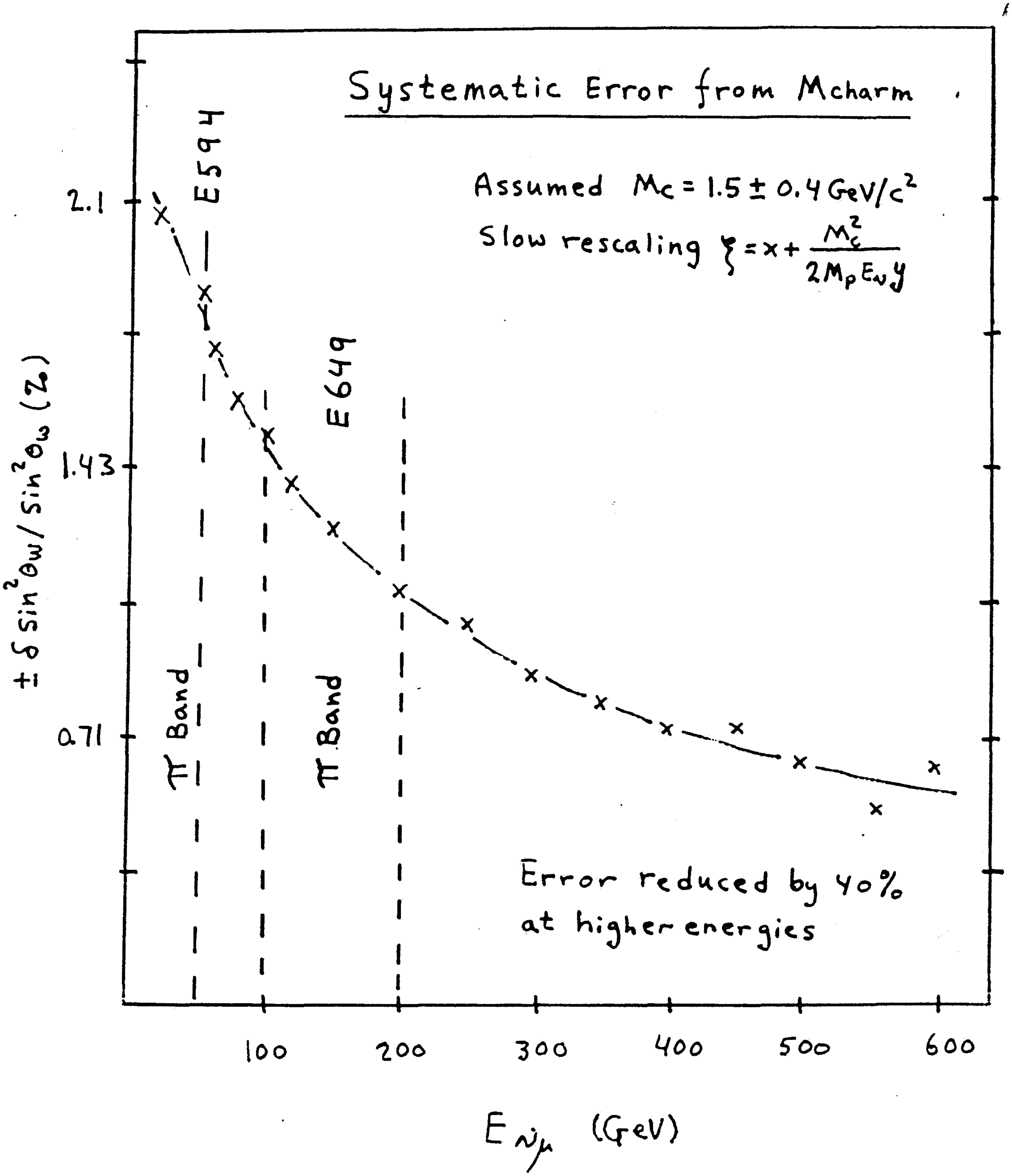

Systematic Error from Mcharm
Assumed $M_c = 1.5 \pm 0.4\ GeV/c^2$
Slow rescaling $\xi = x + \frac{M_c^2}{2M_p E_\nu y}$
E594
E649
π Band
π Band
Error reduced by 40% at higher energies
2.1
1.43
0.71
$\pm\,\delta\sin^2\theta_W/\sin^2\theta_W$ (%)
100
200
300
400
500
600
E_{ν_μ} (GeV)

Figure 14

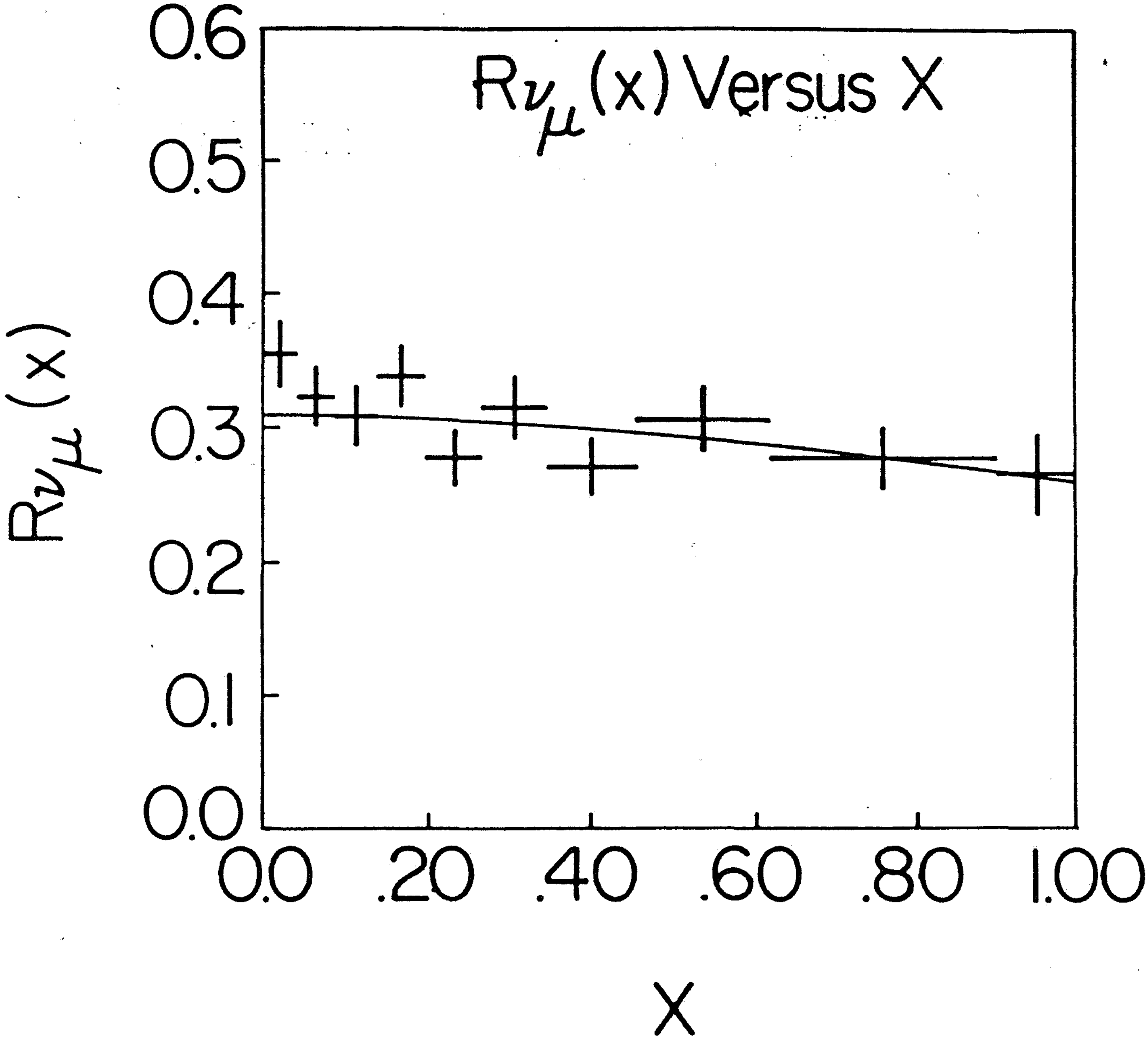

Figure 15

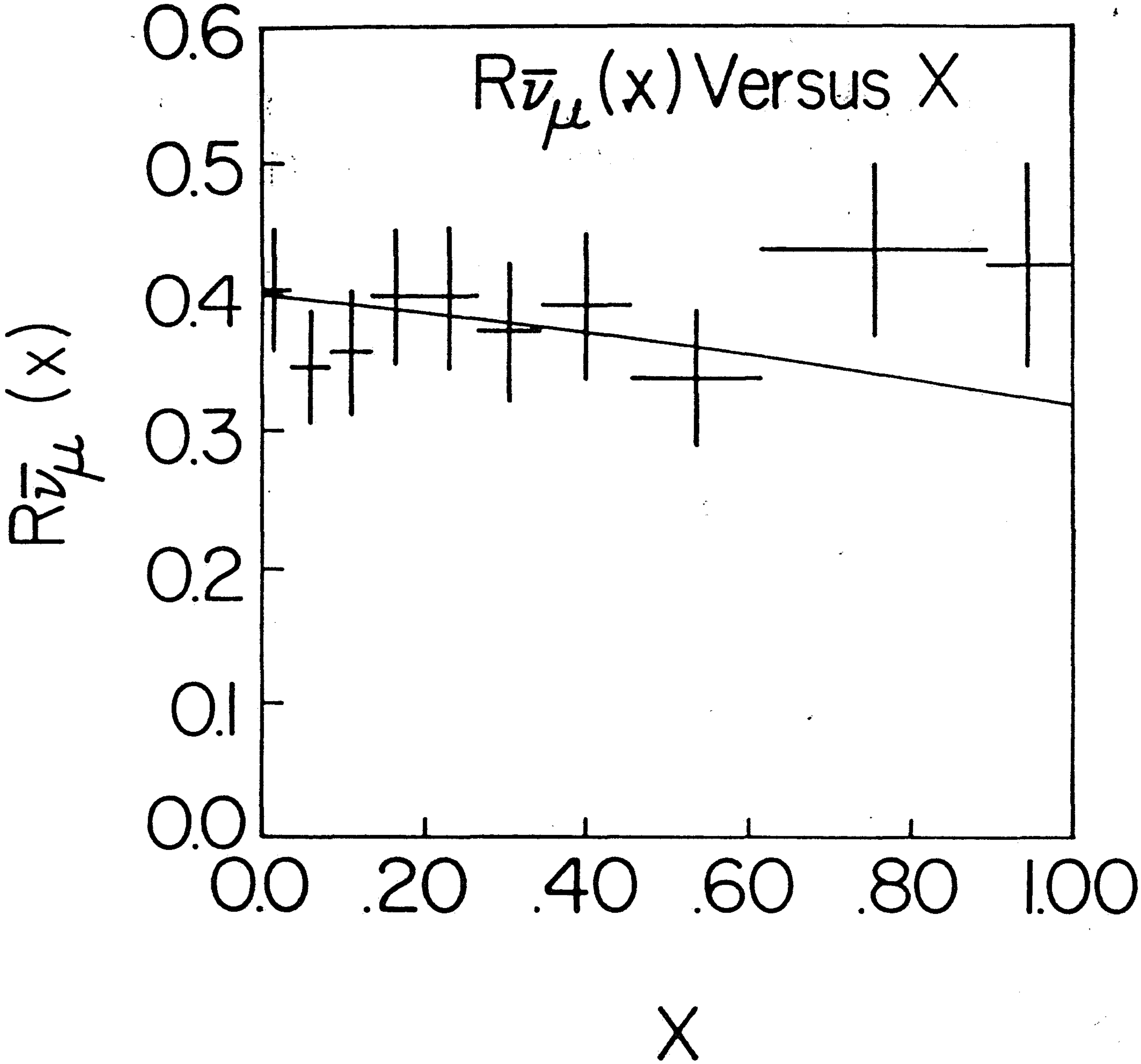
$R\bar{\nu}_\mu(x)$ Versus X
$R\bar{\nu}_\mu$ (x)
0.6
0.5
0.4
0.3
0.2
0.1
0.0
0.0
.20
.40
.60
.80
1.00
X

Fig. 15b

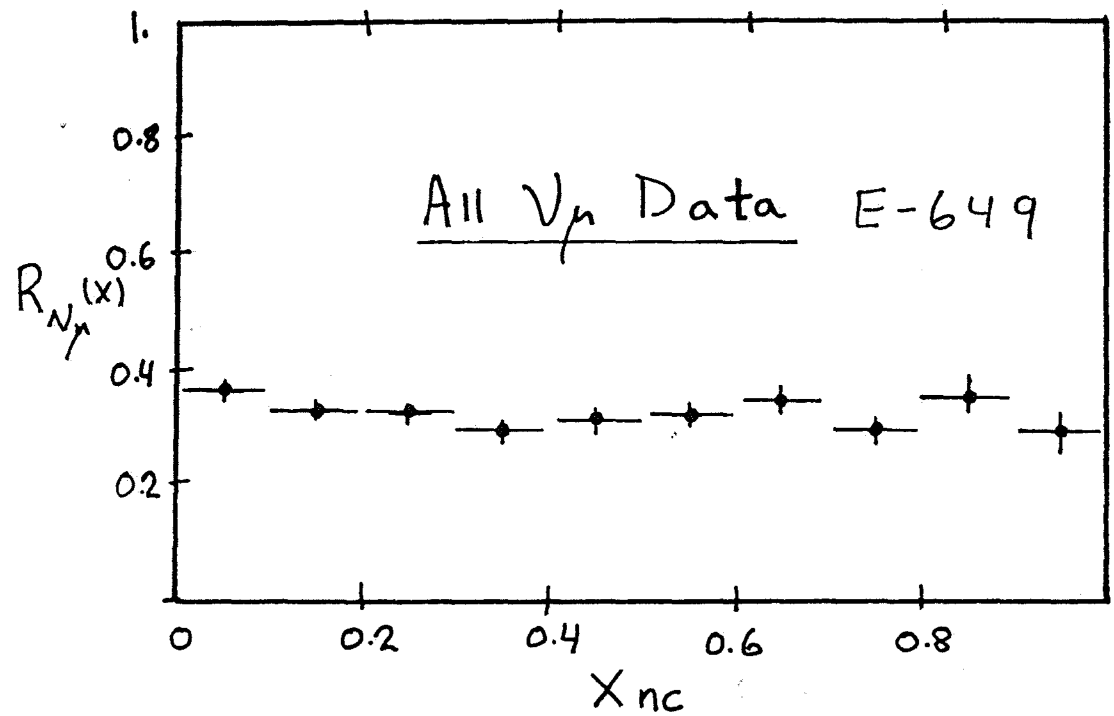
All ν_μ Data
E-649
$R_{\nu_\mu}(x)$
1.
0.8
0.6
0.4
0.2
0
0.2
0.4
0.6
0.8
X_{nc}

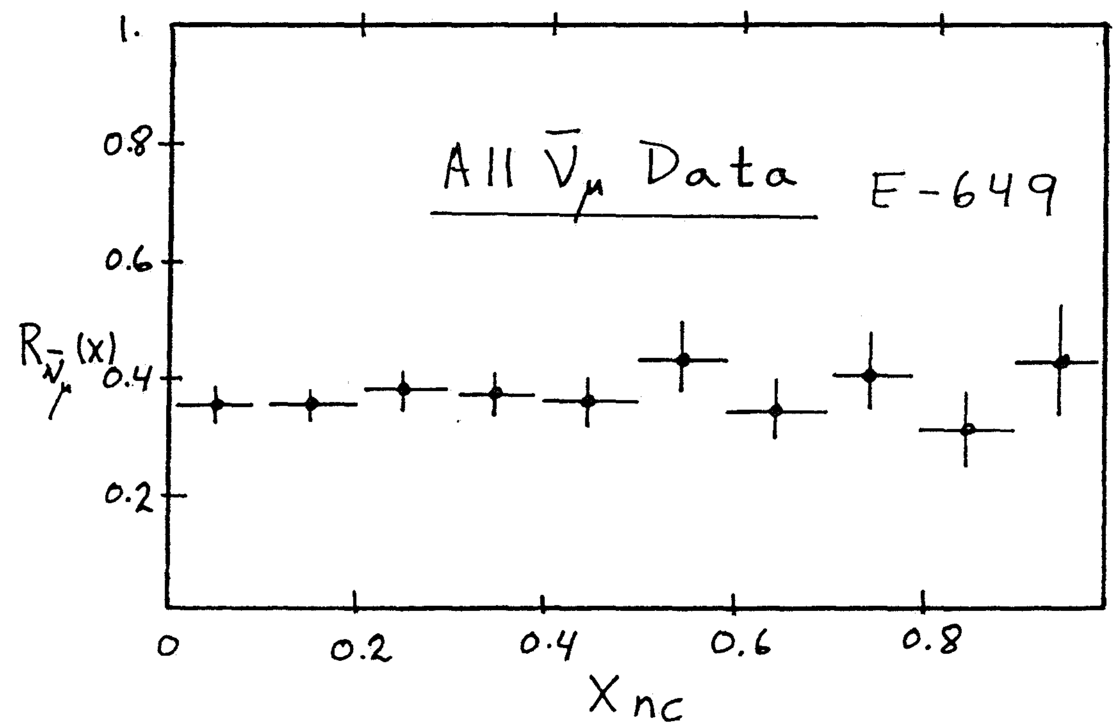
All $\bar{\nu}_\mu$ Data
E-649
$R_{\bar{\nu}_\mu}(x)$
1.
0.8
0.6
0.4
0.2
0
0.2
0.4
0.6
0.8
X_{nc}

Figure 16

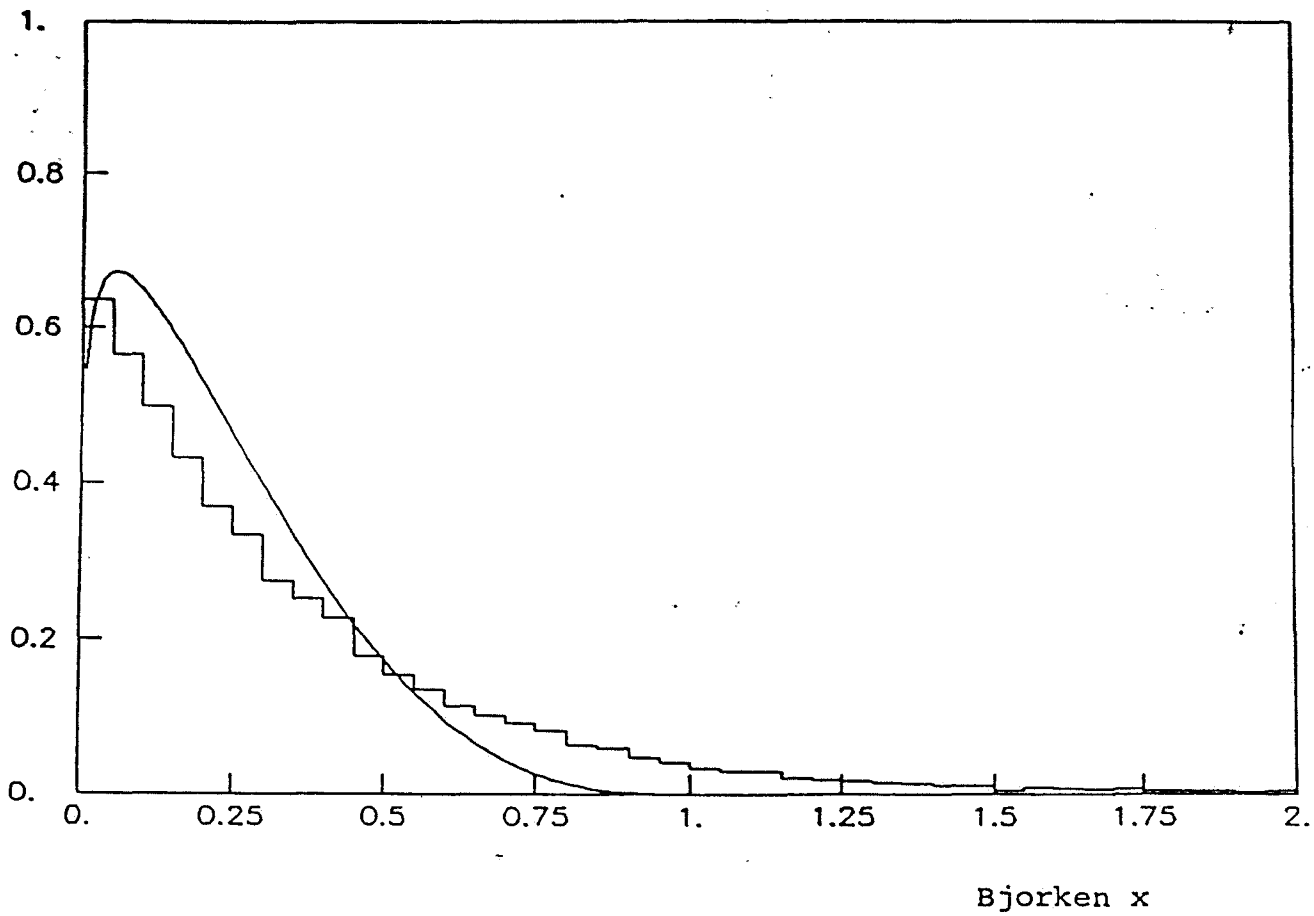

Figure 17

True (curve) and Observed (histogram)
Neutral Current x Distributions

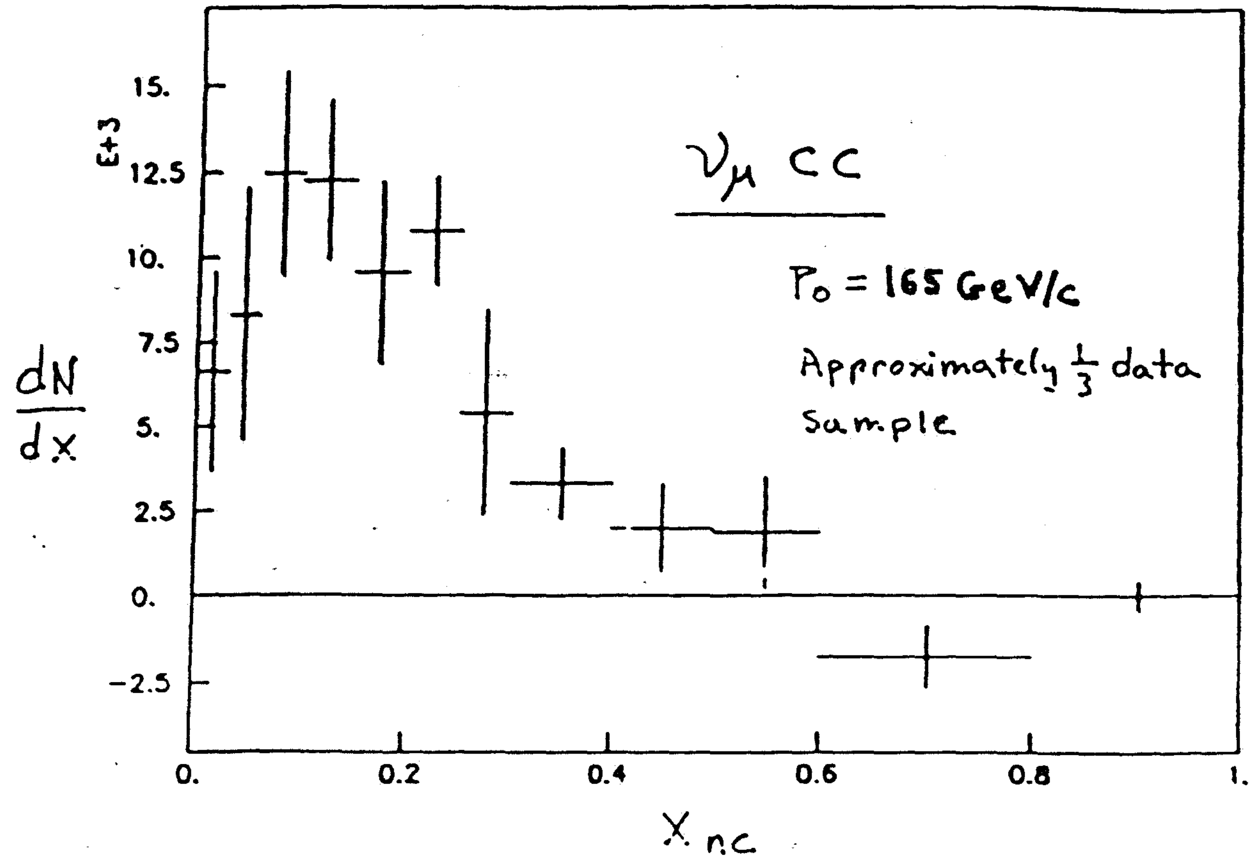

15.
12.5
10.
7.5
5.
2.5
0.
-2.5
E+3
dN/dx
ν_μ CC
P_0 = 165 GeV/c
Approximately $\frac{1}{3}$ data sample
0.
0.2
0.4
0.6
0.8
1.
X nc

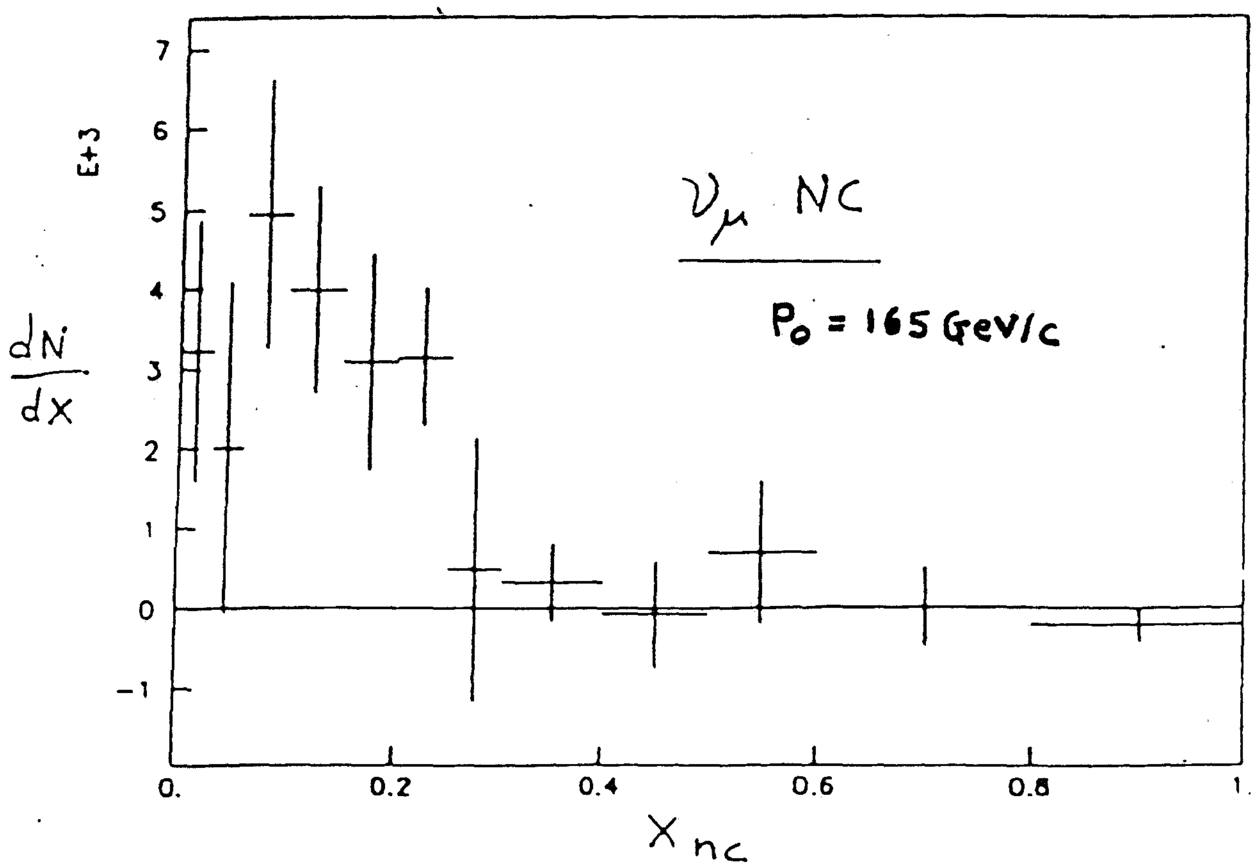

7
6
5
4
3
2
1
0
-1
E+3
dN/dx
ν_μ NC
P_0 = 165 GeV/c
0.
0.2
0.4
0.6
0.8
1.
X nc

Figure 18

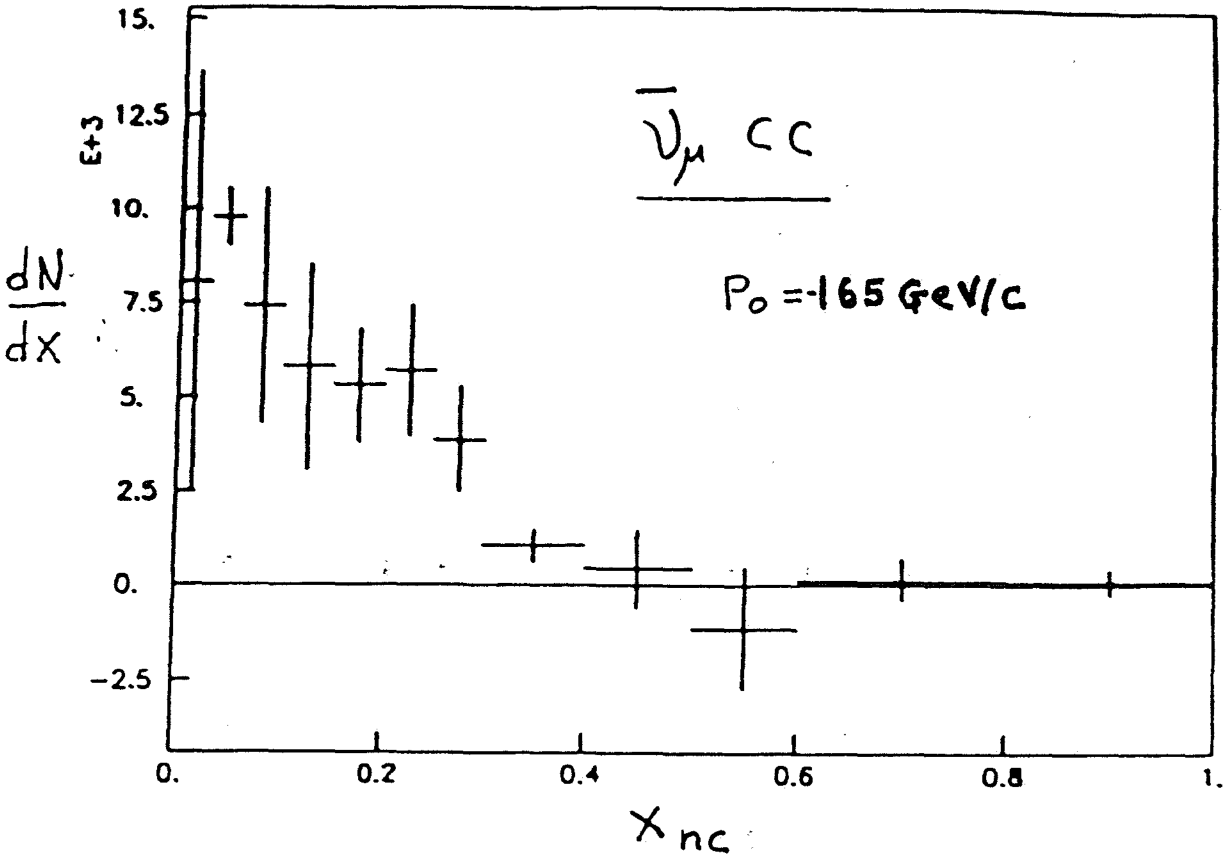

$\bar{\nu}_\mu$ CC
P_o = -165 GeV/c
dN/dX
E+3
X_{nc}

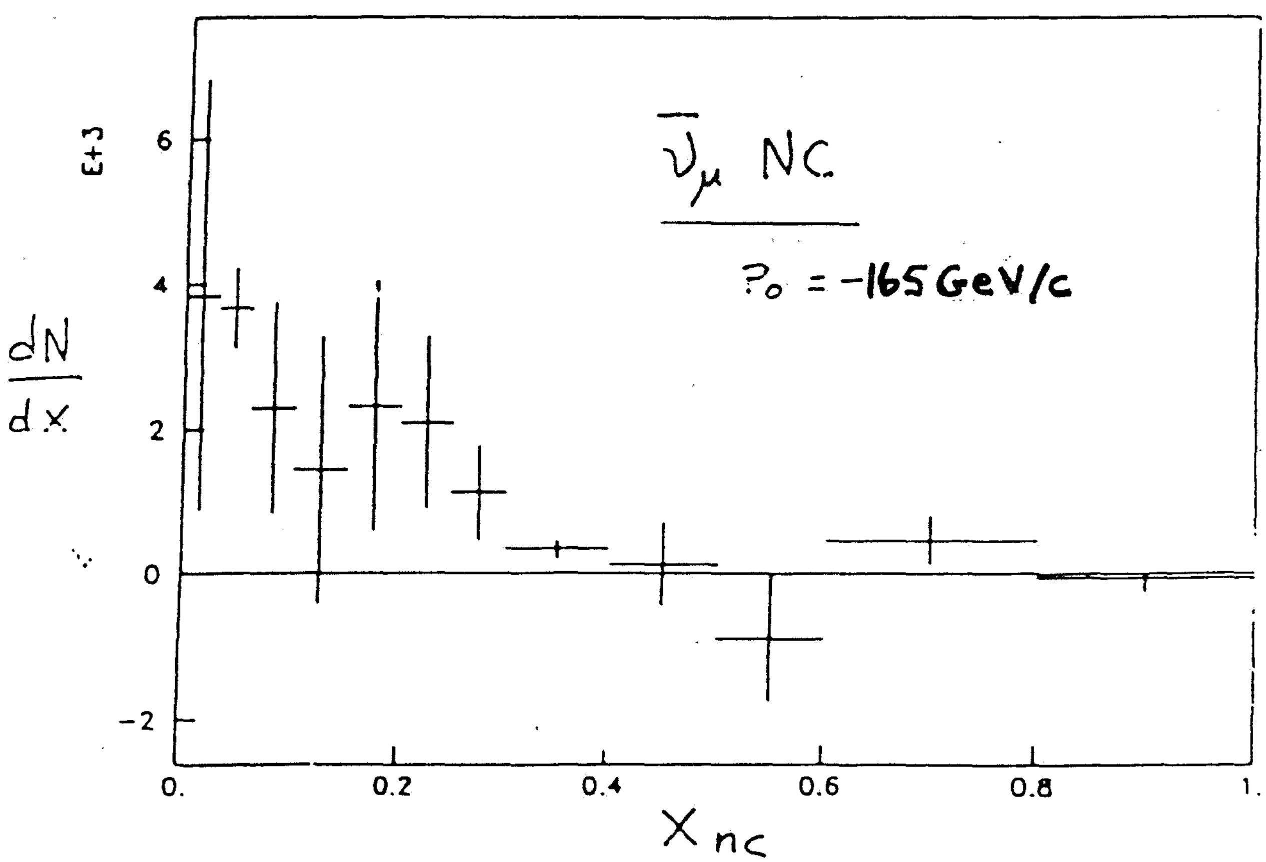

$\bar{\nu}_\mu$ NC
P_o = -165 GeV/c
dN/dx
E+3
X_{nc}

Fig. 18b

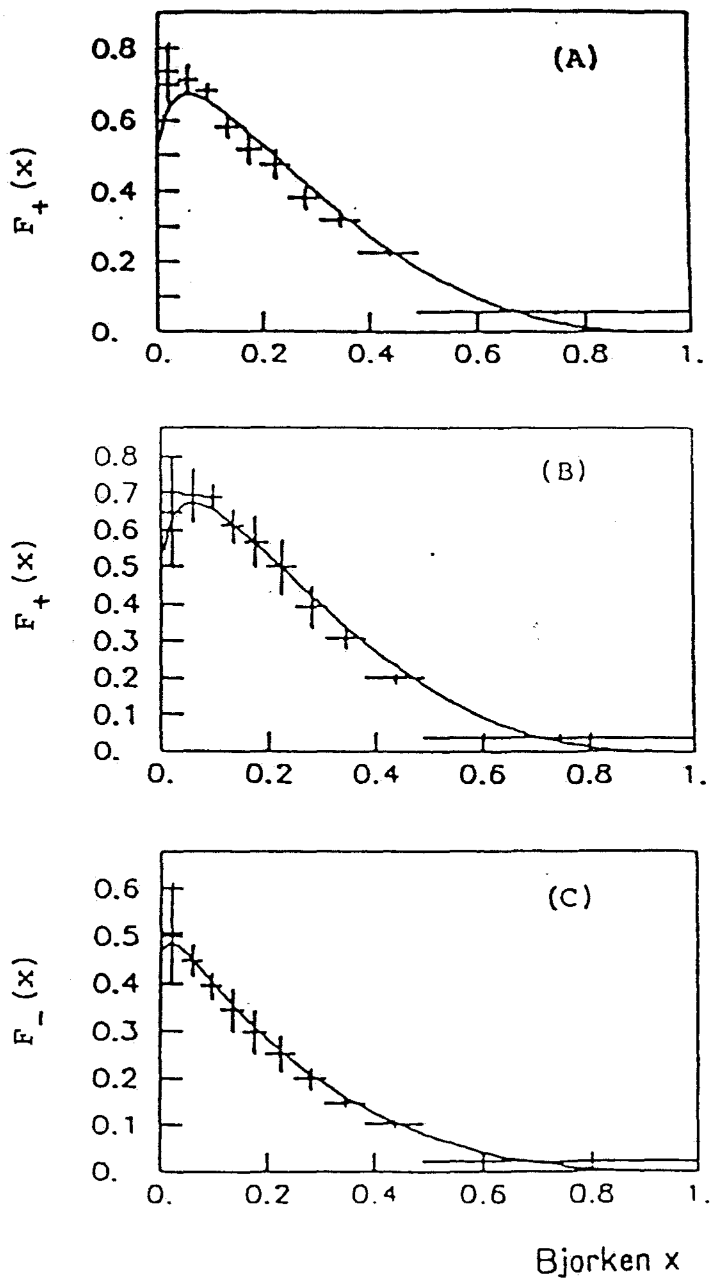

Figure 19

Neutral Current Structure Functions $F_{\pm}$

(A) +500 (B) +300 (C) -300

Error bars represent the unfolded solutions.
Curves indicate the exact distributions.

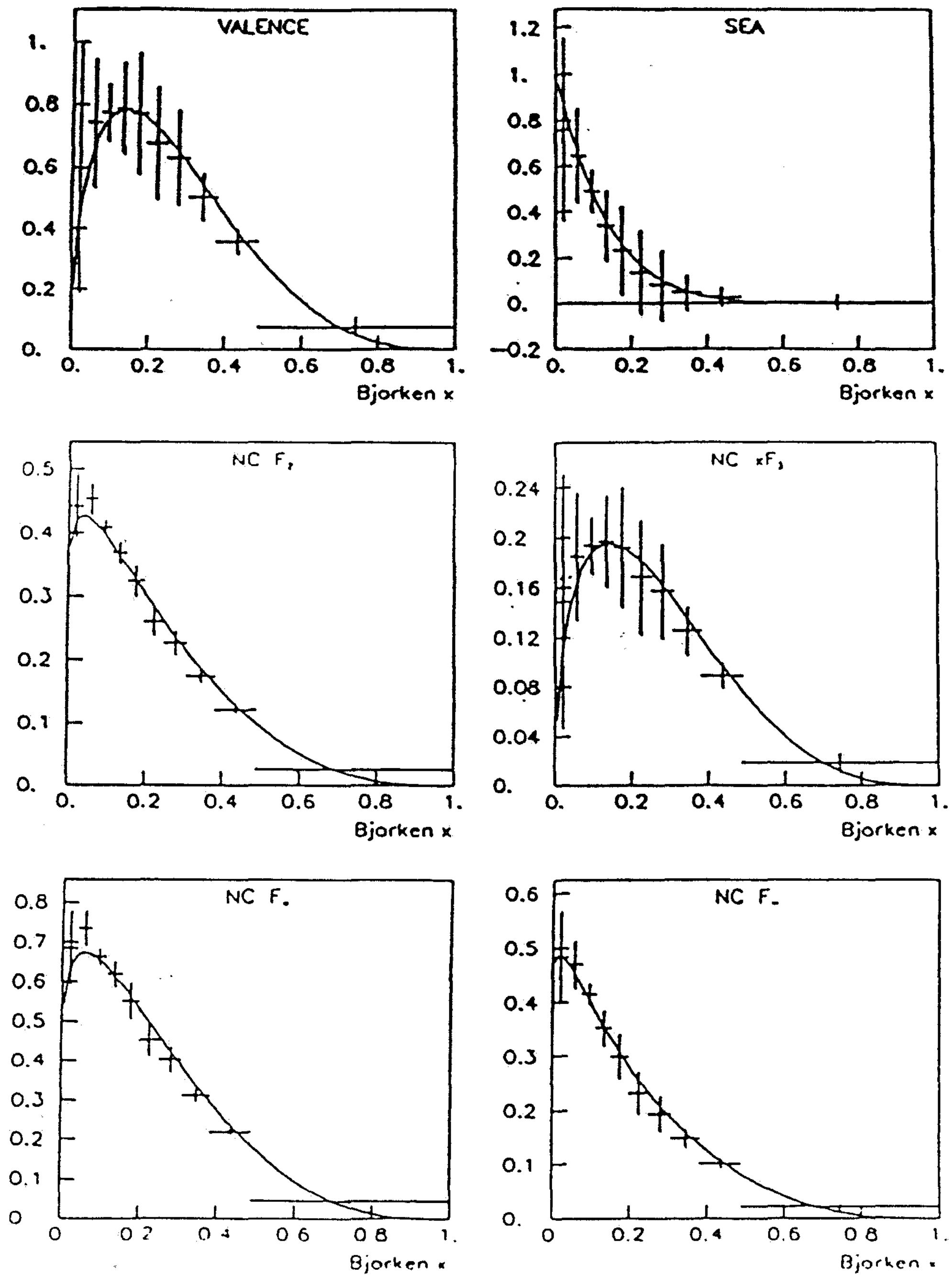

Figure 20

Valence and Sea Quark Distributions
and Neutral Current Structure Functions

Error bars represent the unfolded solutions.
Curves indicate the exact distributions.

Monte Carlo $m_L = 2\ GeV/c^2$ $\tau_0 = 1\ nsec.$

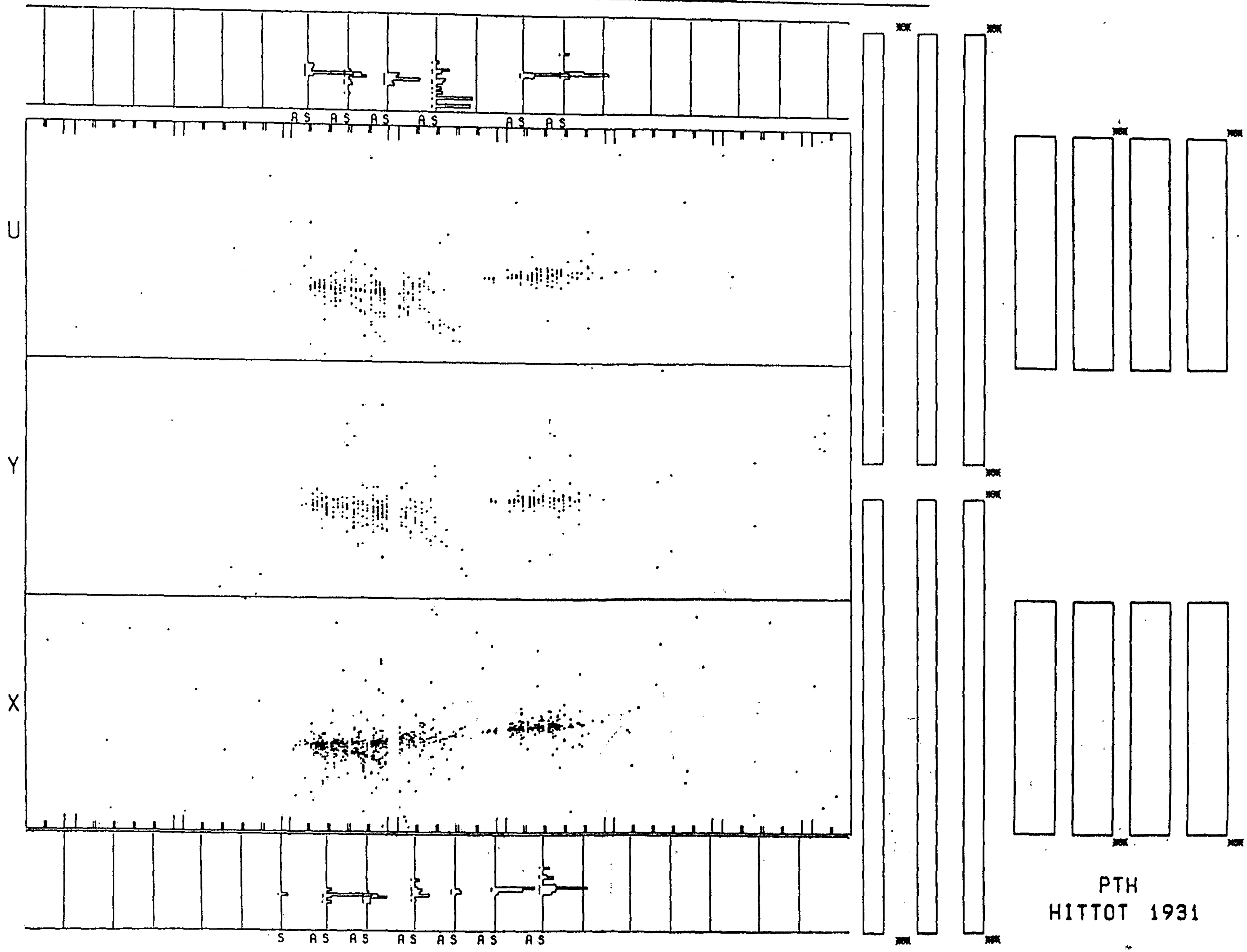

Figure 21

Detection Efficiency Vs τ_0 and m_L

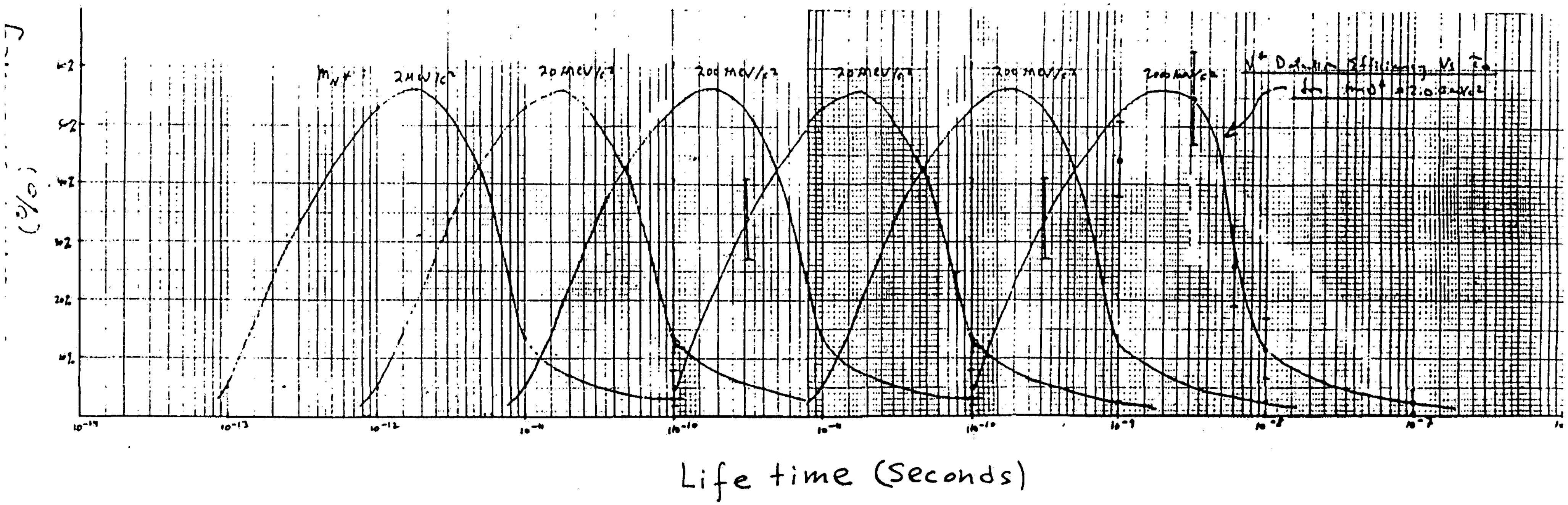

Figure 22

RUN 4394 EVENT 295

$\nu_\mu + N \rightarrow X + \mu \hookrightarrow \mu \gamma$ bremsstrahlung

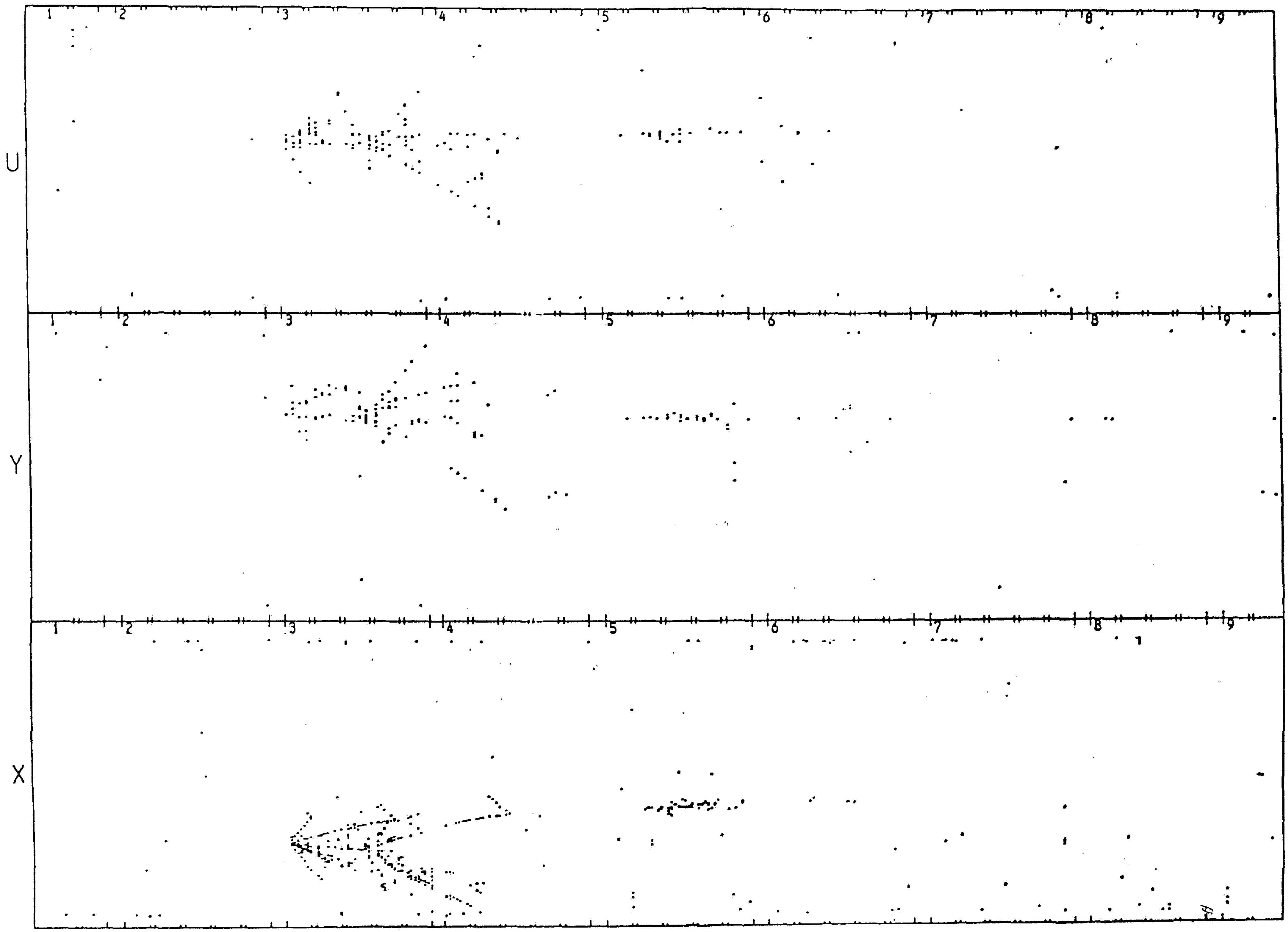

Figure 23

CLEAN DIMUON EVENT

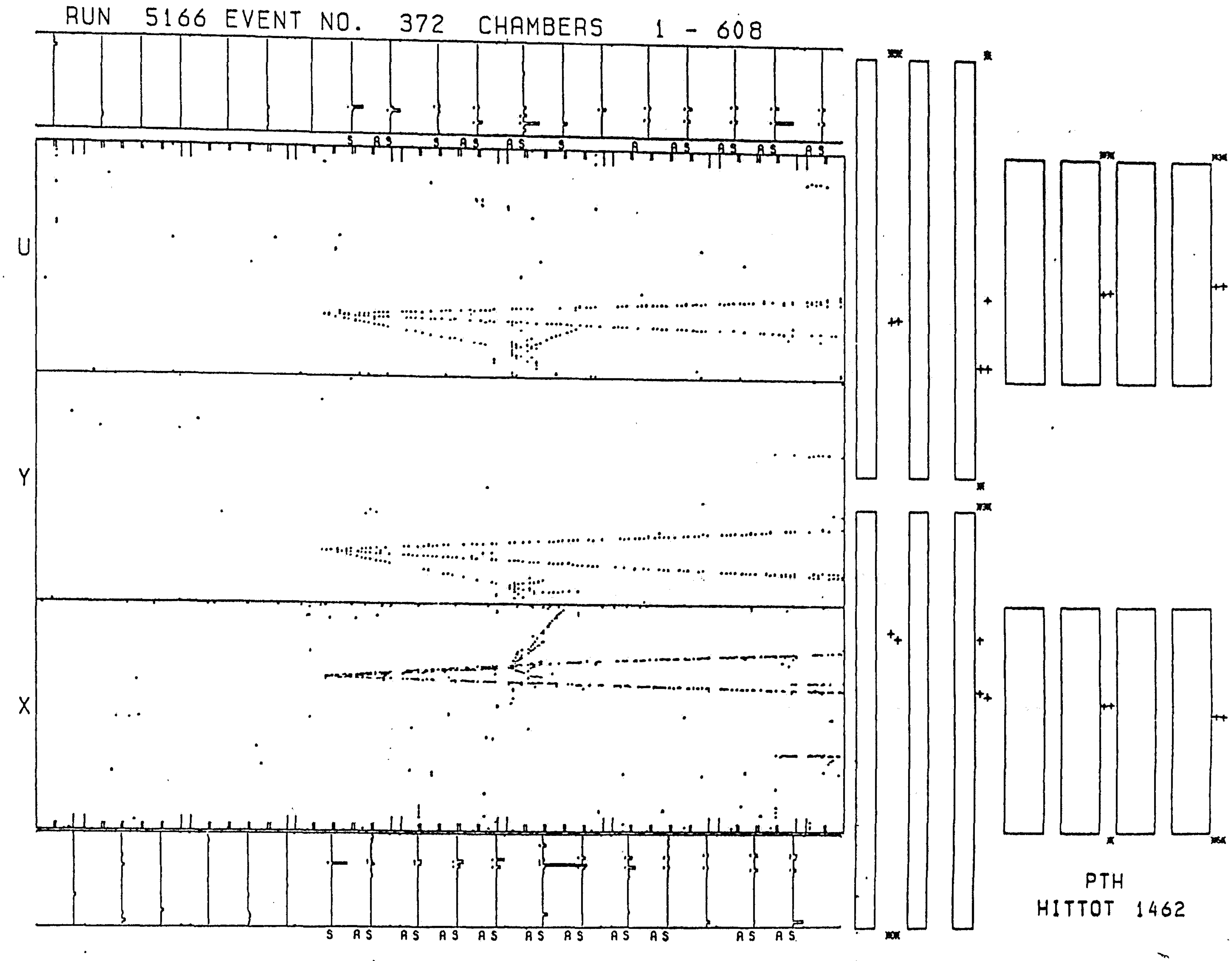

Figure 24

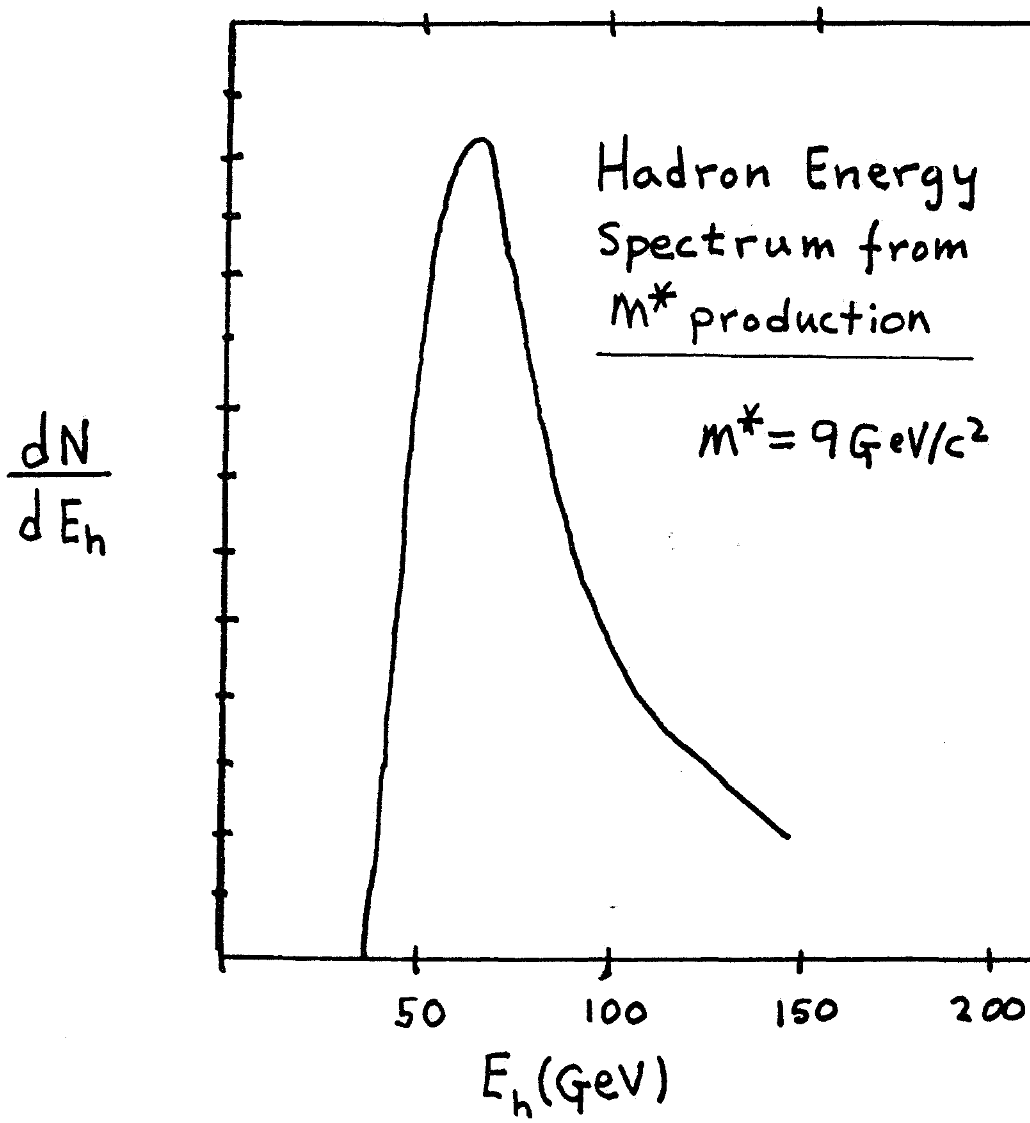

Hadron Energy Spectrum from M^* production
$M^* = 9\ GeV/c^2$
$\frac{dN}{dE_h}$
50
100
150
200
E_h(GeV)

Figure 25

APPENDIX A: THE NCI DICHROMATIC BEAM TESTS

INTRODUCTION

The new dichromatic train[1] was designed to meet a variety of goals:

1. Reach secondary beam momenta up to 750 GeV (x_F=3/4).
2. Dump the non-interacting fraction of the primary proton beam cleanly in external dumps at all secondary momenta.
3. Reduce the wide-band background component of the beam as much as possible (better or at least as well as the old beam).
4. Obtain an energy resolution dE/E approximately 10% at all secondary momenta for radii up to one meter in the neutrino detectors.
5. Obtain the highest flux of secondaries possible while keeping the momentum bite of the beam at approximately 10%.
6. Contain the physical size (both longitudinal and transverse dimensions) of the beam layout in order to minimize costs.

As in all design efforts, some parameters must be optimized at the expense of others. The NCI design was chosen to emphasize increased flux as the most important of the above list, since, even with large mass detectors, the event rates are limited to a few events per pulse. (See Figure A-1, which gives event rates at 1 TeV, as a function of secondary momentum selected.) As a consequence, wide-band background rejection and energy resolution at the detectors are not optimum, but are still within the design goals.

A conceptual layout of the NCI dichromatic beam is shown in Figure A-2. All magnets used in the beam have large apertures (6-3-120 dipoles, and 4-Q-120 and 8-Q-32 quadrupoles) in order to obtain the maximum possible flux.

The beam bends in both the horizontal and vertical planes in order to minimize wide band background; the secondaries only point toward the neutrino detectors when momentum and sign selection are complete.

The first bend after the target (8.67 mr) and the length of drift spaces determine the maximum momentum acceptance of the train, which is about 15%. This parameter was chosen to maximize flux, while still maintaining reasonable energy resolution at the neutrino detectors. The production spectrum at higher secondary momenta reduces the momentum bite of the beam to about 8% at 600 GeV.

Beam defining liners[2] are installed in the first two dipoles after the target. These liners, along with the two collimators shown in the figure, are used to remove off-axis particles which contribute to the divergence of the beam. It is important to minimize the beam divergence in order to provide good energy resolution at the neutrino detectors, and to insure that secondary particle fractions can be measured for a flux determination, using Cerenkov counter techniques.

A large engineering effort went into the design and construction of two 70 ton dump modules[3], to contain the non-interacting fraction of the primary proton beam. These dumps had to be large enough to prevent ground water activation, and to protect workers who may have to work on near-by equipment; but also had to be transportable, since other neutrino beams may be installed in the target hall.

The NCI dichromatic train was assembled in 1983, and installed in Enclosure NW1 for the first 800 GeV run of the Tevatron, in order to get a first look at the properties of the train[4]. For most of this run, the train was used to provided a passive transport for the primary beam to the NWest test beam production target. Some 60 hours were scheduled for dichromatic tests in order to measure the momentum bite and the angular divergence of the train. Accelerator performance and other equipment failures allowed only a fraction of this test time to be obtained. The results of those measurements are detailed in the following sections.

Figure A-3 shows an overall layout of the equipment used for the tests. Intensity information was obtained from a SEM[5] placed in the primary proton beam upstream of the target, and from a large ion chamber[6] placed downstream of the train in the secondary beam. Primary beam shape and position were monitored with SWICs (segmented wire ion chambers) located at the entrance to the target hall (2 mm wire spacing) and just in front of the target (1/4 mm wire spacing). The secondary beam had two SWICs, both located about 1000 feet from the target. These were used in the angular divergence measurement. One SWIC had variable wire spacing[7] (6 mm in the center and 10 mm near the edges). The other SWIC[8] had 0.240 inch copper etched strips separated by 0.040 inch gaps (approximately 7 mm sampling). A differential Cerenkov counter[9] used in the momentum bite determination was at the same z location. Data from all these monitors as well as the currents of all the pre- and post-target magnets were recorded on magnetic tape after each spill.

MOMENTUM BITE MEASUREMENT

Figure A-4 shows a layout of the Cerenkov counter used in this measurement. This counter was constructed to operate in the previous generation dichromatic neutrino beam. Because of the high instantaneous rate of secondary beam particles (about

10^{13} /sec in a 1 msec fast spill), the signal output from the phototube was integrated over the spill time, thus providing a relative measure of beam particle composition. Although these tests used 20 second slow spill and utilized 100 times fewer protons on target/pulse than during previous neutrino data taking, the phototube output was still integrated over the entire spill.

Radiated Cerenkov light follows the optical path shown in Figure A-4. The parabolic mirror M1 has a 305 cm focal length. Located about 5 cm beyond this focal plane is a rotatable disk, labelled 'iris', with a selection of apertures, allowing light of selected angular range to reach the phototube. Annular rings which subtended angular ranges of 0.7-1.0 mr and 1.7-2.0 mr (used in these measurements) as well as a variety of circular penetrations are available. As the pressure of the radiator is increased, the phototube sees Cerenkov light from pions, then kaons and finally protons. The Cerenkov phototube output at each pressure point is then normalized to the secondary beam flux as measured by the ion chamber. The particle fractions are obtained from the relative area under each peak of the response curve as a function of pressure.

Also shown in the figure is a shutter which can be closed so that light produced in the main body of the counter can not reach the phototube. One then has a measure of background light produced outside the radiator, but seen by the phototube. Shutter closed points were taken at a few randomly selected pressures for each momentum. This background is measured to be independent of pressure and has been subtracted from the data to be shown.

One can approximate the Cerenkov relation as:

$$\theta_c^2 = 2KP - (m/p)^2 ,$$

where θ_c is the angle of Cerenkov light, K is the gas constant per unit pressure, P is the pressure of the radiator (here, He gas), and m and p are the mass and momentum of the radiating particle, respectively. Because of the presence of the second term on the right hand side of the above equation, for a beam of finite momentum bite, the larger the mass of the particle, the broader the Cerenkov response. Thus, by measuring the width of the proton peak as a function of pressure, one obtains a measurement of the momentum bite of the beam.

Data were taken at secondary momenta of 200, 400, 500 and 600 GeV, in order to investigate the effects of particle production on the momentum bite. These data are shown in Figure A-5. It should be emphasized that this counter was designed to operate in a lower energy range, and thus is unable to resolve pions from kaons above secondary momenta of approximately 250 GeV.

The results of the momentum bite determination[10] are given in Table A-I, along with the Monte Carlo prediction, as a function of secondary momentum. Errors quoted for the momentum bite are determined by chosing the minimum chi-squared from successive fits as the Monte Carlo input momentum bite was distorted in 2% steps from 96% to 104%. At all secondary momenta, the data are within 2% of the prediction.

It should be noted that an absolute pressure calibration (and thus an absolute momentum determination) was not available. The true pressure was obtained by scaling the measured pressure from the following formula:

$$P_{true} = (P_{meas} + (0.9 +/- 1.4))*(0.880 +/- 0.017) \text{ torr}$$

This is the best average fit to all 4 data sets.

OTHER TESTS USING THE CERENKOV COUNTER

It was found empirically during previous neutrino running with this Cerenkov counter that small adjustments (about 5 cm) to the iris z position relative to the focal plane of the main mirror resulted in improved pion-kaon separation. The reason for this is that the small but finite secondary beam divergence makes it appear as if the beam is originating from a point source in the vicinity of the production target. By the thin lens formula, then,

$$1/f = 1/s + 1/i$$

where f is the focal length of the mirror, s is the source distance, and i is the image distance. Since the source point of this train is at a distance which is large compared to the focal length of the mirror, the sharpest image does not appear precisely at the focal plane, but slightly beyond this point.

Because only a limited amount of time was available for these measurements, the z position of the iris was not adjusted to optimize pion-kaon separation. The NCI beam has a different effective source point than the previous train, and so the iris was not located at the optimum position. Indeed, the counter had been moved several times before this measurement, so that it was decided to fit the iris location by minimizing chi-squared to each of the fits at all secondary momenta. The final value which gave the best overall agreement was Z_{iris} = 303.5 +/- 0.5 cm.

Alignment of the counter relative to the beam can also affect the width of the pion peak, and thus the pion-kaon separation. When time permitted, we did align the counter with the secondary beam by setting the pressure so that the pion light ring was slightly bigger than the iris aperture, and then adjusting both the x and y alignment of the counter to minimize the phototube output.

Since these tests were parasitic, the SWICs in the secondary beam were centered on the line pointing toward the NWest production target, about 0.5 mr off from the line pointing toward the neutrino detectors. It was decided to conduct the measurements with the secondary beam also pointed toward the NWest target, in order to avoid lengthy accesses to move the SWICs. For some of the data, not enough time was available to both align the counter and take a pressure curve, so the counter was aligned parasitically to the 800 GeV primary beam running to the NWest target, and this approximate alignment was used for the pressure curve. Subsequent checks showed that although pion-kaon separation was not optimum, the momentum bite determination was not affected.

As mentioned previously, because of the finite angular divergence of the beam, it appears to originate from a point source near the production target. Because of the specific optical design of this train, the location of the apparent source point of the horizontal plane is at a different z position from that of the vertical plane.

It has been suggested[11] that a third quadrupole located at the end of the train could be used to reduce the difference in the z positions of these apparent source points, and thus give an improved pion-kaon separation. Monte Carlo calculation showed this to be true, giving about a 17% improvement in the effective beam divergence as seen by the Cerenkov counter, with only a 2% degradation in the energy resolution of the neutrino beam at the detectors (see Figure A-6).

Measurements taken with this quad at the theoretical value were indistinguishable from those taken with the quad off. The finite length of the counter (which causes diffraction broadening[9]), non-optimized iris position and approximate alignment could all have contributed to a null result. This measurement should be re-done with the new Cerenkov counter[12] before data taking begins.

Particle fractions determined from these data are given in Table A-II, along with predictions from a particle production model[13]. Only the proton fractions and, at lower momenta, the pion fractions should be taken seriously. Even so, the agreement with prediction is remarkable.

ANGULAR DIVERGENCE MEASUREMENT

Figure A-7 illustrates why it is important to have small angular divergence in a dichromatic beam. For low secondary momenta, the divergence of the beam is a small contributor to the neutrino energy resolution at the detectors compared to the momentum bite of the beam. For momenta in excess of 400 GeV or so, the beam divergence plays an increasingly important part in this energy resolution. In fact, for 600 GeV secondaries, a 0.2 mr divergence produces an unacceptably large resolution at large detector radii, even for a beam with no momentum spread. In addition, if one uses a Cerenkov counter to determine particle fractions in the beam for a flux determination, small angular divergence is crucial for pion-kaon separation.

As part of the initial set of tests of the new dichromatic train, it was thus appropriate to measure the angular divergence of the beam. The technique used is graphically shown in Figure A-8. A (16 inch x 16 inch) 10 foot long steel collimator[14] with a 1/2 inch square hole running down its axis was placed in the path of the secondary beam just before the final set of bending magnets. The collimator was aligned parallel to the trajectory of the central ray. The size of the beam at this point was approximately 6 inches high by 3 inches wide, primarily determined by upstream magnet apertures. This collimator (called the Hole Collimator) was swept across the beam horizontally in 1/4 inch steps and vertically in 1/2 inch steps, sampling small segments of the beam phase space at each position. (Originally it was also planned to utilize 1/4 inch steps vertically, but time did not permit this fine a grid search.)

Located about 825 feet downstream from the Hole Collimator in the Expansion Port were two SWICs, where beam profiles from each individual grid point were recorded, along with primary and secondary beam intensities. Because of inherent design features in the SWIC readout system, 5 scans in time were taken across the spill. Figure A-9 shows these scans for one of the SWICS on a collimator out spill. Scans 2-4 were subsequently combined for this analysis. Because the distance between the Hole Collimator and the SWICs was so large, one can effectively think of each grid point as a point source of particles, and thus the spatial distributions measured by the SWICs can be tranformed into horizontal and vertical angular distributions of rays from each sampled region of the beam. The individual angular distributions, weighted by the intensity in the secondary beam for each point, can then be combined to give a measure of the total angular divergence of the beam. This technique has been used in the past[15] to measure the angular divergence of a previous dichromatic beam.

Several problems complicated this measurement:

1. Monte Carlo study has shown that the angular divergence of the secondary beam is a strong function of the proton beam spot size on target. Figure A-10 shows that this effect is much stronger for a large horizontal extent of the beam than it is for a large vertical extent. Indeed, for horizontal beam sizes

above 1 mm (half width at the base), the divergence rises linearly with beam size. Unfortunately for these measurements, the pre-target optics were constrained by the slow spill test beam program, and the spot size on target was limited to approximately 3 mm H x 1.5 mm V, (see Figure A-11). Subsequent to taking this data, the switchyard optics have been re-done. With this new optics, a horizontal spot size of less than 1 mm can be achieved. Because of this inherent problem, final results for the angular divergence of the beam can not be stated, as they are so strongly coupled to the horizontal beam spot size. Instead results will be presented comparing the data to a Monte Carlo which also had a comparable proton beam spot size.

2. As had been mentioned previously, these data were taken with the secondary beam pointed toward the NWest production target. The bend needed to steer the beam this direction introduced an additional small angular divergence to the beam. This effect was included in the Monte Carlo calculations for purposes of comparison.

3. Because of the large mass of the Hole Collimator, several support mechanisms were attempted before one was found which allowed the collimator to retain the same spatial alignment over its entire field of travel. The final modification was made in situ, and was such that the bottom 1/2 inch of the beam phase space could not be measured. This will be corrected for

future studies. In addition, the final support system was installed near the end of the run, when accelerator failures were increasing due to lead problems in the super-conducting magnets. These time constraints, along with proton economic constraints, limited data taking to one 8-hour scan.

4. It was discovered prior to the Hole Collimator scan that the stepping motor control circuitry for positioning the collimator was strongly temperature dependent, and thus led to a day-night difference in actual movement for a fixed number of input steps (see Figure A-12). Since it was important to sample the beam phase space uniformly, a C-BASIC program was written which operated on the EPICS control system and used the position read-back to correct for this temperature dependence. This technique worked extremely well. For future studies, however, the control electronics should be modified to correct this complication.

5. Probably the most serious problem encountered which compromises analysis of these data is the lack of redundancy in beam monitors. Part way through the scan, electronics associated with the ion chamber (the secondary beam intensity monitor) failed in such a way that the outputs for both the signal and for an off-spill pedestal varied by several times the typical signal level (see Figure A-13). Since these fluctuations were so large, only approximate point to point normalization is possible. This anomaly is evident in about

1/3 of the data taken. At the time, the variation in beam intensity was attributed to mis-steering of the primary beam, as no other monitors were available for cross-check. Time ran out before the affected part of the scan could be repeated once the electronics had again stabilized. In addition, the 6 mm SWIC located in the Expansion Port did not give reliable profiles (many missing wires) at the low intensities encountered during the scan. Thus, this analysis is done solely with the 7 mm strip SWIC.

6. Proton economics also contributed to the complexity of this analysis. Initial calculations showed that about 5 10^{12} protons per pulse were the minimum needed for the scan. Most of the data were taken at about 2 10^{12} protons per pulse. Figure A-14 shows the signal to noise inherent in the data for a point near the edge of the beam phase space, where the intensity is quite low relative to the center of the beam. More protons would have enhanced the signal to noise, however, low intensity points such as this one may never be analyzable. It should be noted that in addition to a beam-off pedestal pattern made by averaging over all beam-off pulses in the course of the scan, a flat background was subtracted from each SWIC display before comparing the data to Monte Carlo prediction. For asymmetric profiles, this will introduce a bias in the tails of the distributions. Probably more sophisticated background methods can also be developed in

future, utilizing a different background level for each side of the peak.

7. The Hole Collimator was not located at the end of the train where the beam is most parallel, in order to utilize the B-dl provided by the final set of dipoles to sweep away any off-momentum particles created by scraping in the collimator. At this intermediate location, the beam still has some divergence, so that not all of the particles which enter the upstream of the collimator aperture are transmitted through to the end. Unless one is able to use a grid whose steps are smaller than the hole size, one obtains an under-estimate of the beam divergence. Time constraints did not permit 1/4 inch sampling in the vertical direction. To compensate for this, the Monte Carlo calculations included a cut on the positions of the rays at the downstream end of the collimator in order to simulate this effect. In future, more points can be taken, or a shorter collimator (of Tungsten) can be used.

For purposes of presentation, the data were divided into 9 roughly equally populated regions in x and y. Figure A-15 shows this division. A representative individual point from each of the 9 regions is shown in Figure A-16 (a-i), along with the Monte Carlo predictions for a 1 mm and a 3 mm horizontal proton beam spot size on target. As can clearly be seen in the figures, the 3 mm spot more closely approximates the data.

Also evident is the increase in the beam divergence, in both the horizontal and vertical planes, for the larger spot size.

Because of the problems inherent in background subtraction, a measure of the width of each curve should provide a more meaningful comparison between the data and the Monte Carlo prediction than the tails of these distributions. For each grid point, both the data and the corresponding Monte Carlo distributions were fit with a gaussian. The ratio of the sigmas of these two fits provided the figure of comparison.

Table A-III shows this ratio averaged over each of the nine regions for both the vertical and horizontal planes. The data and the prediction are seen to agree within about 10% for the horizontal plane, and within about 35% for the vertical plane, with the horizontal plane data being slightly smaller than the prediction, and the vertical plane data being larger than the prediction. Figure A-17 shows a sum over all 9 regions of these ratios, both unweighted, and with each grid point weighted by its intensity as seen by the ion chamber.

It is possible that a quadrupole had been incorrectly set during the scan. A subsequent study of the magnetic field in one of the 4-Q-120 quadrupoles from the train showed that the B vs I response of the quad was within 2% of the theoretical value. It was discovered, however, that the transducer used to measure the current in the quad had a non-linear response for small currents compared to a precision shunt which gave a linear response with input setting (see Figure A-18). An incorrect current in this quadrupole of up to 10% can not be ruled out. Indeed, a Monte Carlo run with a 3 mm horizontal spot and 7.5% less current than design gave slightly better agreement with the data (see Figure A-19). The readouts for all power supplies on the train will be modified for the next run to better measure the actual current.

SUMMARY

The initial tests of the NCI dichromatic train showed that the momentum bite was within 2% of design. Though the data is by no means definitive, the particle fractions measured at 800 GeV are reasonably close to those predicted from 400 GeV data. A first look at the angular divergence of the beam showed it to be within 10% of design in the horizontal plane and about 35% greater than design in the vertical plane. Several problems were discovered which will be corrected before the next run.

References

1. L. Stutte, "Further Design Studies for a Tevatron Era Dichromatic Beam", Fermilab technical memo TM-1091, 1982.

2. Magnet inserts NC1W-1,2, Fermilab drawings 2920-ME-162416,7.

3. Beam dump assembly, Fermilab drawing 2910.100-ME-162243.

4. Participants in these measurements were D. Owen, Michigan State University, and S. Pordes, P. Rapidis and L. Stutte, Fermilab.

5. Secondary Emission Monitor, made by L. N. D. Inc., 3230 Lawson Blvd., Ocean Side, New York, 11572.

6. R. Blair, et al, "Monitoring and Calibration System for Neutrino Flux Measurement in a High-Energy Dichromatic Beam", Nucl. Instr. and Meth. Phys. Res. Sect. 226 ,281 (1984).

7. Expansion Port SWIC, Fermilab drawings 2963-ME-108706,7.

8. Expansion Port strip SWIC, Fermilab drawing 2932-MD-162134.

9. A. Bodek, et al, "Observation of Light Below Cerenkov Threshold in a Short Cerenkov Counter", Zeit. fur Phys. C, 18 ,289, (1983).

10. The analysis of the Cerenkov data was carried out by J. Marko, MIT.

11. F. Sciulli, private communication.

12. F. Borcherding, "A Cerenkov Counter Design for a High Energy, High Intensity, Secondary Beam", Fermilab technical memo, in preparation, March 1986.

13. A. J. Malensek, "Empirical Formula for Thick Target Production", Fermilab note FN-341, 1981.

14. Hole Collimator, Fermilab drawing 9208.050-ME-201032.

15. C. Haber, "A Search for the Inclusive Oscillations of Muon Neutrinos", Ph.D. Thesis, Columbia University, 1985.

TABLE A-I.

Momentum Bite Measurement

Train Momentum GeV	Measured Momentum Bite %	Predicted Value %
200	14.1 +/- 0.3	13.8
400	11.1 +/- 0.3	11.4
500	10.4 +/- 0.3	10.2
600	8.9 +/- 0.3	8.7

TABLE A-II.

Particle Fractions (pion:kaon:proton)

Train Momentum Gev	Measured Fractions %	Predicted Values %
200	58.6 : 5.7 : 35.7	57.9 : 6.6 : 35.5
400	20.2 : 1.6 : 78.5	19.5 : 3.1 : 77.4
500	7.8 : 1.0 : 91.2	8.1 : 1.6 : 90.4
600	2.1 : 0.6 : 97.2	2.8 : 0.7 : 96.4

TABLE A-III.

Comparison of Data/ 3 mm Monte Carlo

for the Angular Divergence of the Beam

VERTICAL

	EAST	CENTER	WEST
TOP	1.30	1.34	0.80
CENTER	1.43	1.53	1.28
BOTTOM	1.31	1.43	1.13

HORIZONTAL

	EAST	CENTER	WEST
TOP	1.27	1.11	1.09
CENTER	1.03	1.09	0.81
BOTTOM	0.99	0.99	0.80

Figure Captions

Figure A-1: Neutrino event rates (cc + nc) per hundred tons per 10^{13} protons in a detector of 1.35 m radius located at Lab C. Rates are shown for pion and kaon (+/-) parents as a function of parent momentum for 1 TeV on target.

Figure A-2: Layout of the NCI dichromatic train, vertical and horizontal projections. The third quad located at the end of the train, used in some of the Cerenkov counter tests, is not shown.

Figure A-3: Layout of the Neutrino area from NW1 to the end of the decay pipe, showing the location of the NCI dichromatic train and various monitors used in the test.

Figure A-4: Schematic of the Cerenkov counter used in the tests.

Figure A-5: Various pressure curves taken during the tests, for 200, 400, 500 and 600 GeV secondaries. The 200 and 400 GeV curves were taken with the 2 mr iris, while the 500 and 600 GeV curves used the 1 mr iris.

Figure A-6: Effects on the actual secondary beam divergence and the effective divergence as seen by a Cerenkov counter placed at two different z locations, as a function of field in a third quadrupole located at the end of the train.

Figure A-7: Energy resolution versus radius at the detectors of neutrinos from kaon decay as a function of secondary beam divergence and momentum bite, for secondary momenta of 400 and 600 GeV.

Figure A-8: Schematic of the Hole Collimator measurement, showing the 10 foot collimator with the 1/2 inch square aperture used to select small segments of the beam phase space, the ion chamber used to measure secondary beam intensity, and the strip SWIC located at the Expansion Port where beam profiles were accumulated as a function of collimator position.

Figure A-9: Five separate SWIC scans during one accelerator spill from the strip SWIC, showing the entire beam profile. (Hole Collimator out data).

Figure A-10: Secondary beam divergence as a function of spot size on target shown separately for increasing horizontal (H) and vertical (V) size.

Figure A-11: Proton beam spot size on target for these tests, as recorded by a 1/4 mm SWIC located 0.5 feet in front of the target. Note the 2 hot wires on the vertical display and the missing wires in both the horizontal and vertical displays.

Figure A-12: Variation in the Hole Collimator motion for a fixed step size as a function of time, showing the temperature dependence of the positioning electronics.

Figure A-13: Variation of the pedestal signal from the ion chamber as a function of time. Plotted for reference is the Hole Collimator horizontal position, indicating about 4 of the 12 scans were affected.

Figure A-14: Vertical and horizontal SWIC pictures and the corresponding Monte Carlo predictions for a low intensity point during the Hole Collimator scan.

Figure A-15: The division of grid points taken during the Hole Collimator scan into 9 aggregate regions.

Figure A-16 (a-i): Vertical and horizontal SWIC pictures selected at random from each of the nine regions. Also included are Monte Carlo predictions for the corresponding Hole Collimator positions, showing separately the predictions for a 1 mm horizontal and a 3 mm horizontal proton beam spot size on target. Note the hot wires at the right side of some of the vertical traces. This affected about 2/3 of the data, and was subtracted for the analysis.

Figure A-17: Histograms of the ratios of sigmas of fits to data divided by sigmas of fits to the 3 mm Monte Carlo cut to simulate the same Hole Collimator position, summed over all collimator positions, for vertical and horizontal data, separately. Data are entered unweighted (left graphs) or weighted by the secondary beam intensity observed for each point (right graphs).

Figure A-18: Nonlinearity in the current readout as a function of current for one of the train quadrupoles.

Figure A-19: Ratios of sigmas of fits to data / fits to a 3 mm Monte Carlo which also has one of the train quadrupoles set to 7.5% less current than design: vertical and horizontal, unweighted and weighted by beam intensity. The high tail on the vertical histograms arises mainly from the bottom sections of the scan.

Figure A-1.

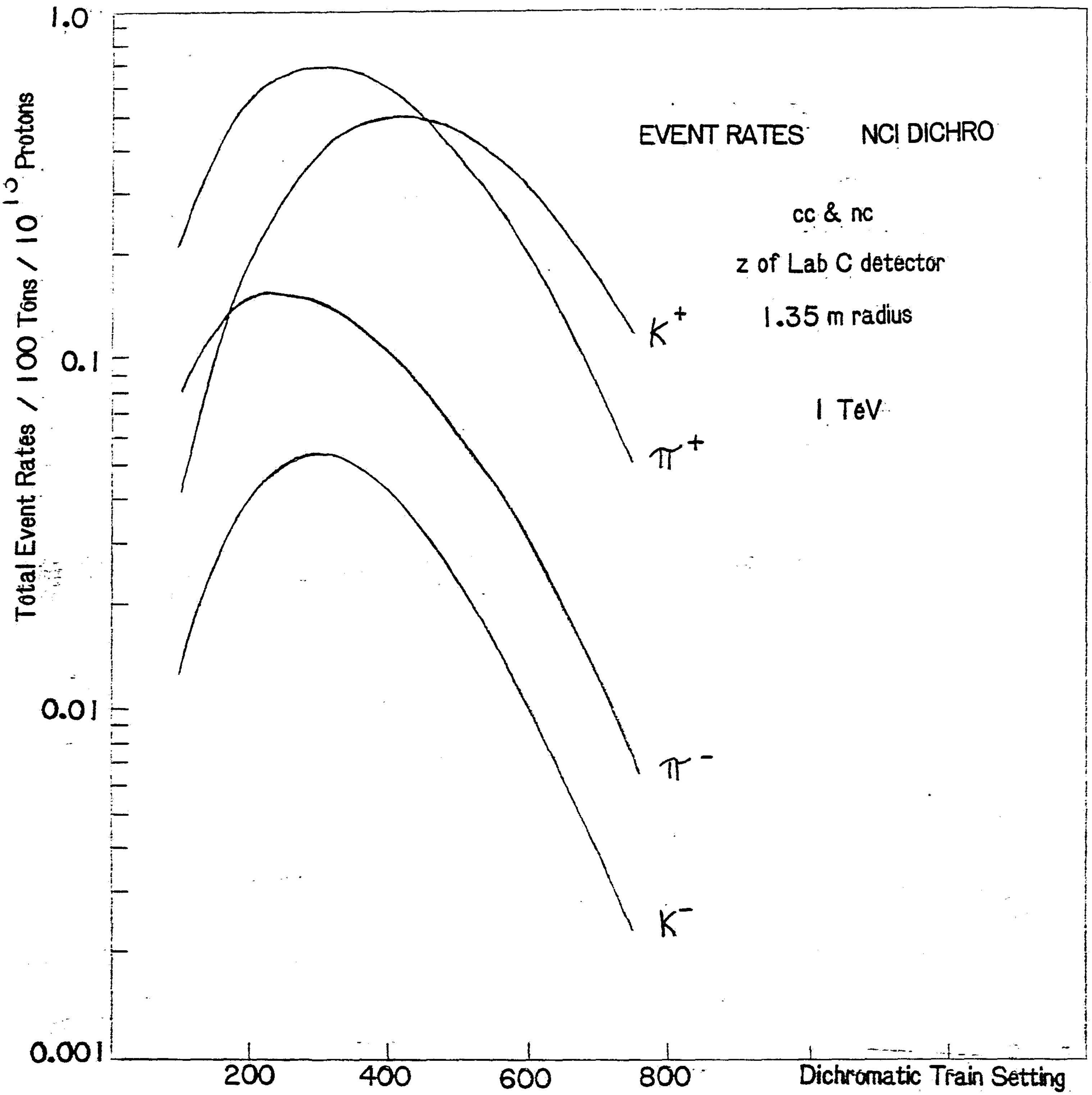

EVENT RATES NCI DICHRO
cc & nc
z of Lab C detector
1.35 m radius
1 TeV
K^+
π^+
π^-
K^-
1.0
0.1
0.01
0.001
200
400
600
800
Dichromatic Train Setting
Total Event Rates / 100 Tons / 10^13 Protons

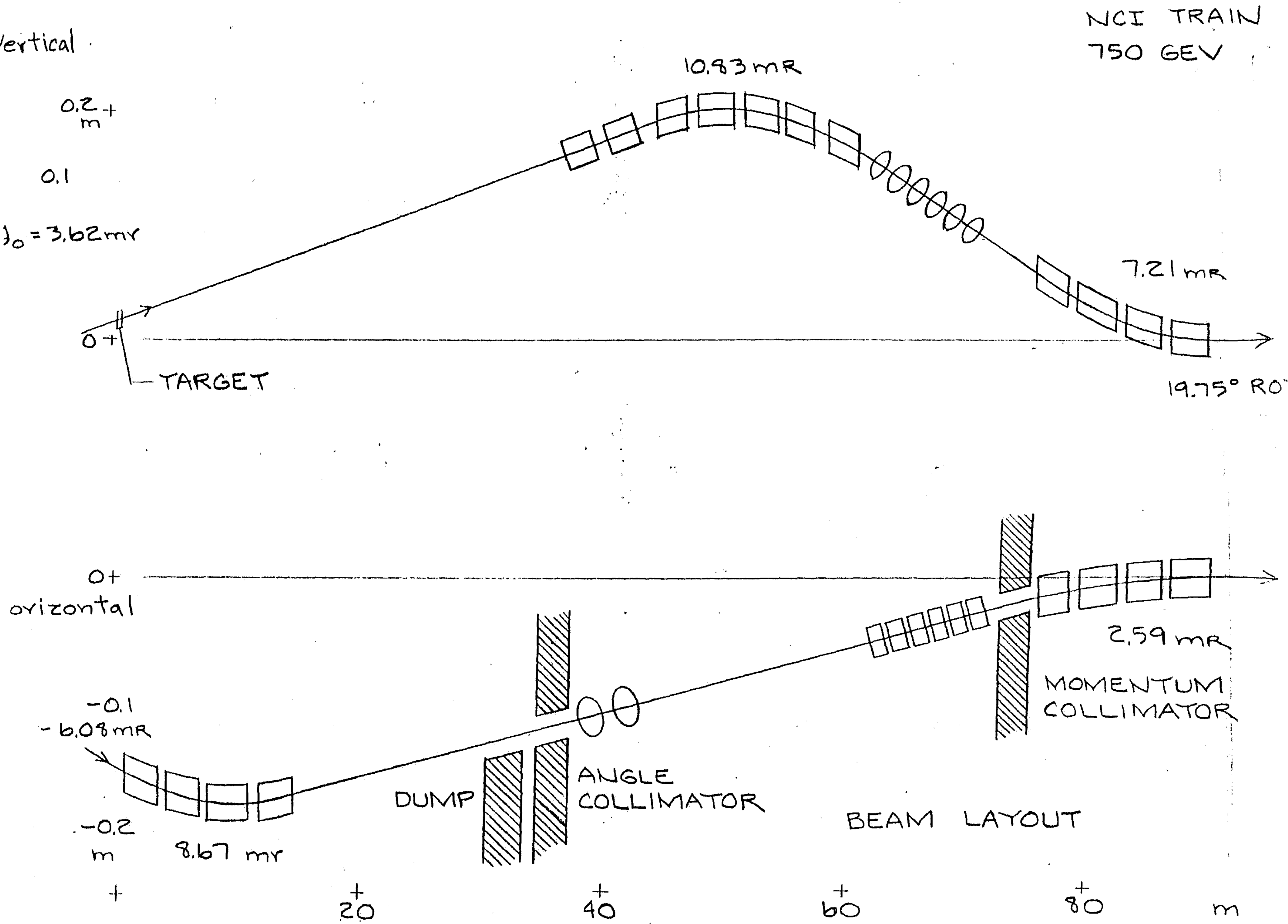
NCI TRAIN
750 GEV
Vertical
10.83 mR
0.2 m
0.1
=3.62mr
7.21 mR
0
TARGET
19.75° RO
0
Horizontal
2.59 mR
MOMENTUM
COLLIMATOR
-0.1
-6.08 mR
ANGLE
COLLIMATOR
DUMP
BEAM LAYOUT
-0.2
m
8.67 mr
20
40
60
80
m

Figure A-2.

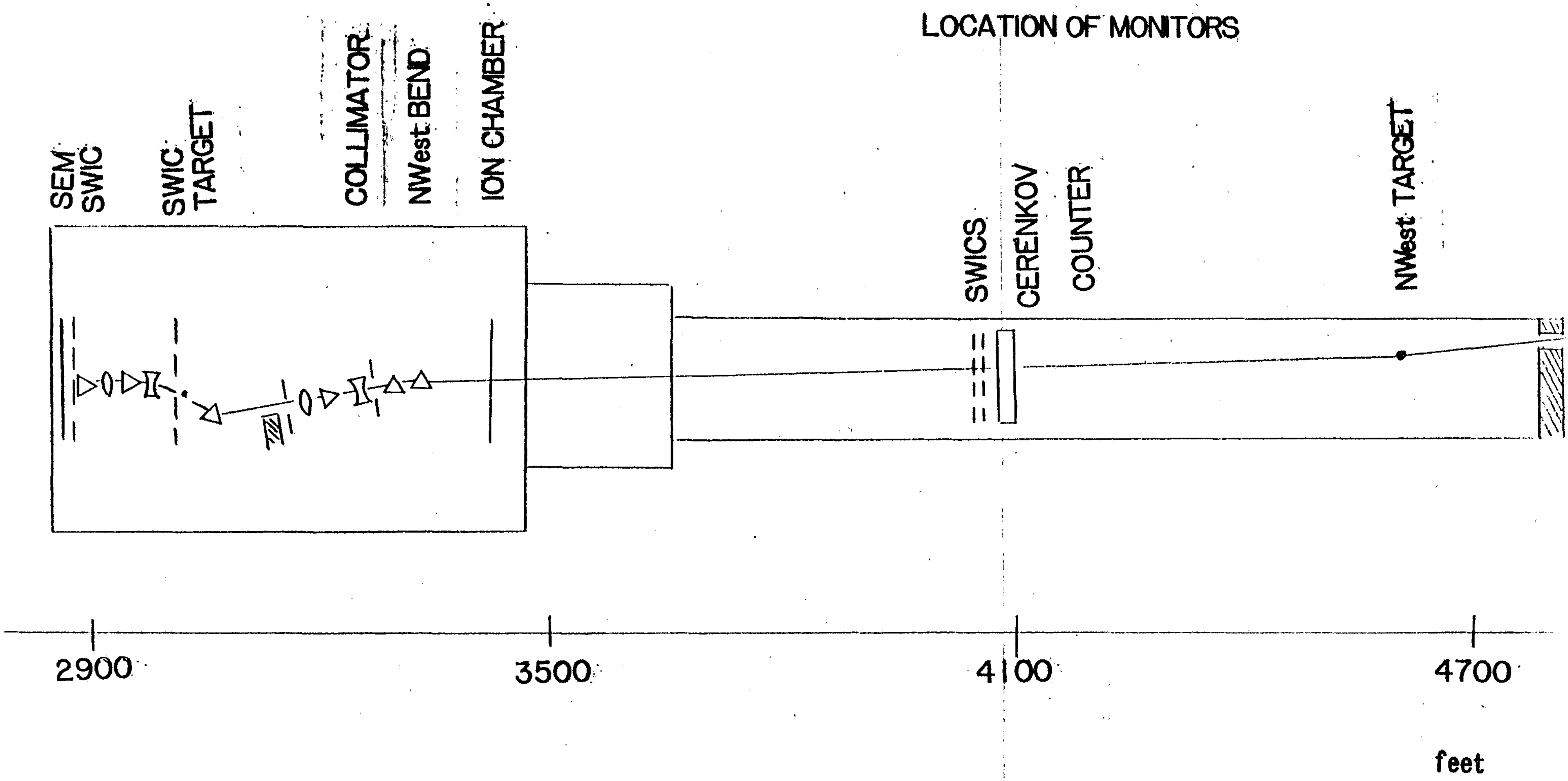
LOCATION OF MONITORS
SEM
SWIC
SWIC
TARGET
COLLIMATOR
NWest BEND
ION CHAMBER
SWICS
CERENKOV
COUNTER
NWest TARGET
2900
3500
4100
4700
feet

Figure A-3.

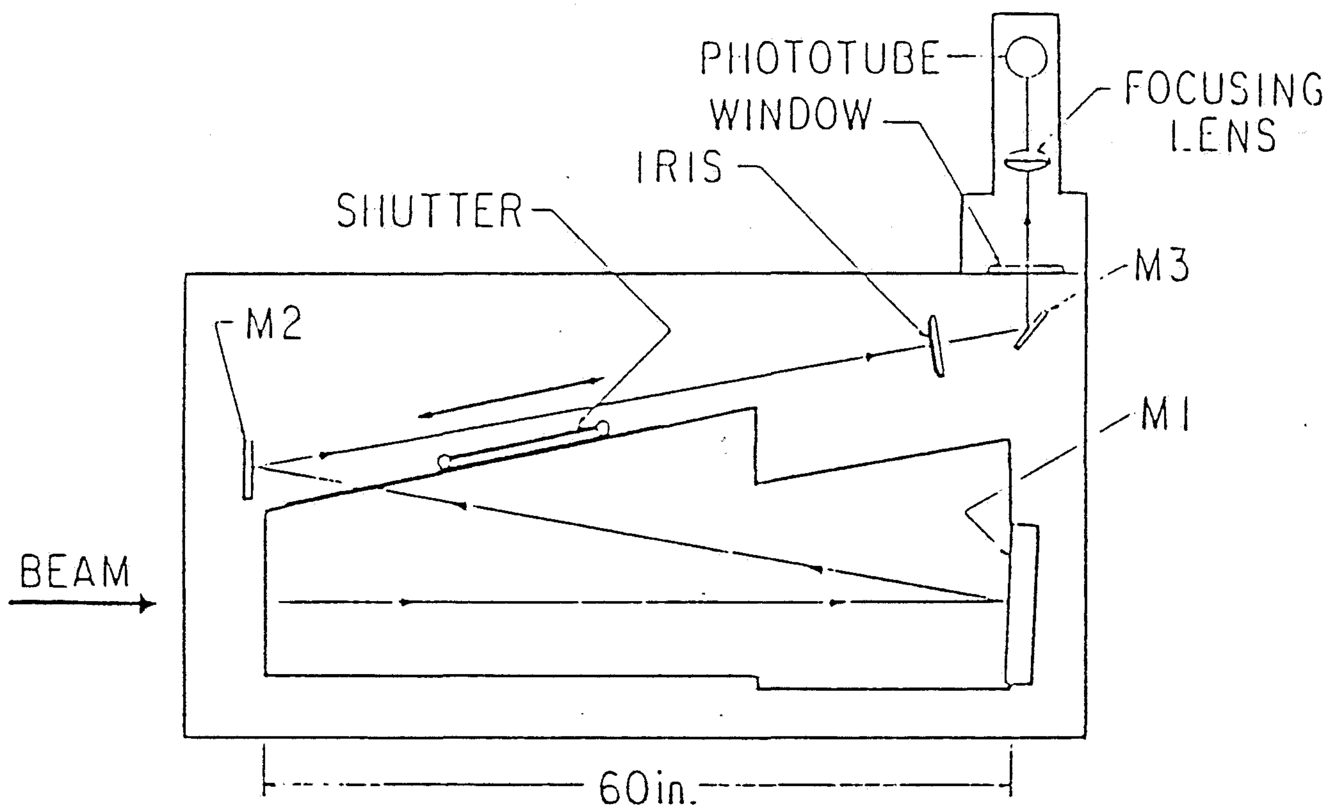

Cerenkov Counter used in the tests

Figure A-4.

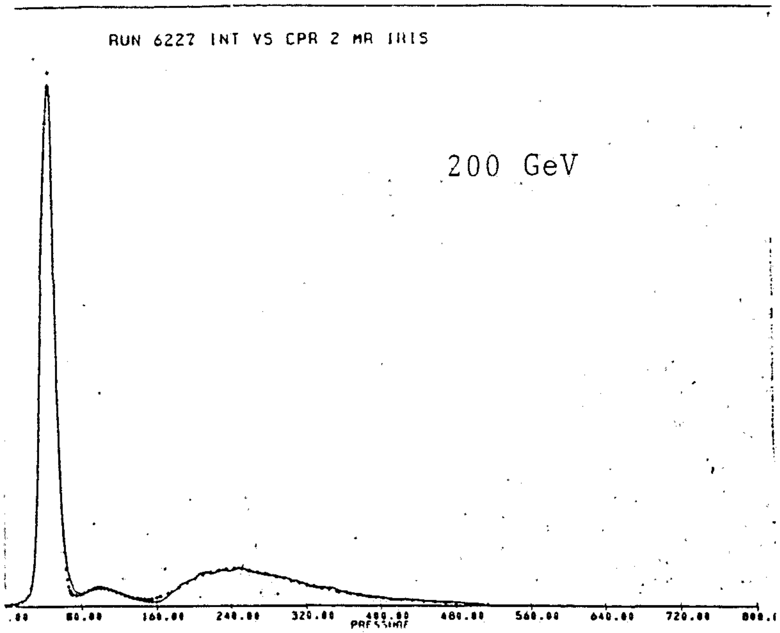

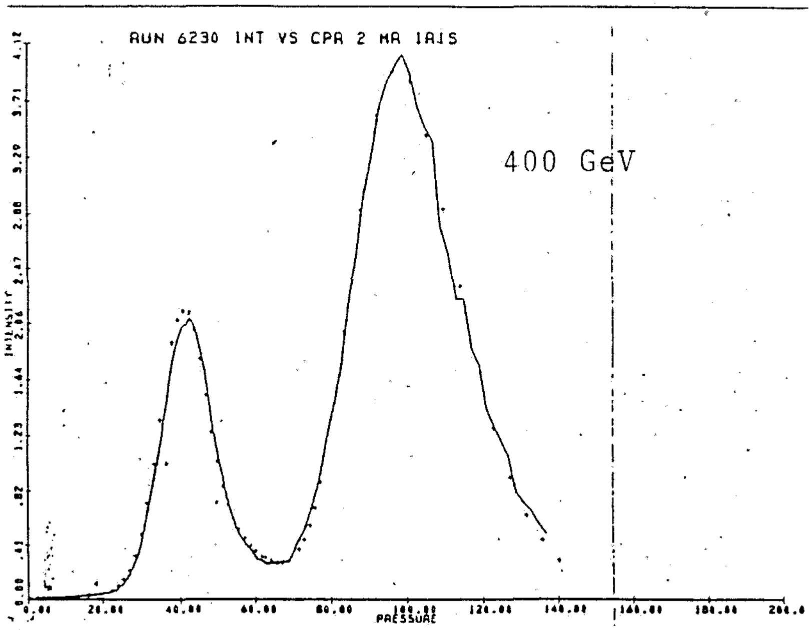

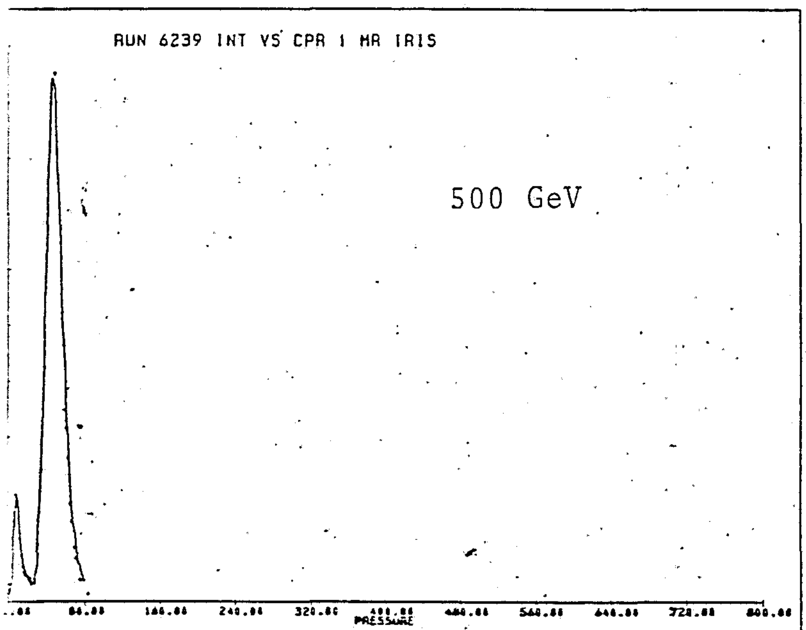

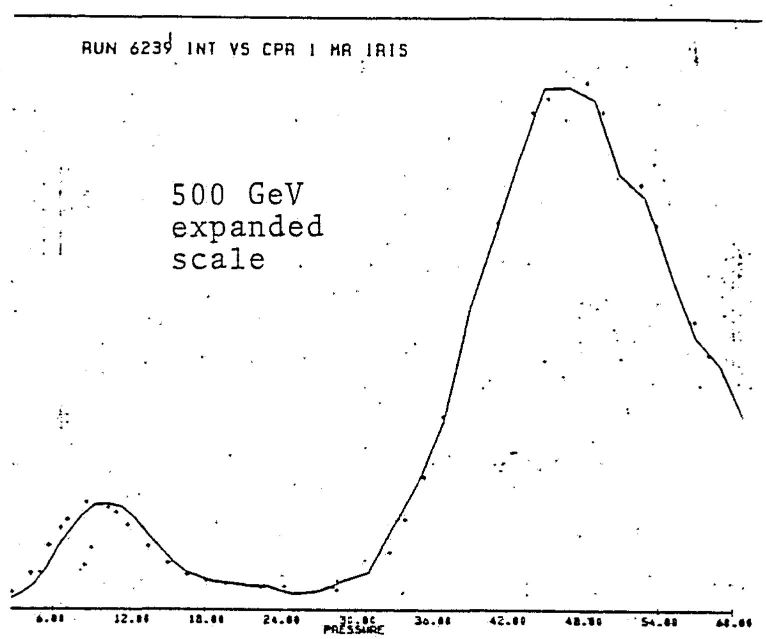

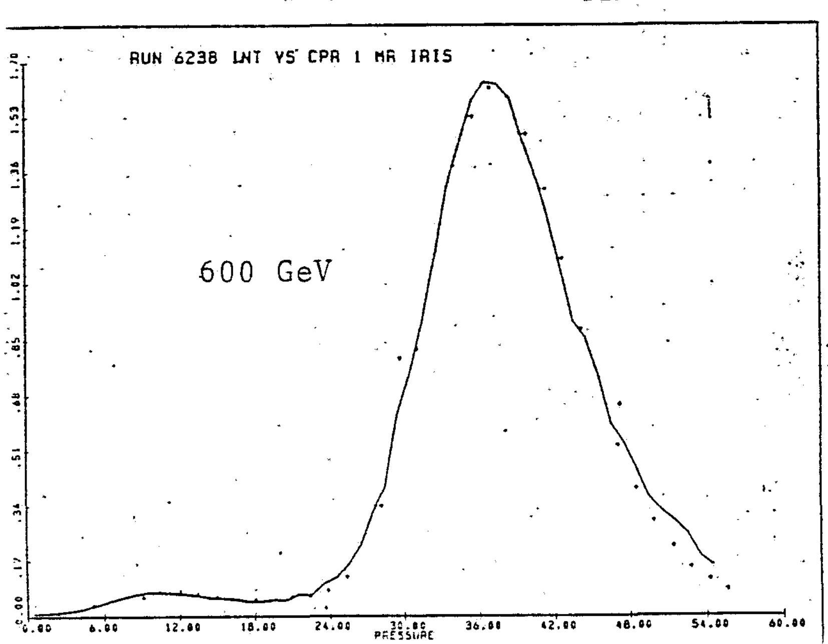

Pressure curves taken with the 5' Cerenkov counter.

Figure A-5.

ADDITION OF A THIRD QUAD AT THE END OF THE TRAIN

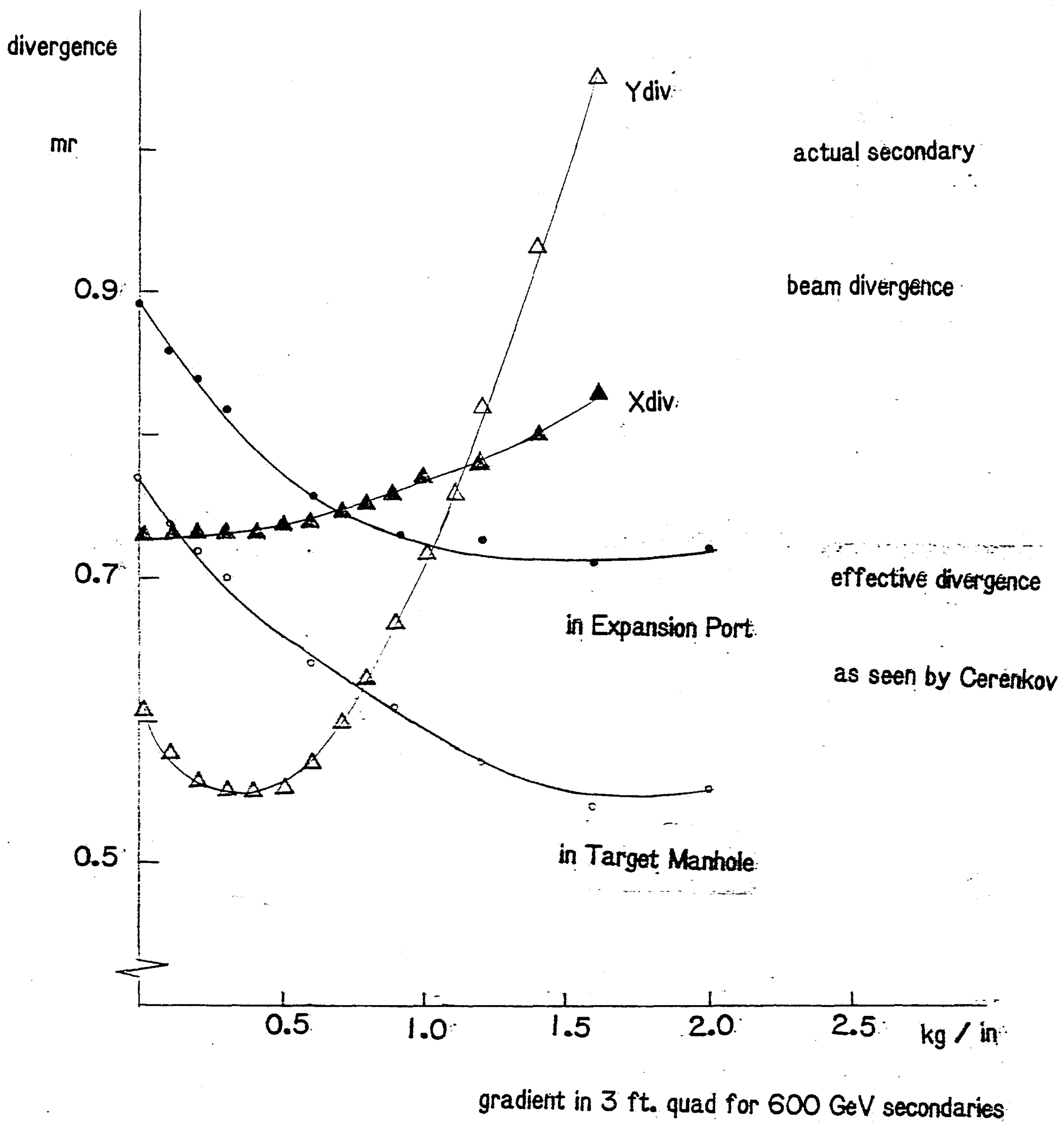

Figure A-6.

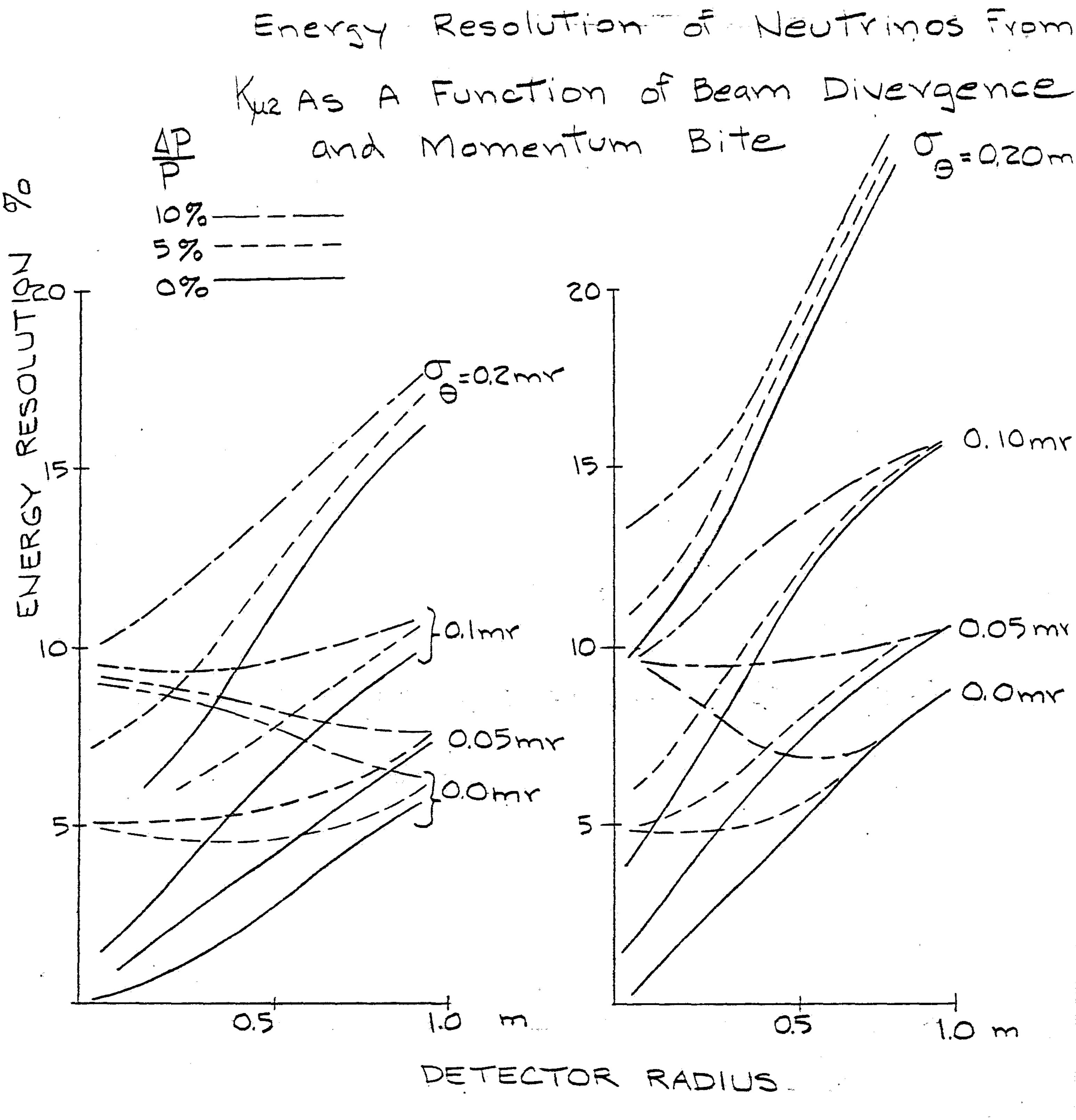

Energy Resolution of Neutrinos From
Kμ2 As A Function of Beam Divergence
and Momentum Bite
ΔP/P
10%
5%
0%
ENERGY RESOLUTION %
20
15
10
5
σθ=0.2mr
}0.1mr
0.05mr
}0.0mr
0.5
1.0 m
σθ=0.20mr
0.10mr
0.05mr
0.0mr
0.5
1.0 m
DETECTOR RADIUS

Figure A-7.

Figure A-8.

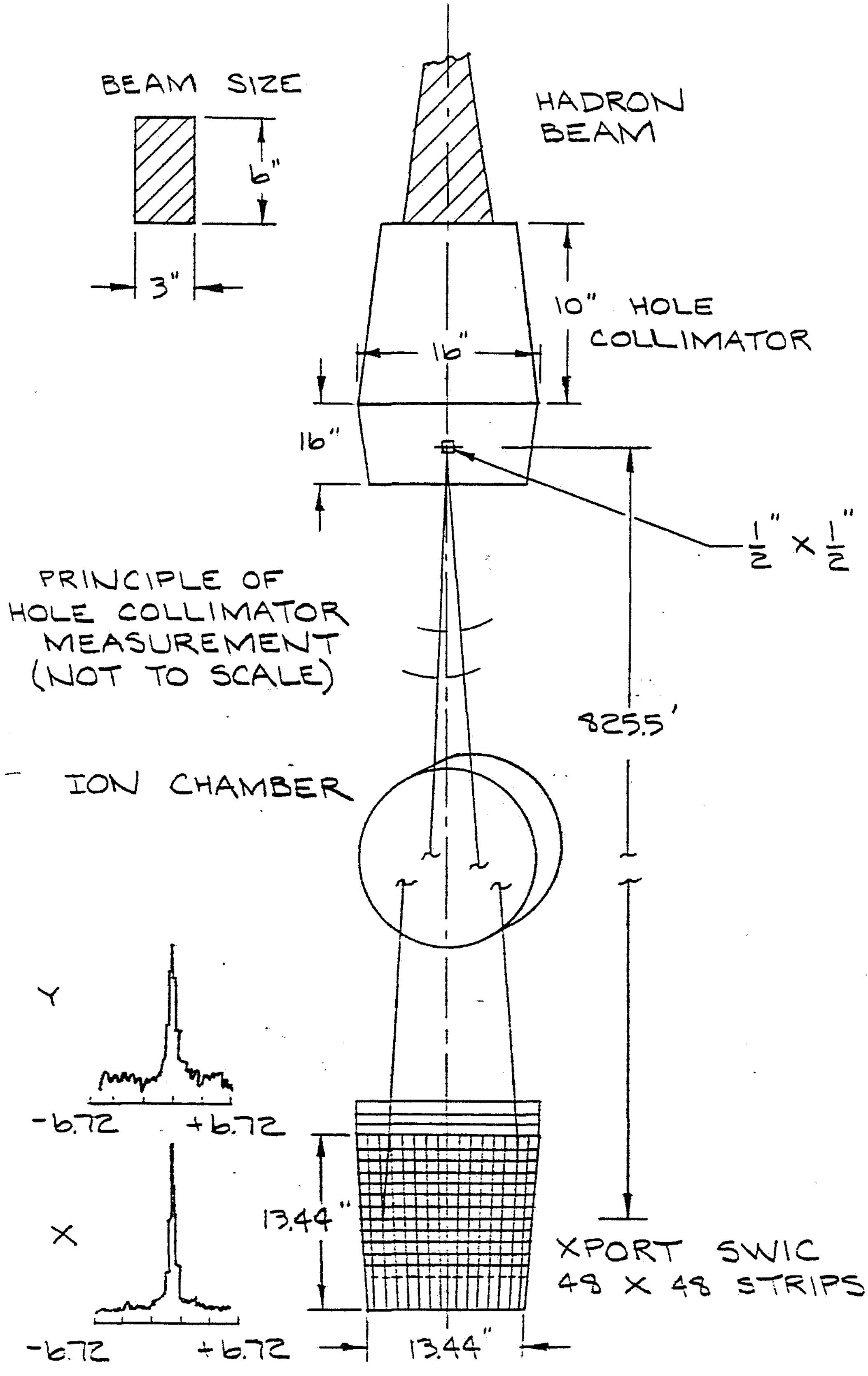
BEAM SIZE
6"
3"
HADRON BEAM
10" HOLE COLLIMATOR
16"
16"
1/2" x 1/2"
PRINCIPLE OF HOLE COLLIMATOR MEASUREMENT (NOT TO SCALE)
825.5'
ION CHAMBER
Y
-6.72
+6.72
X
-6.72
+6.72
13.44"
XPORT SWIC 48 X 48 STRIPS
13.44"

Figure A-9.

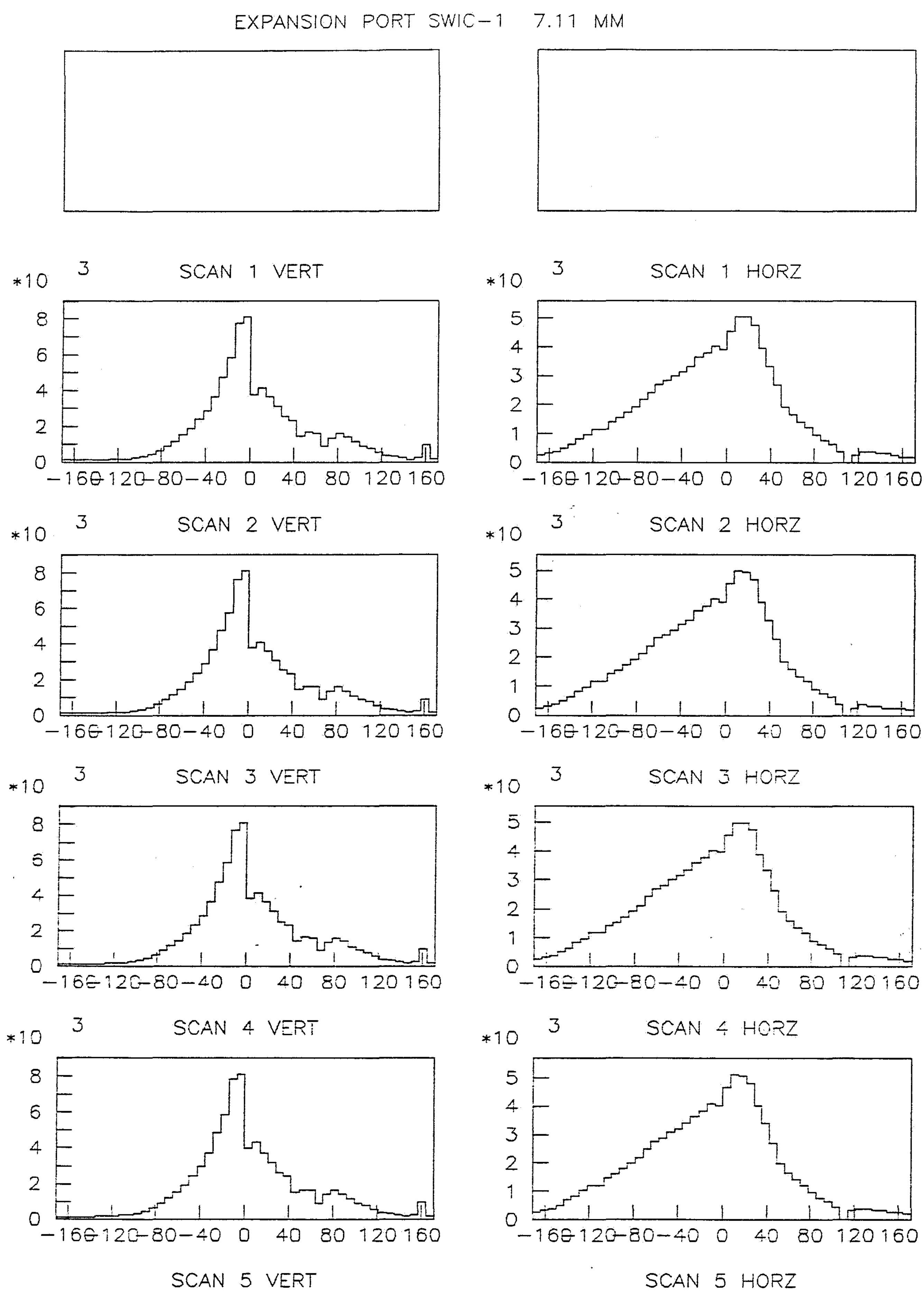

EXPANSION PORT SWIC-1 7.11 MM
*10 3
SCAN 1 VERT
SCAN 1 HORZ
SCAN 2 VERT
SCAN 2 HORZ
SCAN 3 VERT
SCAN 3 HORZ
SCAN 4 VERT
SCAN 4 HORZ
SCAN 5 VERT
SCAN 5 HORZ
0 2 4 6 8
0 1 2 3 4 5
−160 −120 −80 −40 0 40 80 120 160

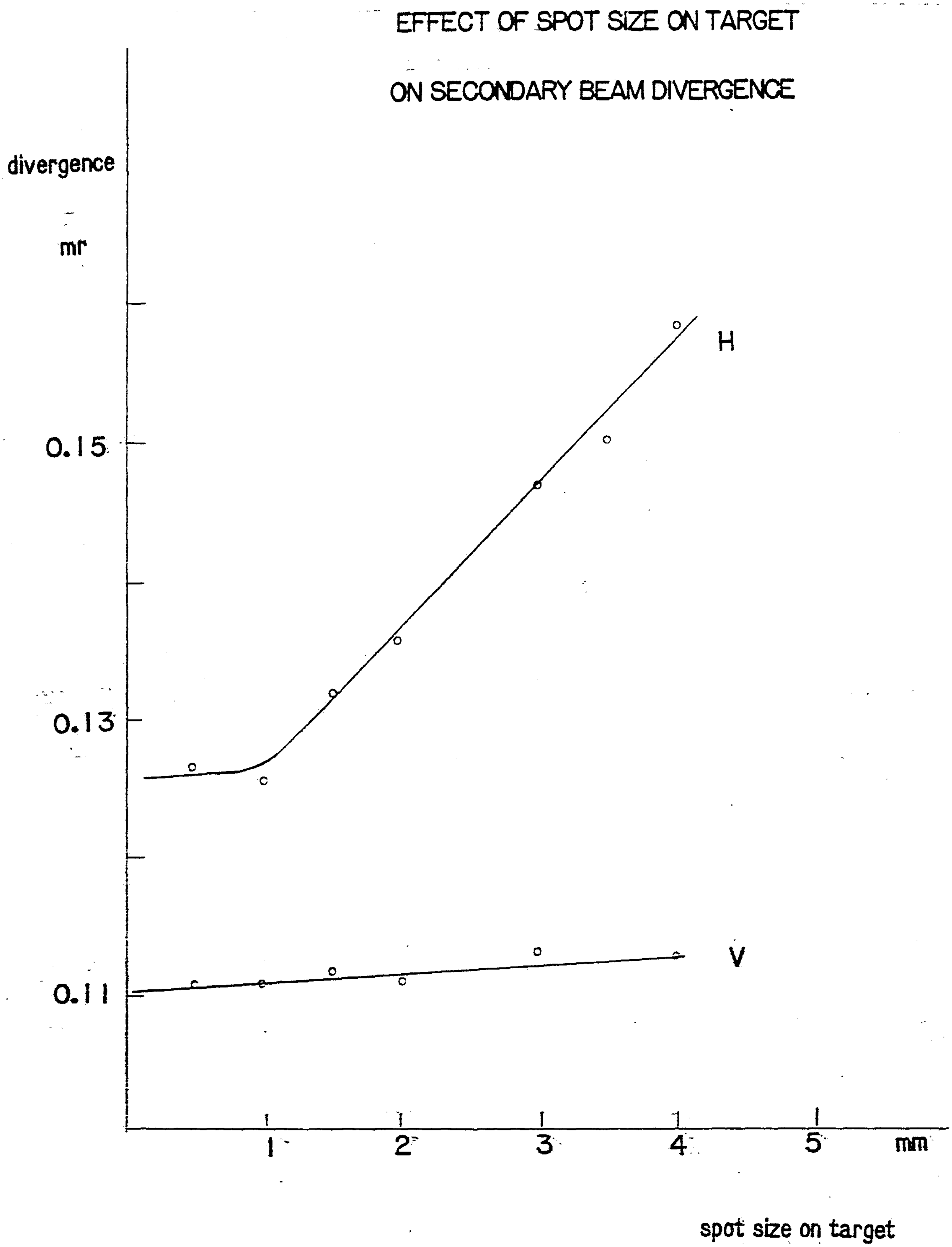
EFFECT OF SPOT SIZE ON TARGET
ON SECONDARY BEAM DIVERGENCE
divergence
mr
0.15
0.13
0.11
H
V
1
2
3
4
5
mm
spot size on target

Figure A-10.

Figure A-11.

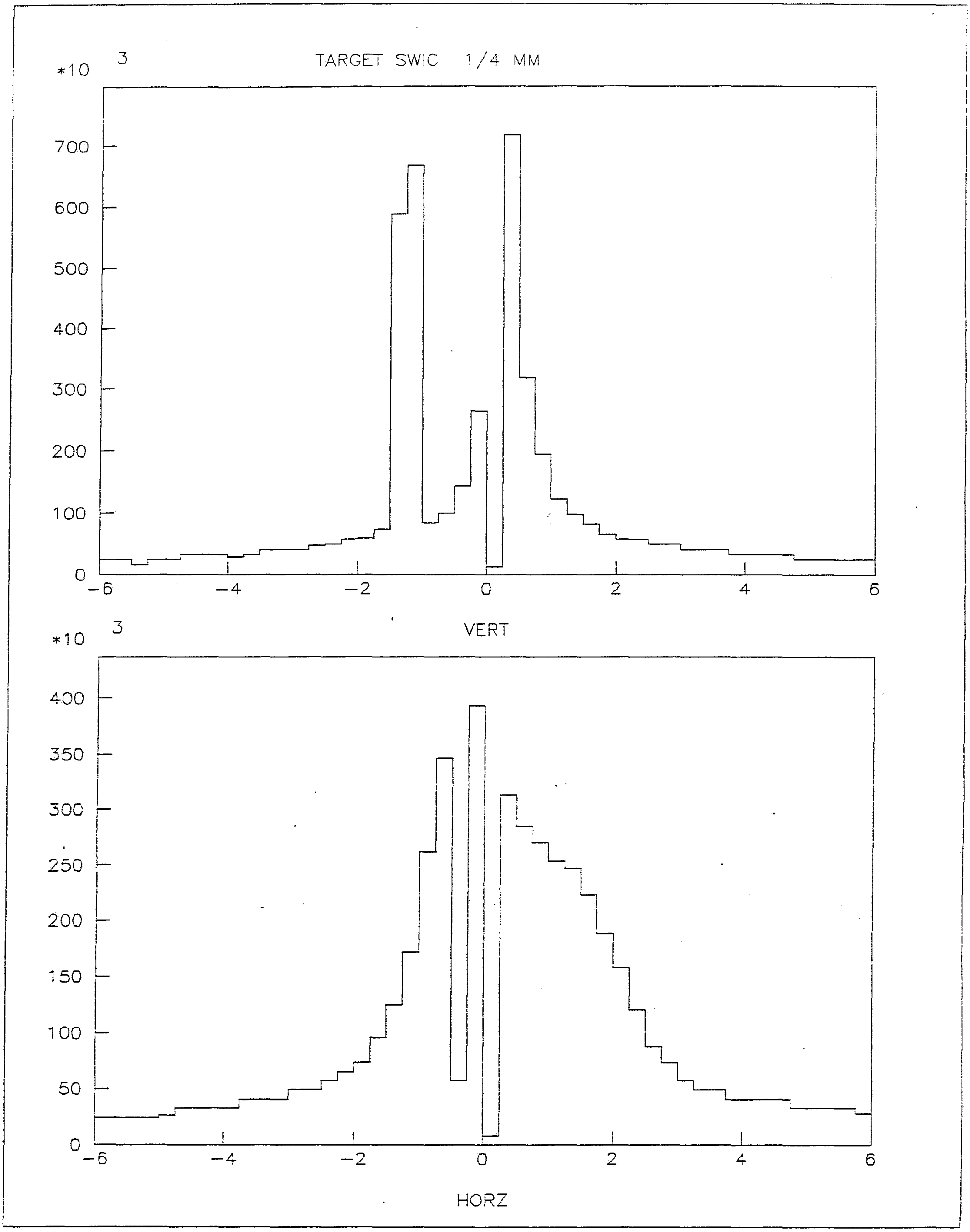
TARGET SWIC 1/4 MM
*10 3
700
600
500
400
300
200
100
0
-6
-4
-2
0
2
4
6
VERT
*10 3
400
350
300
250
200
150
100
50
0
-6
-4
-2
0
2
4
6
HORZ

DIURNAL VARIATION OF HOLE COLLIMATOR MOTION FOR A FIXED STEP SIZE

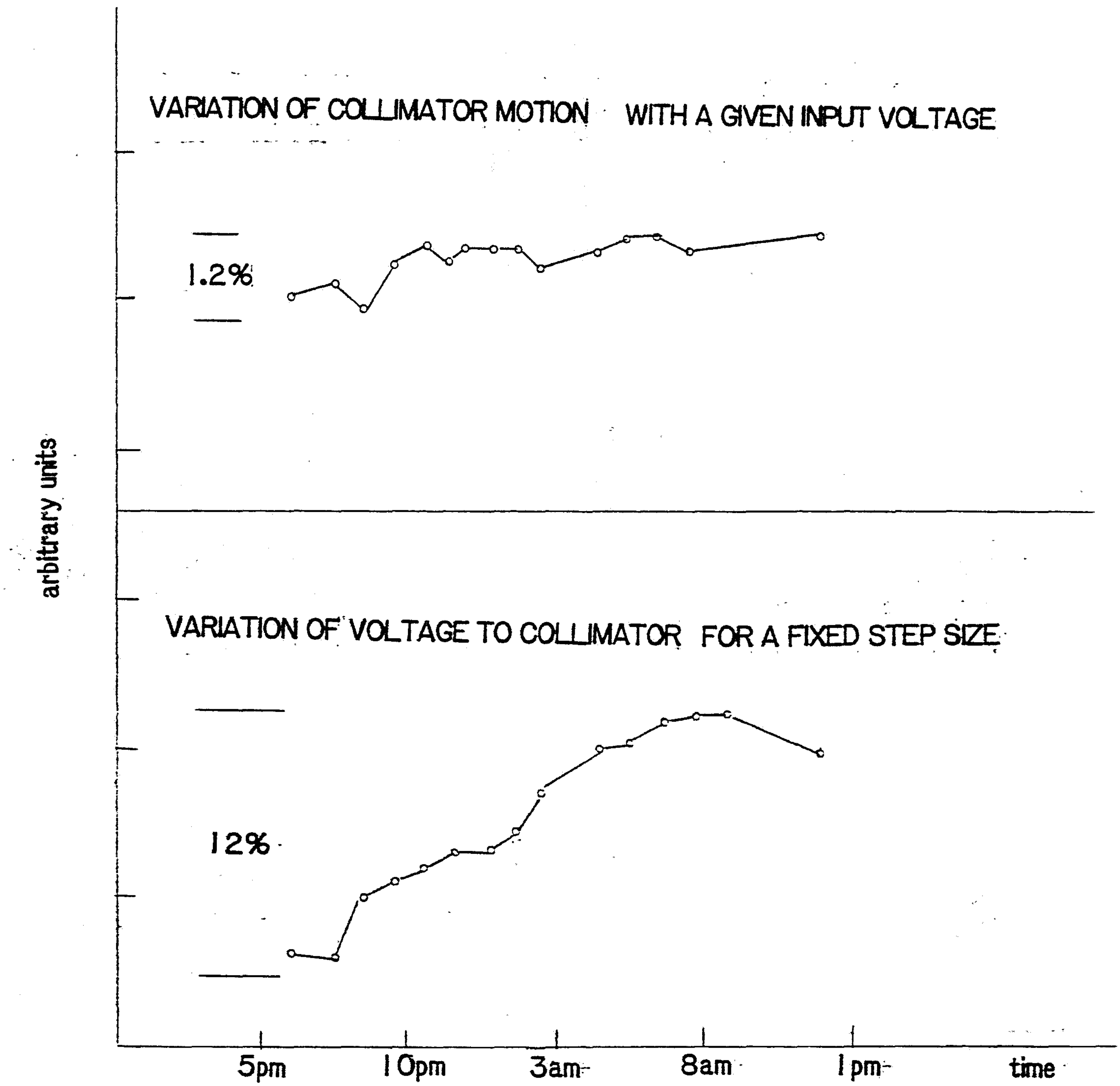

Figure A-12.

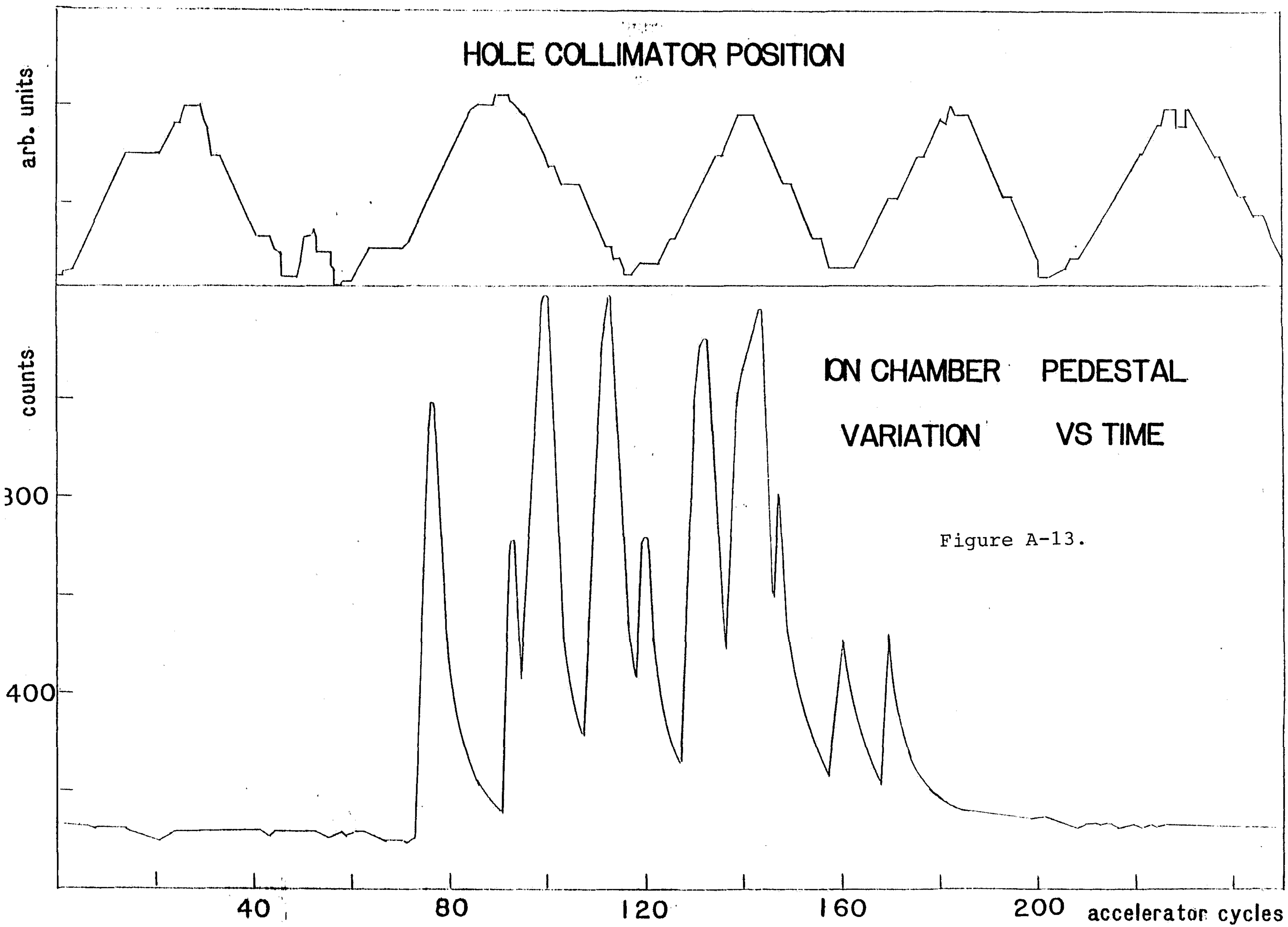
HOLE COLLIMATOR POSITION
arb. units
counts
ION CHAMBER PEDESTAL
VARIATION VS TIME
300
400
40
80
120
160
200
accelerator cycles

Figure A-13.

Figure A-14.

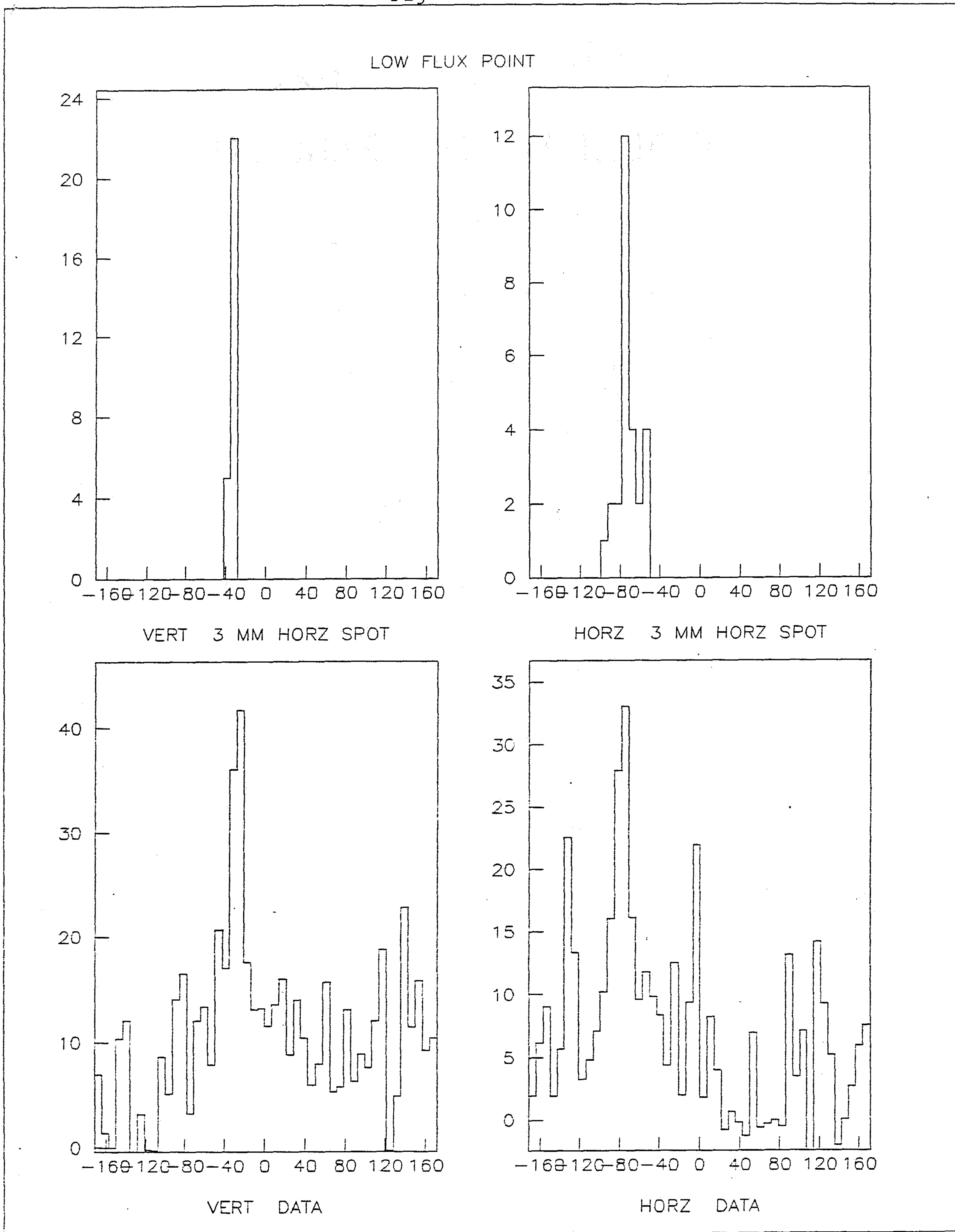
LOW FLUX POINT
VERT 3 MM HORZ SPOT
HORZ 3 MM HORZ SPOT
VERT DATA
HORZ DATA

DIVISION OF HOLE COLLIMATOR POINTS

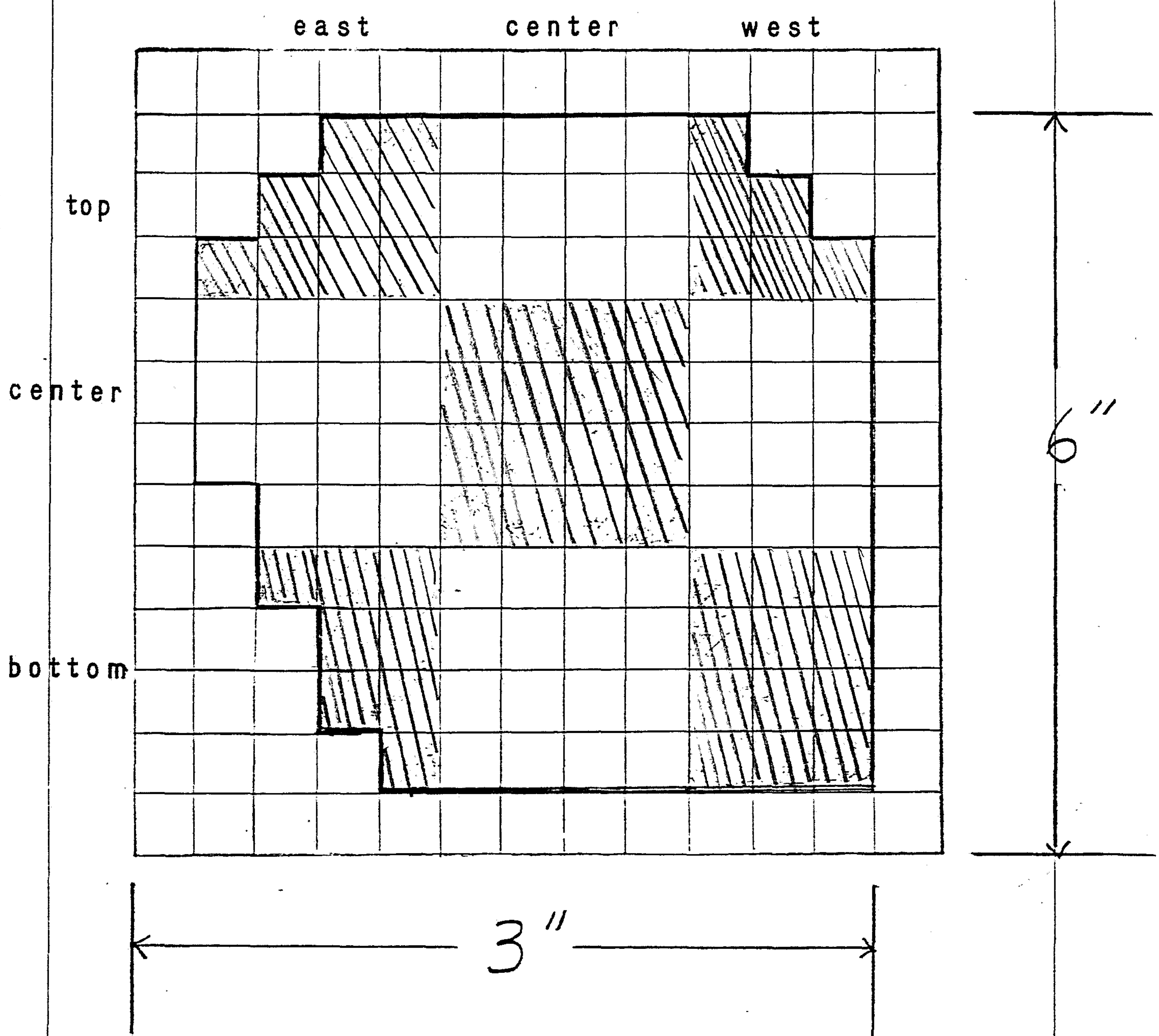

Figure A-15.

Figure A-16 a.

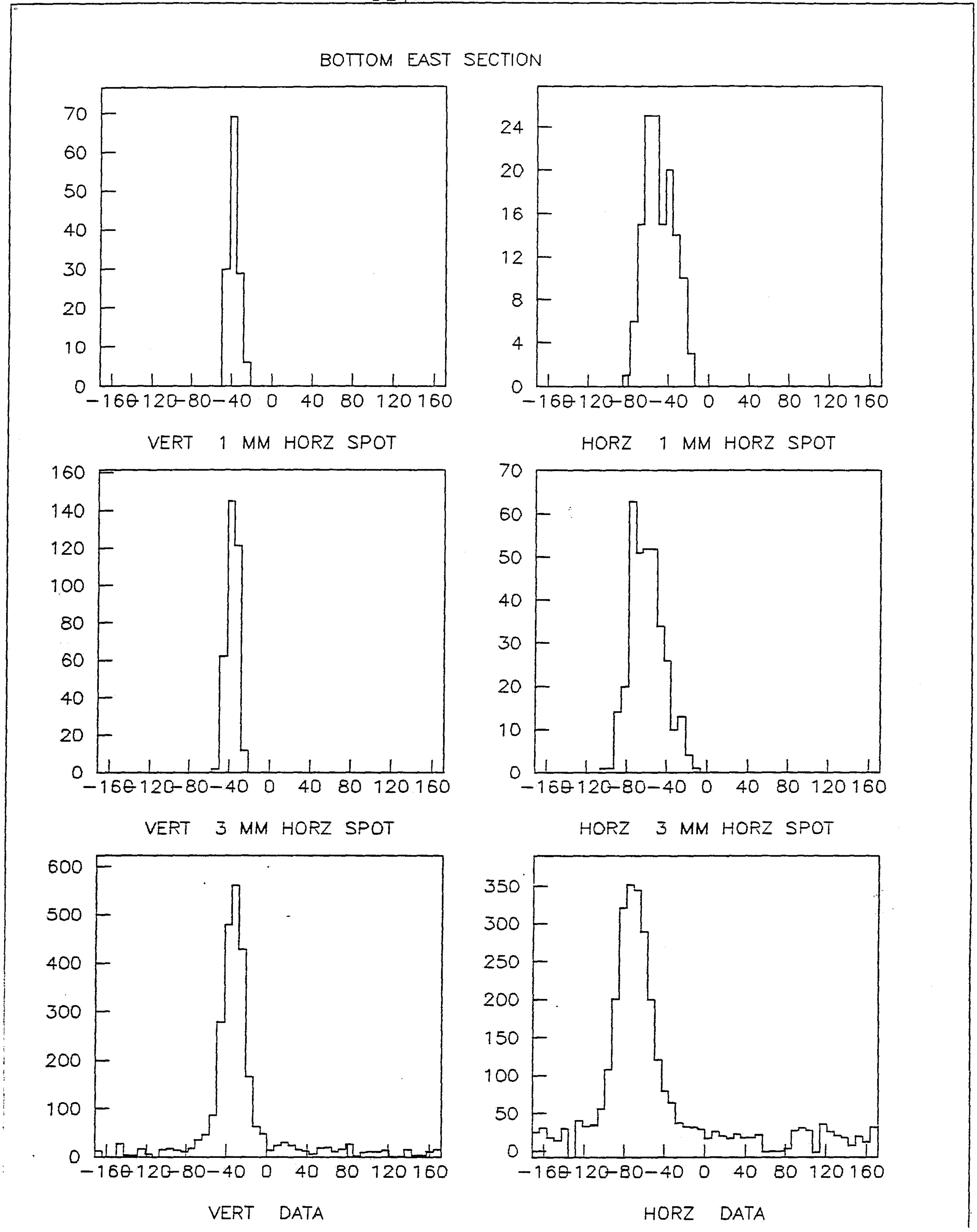
BOTTOM EAST SECTION
VERT 1 MM HORZ SPOT
HORZ 1 MM HORZ SPOT
VERT 3 MM HORZ SPOT
HORZ 3 MM HORZ SPOT
VERT DATA
HORZ DATA

Figure A-16 b.

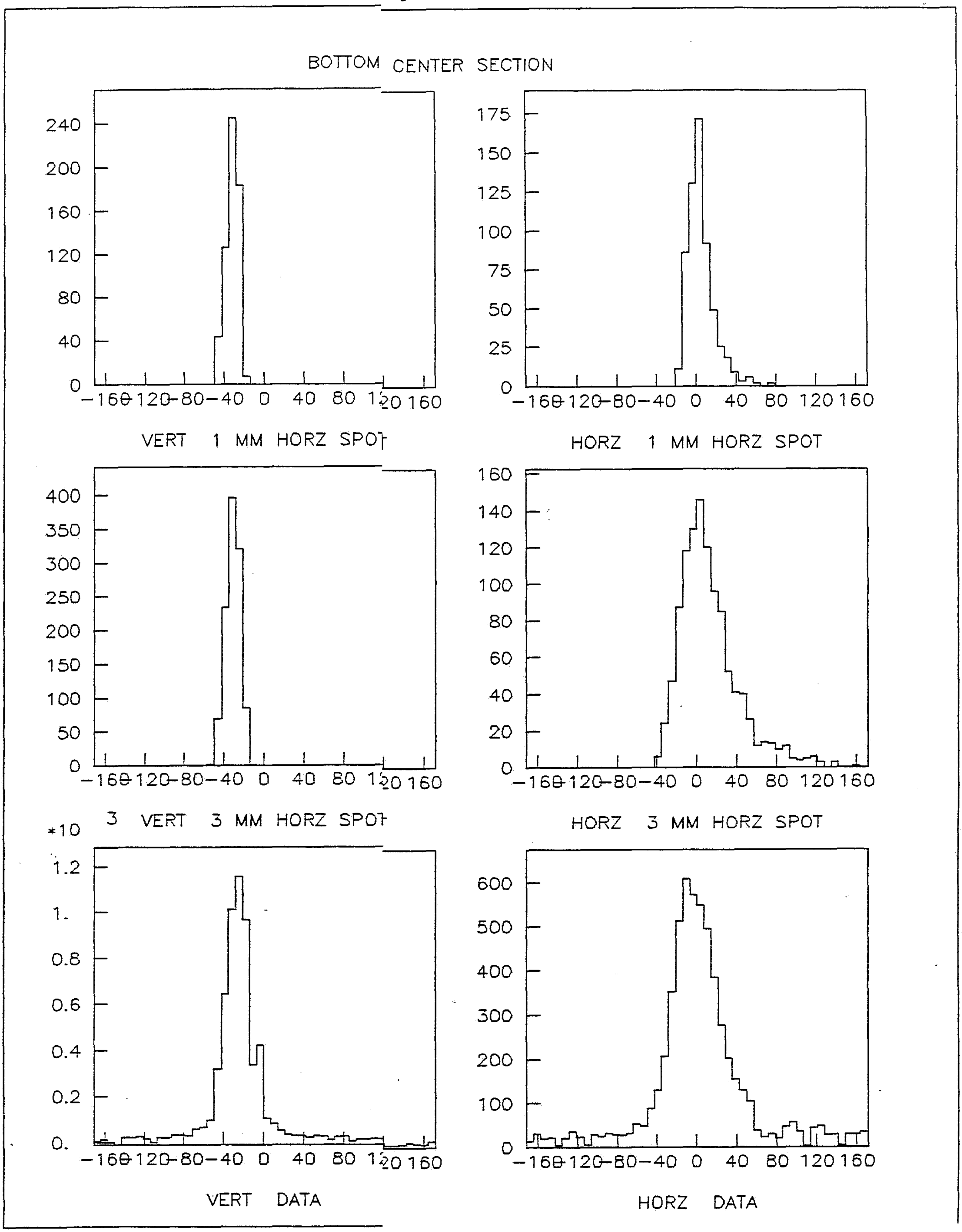

BOTTOM CENTER SECTION
VERT 1 MM HORZ SPOT
HORZ 1 MM HORZ SPOT
VERT 3 MM HORZ SPOT
HORZ 3 MM HORZ SPOT
*10 3
VERT DATA
HORZ DATA
-160 -120 -80 -40 0 40 80 120 160

Figure A-16 c.

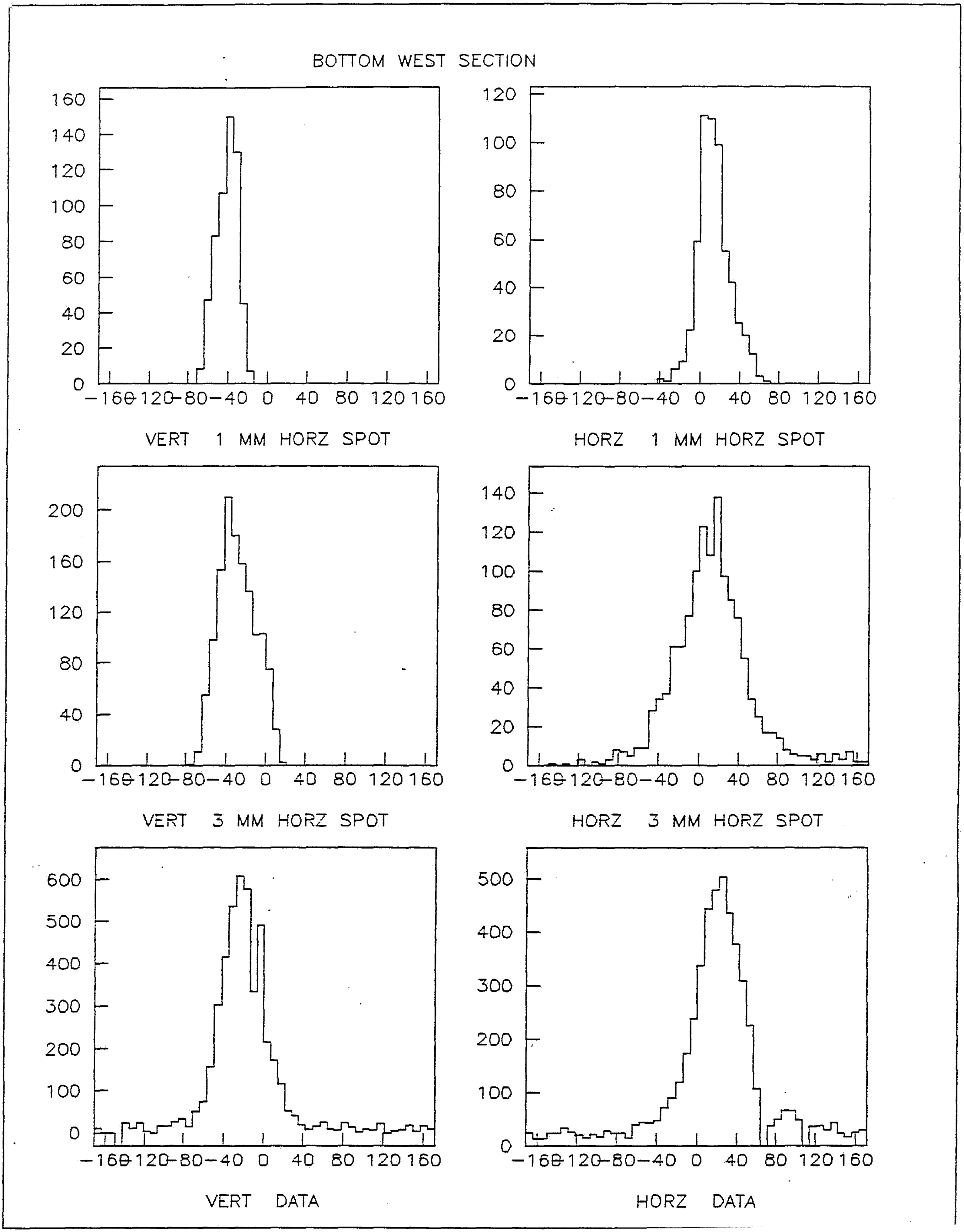

BOTTOM WEST SECTION
VERT 1 MM HORZ SPOT
HORZ 1 MM HORZ SPOT
VERT 3 MM HORZ SPOT
HORZ 3 MM HORZ SPOT
VERT DATA
HORZ DATA

Figure A-16 d.

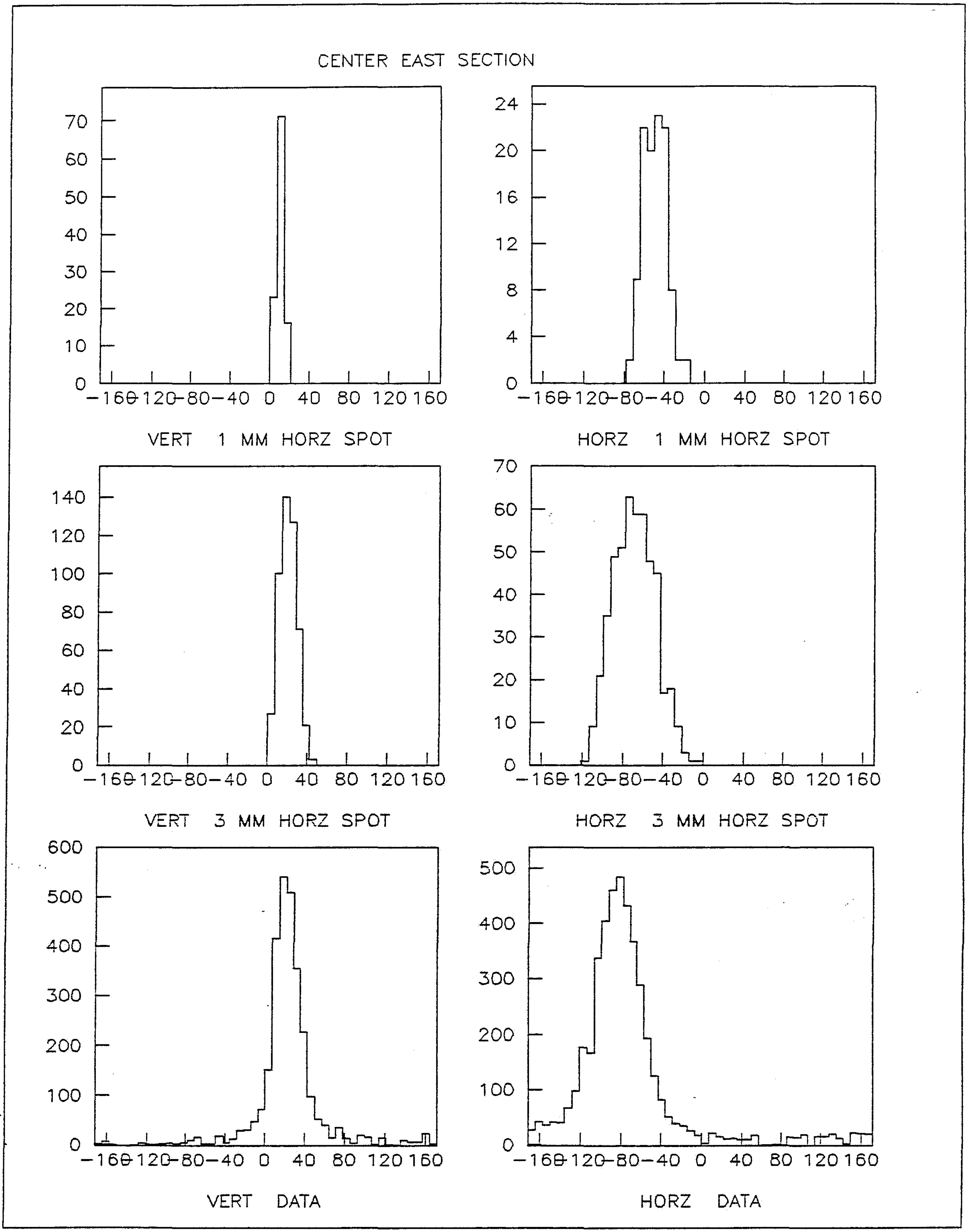
CENTER EAST SECTION
VERT 1 MM HORZ SPOT
HORZ 1 MM HORZ SPOT
VERT 3 MM HORZ SPOT
HORZ 3 MM HORZ SPOT
VERT DATA
HORZ DATA
−160 −120 −80 −40 0 40 80 120 160

Figure A-16 e.

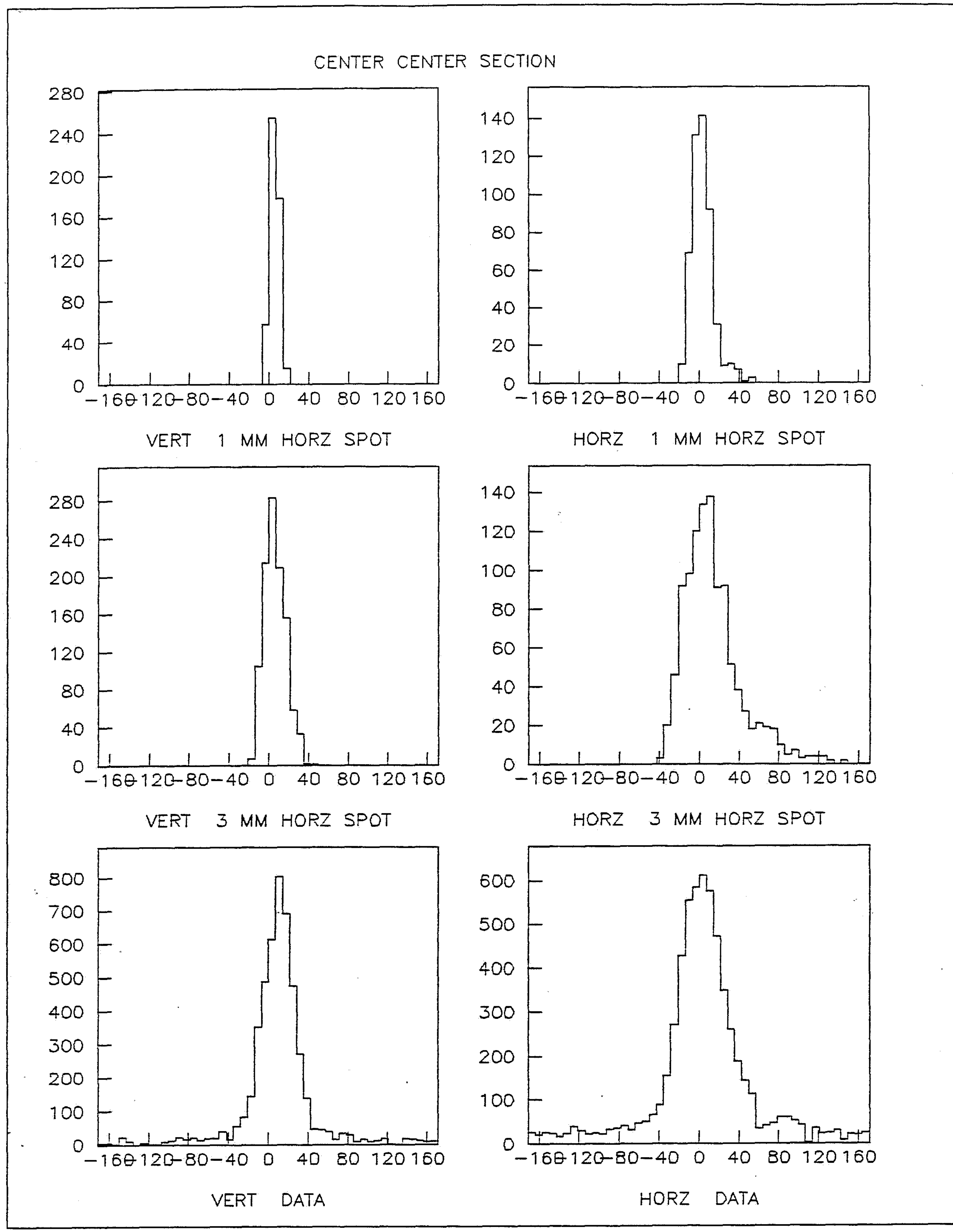
CENTER CENTER SECTION
VERT 1 MM HORZ SPOT
HORZ 1 MM HORZ SPOT
VERT 3 MM HORZ SPOT
HORZ 3 MM HORZ SPOT
VERT DATA
HORZ DATA

Figure A-16 f.

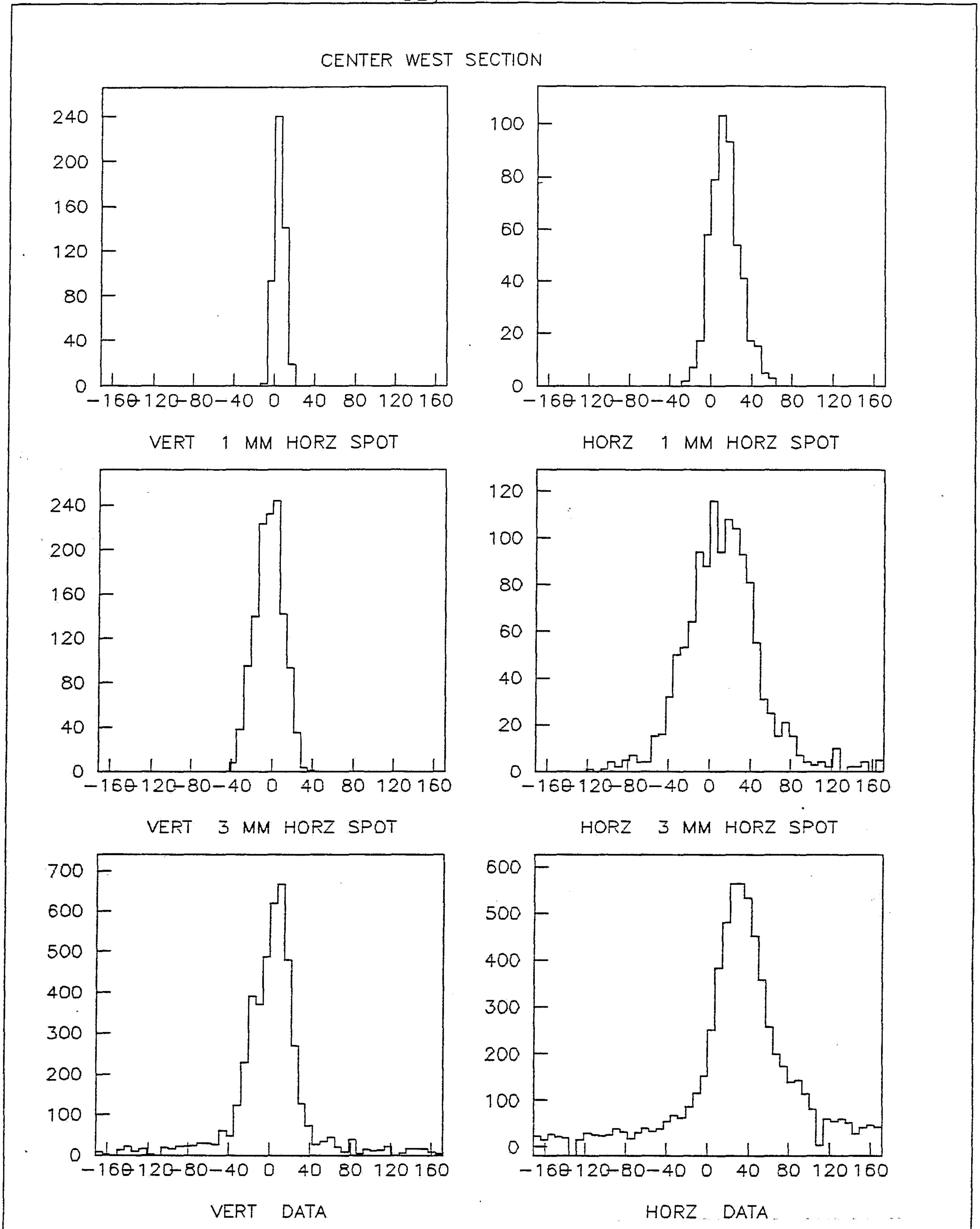

CENTER WEST SECTION
VERT 1 MM HORZ SPOT
HORZ 1 MM HORZ SPOT
VERT 3 MM HORZ SPOT
HORZ 3 MM HORZ SPOT
VERT DATA
HORZ DATA

Figure A-16 g.

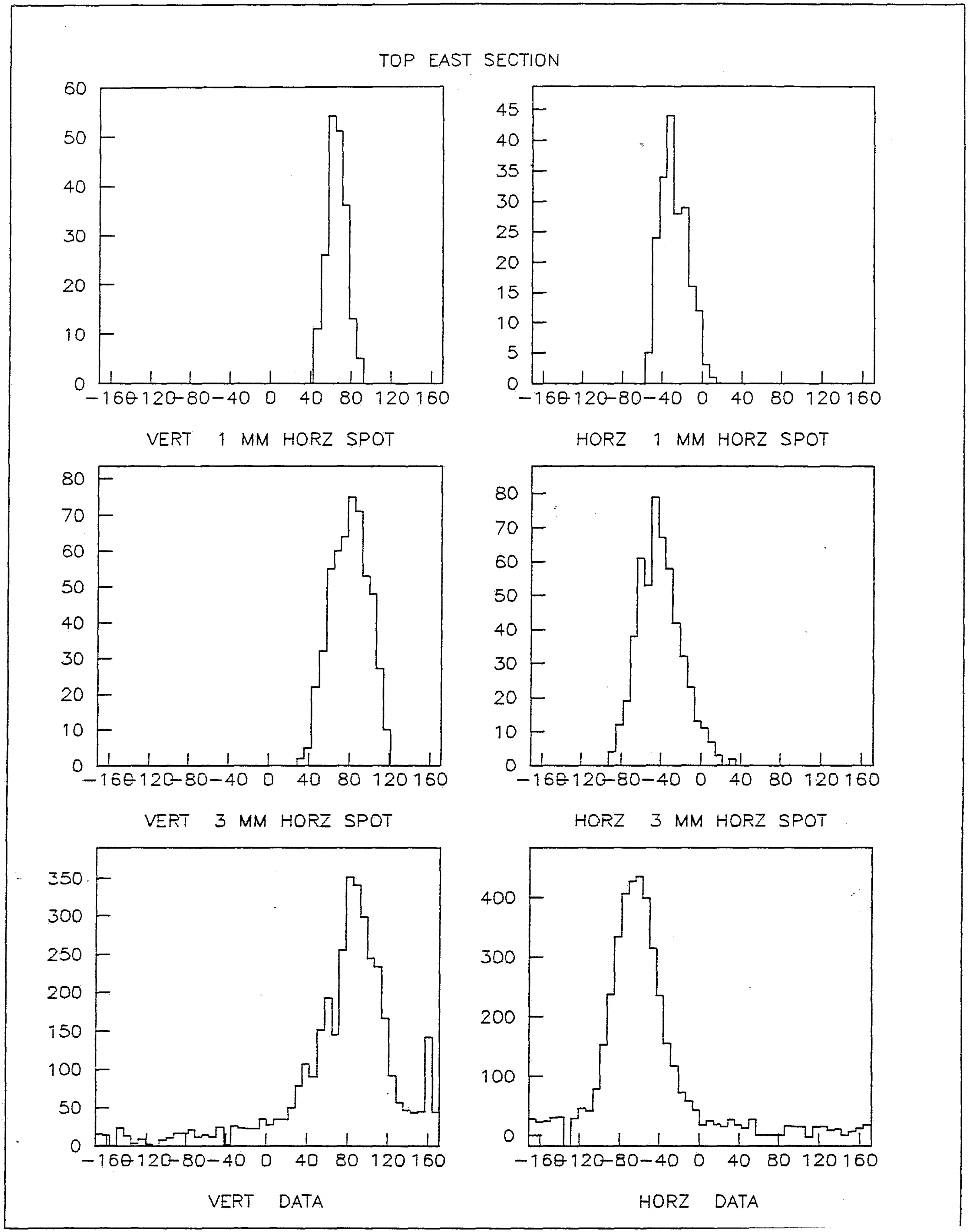
TOP EAST SECTION
VERT 1 MM HORZ SPOT
HORZ 1 MM HORZ SPOT
VERT 3 MM HORZ SPOT
HORZ 3 MM HORZ SPOT
VERT DATA
HORZ DATA

Figure A-16 h.

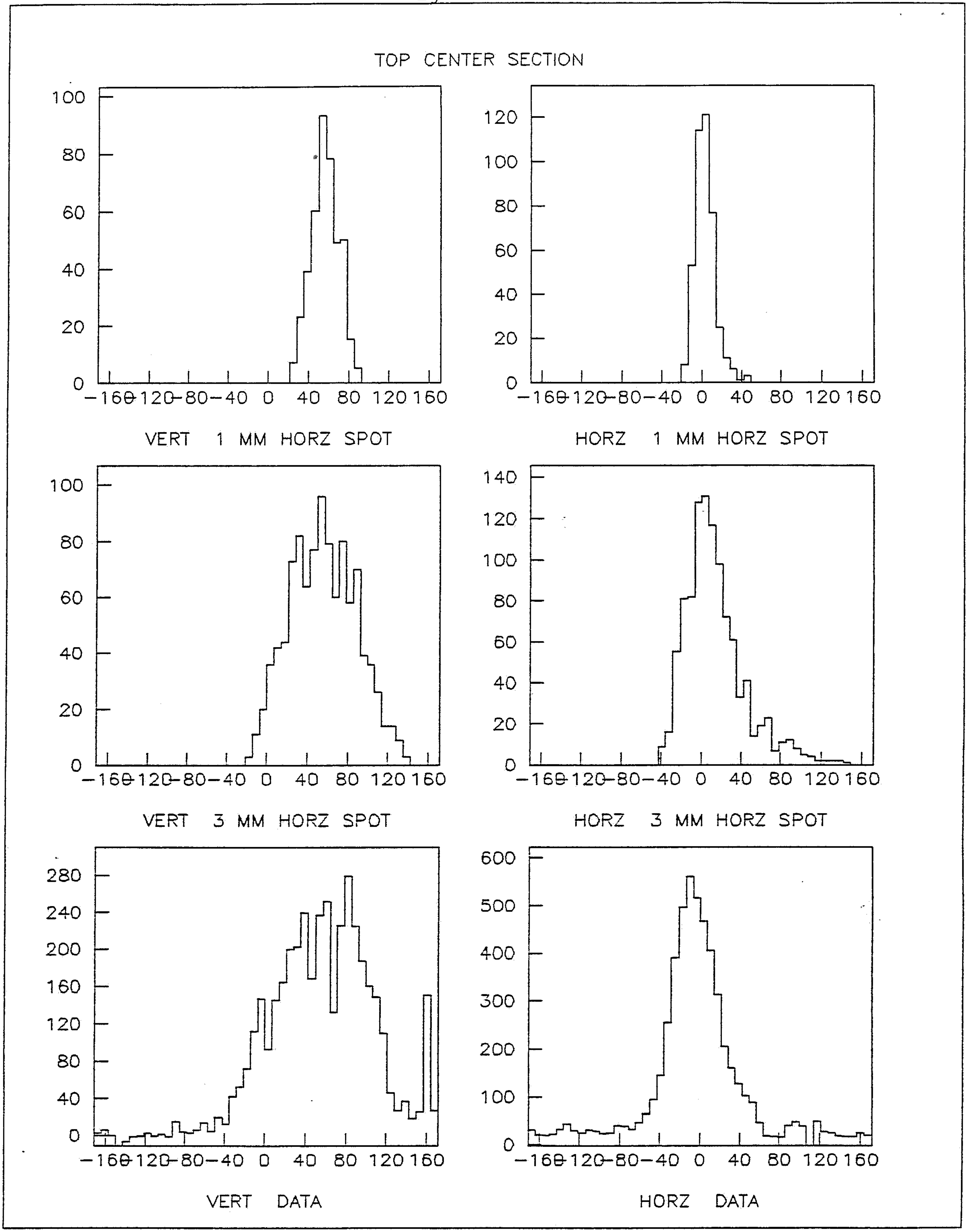

TOP CENTER SECTION
VERT 1 MM HORZ SPOT
HORZ 1 MM HORZ SPOT
VERT 3 MM HORZ SPOT
HORZ 3 MM HORZ SPOT
VERT DATA
HORZ DATA

Figure A-16 i.

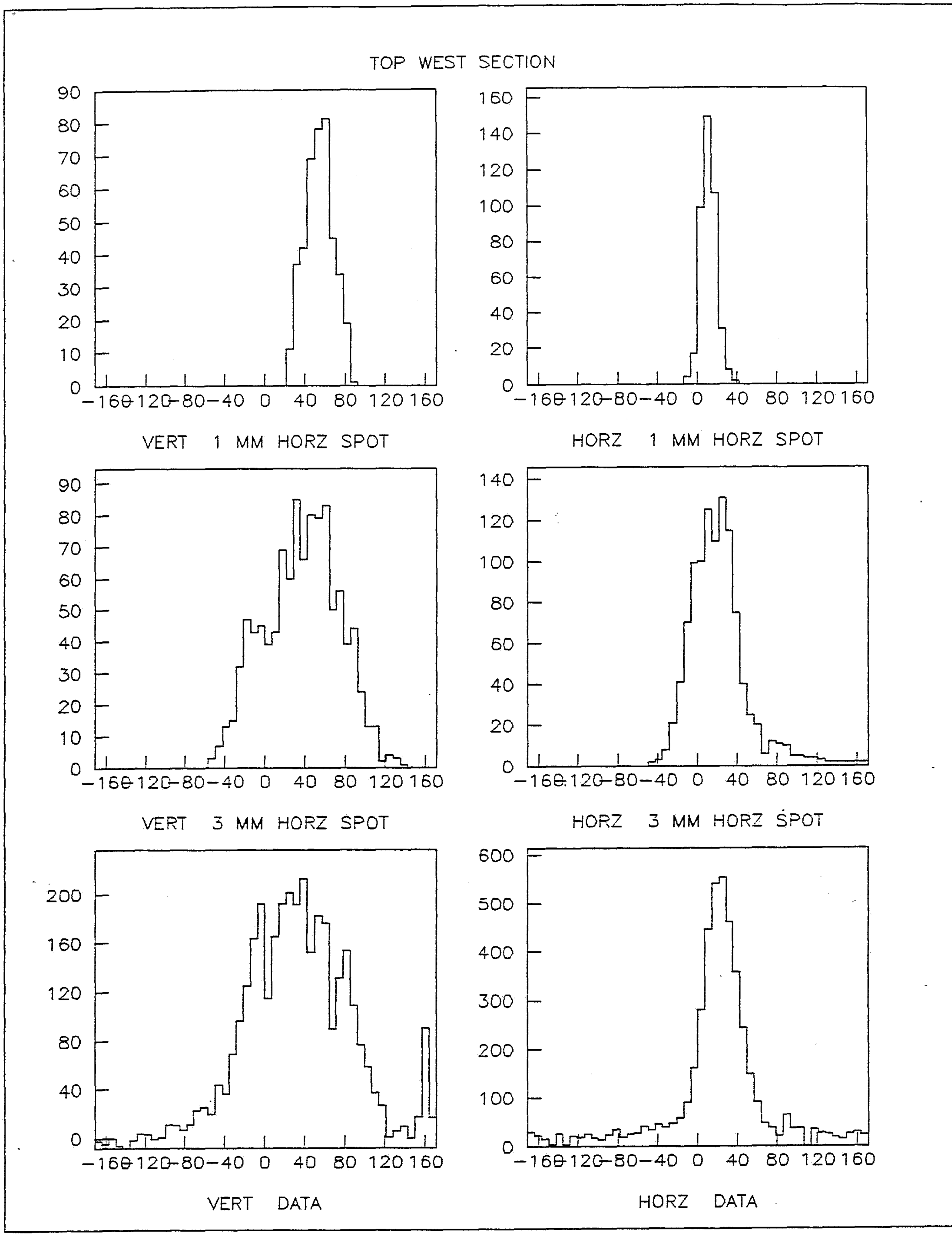
TOP WEST SECTION
VERT 1 MM HORZ SPOT
HORZ 1 MM HORZ SPOT
VERT 3 MM HORZ SPOT
HORZ 3 MM HORZ SPOT
VERT DATA
HORZ DATA

Figure A-17.

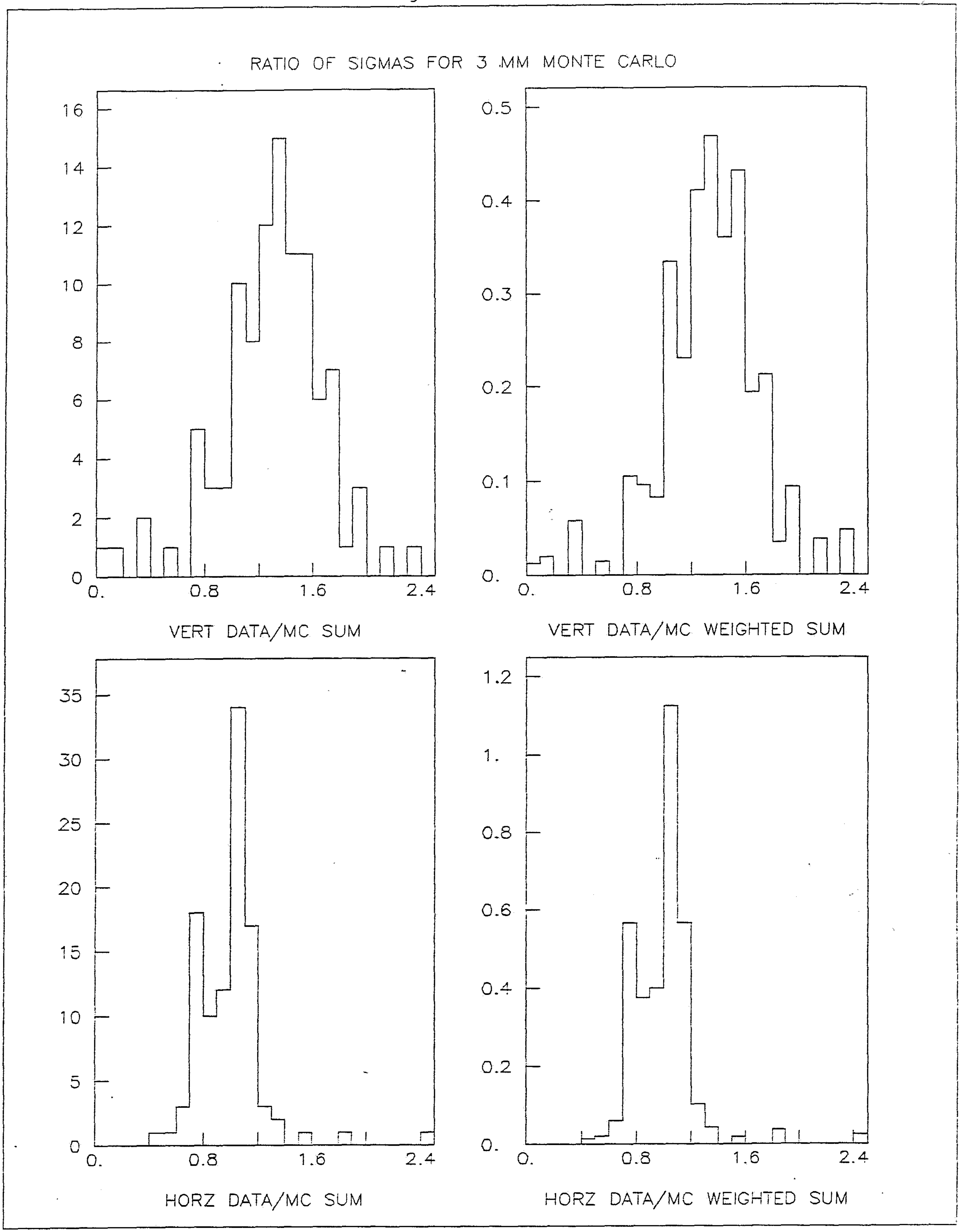
RATIO OF SIGMAS FOR 3 MM MONTE CARLO
VERT DATA/MC SUM
VERT DATA/MC WEIGHTED SUM
HORZ DATA/MC SUM
HORZ DATA/MC WEIGHTED SUM

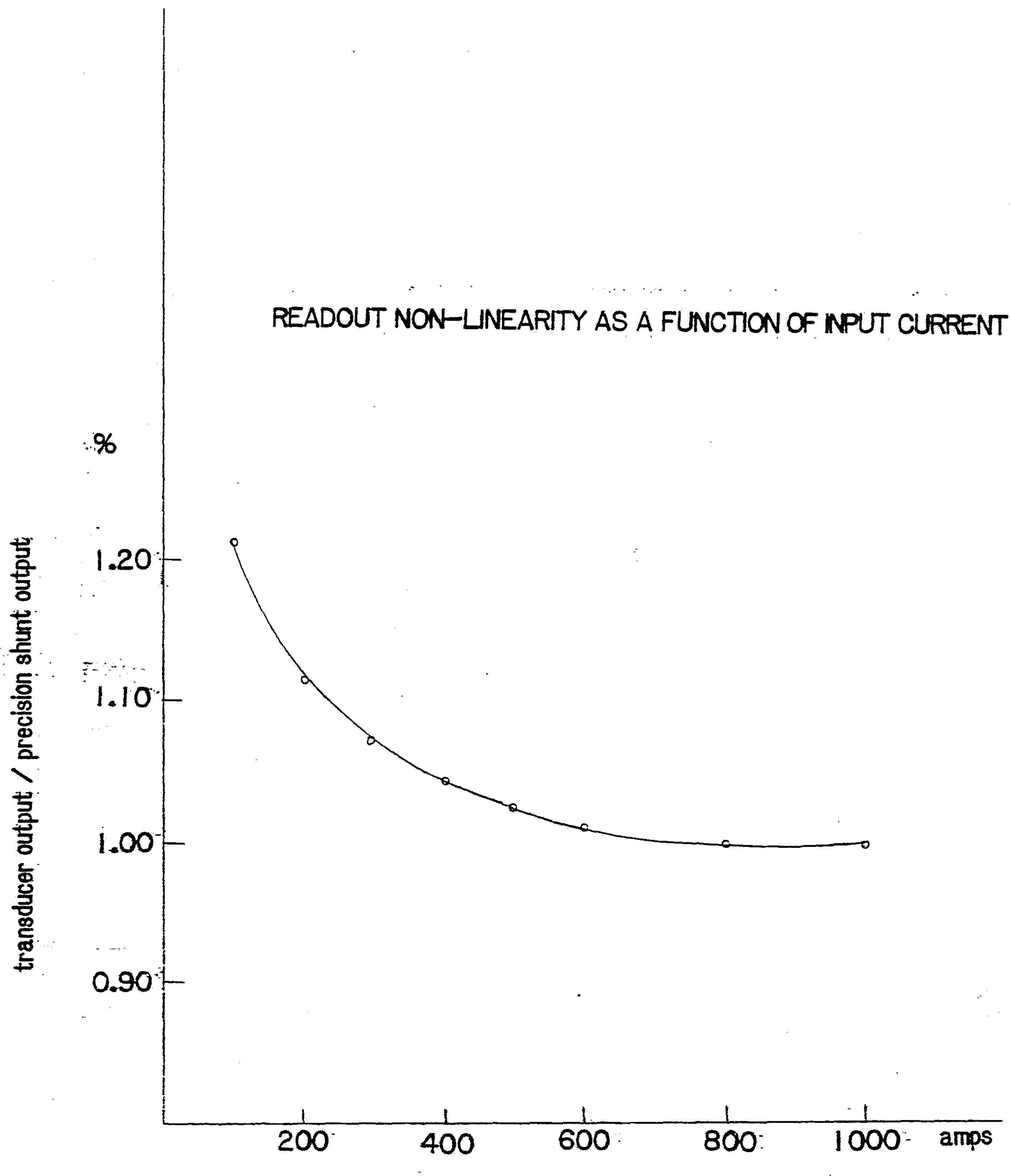
READOUT NON-LINEARITY AS A FUNCTION OF INPUT CURRENT
%
transducer output / precision shunt output
1.20
1.10
1.00
0.90
200
400
600
800
1000
amps

Figure A-18.

Figure A-19.

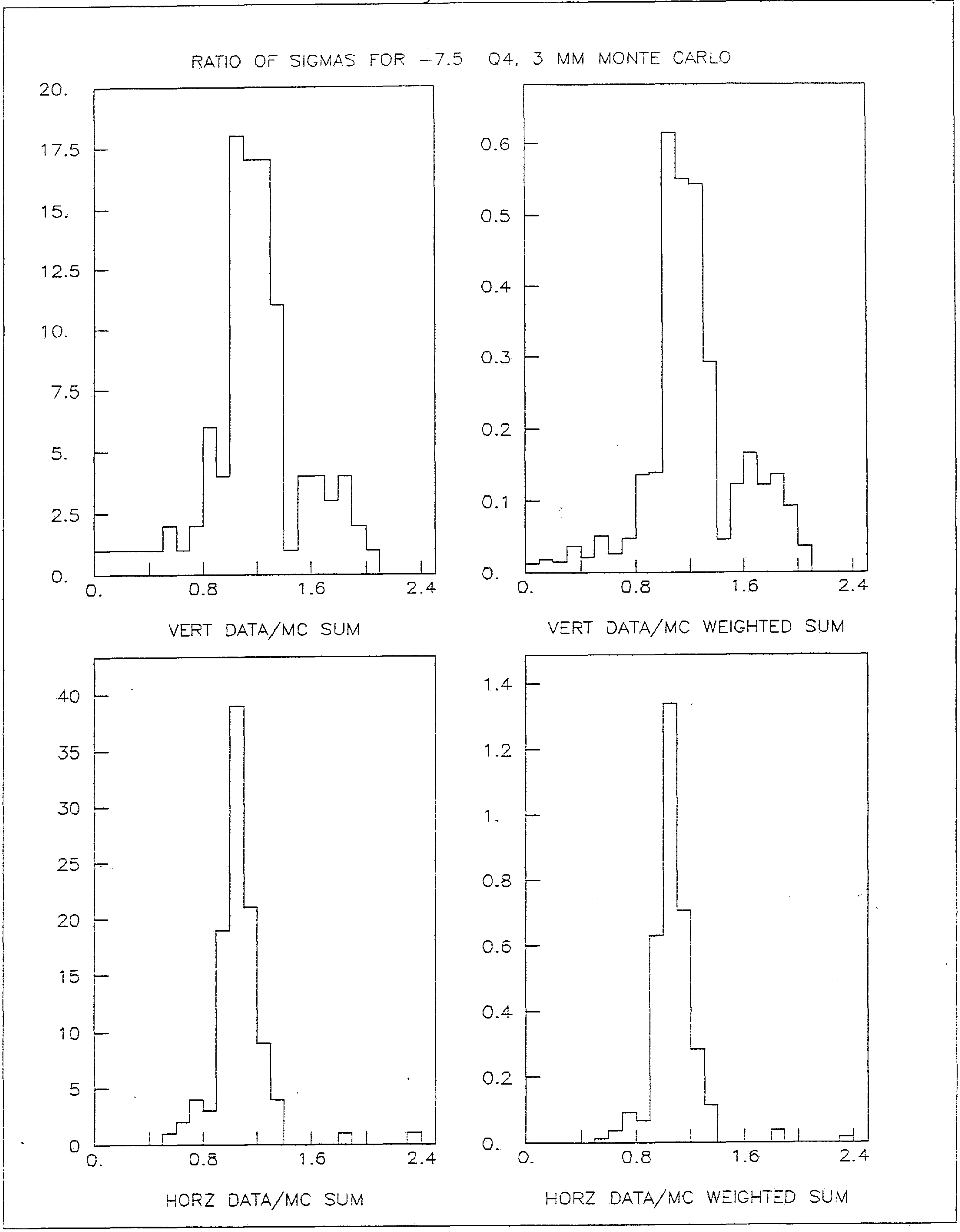
RATIO OF SIGMAS FOR −7.5 Q4, 3 MM MONTE CARLO
20.
17.5
15.
12.5
10.
7.5
5.
2.5
0.
0.
0.8
1.6
2.4
VERT DATA/MC SUM
0.6
0.5
0.4
0.3
0.2
0.1
0.
0.
0.8
1.6
2.4
VERT DATA/MC WEIGHTED SUM
40
35
30
25
20
15
10
5
0
0.
0.8
1.6
2.4
HORZ DATA/MC SUM
1.4
1.2
1.
0.8
0.6
0.4
0.2
0.
0.
0.8
1.6
2.4
HORZ DATA/MC WEIGHTED SUM

Appendix B:

The Apparatus and Calibration Data

(1) The Apparatus:

The construction and some of the operating characteristics of the Lab C calorimeter are described in the attached IEEE article. Since that article was written there has been a significant upgrade of the detector for the Tevatron-era experiments. The charge-division readout of the toroid spectromenter has been upgraded to a drift system. Furthermore, drift planes have been installed in the rear of the calorimeter to give a good angle definition for the muon track as it enters the toroid system. The spatial resolution of the drift system is about 2mm. This will provide a muon momentum resolution of 10 to 15% over the momentum range of E-649.

The magnetizing system for the flash chamber magnetostrictive readout system will be upgraded to operate after every event. This should improve the uniformity of the detector and the reliability of its operation.

Another upgrade will be to construct a new double plane front veto counter. By operating the planes in coincidence, the accidental veto rate from the beam associated soft background (from neutrons?) will be reduced.

(2) Calibration Data:

During 1984 and 1985 the calorimeter was recalibrated up to 400 GeV. The energy response of the flash chambers is shown in Figure B1 and the corresponding plot for the proportional tube calorimeter is given in B2. We see that the flash chambers are linear (after the statistical enhancement technique has been applied) up to about $\approx$ 200 GeV. Above that energy there is a 5% nonlinearity up to 400 GeV.

The <u>preliminary</u> energy resolutions are shown in Figures B3 and B4 for the flash chamber system and the proportional chamber system, respectively. The angle resolution using the flash chambers is shown in B5.

In general we find that the new calibration data agree with our earlier results. Work is continuing on both hardware and software impovements which will enhance our energy and angle resolutions. For example, we are combining the flash chamber and the proportional chamber calorimetry information. This will help to compensate for the nonlinear response of the flash chamber calorimeter and should improve the resolutions at high energy.

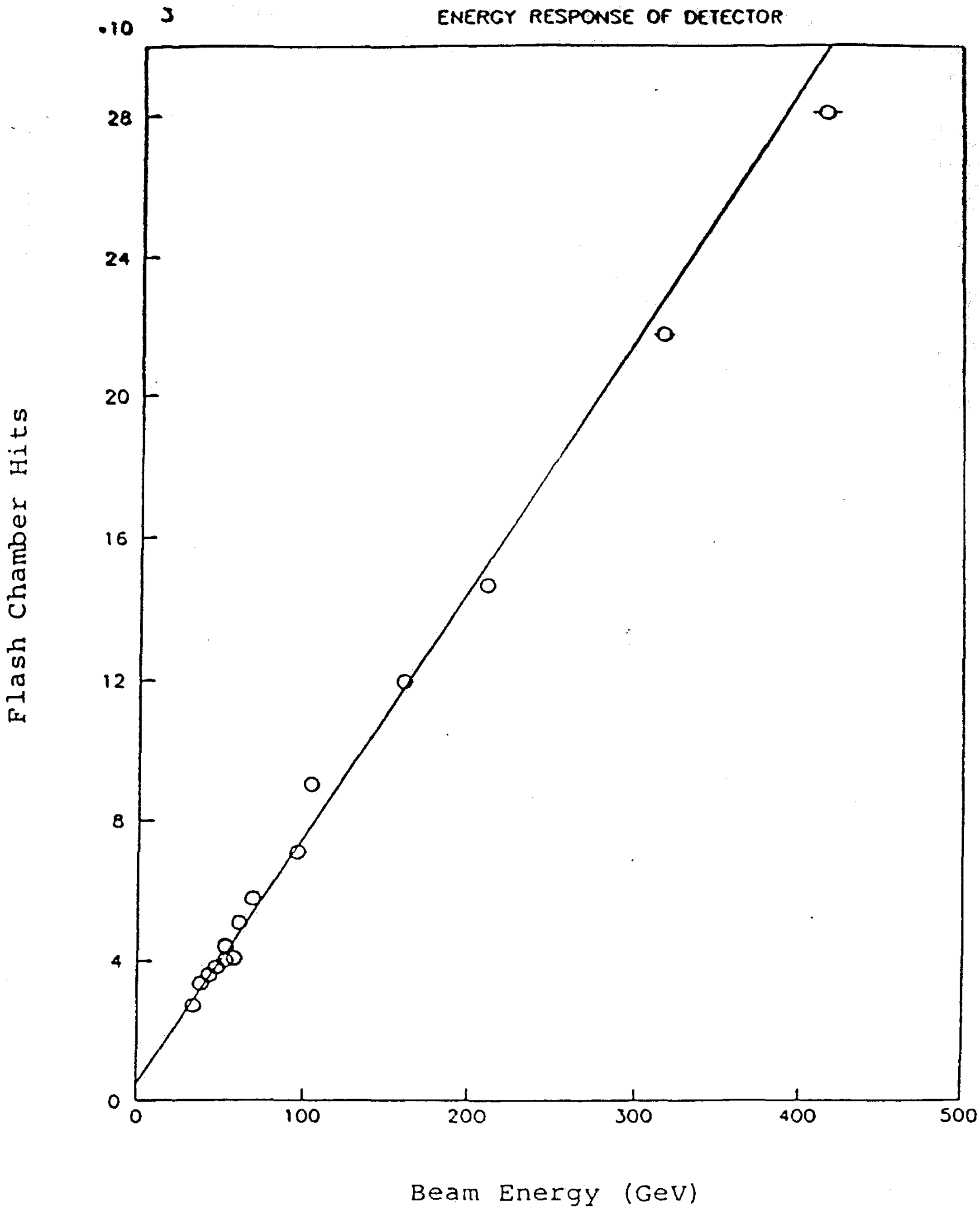

Figure B1

Flash Chamber Shower Energy Response

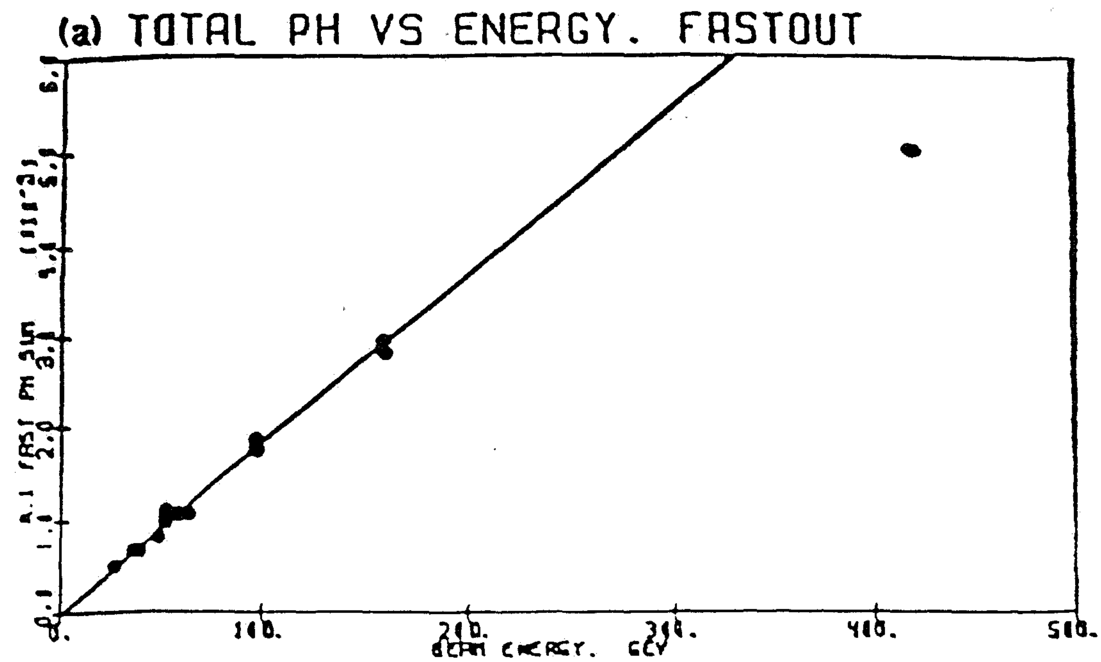

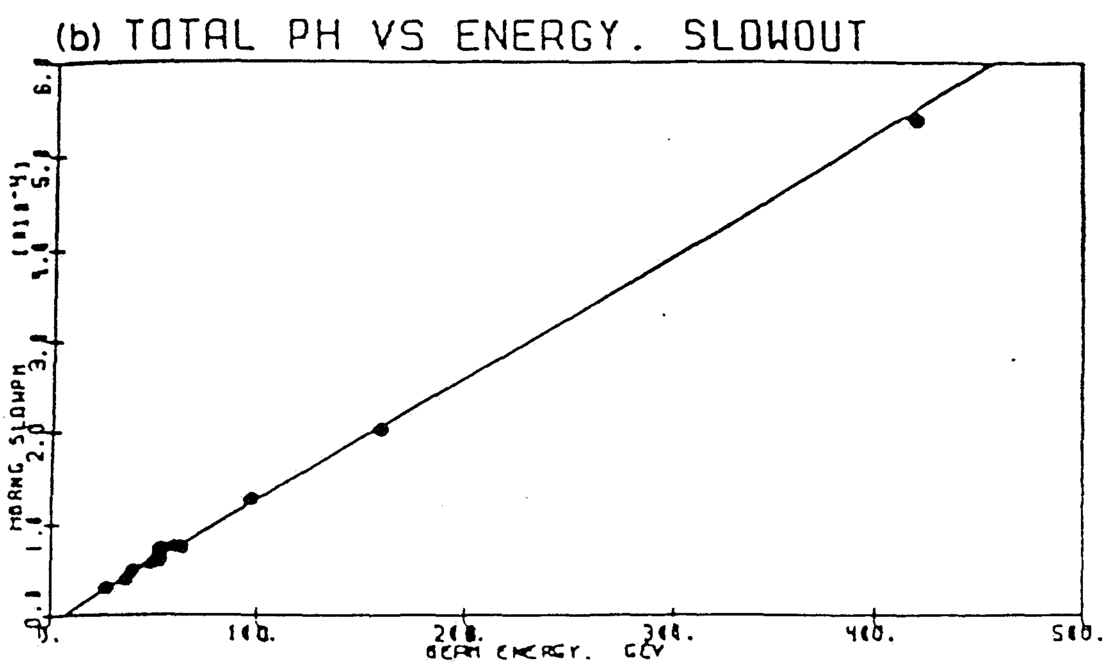

Figure B2

Proportional Tubes Shower Energy Response

Total Pulse Height vs. Beam Energy for
(a) FASTOUT and (b) SLOWOUT.

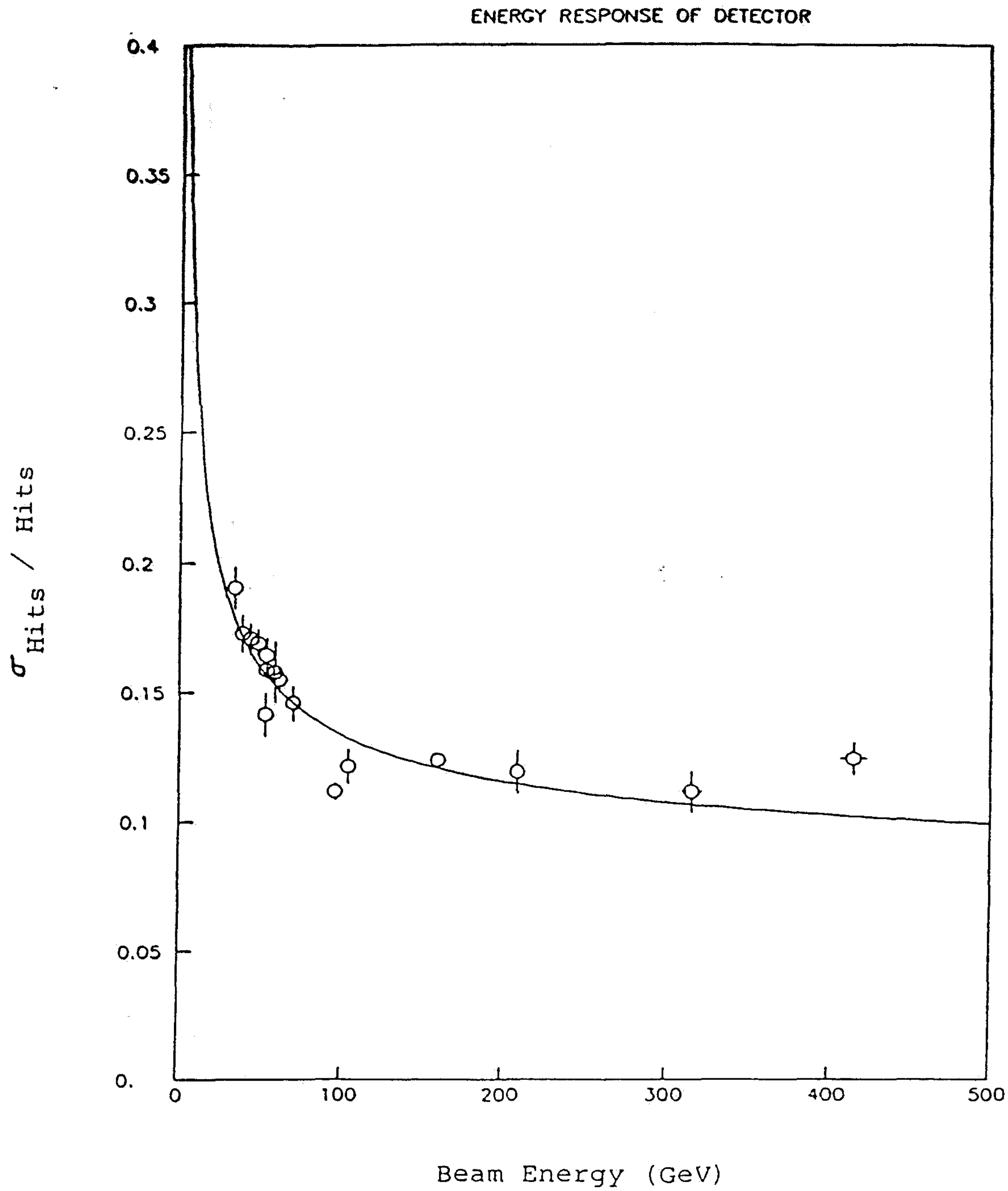

Figure B3

Flash Chamber Shower Energy Resolution

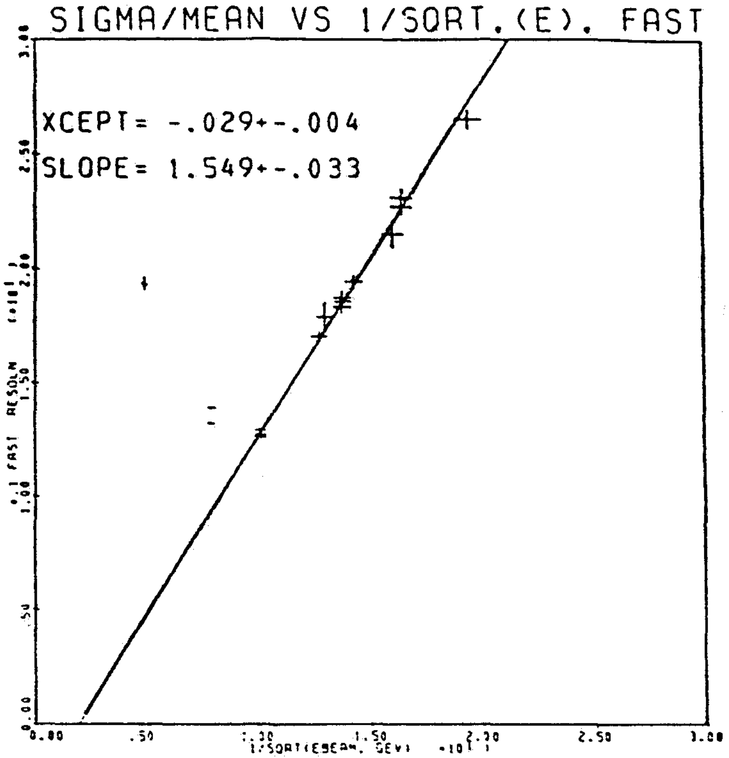

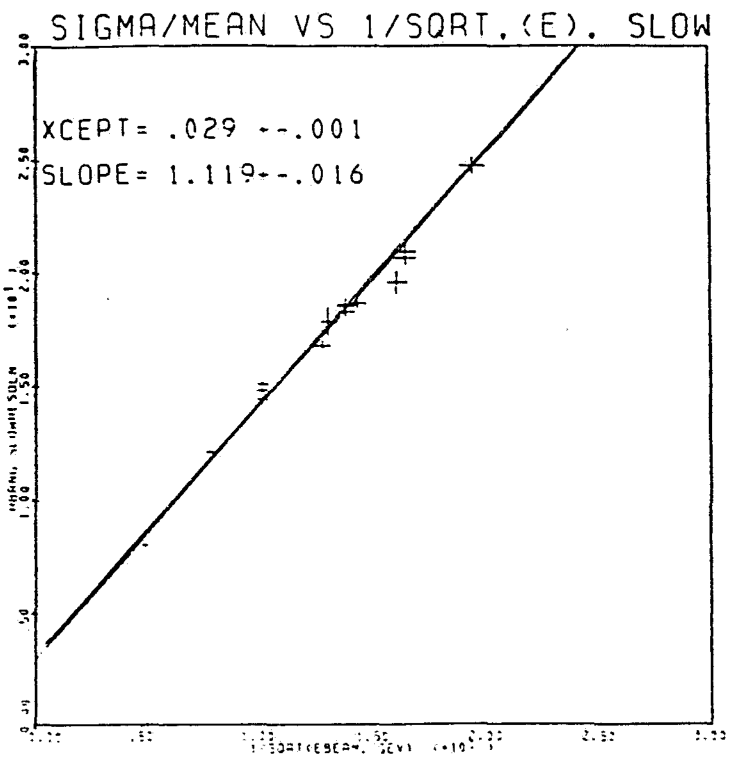

Figure B4

Proportional Tubes Shower Energy Resolution

Fractional resolution, σ/E, plotted as a function of $1/\sqrt{E}$, with linear least squares fit superimposed. The FASTOUT (a) fit was made for E_{BEAM} < 150 GeV, and the SLOWOUT (b) fit for $E_{BEAM} \leq 400$.

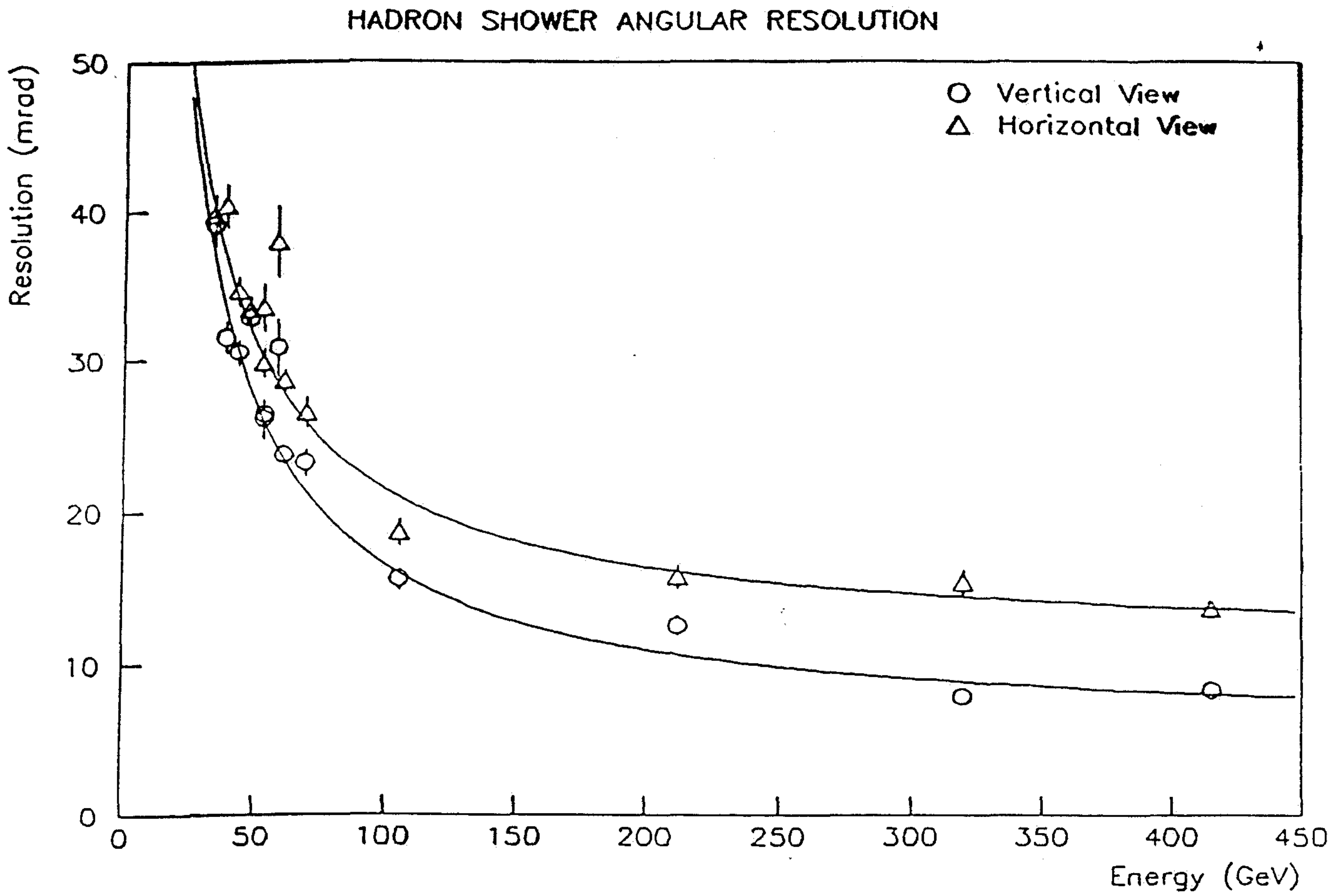

Figure B5

Hadron Shower Angular Resolution
as a Function of Shower Energy

IEEE Transactions on Nuclear Science, Vol. NS-29, No. 1, February 1982

THE OPERATION OF A LARGE FLASH CHAMBER NEUTRINO DETECTOR AT FERMILAB

D. Bogert, R. Brock, R. Burnstein*, S. Fuess, R. Fisk, J. Morfin, M. Peters**, L. Stutte, and J.K. Walker
Fermi National Accelerator Laboratory
Batavia, Illinois

J. Bofill, R. Burg, W. Busza, J.I. Friedman, H.C. Goodman, H.W. Kendall, T. Lyons, T. Mattison, L. Osborne, R. Pitt, L. Rosenson, A. Sandacz, M. Tartaglia, R. Verdier, S. Whitaker, G.P. Yeh
Massachusetts Inst. of Technology
Cambridge, MA

M. Abolins, A. Cohen, J. Ernwein***, D. Owen, J. Slate
Michigan State University
East Lansing, MI

F.E. Taylor
Northern Illinois University
DeKalb, IL

Abstract

The operation of a large flash chamber neutrino detector at Fermilab is described. The detector consists of 608 flash chambers, and 37 proportional chambers with an active area of 12'x12'. Planes of sand and steel shot are interleaved with the flash chambers and proportional chambers to provide a fine grain sampling of recoil showers. The mass of the detector is 340 tons. The calibration of the instrument for electrons and hadrons in the energy range of 5 to 125 GeV is described.

* Perm. address Illinois Inst. of Technology Chicago, Illinois 60616
** Perm. address University of Hawaii Honolulu, Hawaii 96822
*** Perm. address CEN Saclay B.P. No2, 91190 Gif-Sur-Yvette, France

Introduction

To study neutrino-induced weak neutral current interaction it is necessary to have a massive neutrino detector capable of measuring both the energy and the direction of the reaction products. A pattern recognition capability of the showers resulting from the primary neutrino interaction is also a useful design consideration, and allows the study of rare processes. To realize these latter capabilities, the neutrino detector must be fine grained. In this paper we describe such a fine grained detector which we have built at Fermilab. The detector is based on polypopylene flash chambers and proportional tube chambers. These devices allow a very high degree of segmentation in both the data as well as selectivity to rare processes in the trigger. The experience we have obtained in long period operation of the detector in quadrupole triplet and single horn neutrino beams and the results of a calibration of the detector for electrons, hadrons and muons will be described in this paper.

The Detector-General Description

The flash chamber - proportional tube calorimeter is 60 feet long (18.3m) and has a 12'x12' (3.66mx3.66m) cross section and a mass of approximately 340 metric tons. The flash chambers are used to determine the pattern of the neutrino reaction products thereby furnishing an identification of the event type as well as determining the energy and angle of energy flow. The proportional tube chambers are used to trigger the flash chambers and to provide another measurement of the energy of the shower. The layout of the detector is shown in Figure 1.

The flash chambers are arranged in three views (x,y,u) with cells which run 0°, 80°, 100° relative to the horizontal plane respectively. Each flash chamber plane is

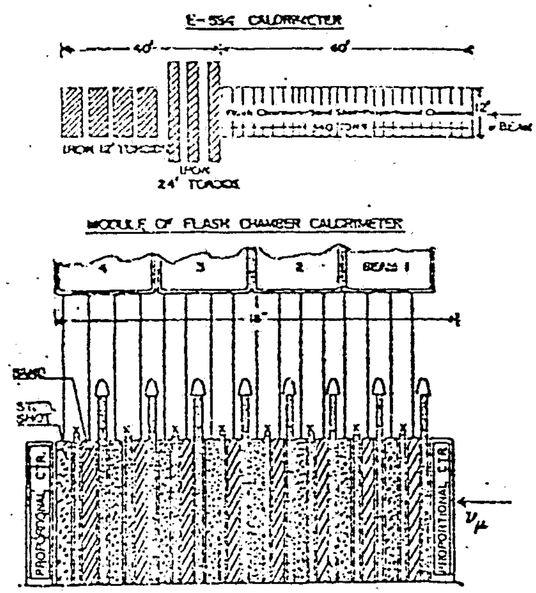

Fig. 1: Layout of the detector.

sandwiched between a sand filled plastic extrusion plane and a steel shot plane. The flash chambers are read out electronically. The details of this system have been described earlier[1].

The proportional tube planes are located every 16 flash chamber planes (one module) in an alternating horizontal - vertical pattern. Each module weighs approximately 9 tons.

The proportional tube chambers are instrumented with an amplifier for every 4 wires with a wire separation of 1 inch (2.54 cm). This high level of segmentation gives pattern recognition at the trigger level as well as analog information on the energy deposition of the shower profile.

This arrangement of flash chambers - proportional tube chambers - sand and steel shot has an average radiation length of 12 cm sampled every 22% X_0 by the flash chamber and every 3.5 X_0 by the proportional tube chambers. The average absorption length is 83 cm (116 g/cm^2) and is sampled every 3%λ by the flash chambers and every 50%λ by the proportional tube chambers. The average density is 1.4 g/cm^3 and the average Z is approximately 21. This property of low density and low Z is important in achieving good energy flow measurements for hadron showers.

Downstream of the flash chamber - proportional tube chamber calorimeter is an iron toroid muon spectrometer. This spectrometer is instrumented with double plane proportional tube chambers and is described in detail elsewhere in this conference.

In addition to the proportional tube chambers there are 10 12'x12' liquid scintillation counters. One plane is at the upstream end of the detector to act as a charged particle veto, one plane is downstream of the muon spectrometer, and one plane is placed every 80 flash chamber planes. They are used to provide an independent muon trigger of the calorimeter for dignostic and monitoring purposes.

The pattern recognition capabilities of the detector are evident in Figure 2, which shows an online display of a high energy neutrino interaction taken during the spring 1981 engineering run. Shown are the 3 views of flash chamber planes (x,u,y on the display). Each dot drawn on the display represents a struck cell in the calorimeter. The total number of struck cells is shown as the quantity HITSUB, which is 1036 in this event. (There are roughly 400,000 cells in the calorimeter.) Since the total number of hit cells is proportional to the energy of the shower, we estimate the energy of this event to be ~25 GeV.

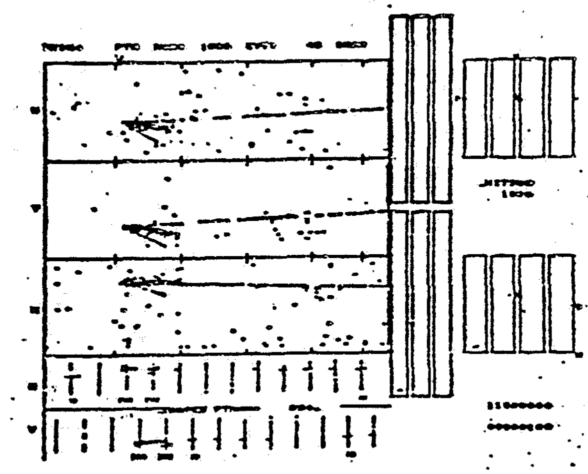

Fig. 2: Typical high energy charged current neutrino interaction. The high degree of segmentation of the data is evident.

Also shown in Figure 2 are the pulse heights of the proportional tube planes which provided the trigger of this event. These pulse heights appear as bar graphs along the lower edge of the picture for the horizontal (H) and vertical (V) plane orientation. The lateral profile of energy deposition of the 150 GeV shower is evident.

The toroids are shown at the right of Figure 2. The "+" signs indicate the track of the muon through the spectrometer in the horizontally (bottom) and vertically (top) oriented proportional planes.

We have operated the calorimeter for two major running periods. The first period was April to June 1980 during which time 180 tons of the detector were instrumented. Data were taken during this running period on neutrino interactions in the quad-triplet beam and the response of the detector was measured to a test beam consisting of electrons, muons, and hadrons. The second running period was January to May 1981, during which time 240 tons of the detector were instrumented. The detector was exposed to a single horn wide band neutrino beam. Various selective triggers were developed during this period and data were accumulated on deep inelastic neutrino scattering as well as various rare processes.

1) Operation of the Flash Chamber

The flash chamber system of the calorimeter has three major components: 1) the gas system, 2) the high voltage pulsing system, and 3) the readout system.

1) Operation of flash chamber gas system

The gas mixture and the gas purity affect the efficiency, reignition probability and the sensitive time characteristics of the flash chambers. Owing to the diffusion of the gasses through the (0.5mm thick) polypropylene walls of the flash chambers, and the long term outgassing of the polypropylene, it is necessary to change the gas in the flash chambers at a rate of approximately one chamber volume/hour. The gas is recirculated and purified by a two sieve gas purification system, which can purify up to 5.4×10^{4} liters/hour.

The initial operation of the flash chambers was carried out with a standard Ne-He (90%-10%) mixture. (Under long term operation conditions this gas mixture changes to 96% Ne, 4% He by the diffusion of He gas out of the system.) This mixture gave a good HV plateau with good efficiency versus delay characteristic, and was used during the 1980 run. However, the reignition probability, that is, the probability that a given hit cell in the flash chamber will refire, was rather high (6 to 8%), and gave rise to an after-imaging of the previous event, even with a time between events of 10 seconds.

Considerable experimentation was invested in reducing this reignition probability. A two phase solution was found:

a) By introducing a small amount of argon at the concentration of ~0.2% of the Ne-He gas content the long lived meta-stable excited states of Ne were de-excited by the Penning effect. The exact amount of Ar was determined by the chamber performance, and by the practical constraint that too much Ar would rapidly contaminate the cold sieve of the gas purification system. The addition of the Ar gas makes the plasma discharge stronger at a given high voltage and therefore allows the high voltage operating point to be lowered. Measurements have shown that the reignition probability is unaffected by the addition of Ar at a given HV, but since the Ar allows the operating point to be lowered, a reduction in the reignition probability is achieved.

b) A small amount of electronegative gas was introduced into the Ne-He-Ar mixture. This was accomplished by passing roughly 1/3 of the recirculating gas back into the chambers without going through purification by the gas system. The electronegative gases were the O_2, N_2 and H_2O which naturally contaminate the flash chamber gas through diffusion and outgasing. The electronegativity was controled by monitoring the O_2, N_2 and H_2O content with a gas chromatograph. The gas mixture returning to the flash chambers was 96%Ne, 4% He, 0.17% Ar, 0.10% H_2O and 0.04% O_2 and N_2.

The flash chamber characteristics for various gas mixtures are shown in Figure 3. It is evident from this Figure that the reignition probability is not reduced at a fixed high voltage by the addition of the Ar gas alone, but by the lowering of the high voltage operating point allowed by the lower HV characteristics of the Ne-He-Ar mixture, <u>and</u> by the addition of small levels of electronegative gases, the reignition probability is reduced from 6 to 8% to 1 to 2% at a 10 second repetetion rate. The efficiency remains the same under this condition. The addition of too much Ar or too much electronegative gas degrades the uniformity of the single muon efficiency across the 12' sensitive area of the flash chambers.

Other gas mixtures using a different ratio of Ne to He were investigated. It was found that the flash chambers work well for a mixture of 30% Ne and 70% He with roughly 0.17% Ar. This gas mixture is less expensive than the 90% Ne-10% He, but the gas losses from He diffusion are greater, making gas replacement larger. More experimentation using this gas mixture is planned.

The various chamber characteristics were measured throughout the run, and were found to be reasonably stable. The chamber efficiency was slightly affected by the ambient humidity, degrading by roughly 1.4% for every additional g/m^3 of H_2O in the surrounding air. This small variation can be controlled by air conditioning.

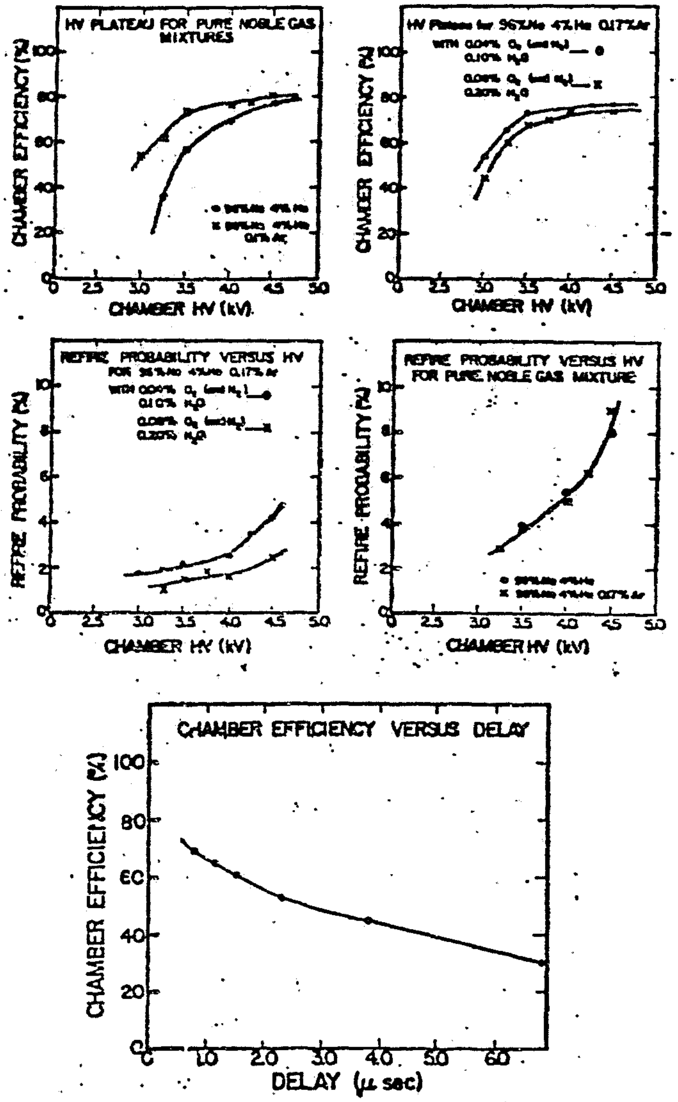

Fig. 3: Flash chamber operation characteristics for various gas mixtures.

2) Operation of the HV System

Each flash chamber is equipped with a pulse forming network (pfn) (see Figure 4) which generates a high voltage pulse of roughly 60 nsec rise time, 4.5 kV magnitude, and 500 nsec duration. The pfn's are triggered roughly 700 nsec after the event. In order to maintain consistency in the HV pulse quantity, a computer based monitoring system was designed.

The system measures the total charge in each of the high voltage pulses applied to the chambers, checks the front-edge timing, and verifies that no spurious pulsing takes place between triggers.

The system, shown in Figure 5a, has a capacity of monitoring 640 channels and consists of 8 special crates of electronics controlled by an LSI 11-23 based computer system. Each of the crates holds a crate controller module and five data modules. Each data module contains the electronics to monitor 16 pulsers as well as an 8 bit serial shift register readout system shown in Figure 5b. The inputs to the data modules come from a monitor output connector on each high voltage pulser via RG-174 coaxial cable which are derived from the high voltage pulse through a 100 to 1 resistor voltage divider.

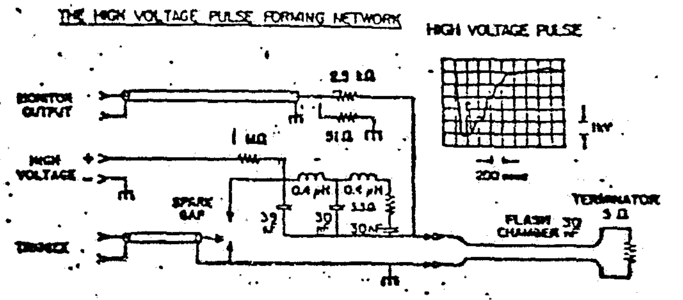

Fig. 4: Circuit diagram for the HV pulses (pulse forming networks -pfn).

The high voltage pulsers, shown schematically in Figure 4, upon receiving a trigger, switch the charge stored in their capacitors (99 nF) across the chambers. The pulse monitor system then a) checks whether the front edges arrive in proper synchronism with the trigger, b) determines whether there is spurious pulsing, and c) measures the total charge in each pulse.

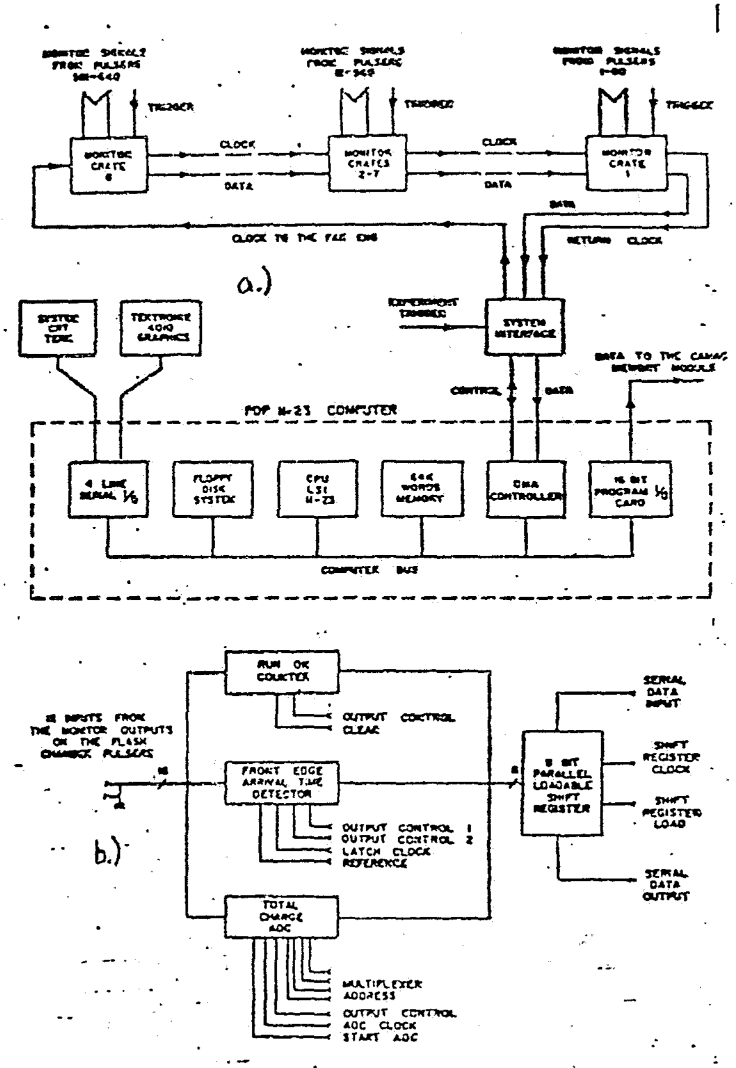

Fig. 5: The HV monitoring system.

a) The front edge arrival time is considered satisfactory if the pulse amplitude exceeds a preset comparator level by the time a signal derived from the trigger arrives at the crate controller. A channel with a bad front edge is flagged by setting a bit in a storage register for later readout. The comparator level for all 80 channels in a crate is set by adjusting a ten-turn potentiometer on the controller module.

b) To check for spuriously firing (runaway) spark gaps, each 16 channel data module contains two 4 bit "run-on" counters. The input to each of these is the logical "OR" of 8 adjacent monitor channels. This arrangement results in the run-on counters containing a count of 1 if the pulsers have worked properly. In the event of a spurious discharge of any of the 8 pulsers being monitored, the count in the run-on counter is increased by 1. Thus, a runaway pulser can easily by located to a group of eight from where it can be spotted visually.

c) To measure the total charge in the high voltage pulse, the monitor signal for each channel is integrated with a resistor capacitor combination and then digitized using an 8 bit analog - to - digital digital converter (ADC). The details of this circuitry are shown in Figure 5. A single 40 pin integrated circuit contains the necessary analog multiplexer and ADC to service a 16 channel module. The voltage across the 16 integrating capacitors are digitized in succession with each conversion taking about 100 μsec. The capacitors are allowed to discharge during this process with a time constant of 50 msec, a rate that insures complete discharge by the time the next pulse arrives (> 10 sec). No dispersion in the measured pulse-heights is introduced by the capacitor discharge since the digitization of the charge is always done at the same time relative to the monitor pulse.

The information from the three - pulse - analysis section in a data module is read into the computer by a single shift register bit serial data path linking all the modules. The program used for data acquisition and display is an RT-11 version of MULTI[2] with special data handlers to accomodate our hardware configuration. Further details of this readout system can be found in reference[3].

3) Operation of Flash chamber Readout System

The flash chambers are electronically read out using a magnetostrictive system. There are 1216 magnetostrictive amplifiers and a corresponding number of discriminator-comparator circuits. Proper operation of this system is maintained by assuring that the magnetostrictive wire magnatization remains constant. This is achieved by automatically pulsing a solenoidal magnet wrapped around each magnetostrictive wand every 200 flash chamber pulses. The locations of the fiducial markers on the magnetostrictive outputs are monitored and are found to be stable to within -2 mm (1 digitizing clock count) over long periods. This readout system, once set up and tuned, requires very little maintenance.

Calibration of the Calorimeter

The energy and angle resolutions of the calorimeter were determined by measuring the response to beams of known properties. The calibration beam contained electrons, muons or hadrons with electrons identified by a Cerenkov counter. The energy range of the calibration data was 5 to 125 GeV.

1) Electrons

The angle resolution of electron showers is shown in Figure 6a. The electron shower angle was computed by a weighted least squares method using the flash chamber hit cell information. The weights in the fit were determined by the average shower characteristics and the statistics associated with the hit cells.

The electron energy resolution is shown in Figure 6b. The electron energy has been computed by counting the number of hit cells in the shower. We have compensated for the saturation effect caused by more than one particle going through a given cell by estimating the actual number of particles given through each cut from the local density of hit cells. This compensation makes the energy response of the detector nearly linear and improves the energy resolution.

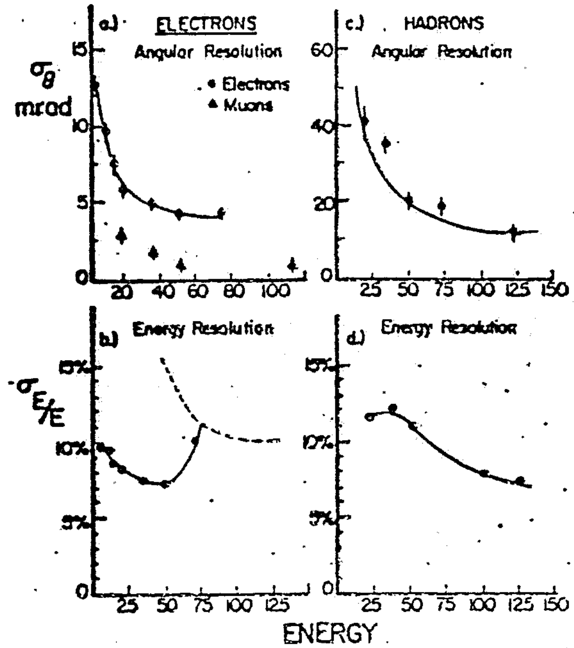

Fig. 6: a) The projected resolution of electron showers and muon tracks versus energy. A fit to the electron resolution is $\sigma(\theta_e)=$ (3.5+53/E) mrad.. b) The electron energy resolution. c) The projected hadron shower angle resolution. A fit to the data is $\sigma(\theta_h)=$ (6+640/E) mrad.. d) The hadronic energy resolution.

2) Muons

The muon angle resolution is shown in Figure 6a. The muon angles were computed by a least squares procedure with a weighting along the track length determined by multiple scattering. The observed resolution is in close agreement with the limit set by multiple scattering and the finite flash chamber cell size (0.577 cm). The muon momentum resolution has not yet been measured but is estimated to be $\Delta p/p \approx 15\%$.

3) Hadrons

The hadron shower angle resolution is shown in Figure 6c. This is computed in the same way as the electron shower angle resolution but with different weights determined by the much larger fluctuations. The quoted resolutions are the average r.m.s. resolutions of the x and of the y/u views.

The hadron shower energy resolution is shown in Figure 6d. The hit cell saturation effect was compensated for as in the electron shower case. This made the energy response of the calorimeter linear and improved the energy resolution by almost a factor of 2 at high energies. The calorimeter energy response to electrons and hadrons as well as the saturation - corrected response is shown in Figure 7.

The electron energy and angle resolutions are roughly what was predicted by a small test calorimeter. The hadron energy and angle resolutions are somewhat degraded from the test calorimeter prediction because of an overly optimistic compensation of the shower noncontainment effects in the test calorimeter.

FLASH CHAMBER ENERGY RESPONSE

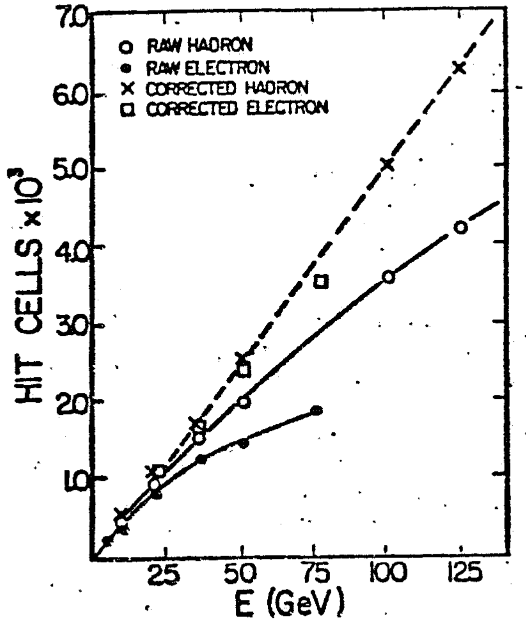

CALORIMETER TRIGGERING SYSTEM

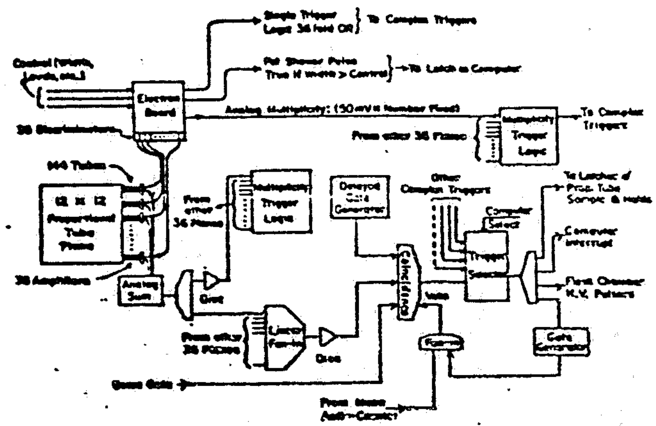

Operation of Proportional Tube Chambers

The proportional tube chambers 12'x12' extruded aluminum planes with 1"x1" cells. Each cell has a 50 m gold-plated tungsten wire ganged four to each amplifier. The system was operated at 1650 v corresponding to a gas gain of approximately 3000. The gas used in these chambers is the standard "P-10" gas 90% Ar - 10% methane. The entire system consists of roughly 5,300 wires and 1,300 amplifiers. The gains of the proportional tubes were monitored by taking source calibration data of the end of every spill. The pedestals were monitored every 2 to 4 hours and were found to be stable to within 10%. The temperature and barametric pressure influences on the proportional tube gains were monitored in the calibration cycle.

Event Triggering and Electronics

Minimizing the response time of the detector to neutrino-induced events is a key consideration in the design of a trigger. Further, in order to trigger the detector with many interactions occuring in a given spill requires real-time pattern recognition capabilities. In this section we describe a system using the proportional tubes designed to satisfy these requirements.

The funadamental constraint on a proportional tube based trigger system is the fluctuations in the time response due to the different drift times of different through particles. We have reduced these fluctuations to a minimum by employing a simple and fast pre-trigger. The "higher level" (and slower) logic then follows the satisfaction of the pre-trigger requirement allowing for signal development without introducing further significant delays.

Each of the 36 amplifier channels in a proportional plane is capable of generating a fast, differential analog output pulse (F0). The trigger electronics are block-diagrammed in Figure 8. Fast processing electronics on each plane distriminates these 36 F0 signals with respect to a programmed threshold. These discriminated F0 signals are then combined to generate the several analog and logic signals used in an event trigger. A brief description of each follows:

1. Sumout (Σ_i):

   This signal is the linear sum of the undiscriminated individual F0 signals from plane i making a single analog output pulse for each plane.

2. Analog Multiplicity (AM_i):
   This is an analog signal with a pulse height equaling a constant (60 mV) times the number of F0 above the discriminator threshold of 20 mV in plane i.

3. Single (S_i):
   This output is the logical "OR" of all discriminated F0 in plane i. The single plane efficiency for a single muon at the 20 mV operating threshold is 80%.

4. Fat Shower Veto (FSV_i):
   This output is a logic pulse generated when the ionization pattern width in plane i is determined to have exceeded a programmed width (a multiple of 4" segments).

The pre-trigger requirement (M) demands that the Σ_i signals of any two or more planes be above a common threshold of 50 mV which is slightly below the minimum ionizing particle pulse height.

The simplest second level criterion employed in an event trigger was the requirement that the total pulse height summed from all proportional planes ($\Sigma\Sigma$) be above some predetermined threshold level. This is essentially a requirement of a minimum energy deposition. The level was chosen by the requirements of the physics reaction of interest and the requirement of minimizing the additional dead time from cosmic rays and spurious coincidence triggers. These false triggers contributed about 8% and 2% respectively to the low-bias trigger with $\Sigma\Sigma$ = 750 mV.

This unique, versatile triggering system allows the exploitation of trigger-time pattern recognition required for minimal dead time in rare-reaction searches.

Summary

The flash chamber-proportional tube calorimeter has been calibrated, has taken data in an engineering run, and has remained stable for long periods of time. Various improvements in the operating characteristics have been made. Additional data will be taken with the full 608 flash chambers - 37 proportional tube chambers in operation in a narrow band neutrino beam during 1982.

References

1. F.E. Taylor et al., IEEE NS-25, 312 (1978).

   F.E. Taylor et al., IEEE NS-27, 30 (1980).

2. J.F. Bartlett et al., IEEE NS-26, 4427 (1979).

3. D.L. Edmonds et al., "A High Voltage Pulse Monitor System for a Flash Chamber Neutrino Detector," to be published in Nuclear Instruments and Methods. 1981.

Appendix C

Design of the Cerenkov Counter

(CI) <u>General Considerations:</u>

To calculate the neutrino flux from the narrow band beam, it is necessary to measure the particle fractions in the momentum analyzed secondary beam. It is proposed that this be done by a Cerenkov counter. This technique has been used successfully in the narrow band beam at the 400 GeV machine. However the extension of this method to the energies of the Tevatron is a significant extrapolation and therefore deserves considerable study. In this Appendix we examine some of the design characteristics of a Tevatron Cerenkov counter. Other preliminary design studies have been performed on this subject[1] and we find that we are essentially in agreement with them.

Since we want to operate the narrow band train in the 500 GeV energy range, the separation of pions from kaons involves distinguishing differences in particle velocities which are very small. The difference in the pion and kaon velocities is given by the following:

$$\Delta\beta = \beta_{\pi} - \beta_{K} \approx (m^2_K - m^2_{\pi})/2p^2 = 4.5\times10^{-7} \qquad \text{(C1)}$$

This is the major consideration in the design of the counter.

Neglecting the diffractive broadening effects for a moment, the Cerenkov light is emitted at a characteristic angle:

$$\cos\theta_C = 1/\beta n \qquad \text{(C2)}$$

which is conveniently written in the small angle limit as:

$$\theta_C = [\,2(n-1) - m^2/p^2\,]^{1/2} \qquad \text{(C3)}$$

Since the meaurement of β is accomplished through the measurement of θ_C, the maximum dependence of θ_C on the particle mass m occurs at low refractive indices near the Cerenkov threshold. The dependence of the

Cerenkov angle on the particle mass m is given by:

$$d\theta_C/dm \approx -m/p^2\theta_C. \qquad (C4)$$

This requires the counter to be operated at small Cerenkov angles which decreases the amount of light emitted and increases the sensitivity to beam angle divergence. Studies indicate that the Cerenkov angle θ_C should be less than 0.3 mrads to get sufficient discrimination of pions from kaons. At 500 GeV/c, $\theta_C < 0.3$ mrads gives 3 times better discrimination than 0.3mrads $< \theta_C <$ 0.6 mrads.

A further complication arises from the diffractive effect in the angle pattern of the emitted Cerenkov light[2]. This effect tends to broaden the characteristic angle θ_C. The emission of Cerenkov light is a coherent process where the wavelets are added over the entire length of the radiator resulting in a characteristic diffraction pattern. The controlling parameter in this addition is the ratio of the wavelength of the emitted Cerenkov light λ to the length of the radiator L. Even for visible light where λ = 500 nm and for a Cerenkov counter measuring meters, this diffraction effect is important.

The number of Cerenkov photons emitted per wave length λ at an angle θ is given by:

$$d^2N/d\lambda d\cos\theta = 2\pi\alpha(L/\lambda)^2 [\sin(x)/x]^2 \sin^2\theta/\lambda \qquad (C5)$$

where $x = \pi L/\lambda[1/\beta n - \cos\theta]$. In the small angle approximation the variable x is given by $x \approx \pi L/\lambda\, [m^2/2p^2 - \epsilon + \theta^2/2]$, where $\epsilon = n-1$. Thus the width of the Cerenkov angle peak will be given by the following:

$$\Delta\theta_{peak} \approx \sqrt{2\lambda/L\theta_C}\,. \qquad (C6)$$

Hence operating at small θ_C makes further demands on the length requirement of the counter.

Figures C1a and C1b show the diffraction pattern for a 1.5m long counter and a 20 m long counter operated at 500 GeV at a constant pressure of 50 mm of Hg helium gas. Note the difference in the angle scales. It is appearent that the 1.5m long counter has a very wide pattern of Cerenkov light making it of limited use in separating pions from kaons.

Operating the counter at such low Cerenkov angles requires that the refractive index of the gas radiator be carefully controlled. For example to separate pions and kaons at 500 GeV to an accuracy of 1/10 of the difference in velocities, the refractive index of the gas radiator has to be set to an accuracy of: $\Delta n/n = (1/10)(\beta_\pi - \beta_K)/\beta \approx 4.5\times10^{-8}$. To estimate the pressure steps this corresponds to we note that the refractive index of the gas radiator is dependent on the gas density by the following relation:

$$(n^2-1)/(n^2+2) = (R/M)\,\rho \qquad \text{(C7)}$$

where R is the molecular refractivity of the gas, M is its molecular weight, and ρ is the density. In the limit of small pressures the refractive index of the gas is given by: $n - 1 = \epsilon \approx (3/2)(R/M)\rho$ and thus n will be linear in the pressure of the gas. For He at 440 nm the refractive index of the gas is approximately $n - 1 = \epsilon \approx 32.67\times10^{-6} \times (P/760)$, where the pressure P is in mm of Hg. Thus 1 mm Hg steps of pressure will change the refractive index by 4.3×10^{-8} which is the desired accuracy discussed above.

Dispersion effects in the emission of the Cerenkov light also degrade the resolution in β. The characteristic Cerenkov angle will change with the wavelength of the Cerenkov light by : $d\theta/d\lambda = (1/\theta)\, d\epsilon/d\lambda$. The dispersion becomes large at short wavelengths

$\lambda < 280$ nm, and if the counter is operated in the wavelength range of 280nm to 440nm, the Cerenkov angle will change by about 0.2 mrad. This is sizable when the operating range is < 0.3 mrad. This effect suggests that longer wavelengths be used where the dispersion effects are smaller. Band pass filters can also be employed to limit the wavelength range of the Cerenkov light and minimize the dispersion effects.

Another loss of accuracy in the separation of pions from kaons at high momentum is caused by the beam momentum and angle divergence. Simulations of the narrow band train (see Appendix A) indicate that the momentum bite of the beam is $\sigma p/p \approx 10\%$, and the angle divergence is approximately $\sigma\theta_x \approx 0.065$ mrads and $\sigma\theta_y \approx 0.048$ mrads. The angle and momentum divergences are correlated. (See Appendix A.)

The momentum bite affects protons to the greatest extent since the change in the Cerenkov characteristic angle is given by: $\Delta\theta_c \approx (1/\theta_c)\ (m^2/p^2)\ (\Delta p/p^2)$. The resulting spread in the Cerenkov angle for a 10% momentum bite at 500 GeV is given by: 1) pions $\Delta\theta \approx$ 0.026 mrads, 2) Kaons 0.32 mrads, and 3) protons 1.2 mrads. Thus the momentum bite is significant for the proton Cerenkov peak and contributes to the width of the Kaon peak. This sensitivity to the proton momentum can be used to actually measure the momentum bite of the beam.

The angle divergence smears out the Cerenkov angle peak by an amount proportional to the divergence. But some of the divergence is attributable to a roughly pointlike source in the narrow band beam optics. By refocussing the Cerenkov optics, some compensation can be made for this effect. In fact, compensation for the difference in the longitudinal position of the source in the x and y coordinates can be achieved by making the Cerenkov parabolic mirror slightly off axis making the resulting astigmatism partially cancel this effect.[3]

(CII) Monte Carlo Simulation:

To simulate operation of the Cerenkov counter we have written a Monte Carlo program which generates the angle distribution given by equation C5 above. The particle fractions were taken from our measurements in E-594 for 400 GeV incident proton energy. The beam momentum and angle divergences were approximated by gaussian distributions. For the momentum bite we assumed $\sigma p/p = 10\%$, and for the angle divergences we took $\sigma\theta_{polar} = 0.1$ mrad. Different counter lengths L, wavelength ranges $\Delta\lambda$ were taken to study the dependence on these parameters.

The particle fractions used in the simulation are given in the Table below. These were determined in our E-594 narrow band beam exposure.

Table CI

Particle Fractions

Momentum(GeV/c)	π-fraction	K-fraction	p-fraction
165/330	29.0±0.3%	4.15±0.2%	66.6±0.6%
200/400	18.9±0.1%	2.83±0.1%	78.2±0.2%
250/500	7.75±0.2%	1.35±0.06%	90.9±0.2%
-165/-330	90.0±0.4%	5.9±0.3%	1.2±0.3%
600*	2.80%	0.7%	96.5%

* These numbers are from the Atherton parameterization scaled to a 800 GeV primary proton energy.

We will concentrate on 500 GeV/c where the separation of pions from kaons is the most difficult. A typical Cerenkov pressure curve is shown in Figure C2 where the pressure has been varied in 1 mm Hg steps. The length of the counter has been fixed at L=40m and the wavelength range was 400nm $<\lambda<$ 600nm. The pressure response is shown for each particle as well as the integral pressure curve. The Cerenkov light within measured angle (including the beam angle divergence) of 0.3 mrads has been integrated. There are roughly 0.1 photons per particle at $\theta_C \approx 0.3$ mrads, so that at 10^{11} particles per burst there is plenty of Cerenkov light.

As a figure of merit we computed the ratio of the kaon peak to the valley between the pion and kaon peak. In Figure C3 we plot this ratio as a function of the beam angle divergence. It is appearent that for angle divergences of < 0.1 mrads the ratio P/V is not strongly affected. In Figure C4, the figure of merit P/V is plotted as a function of the counter length L. We note that there continues to be improvement even at counter lengths of 80 meters. Practical considerations will ultimately limit the length of the counter L. Note that operating at shorter wavelengths has the same effect as lengthening the counter.

For comparison, the simulated E-594 P/V ratios for +165 GeV/c and +250 GeV/c are 10 and 3, respectively. Under these conditions we were able to determine the kaon fraction to about ±5%. Thus we believe that the same accuracy will be obtained in E-649.

The estimated Cerenkov response for the 300 GeV/c setting is shown in Figure C5. The corresponding plot for - 300 GeV/c is given in Figure C6. The demands on the technique are considerably less at the lower momentum settings. In our simulation, we think that it is possible to operate the counter at 600 GeV/c. The P/V ratio there is estimated to be 11:1 compared to 25:1 at 500 GeV/c for a 40m long counter. The corresponding pressure curve at 600 GeV/c is shown in Figure C7.

Another figure of merit was used to study the separation of kaons from pions and protons. For this measure we took the ratio of the pion or proton light within the 95% containment bounds of the kaon peak. The results are given in the table below.

Table CII

Separation of the Kaon Peak

Po (GeV/c)	π/K	p/K
-300	0.087%	0.00173%
300	0.34%	0.078%
500	0.91%	1.65%
600	1.3%	5.2%

The background rises rapidly with increasing Po, but remains small over the proposed momentum range. The momentum dispersion was taken to be 10% and the angle divergence 0.1 mrad.

We have seen that a pressure curve in steps of 1mm Hg is necessary to determine the particle ratios at 500 GeV/c. For 100 points this would require 1.7 hours of steady beam operation. Taking both beam shutter open and closed points at each pressure will double the time. Further requirements are imposed on the stability of the beam by alignment data and various cross checks which are necessary to insure the quality of the data.

Therefore it would be convenient to have a light transducer which would diminish the sensitivity to beam instabilities. A CCD array would allow the beam center to be experimentally determined for each beam pulse by finding the center of the focused Cerenkov ring of light. Cuts on the radius of the ring would be equivalent to any light collimator size allowing considerable flexability in the Cerenkov angle selected. The CCD technology is now mature and suitable devices can be purchased at a reasonable price[4]. Back sided illuminated CCDs would extend the response into the blue wavelength region with good quantum efficiency.[4]

A schematic design of the counter is shown in Figure C8. The counter will be at least 40m long and will probably be located in the Expansion Port. The sensitive optical elements have to be mounted on a rigidly supported table to be insensitive to pressure changes as the Cerenkov curves are taken. An investigation is underway to see if it is possible to use the old 400 GeV/c counter optics with the radiator extended to ≈ 40 meters.

The preliminary design of the Cerenkov counter indicates that it will separate pions and kaons up to 500 GeV/c. But since the design involves a considerable extension of technique, it would be advisable to test its main components before the narrow band beam data run. This could be accomplished in the 800 GeV/c primary proton beam which is used for the NW test beam.

<u>Footnotes and References:</u>

1) D. Cooke and F. Scuilli; Internal experiment memo Aug. 22,1983; and F. Borcherding, March 1986, FNAL TM (in preparation)

2) J. D.Jackson, <u>Classical Electrodynamics</u>, John Wiley, New York; A. Bodek et al. Z. fur Physik C18,289,(1983)

3) F. Borcherding, ibid.

4) M. Blouke, Tektronics Corporation-private communication; M.M. Blouke, et al. SPIE, V570,82,(1985); J.R. Janesick et al. IEEE Transactions on Nucl. Sc. (Nov.1984); J.R. Janesick, SPIE (Aug. 1985)

Figure Captions:

Figure C1a: The diffraction pattern of Cerenkov light for a 1.5 meter long counter operated at 20 mm Hg exposed to a 500 GeV/c pion beam.

Figure C1b: The same conditions but for a 20 meter long counter.

Figure C2a: The pressure curve for pions for a 40 meter long counter operated at $\theta_C < 0.3$ mrads at 500 GeV/c.

Figure C2b: The pressure curve for kaons.

Figure C2c: The pressure curve for protons.

Figure C2d: The composite pressure curve.

Figure C3: The P/V figure of merit in separation of the kaon fraction from the pion fraction as a function of the beam divergence. A momentum bite of 10% was assumed.

Figure C4: The P/V ratio as a function of counter length.

Figure C5: The composite pressure curve for the +300 GeV/c setting.

Figure C6: The composite pressure curve for the -300 GeV/c setting.

Figure C7: The composite pressure curve for +600 GeV/c secondaries.

Figure C8: The schematic design of the Cerenkov counter.

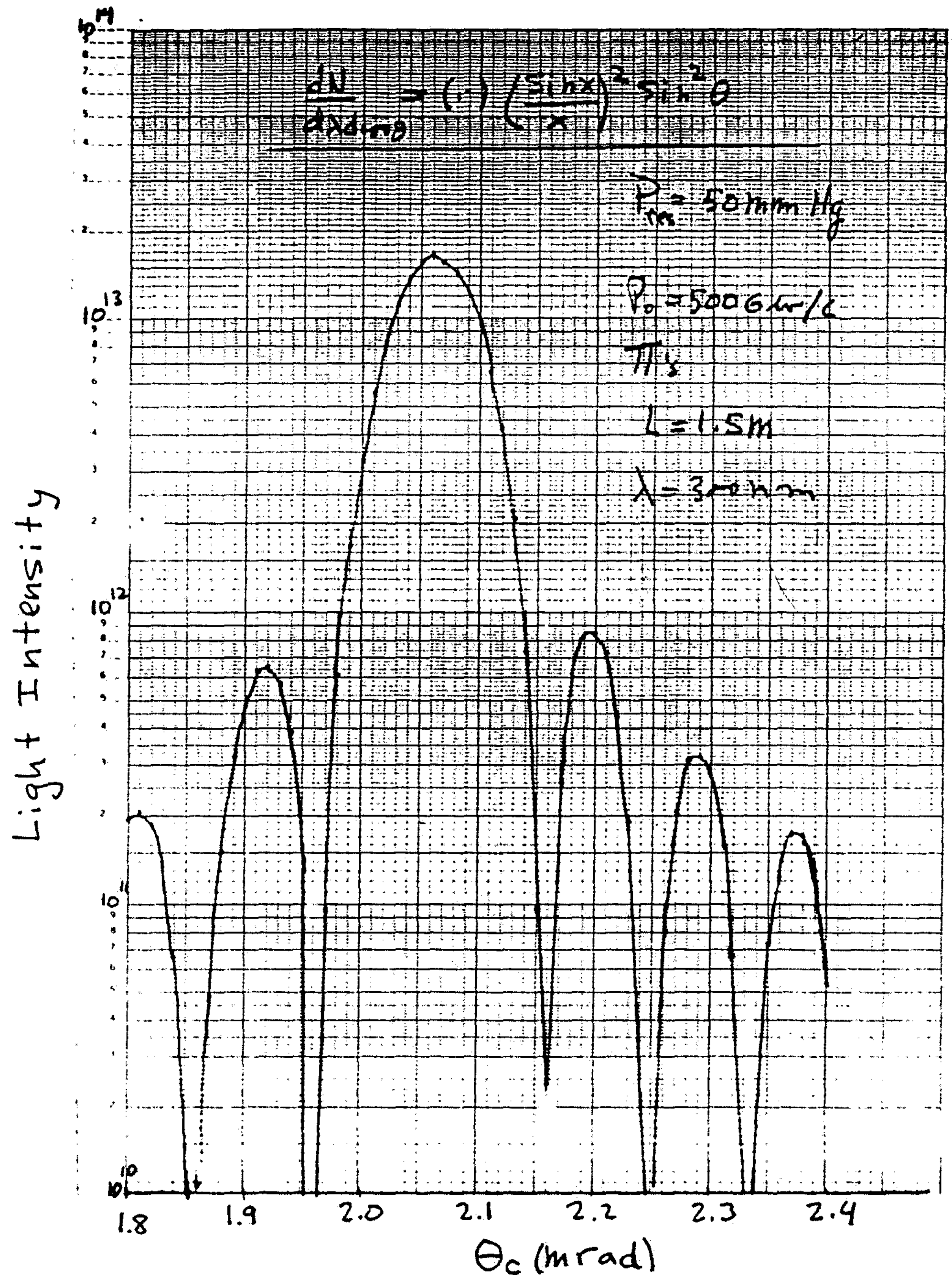

$\frac{dN}{dx\,d\cos\theta} \Rightarrow (\cdot)\left(\frac{\sin x}{x}\right)^2 \sin^2\theta$
$P_{res} = 50$ mm Hg
$P_o = 500$ GeV/c
π's
$L = 1.5$ m
$\lambda = 300$ nm
Light Intensity
10^{14}
10^{13}
10^{12}
10^{11}
10^{10}
1.8
1.9
2.0
2.1
2.2
2.3
2.4
θ_c (mrad)

Figure Cla

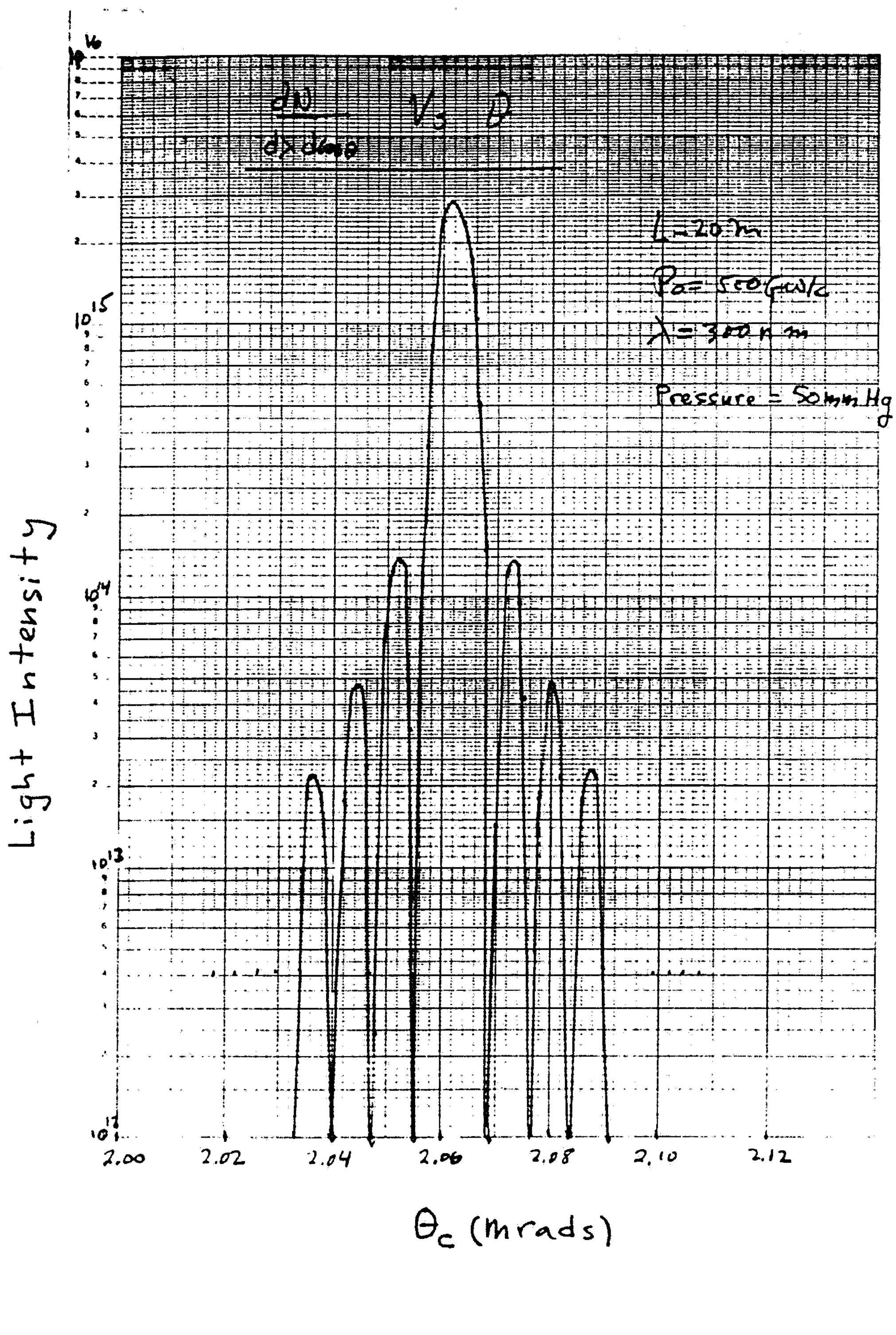

dN / dx dcosθ Vs θ
L = 20 m
Po = 500 GeV/c
λ = 300 nm
Pressure = 50 mm Hg
Light Intensity
θc (mrads)
2.00
2.02
2.04
2.06
2.08
2.10
2.12

Figure C1b

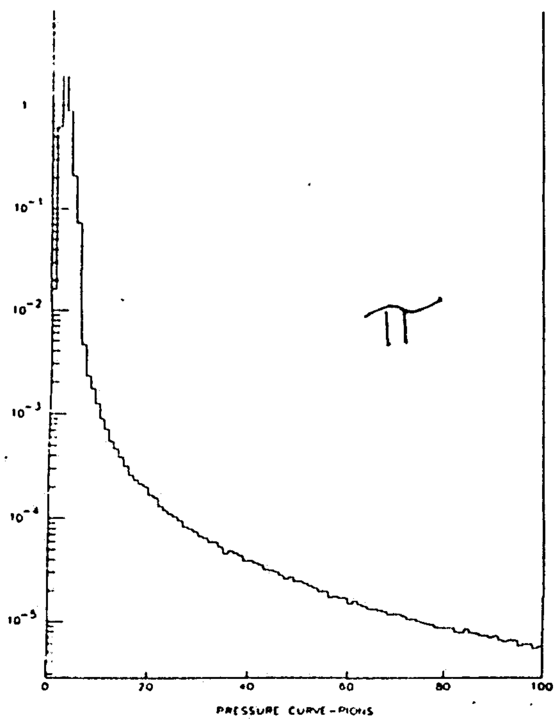

Figure C2a

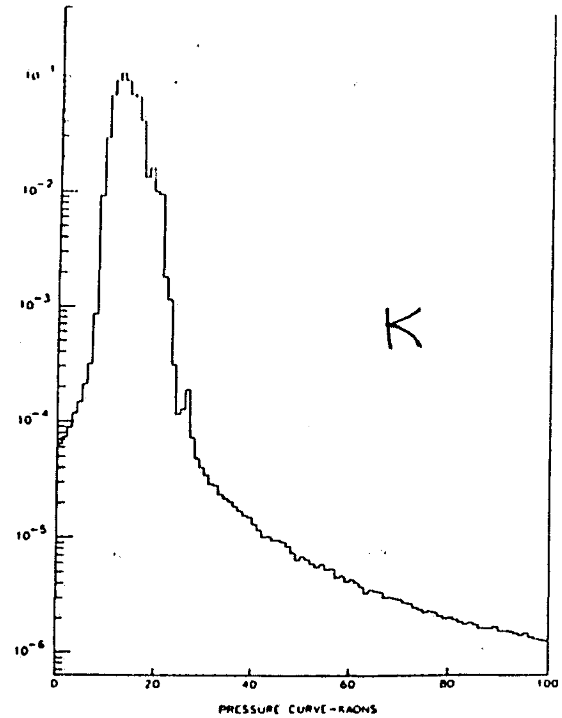

Figure C2b

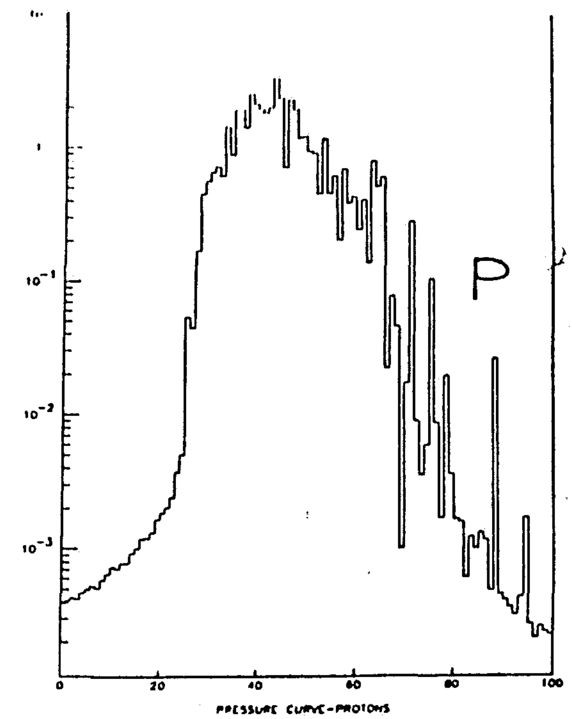

Figure C2c

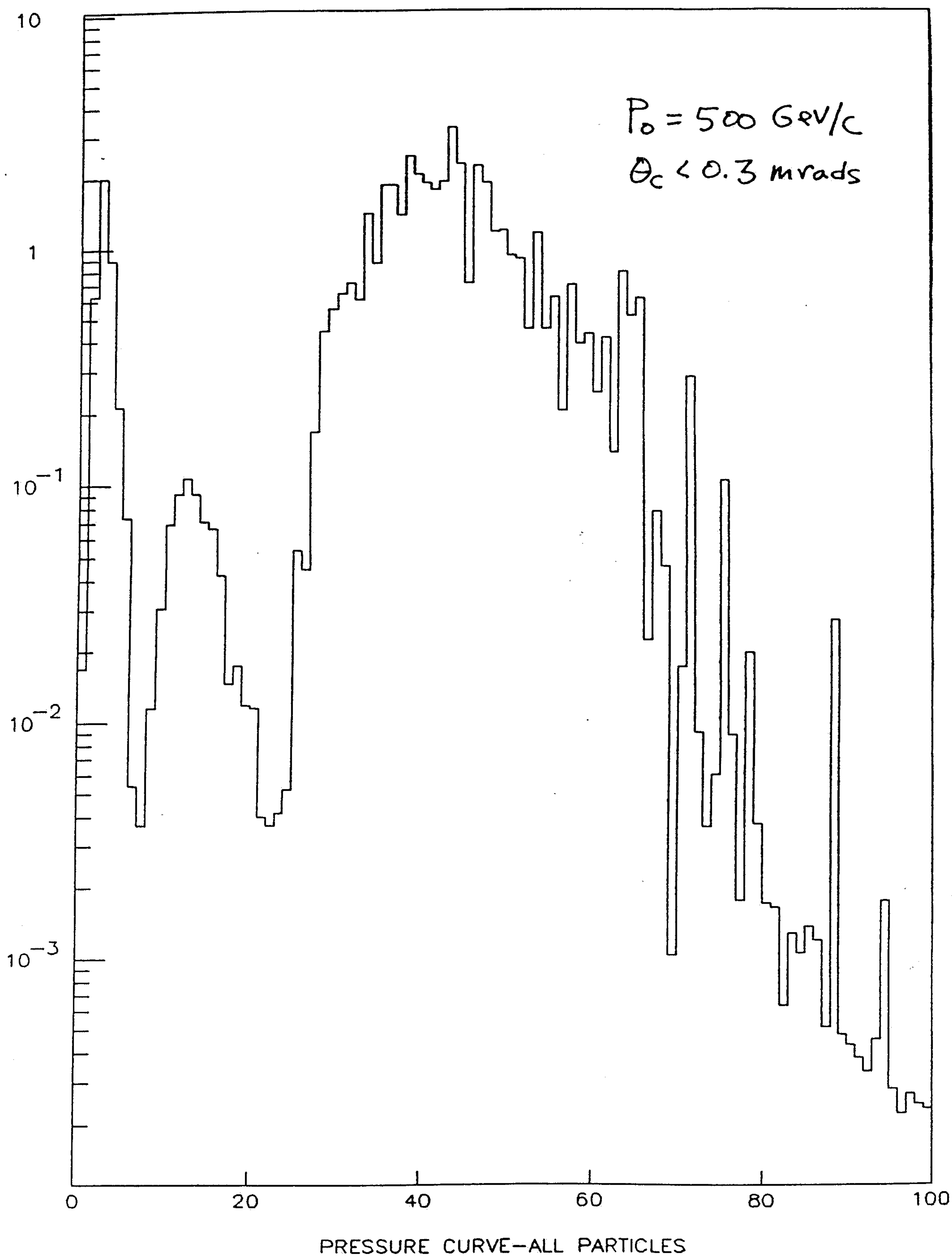

$P_0 = 500$ GeV/c
$\theta_c < 0.3$ mrads
10
1
10^{-1}
10^{-2}
10^{-3}
0
20
40
60
80
100
PRESSURE CURVE—ALL PARTICLES

Figure C2d

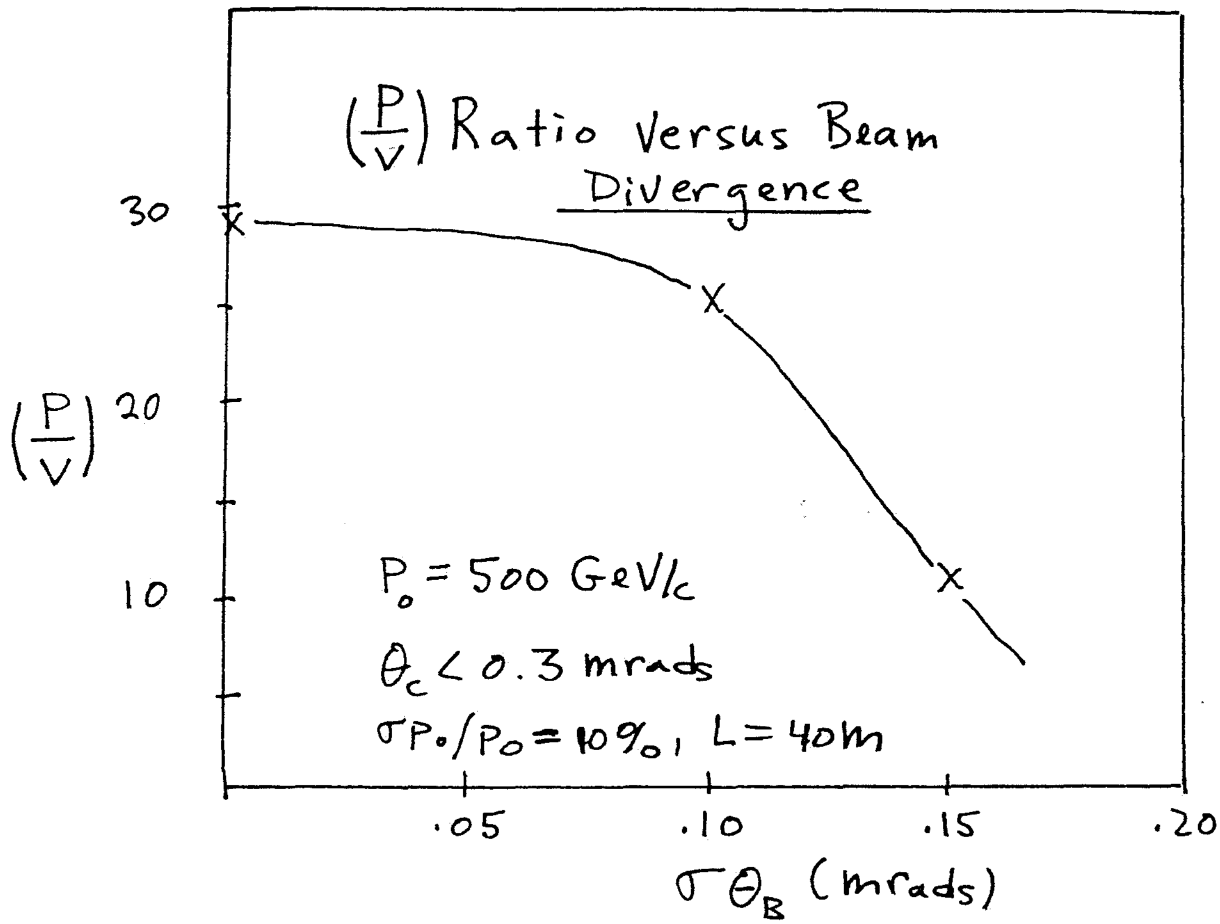

$\left(\frac{P}{V}\right)$ Ratio Versus Beam Divergence
30
20
10
$\left(\frac{P}{V}\right)$
$P_o = 500$ GeV/c
$\theta_c < 0.3$ mrads
$\sigma P_o/P_o = 10\%$, $L = 40$m
.05
.10
.15
.20
$\sigma\theta_B$ (mrads)

Figure C3

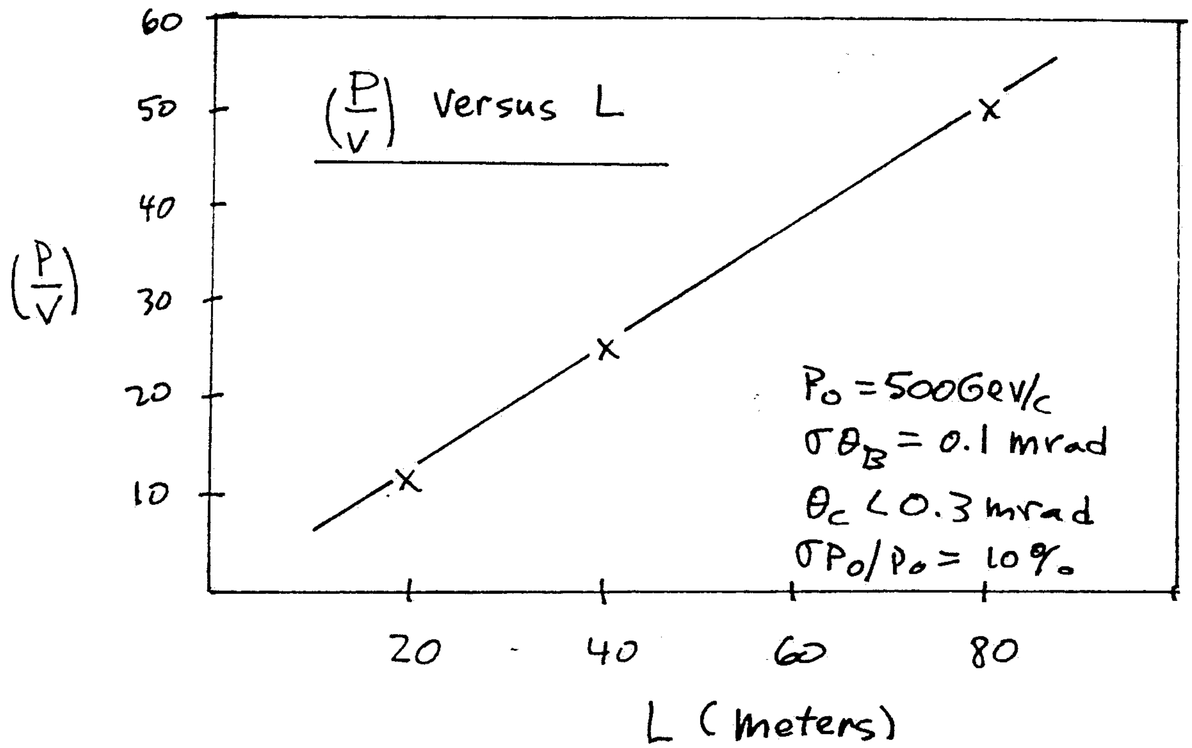

60
50
40
30
20
10
$\left(\frac{P}{V}\right)$
$\left(\frac{P}{V}\right)$ Versus L
$P_0 = 500\,GeV/c$
$\sigma\theta_B = 0.1$ mrad
$\theta_c < 0.3$ mrad
$\sigma P_0/P_0 = 10\%$
20
40
60
80
L (meters)

Figure C4

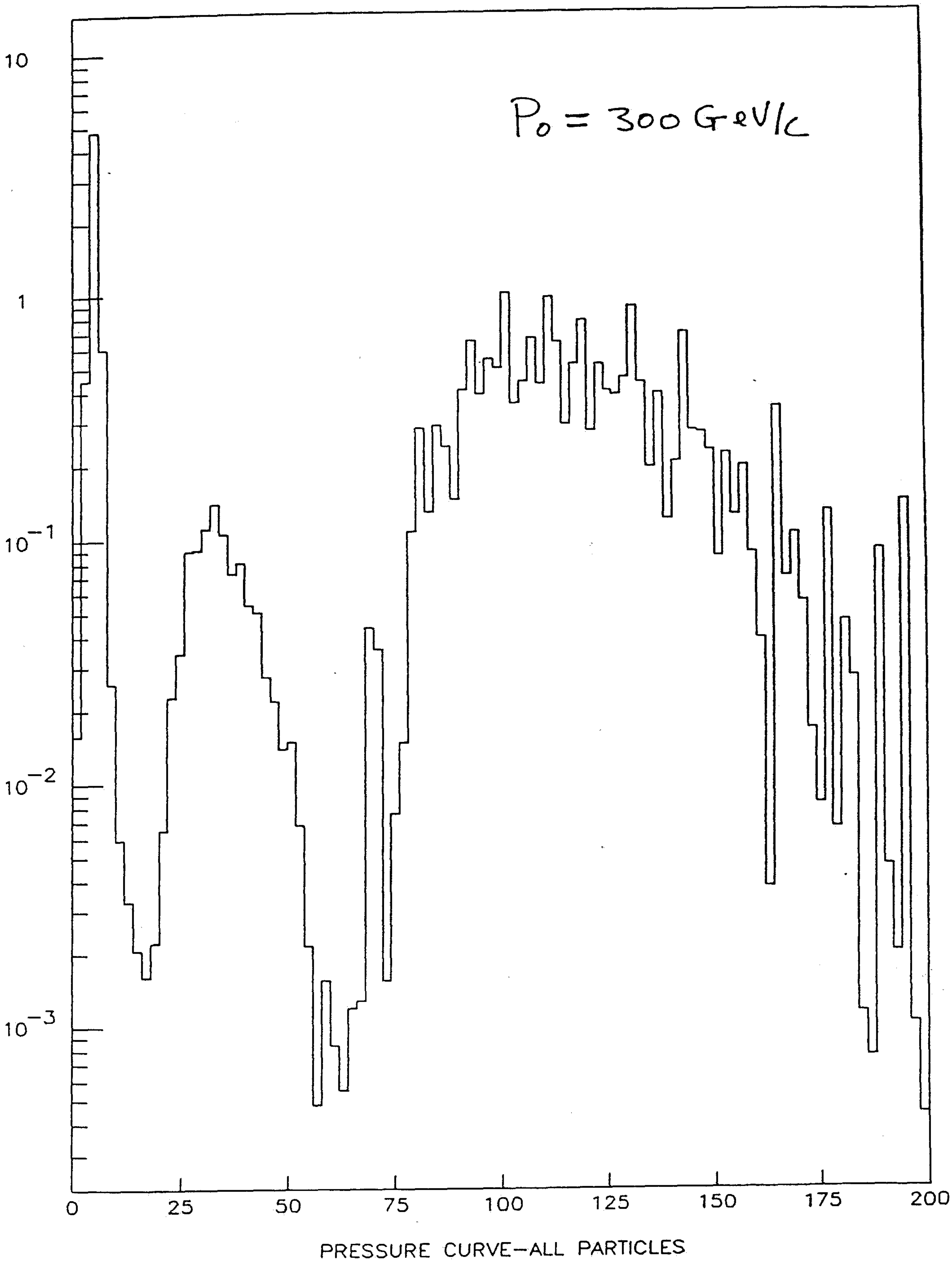

10
1
10^{-1}
10^{-2}
10^{-3}
0
25
50
75
100
125
150
175
200
$P_0 = 300$ GeV/c
PRESSURE CURVE–ALL PARTICLES

Figure C5

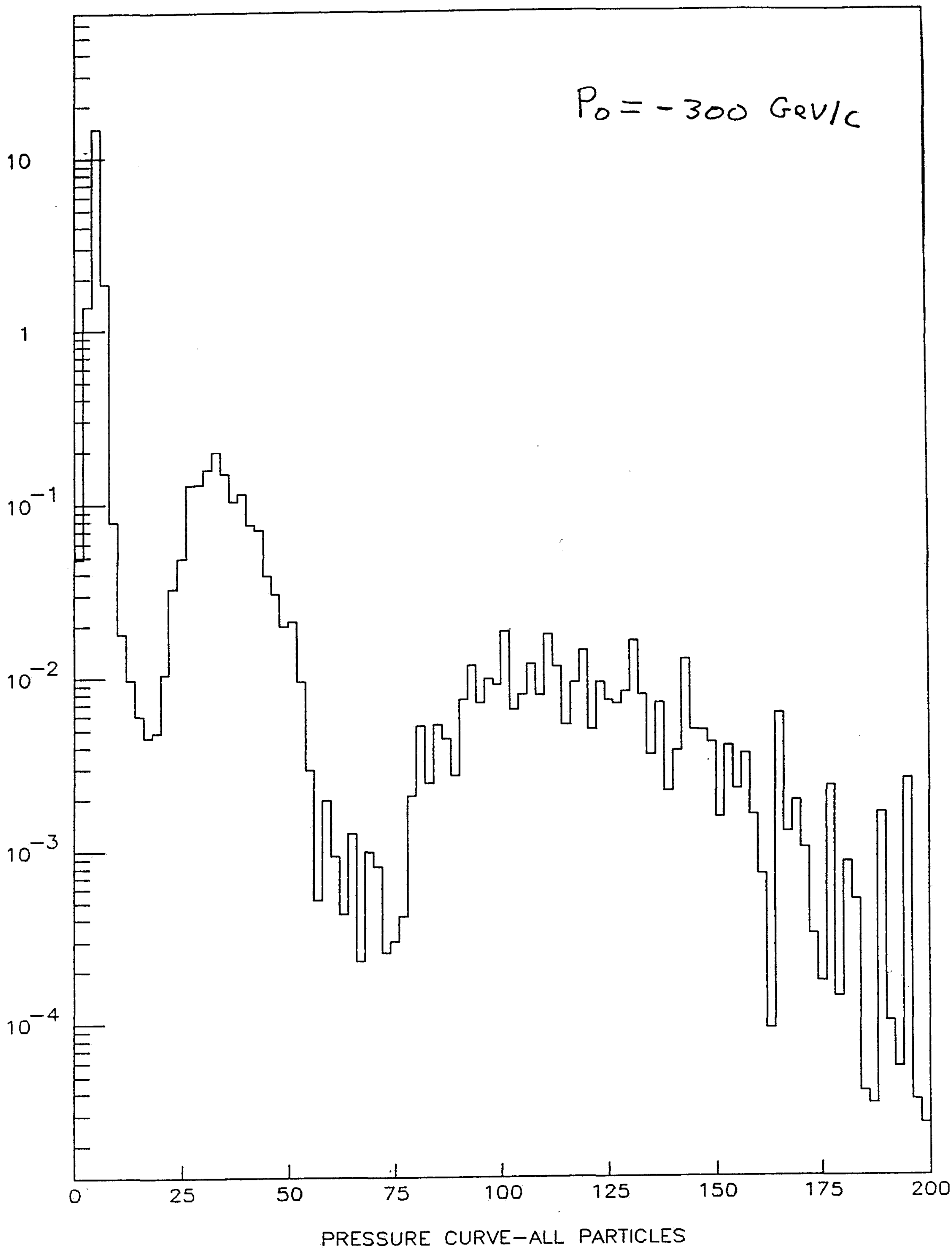

$P_0 = -300$ GeV/c
10
1
10^{-1}
10^{-2}
10^{-3}
10^{-4}
0
25
50
75
100
125
150
175
200
PRESSURE CURVE—ALL PARTICLES

Figure C6

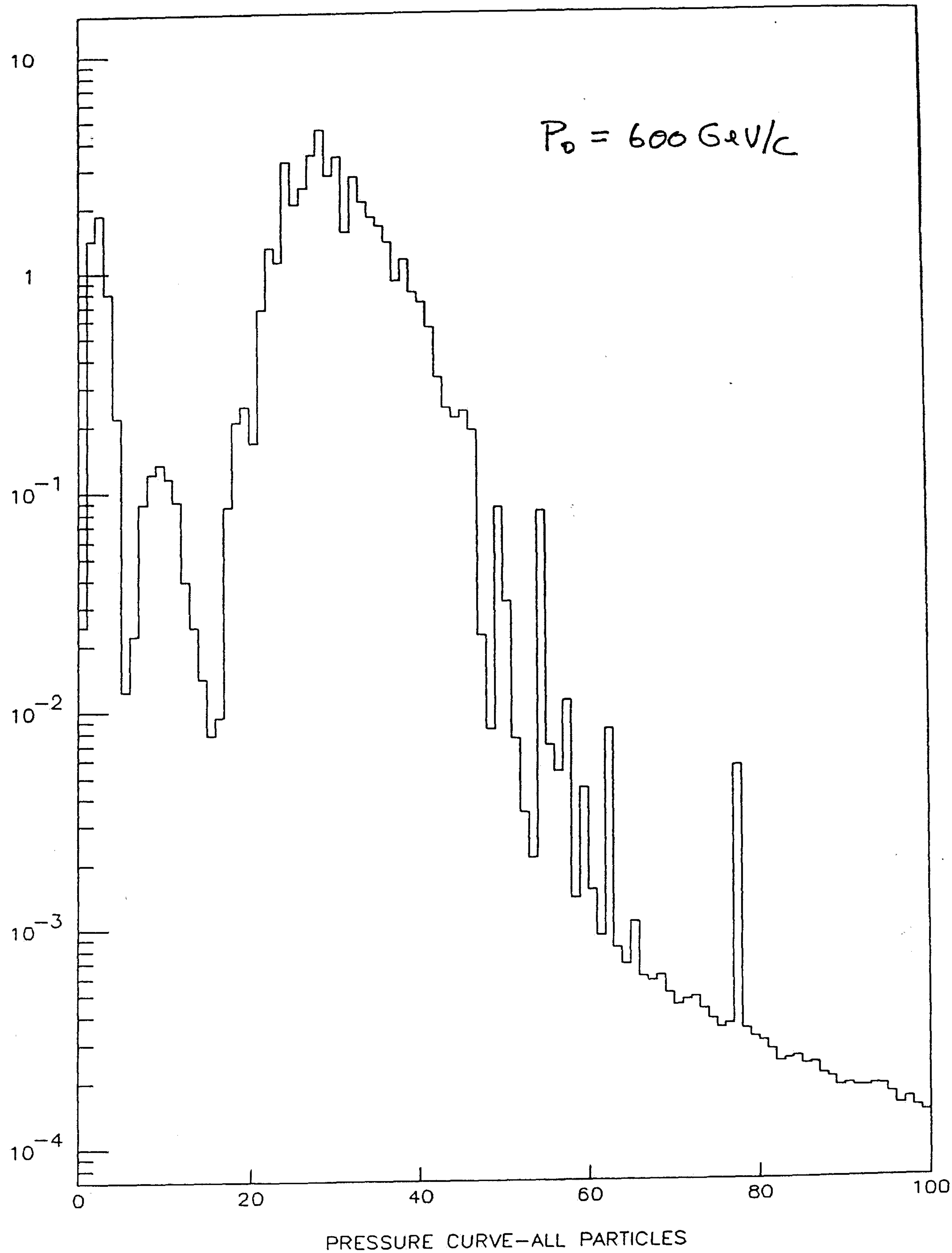
$P_0 = 600$ GeV/c
10
1
10^{-1}
10^{-2}
10^{-3}
10^{-4}
0
20
40
60
80
100
PRESSURE CURVE–ALL PARTICLES

Figure C7

Cerenkov Schematic Design

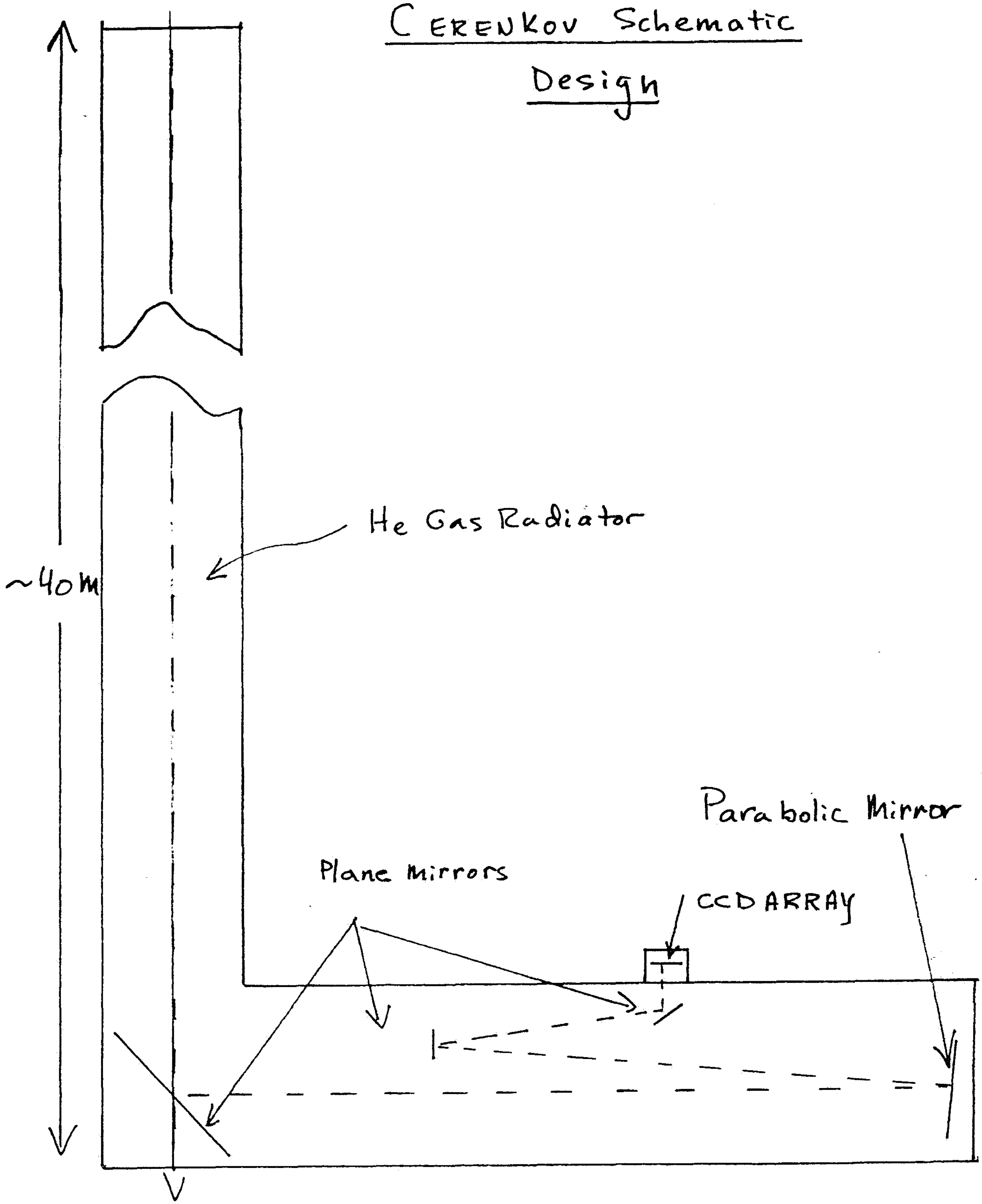

Figure C8

Appendix D

Determination of $\sin^2\theta_w$ and ρ in Deep-Inelastic Neutrino-Nucleon Scattering

Physical Review Letters
Volume 55, Number 19
4 November 1985